Measurements of Azimuthal Angle Dependence of HBT radii with respect to the event plane in $\sqrt{s_{\mathrm{NN}}}$ = 2.76 TeV Pb-Pb collisions at LHC-ALICE

Naoto Tanaka

March 2018

Measurements of Azimuthal Angle Dependence of HBT radii with respect to the event plane in $\sqrt{s_{\mathrm{NN}}} = 2.76$ TeV Pb-Pb collisions at LHC-ALICE

Naoto Tanaka
Doctoral Progam in Physics

Submitted to the Graduate School of
Pure and Applied Sciences
in Partial Fulfillment of the Requirements
for the Degree of Doctor of Philosophy in
Science

at the
University of Tsukuba

Abstract

Quark is a fundamental particle of matter and normally confined in composite particles called hadrons such as protons and neutrons which are the constituents of all kinds of atoms and molecules. On the other hand, for a few millionth seconds after the Big Bang, universe was in extremely high temperature and quarks and gluons were almost not bound together and freely moving at the limitted space. It is like "plasma" state in quark and gluon matter so-called Quark Gluon Plasma (QGP). Therefore, precise understanding of the properties of QGP is a key to access how our universe evolves.

Experimentally, relativistic heavy ion collision is an unique tool to recreate QGP on the earth. The study of nucleus-nucleus collisions at ultra-relativistic energies aims to characterize the properties of QGP. This requires a precise understanding of spatio-temporal evolution.

Hanbury-Brown and Twiss interferometry is an unique tool to access the geometrical source size, freeze-out time, and emission duration of the system, which is an essential study for research of QGP.

Due to the large pressure gradient, QGP is largely expanded toward the surface, and initial elliptic shape which is determined by collision geometry leads to an anisotropy of pressure gradient. If the local thermal equilibrium is established, system evoluion can be described with hydrodynamics, and initial geometrica anisotropy is converted as azimuthal anisotropy in momentum space. Event plane (Ψ_2) is an experimentally measured direction of the short axis of initial elliptic shape based on the charactristics of azimuthal anisotropy itself. Basically HBT interferometry is the method to measure the source size. By combining the HBT measurements and event plane method, HBT interferometry is extended to the method to measure not only the source size but also the source shape at freeze-out. That is measurements of azimuthal angle dependence of HBT radii with respect to event plane. At RHIC, a relation between the initial eccentricity and the final eccentricity was extensively studied with this method. This relation is sensitive to flow profile, expansion time, and viscosity of the source. Results indicate the initial elliptic shape is significantly diluted by collective expansion, but out-plane elongated ellitic shape still remains at freeze-out.

If a huge number of nucleons exist in the nucleus, the shape of initial overlap region would be perfectly elliptic shape. Since intial density distribution largely fluctuations, Initial geometry can have higher order geometrical anisotropy (triangular, quadrangle shape, and higher order anisotropic shape). This triangular shape could be also preserved at freeze-out and obserbed with HBT measurements. Model simulation suggests that finite oscillations of HBT radii with respect to Ψ_3 (an direction perpendicular to the side of a initial triangular shape) can be observed, and first measurements of the azimuthal angle dependence of HBT radii with respect to Ψ_3 are performed at PHENIX. However the oscillation sign of HBT radii with respect to Ψ_3 could not be determined, due to large uncertainties. In order to extract the triangular shape at freeze-out and constrain theoretical model, it is important to disentangle the oscillation sign of HBT radii relative to Ψ_3. In LHC energy, large multiplicity and excellent event plane resolution in ALICE detector allows us to measure the azimuthal angle dependence of HBT radii with respect to Ψ_3 much more precisely. Furthermore, hydrodynamical model predicts oscillatons of HBT radii with respect to Ψ_2 in LHC energy could be different to those in RHIC. Measurement of azimuthal angle dependence of HBT radii with respect to Ψ_2 and Ψ_3 in LHC energy is one of the important studies to understand the system evolution of heavy ion collisions.

Since ellipticity of participant becomes larger from central to peripheral collisions, "centrality" is one of the good probes for initial geometry. Also a triangular shape slightly changes with centrality due to the difference of the number of participating nucleons. However, when centrality changes from central to peripheral, not only initial geometry but also system size, freeze-out temperature and flow velocity changes simultaneously. In order to separate the difference of system size and system shape, another probe to initial geometry is indispensable. Recently Event Shape Engineering technique is developed, which is method to select initial geometry within a certain centrality This technique gives us the new insight of relation between the initial geometry and other observables.

In this thesis, measurements of azimuthal angle dependence of pion HBT radii with respect to Ψ_2 and Ψ_3 in Pb-Pb collisions at $\sqrt{s_{\rm NN}}$ = 2.76 TeV with ALICE detector is performed and the space time evolution of heavy ion collisions is discussed with the relation between the initial collision geometry and geometrical source shape at freeze-out. Explicit oscillation can be observed in azimuthal angle dependence of HBT radii with respect to Ψ_2. Final source eccentricity was extracted with relative amplitudes of HBT radii and a relation to initial eccentricity calculated with Glauber simulation. it indicates that ,in heavy ion collisions, large collective flow strongly expands the source along the short axis of elliptic shape during QGP state and final source eccentricity are significantly diluted. For azimuthal angle dependence of HBT radii with respect to Ψ_3, no significant oscillation of HBT radii can be found in the direction of beam axis. However, in the azimuthal plane, we can determine the oscillation sign of HBT radii with respect to Ψ_3.

Also, Event Shape Engineering technique is applied to the measurements of azimuthal angle dependence of pion HBT radii with respect to Ψ_2. This is the first measurements. Relation between initial geometrical source shape and final source shape at freeze-out within a certain centrality are measured as a function of centrality. Oscillation amplitudes of HBT radii in azimuthal plane with respect to Ψ_2 are significantly modified with Event Shape selection. The difference of oscillation amplitudes of HBT radii within a certain centrality is scaled with $2^{\rm nd}$-order azimuthal anisotropy. Blast wave model is an analytical tool to extract freeze-out paramaters by fitting spectra of identified hadrons, azimuthal anisotropy, and azimuthal angle dependence of HBT radii with respect to event plane. Blast wave fitting is performed to HBT measurements with Event Shape Engineering in order to interpret the difference of oscillation amplitudes of HBT radii.

Event Shape Engineering is also applied to the measurements of azimuthal angle dependence of pion HBT radii with respect to Ψ_3. This is also the first measurements. Contrary to HBT measurement with respect to Ψ_2, no significant modification can be found in Event Shape Engineering selection to azimuthal angle dependence of HBT radii with respect to Ψ_3, though $3^{\rm rd}$-order azimuthal anisotropy is explicitly modified with Event Shape selection.

Contents

List of Figures

List of Tables

Acknowledgement

This thesis would not have been possible if not for Prof. Yasuo Miake. He gave me an opportunity to have great experiences in the field of heavy ion collisions. His extensive knowledges of heavy ion physics, detector, and electronics always stimulate my interest to this field. I am deeply grateful to Prof. ShinIchi Esumi for daily discussion and a great deal of ideas which not only enlightened my analysis, but also gave me an encouragement to never give up. I have learned a lot of things from him, knowledge of heavy ion physics, experimental techniques, and how interesting physics on heavy ion collisions is. I would like to thank Prof. Tatsuya Chujo for giving me comments and many opportunities to talk at workshops. I would like to thank Prof. Motoi Inaba. His knowledge and experience of hardwares always help me to solve some problems of detectors and electronics. I would also like to thank Prof. Oliver Busch, Prof. Shingo Sakai, Prof. Yosuke Watanabe, Prof. Kyoichiro Ozawa, and Prof. Hiroyuki Sako for giving me a lot of comments and suggestions of this analysis. I would like to express my gratitude to Prof. Kazuhiro Yabana for his comments and advices for my thesis. Comfort and useful computing sytems in our group would never been possible without Mr. Sumio Kato.

This work was also supported by Takafumi Niida. I am deeply grateful to him for his careful reading of my thesis and always giving me new insights, useful commets, and advices for my analysis. I have learned knowledge and tecnique of HBT from him. I also thank Dr. Dosatsu Sakata and Dr. Juhyun Bohm for their support.

I would like to thank Dr. Sanshiro Mizuno, Dr. Hiroshi Nakagomi, Dr. Daisuke Watanabe, Ms. Tomo Nakajima, Ms Kaoru Gunji, and Mr. Satoshi Horiuchi for encouragement and interesting conversations.

I also thank all the members of High Energy Nuclear Physics Group at University of Tsukuba, Mr. Hiroki Yokoyama, Dr. Toshihiro Nonaka, Mr. Ritsuya Hosokawa, Mr. Ryo Aoyama, Mr. Tetsuro Sugiura, Mr. Lee Joonil, Mr. Byungchul Kim, Mr. Kazuki Sato, Mr. Yoshimi Rebaza, Mr. Taichi Ichisawa, Mr. Hiroki Kato, Mr. Yota Kawamura, Mr. Daichi Kawana, Mr. Kazuya Nakagawa, Mr. Toma Suzuki, Ms. Mina Hatakeyama, Ms. Yukiko Hoshi, Ms. Kana Nakagawa, Mr. Hiroshi Saito, Mr. KenIchi Tadokoro, Mr. Masahiro Takamura.

Finally, I would like to thank my family Hideo, Kimiyo, and Ayano. This thesis would have never been completed without their countinuos supports and understanding.

Chapter 1

Introduction

A quark is a fundamental particle of matter and normally confined in composite particles called hadrons such as protons and neutrons which are the constituents of all kinds of atoms and molecules. On the other hand, for a few millionth seconds after the Big Bang, universe was in extremely high temperature and quarks and gluons were almost not bound together and freely moving at the limitted space. It is just like "plasma" state in quark and gluon matter so-called Quark Gluon Plasma(QGP). That is to say, precise understanding of the properties of Quark Gluon Plasma is a key to access how our universe evolves.

In this chapter, we introduce Quantum Chromodynamics, where the QGP is predicted, and relativistic heavy ion collisions.

1.1 Quantum Chromodynamics and Quark Gluon Plasma

Strong interaction between quarks and gluons are described in Quantum Chromodynamics(QCD), where gluons mediate strong interaction of quarks. It is analogous to Quantum Electrodynamics(QED) which describes the electro-magnetic interaction between two charged particles. In QED, photons mediate the electro-magnetic interaction. Unlike photons, gluons themselves have color charge and participate in the strong interaction.

For a quark with invariant mass m_f, the classical Lagrangian density can be expressed by:

$$\mathscr{L} = \sum_{f}^{Nf} \bar{q}_f \left(i\gamma^{\mu} D_{\mu} - m_f \right) - \frac{1}{4} F^{a}_{\mu\nu} F^{a}_{\mu\nu}, \tag{1.1}$$

where q_f denotes quark field in three different flavor $f\,(=1,2,3)$, γ^{μ} is the Dirac matrix, D_{μ} is the co-variant derivative of QCD and gluon field strength tensor is presented as $F_{\mu\nu}$. D_{μ} and $F_{\mu\nu}$ are given by:

$$D_{\mu} = \partial_{\mu} + ig\frac{\lambda_a}{2}A^a_{\mu}, \tag{1.2}$$

$$F^a_{\mu\nu} = \partial_{\mu}A^a_{\nu} - \partial_{\nu}A^a_{\mu} - gf_{abc}A^b_{\mu}A^c_{\nu}, \tag{1.3}$$

where $A^a_{\mu\nu}$ is gluon field in eight different flavour $a\,(=1,...,8)$, λ_a is eight Gell-Mann matrices, g denotes the dimensionless coupling constant in QCD, which indicates the interaction strength of quark to quark and quark to gluon. Coupling constant g can be defined with fine structure constant α_s by:

$$g \equiv \sqrt{4\pi\alpha_s}. \tag{1.4}$$

Using perturbative QCD (pQCD) theory, α_s can be expressed as a function of momentum transfer Q given by:

$$\alpha\left(Q^2\right) = \frac{1}{\beta_0 \ln\left(Q^2/\Lambda_{QCD}\right)}, \tag{1.5}$$

where Λ_{QCD} is called QCD scale parameter, which denotes the coupling strength in QCD, β_0 represents the first term of β-function. Equation 1.5 indicates pQCD suggests the coupling constant α_s is not "constant" any more but the function of Q. Figure 1.1 shows the running coupling constant α_s as a function of momentum transfer Q, which is measured from various reaction such as τ decay, deep inelastic scattering [1], Υ decay, e^+e_- annihilation, Z decay, and p_{T} dependence of jet cross section in $p\bar{p}$. pQCD calculation shows excellent agreement to experimental results. One can find the important characteristic of strong interaction in QCD from Fig. 1.1. Coupling constant α_s becomes rapidly weaker from small Q to large Q. It indicates when the momentum scale increases, interaction of quark-gluon and quark-quark significantly decreases, called "asymptotic freedom". Therefore, at the limit as Q approaches infinity, quarks and gluons can be free to move as if they were "free particle".

At small momentum scale Q, however, pQCD calculation is no longer able to be relied on, as perturbative approximation does not converge at small Q (< 1 GeV/c) due to large α_s. A Lattice QCD is an ideal tool of non-perturbative QCD calculation to describe the interaction of quarks and gluons at small momentum scale. Figure 1.2 shows the static quark potential as a function of the distance of quark to anti-quark in 2+1 flavor Lattice QCD calculation [2]. Result of quark potential $V\left(r\right)$ in Lattice QCD is fitted with the following equation :

$$V\left(r\right) = V_0 - \frac{\alpha}{r} + \sigma r, \tag{1.6}$$

where V_0, α, and σ are free parameter for fitting and the simulated results are well reproduced with the fitting function. Equation 1.6 indicates strong interaction can be described as $1/r$ such like Coulomb potential at short range and are proportional to the distance r at long range. At the limit as the distance r approaches to infinity, quark potential $V(r)$ becomes infinity, which indicates quarks are confined in the hadrons and can not be isolated from them. This is called "color confinement" and also important characteristics of strong interaction, as is the case with the asymptotic freedom.

Phase transition is frequently used to describe transitions between solid, liquid, and gaseous states of matter. It is well known that first-order phase transition of water (liquid-vapor and liquid-solid) occurs when its temperature and pressure exceed the transition line. Based on the asymptotic freedom, phase transition in QCD is predicted. In extemely high temperature or high baryon density, quarks and gluons are de-confined from the hadrons into a deconfined matter, so-called Quark Gluon Plasma. Lattice QCD suggests one of the numerical calculations of phase transition in QCD matter, though Lattice QCD can be applicable at the limit as baryon density approaches to zero.

Figure 1.3 shows energy density and 3 times pressure normalized by temperature to the fourth calculated on Lattice QCD [3]. Both ε/T^4 and $3\mathrm{p}/T^4$ rapidly rise at the vertical band dipicted in Fig. 1.3 (185 MeV < T < 195 MeV). ε/T^4 indicates the degrees of freedom of quarks and gluons. This significant rise of degrees of freedom indicates the phase transition of hadrons-Quark Gluon Plasma. Horizontal line on ε_{SB} denotes the Stefan Boltzmann limit where the interaction of quarks and gluons are ignored. Excess from the Lattice QCD results(red and blue) comes from the interaction of quarks and gluons.

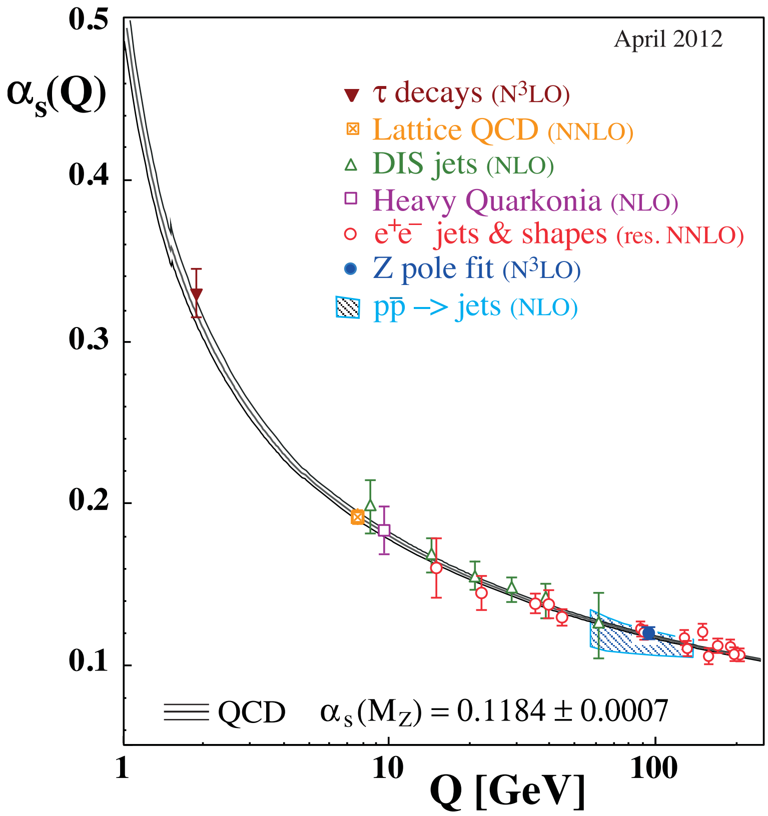

Figure 1.1: The running strong coupling constant α_s as a function of momentum transfer Q , which is determined from τ decay, deep inelastic scattering process, radiative Υ decay, hadronic final states of e^+e^- annihilation, hadronic Z decay width and inclusive jet cross section in $p\bar{p}$ [1]. Data is compared with pQCD calculation shown in black line.

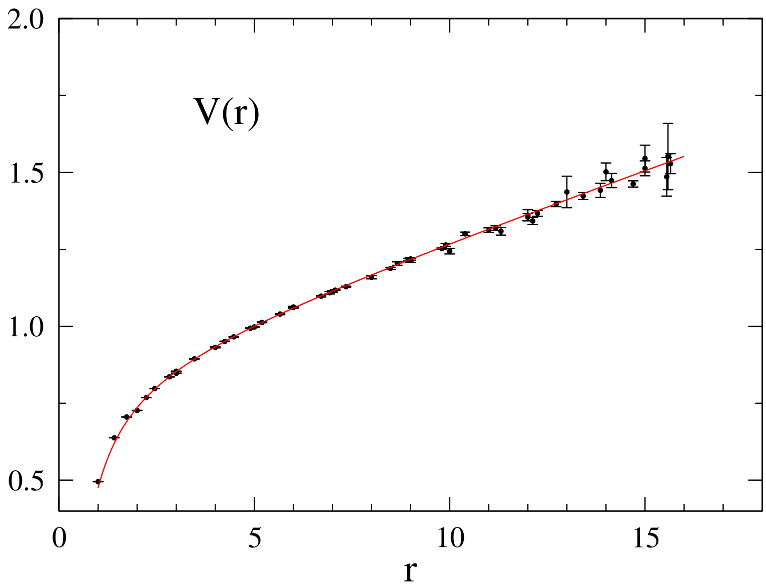

Figure 1.2: Static quark potential as a function of distance between quark and anti-quark in 2+1 flavor Lattice QCD calculation [2]. Simulation result (black marker) is fitted with Eq. 1.6.

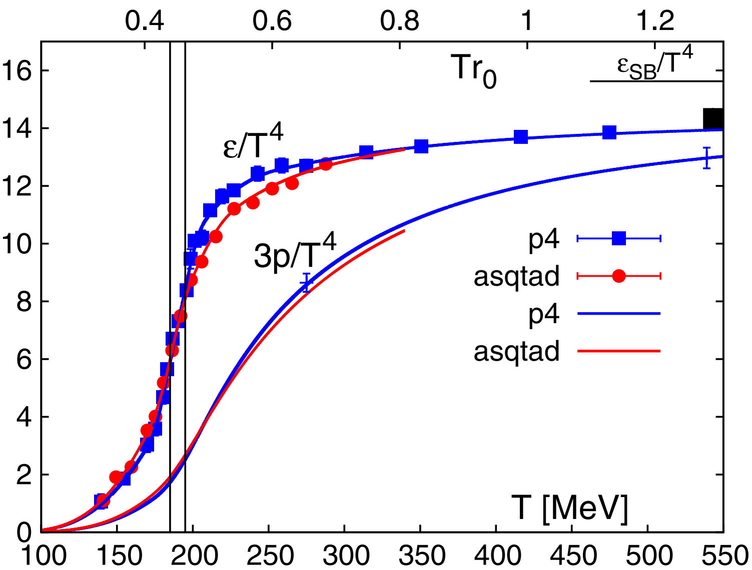

Figure 1.3: Energy density and 3 times the pressure normalized by T^4 calculated on Lattice QCD as a function of temperature [3]. ε_{SB}/T^4 denotes the Stefan-Boltzmann limits where the interaction of two particles are ignored. The vertical band indicates the transition region 185 MeV < T < 195 MeV. The black bars at high temperatures indicate the systematic shift of data that would arise from matching to a hadron resonance gas at T = 100 MeV.

1.2 Relativistic Heavy Ion Collisions

In order to study the properties of Quark Gluon Plasma, sufficient energy density and temperature to bring the QCD phase transition is necessary. Experimentally, relativistic heavy ion collision is the unique tool to recreate QGP on the earth. Two massive ions such as gold and leads are relativistically accelerated at nearly speed of light with the accelerator complex and two ions have a head-on collisions at the energy of upwards of a few TeV. In order to recreate QGP, powerful heavy ion accelerators are necessary.

Currently, high energy heavy ion experiments are performed with accelerator complex at European Organization for Nuclear Research (CERN) and Brookhaven National Laboratory (BNL). Large Hadron Collider (LHC) and Relativistic Heavy Ion Collider(RHIC) are built in CERN and BNL, respectively. At LHC, in particular studies on energy loss in QCD matter and detailed bulk properties are ongoing through world top energy $\sqrt{s_{\mathrm{NN}}}$ = 5.02 TeV Pb-Pb collisions. On the other hand, study of phase diagram in QCD and to find the critical end point are performed with beam energy scan at RHIC.

Table 1.1 shows the summary of relativistic heavy ion collisions experiments. Data used in this analysis is $\sqrt{s_{\mathrm{NN}}}$ = 2.76 TeV Pb-Pb collision events obtained by A Large Ion Collider Experiment (ALICE) at LHC.

In order to recreate Quark Gluon Plasma, filling the large area with high baryon density state is important. therefor massive ions are used to study Quark Gluon Plasma. Pb and Au nucleus are often used and their radius are approximately 7 fm. Recently, it is expected that QGP might can be regenerated even in small system collisions, such as p-Pb, d-Au and related analysis is actively performed.

Table 1.1: Summary of relativistic heavy ion collisions

Year	Accelerators	Location	Species	$\sqrt{s_{\mathrm{NN}}}$ Energy(GeV)
1986	AGS	BNL	^{16}O, ^{28}Si	5.4
1992			^{197}Au	4.8
1986	SPS	CERN	^{16}O, ^{32}S	19.4
1994			^{208}Pb	17.4
2000	RHIC	BNL	^{197}Au	130
2001			^{197}Au	200
2003			d-^{197}Au	200
2004			^{197}Au	200, 62.4
2005			^{63}Cu	200, 62.4, 22.4
2007			^{200}Au	200
2008			d-^{197}Au	200, 62.4
2010			^{197}Au	200, 62.4, 39, 11.5, 7.7
2011			^{197}Au	200, 19.6, 27
2012			^{238}U	193
2012			^{63}Cu-^{197}Au	200
2014			^{197}Au	200, 14.6
2014			^{3}He-^{197}Au	200
2015			p-^{197}Au	200
2015			p-^{197}Al	200
2016			^{197}Au	200
2016			d-^{197}Au	200, 62.4, 19.6, 39
2017			^{197}Au	54
2010	LHC	CERN	^{208}Pb	2760
2011			^{208}Pb	2760
2013			p-^{208}Pb	5020
2015			^{208}Pb	5020
2016			p-^{208}Pb	5020, 8160
2017			^{129}Xe	5440

1.2.1 Participant Spectator Picture

Figure 1.4 shows the schematic illustration of colliding nuclei before and after a collision. Since two colliding nuclei are accelerated at the nearly speed of light, The longitudinal size shrinks due to Lorentz contracted shown in Fig. 1.4(left). Longitudinal size is expressed as $2R/\gamma$, where R is a radius of each nucleus and γ denotes Lorentz factor.

The degree of overlap area is defined as impact parameter b, which is the distance between the centers of the two colliding nuclei in a transverse plane to the beam axis.

Since the time scale in relativistic heavy ion collisions is much shorter than Fermi motion of nucleons in two colliding nuclei, "Participant Spectator picture" can be applicable to describe the collision geometry. After the collision, nucleons in two colliding nuclei are categorized into two types, participant and spectator. Participant is the nucleons which participate to the collision shown as red, blue, and green particles in Fig. 1.4(right). Spectator is the nucleons which does not participate to the collision shown as white particles in Fig. 1.4(right).

In order to understand the property of QGP, initial collision geometry, such as impact parameter b, number of participant N_{part} and participant shape is essential. However these value cannot be directly measured in experiment. Instead of measuring impact parameter b, "centrality" is estimated by measured multiplicity. The other valuables are determined with Glauber model simulation [5].

Based on the Wood-Saxon potential, density distribution of nucleons are expressed by:

$$\rho_A(r) = \frac{\rho_0}{1+\exp\left(\left[r-R_A\right]/a\right)}, \tag{1.7}$$

where r denotes radius of each nucleon, R_A is nucleus radius, a is diffusion parameter in nucleus surface. ρ_0 represents the normalization factor where $\int d^3r\rho^A(r) = A$. Density function of nucleon is given with the integration of Eq 1.7 in the direction of z axis, which is given by:

$$T_A(x,y) = \int_{\infty}^{\infty} dz\rho_A(x,y,z). \tag{1.8}$$

Number of participant in a certain x, y coordinate is represented as n_{part} and given by:

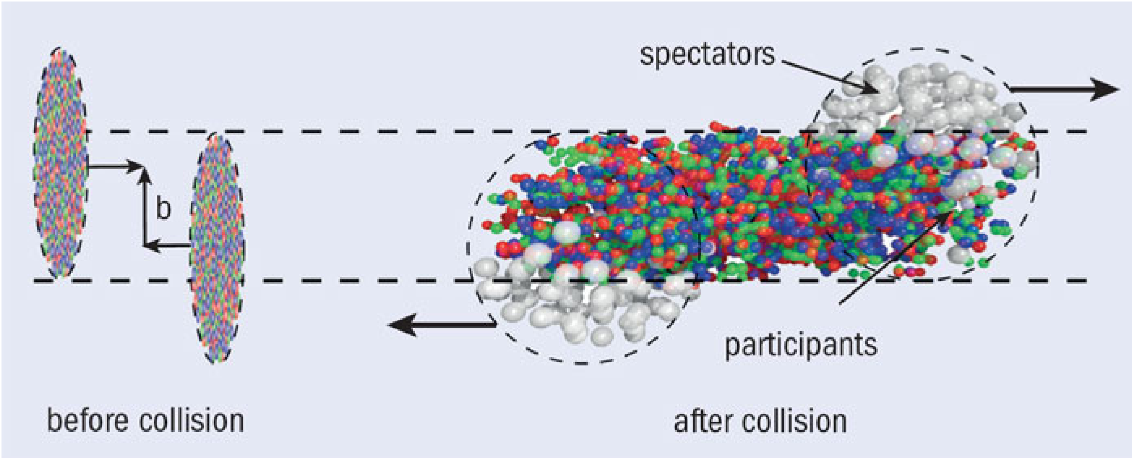

Figure 1.4: Schematic illustration of colliding nuclei before and after the collision [4]. Impact parameter is defined as the distance between the centers of the two colliding nuclei in a transverse plane to the beam axis. In relativistic heavy ion collision colliding nuclei is divided into participant ,which participate to collisions, and Spectator that does not participate to collisions.

$$
\begin{aligned}
n_{part} = T_A\left(x+b/2,y\right)\left[1-\left(1-\frac{\sigma_0}{T_B\left(x-b/2,y\right)}\right)^B\right] \\
+T_B\left(x-b/2,y\right)\left[1-\left(1-\frac{\sigma_0}{T_A\left(x+b/2,y\right)}\right)^A\right],
\end{aligned}
\tag{1.9}
$$

where the centers of two colliding nuclei are shifted by impact parameter b, A and B are mass of two nuclei, σ_0 denotes the cross section of an inelastic p-p collisions at corresponding collision energy. Then the number of participant N_{part} is expressed as integration of Eq 1.9 :

$$
N_{part}\left(b\right) = \int dxdyn_{part}\left(x,y;b\right), \tag{1.10}
$$

1.2.2 Space Time Evolution

After the collision, if the energy and baryon density are sufficient, phase transition to Quark Gluon Plasma occurs in overlap region of two colliding nuclei. System cools down as it expands significantly and eventually phase transition to hadron state takes place. Figure 1.5 shows the schematic diagram of space-time evolution in relativistic heavy ion collisions. Two nuclei are approaching from z > 0 (< 0) and t < 0. Two nuclei collide at z = 0 and t = 0.

In Fig. 1.5, space time evolution of heavy ion collisions is classified into 4 stages.

- Parton Cascade (Pre-equilibrium)
- QGP state
- Chemical freeze-out
- Kinetic freeze-out

Parton Cascade (Pre-equilibrium)

After the collision, huge number of partons are created by hard scattering and large energy density, which is deposited by the nucleus collision, in initial overlap region in two colliding nuclei. Some of the models are predicted to describe this state, such as color string model [6] and Color Glass Condensate (CGC) [7]. But the real mechanism of pre-equilibrium is still open question in heavy ion collisions. As parton production and parton scattering occurs one after another, energy density and entropy increases. Partonic matter reaches the local thermal equilibrium at proper time τ_0.

QGP state

Once phase transition occurs and local thermal equilibrium is established in a QCD matter, system drastically expands due to the pressure gradient. Space time evolution of Quark Gluon Plasma can be described by relativistic hydrodynamics based on the conservation laws of energy-momentum tensor and baryon number, which is given by:

$$\partial_\mu T^{\mu\nu} = 0, \tag{1.11}$$

$$\partial j^\mu = 0, \tag{1.12}$$

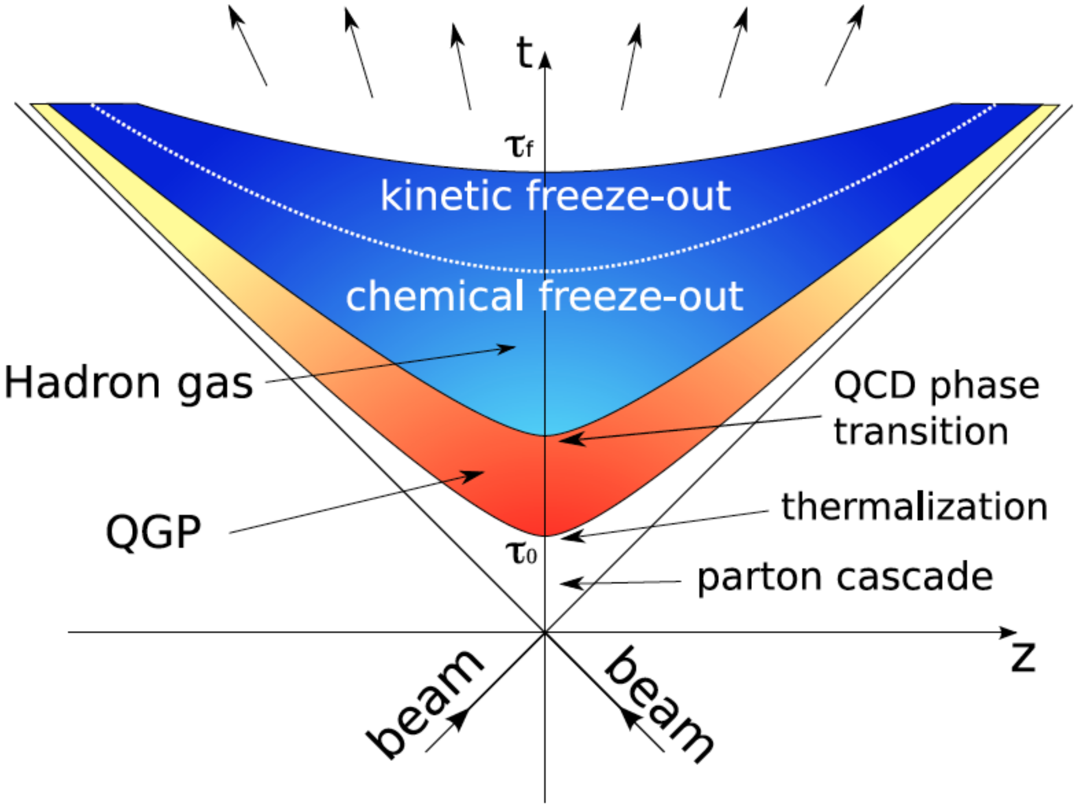

Figure 1.5: Schematic diagram of space-time evolution in relativistic heavy ion collisions. Two colliding nuclei is approaching from t < 0 shown as "beam". Collision time is defined as t = 0, z = 0. QGP phase is shown orange-yellow gradation and after the hadronization hadron phase is shown in blue gradation.

where $T^{\mu\nu}$ denotes the energy-momentum tensor, j^{μ} is baryon number current. Suppose no viscosity of its hydro model (perfect fluid), energy momentum tensor and baryon number current are given by:

$$T^{\mu\nu} = (\varepsilon + P)\,u^{\mu}u^{\nu} - Pg^{\mu\nu}, \tag{1.13}$$

$$j_i^{\mu} = n_i u^{\nu}, \tag{1.14}$$

$$u^{\nu} = \gamma(1, v_x, v_y, v_z)\,, \tag{1.15}$$

where ε denotes local energy density, P is local pressure, n_B represents baryon number and u^{ν} is fluid four velocity. $g^{\mu\nu}$ is Minkowski metric tensor.

In Eq. 1.14, five unknown parameters exists, P, ε, n_B and velocity parameters : v_x, v_y, v_z , while 4 unknown parameters which are n_B and velocity parameters are contained. If the equation of state related to local energy density and local pressure are given, all parameters are determined.

Once all parameters in hydrodynamics are fixed, space-time evolution of Quark Gluon Plasma can be calculated until the freeze-out (hadronization).

Chemical and Kinetic freeze-out

During QGP stages, mean free path of partons are shorter than the dimensions of the system. As the system strongly expands due to internal pressure, temperature of the system decreases and mean free path is longer and longer. At the time when mean free path of the partons becomes comparable with the system size, QGP break up into individual hadrons. This is called "freeze-out". Freeze-out is categorized into 2 stages, chemical freeze-out and kinetic freeze-out.

Species of hadrons are determined at the "Chemical freeze-out". Suppose the uniform fireball in chemical equilibrium, the number of particle density n_i is expressed with the simple statistical model :

$$n_i = d_i \int \frac{d^3\mathbf{p}}{8\pi^3} \frac{1}{\exp\left[\left(E_i - \mu_i\right)/T\right] \pm 1}, \tag{1.16}$$

where d_i is spin degeneracy, $\mathbf{p}$ is momentum, E_i denotes total energy, μ_i is chemical potential and T is temperature of the system.

After the chemical freeze-out, no more hadrons are produced from the system, though hadron-hadron scattering still ongoing and they exchange their momentum and energy. When mean free path becomes equal to the system size, momentum and energy of hadrons are fixed and fly away without interaction each other. This is called "Kinetic freeze-out".

1.3 Experimental Observables

In this section, Experimental observables related to this analysis is presented.

1.3.1 Transverse momentum spectra and radial flow

Transverse momentum (p_{T}) of generated hadrons are one of the important tools to extract property of QGP because transverse momentum of produced particles originated from only collision dynamics. It is thought transverse momenta are generated by two processes, soft and hard components. Hard process is quark-quark and quark-gluon hard scattering with large momentum transfer and high transverse momentum quarks fragment into high p_{T} hadrons. High p_{T} component is expressed by:

$$\frac{dN}{dp_{\mathrm{T}}} = Ap_{\mathrm{T}}^{-n}. \tag{1.17}$$

The other soft process is thermal particles production. Low p_{T} (p_{T} < 2 GeV/c) particle production is expressed as invariant cross section given by:

$$\begin{aligned} E\frac{d^3\sigma}{d^3p} &= \frac{1}{2\pi p_{\mathrm{T}}}\frac{d^2\sigma}{d_{p_{\mathrm{T}}}dy}, & (1.18)\\ &= \frac{1}{2\pi m_{\mathrm{T}}}\frac{d^2\sigma}{d_{m_{\mathrm{T}}}dy}, & (1.19)\\ &\approx \exp\left(-\frac{-m_{\mathrm{T}}}{T}\right), & (1.20)\end{aligned}$$

where y is rapidity, m_{T} is transverse mass represented as $m_{\mathrm{T}} = \sqrt{E^2 - p_z^2}$, and T is an inverse slope parameter of charged hadron p_{T} spectrum, so-called effective temperature. In pp collisions, this inverse slope parameter T is independent of particle mass, which is called m_{T} scaling [8]. On the other hand, in nucleus-nucleus collisions, the inverse slope parameter T is proportional to particle mass as if all particles are emitted with common velocity. This effect is induced by the pressure gradient of QGP and called as "radial flow" which indicates the isotropic expansion in the azimuthal plane. The inverse slope parameter is given by:

$$T = T_f + \frac{1}{2}m_0\langle\beta^2\rangle, \tag{1.21}$$

where T_f denotes the kinetic freeze-out temperature, $\langle\beta^2\rangle$ is average expansion velocity and m_0 is mass.

Kinetic freeze-out parameter and radial flow velocity can be analytically extracted by the Blast-wave model. Blast-wave model is phenomenological hydrodynamic model and each parameter T_f and $\langle\beta\rangle$ can be estimated with fitting the spectra of hadrons.

Figure 1.6 shows the centrality dependence of positive and negative π, K, p spectra in $\sqrt{s_{NN}} = 2.76$ TeV Pb-Pb collisions from ALICE [9]. Positive and negative particle spectra are comparable within the systematic uncertainties. Each spectra are fitted with the following Blast-wave parametrization:

$$\frac{1}{p_{\mathrm{T}}}\frac{\mathrm{d}N}{\mathrm{d}p_{\mathrm{T}}} \propto \int_0^R r\mathrm{d}r m_{\mathrm{T}} I_0\left(\frac{p_{\mathrm{T}}\sinh\rho}{T_{\mathrm{kin}}}\right) K_1\left(\frac{m_{\mathrm{T}}\cosh\rho}{T_{\mathrm{kin}}}\right), \tag{1.22}$$

where I_0 and K_1 are modified Bessel functions, r is the radial distance in the azimuthal plane, R is the radius of fire ball, T_{kin} is kinetic freeze-out temperature, ρ is the velocity profile , and m_{T} is the transverse mass which is given by $m_{\mathrm{T}} = \sqrt{p_{\mathrm{T}}^2 + m^2}$. The velocity profile ρ is given by:

$$\rho = \tan^{-1}\beta_T, \tag{1.23}$$

where β_T denotes the expansion velocity in transverse plane.

Fit range is shown as horizontal line int the top-left pale of Fig. 1.6. π, K, p combined fitting is well described with Blast-wave function. The extracted parameters, T_{kin} and $\langle\beta_T\rangle$, are shown as a function of centrality in Fig. 1.7. Average transverse velocity increases from peripheral to central collisions ,while the kinetic freeze-out temperature decreases with increasing centrality. ALICE results are compared with the results in Au-Au collisions at $\sqrt{s_{\mathrm{NN}}}$ = 200GeV Au-Au from STAR. For central collisions, 10% stronger radial flow can be observed at LHC energy than RHIC energy. For central collisions, the radial flow in LHC energy is 10% stronger than that in RHIC energy.

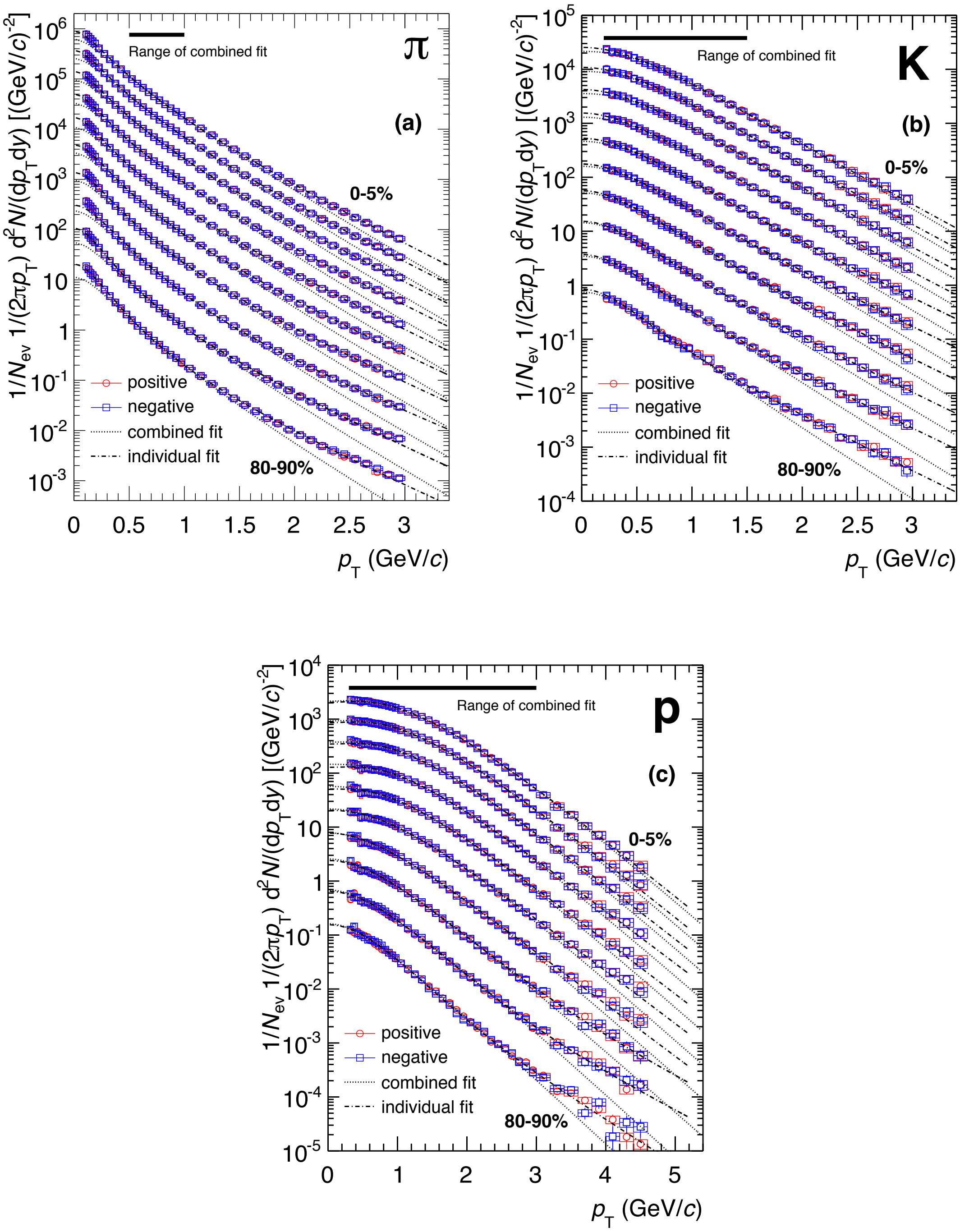

Figure 1.6: p_T spectra of π, K and p as a function of centrality, for positive (red circle) and negative (blue square) hadrons measured in $\sqrt{s_{NN}}$ = 2.76 TeV Pb-Pb collisions [9]. Each panel shows central (0-5%) to peripheral (80-90%); spectra scaled by factors 2^n (n denotes the centrality bin, which most central collisions are corresponding to n = 0 and n becomes larger from central to peripheral). Two different fits are performed, individual fit to each particles (dashed lines) and simultaneous fit to π, K, p (dotted lines).

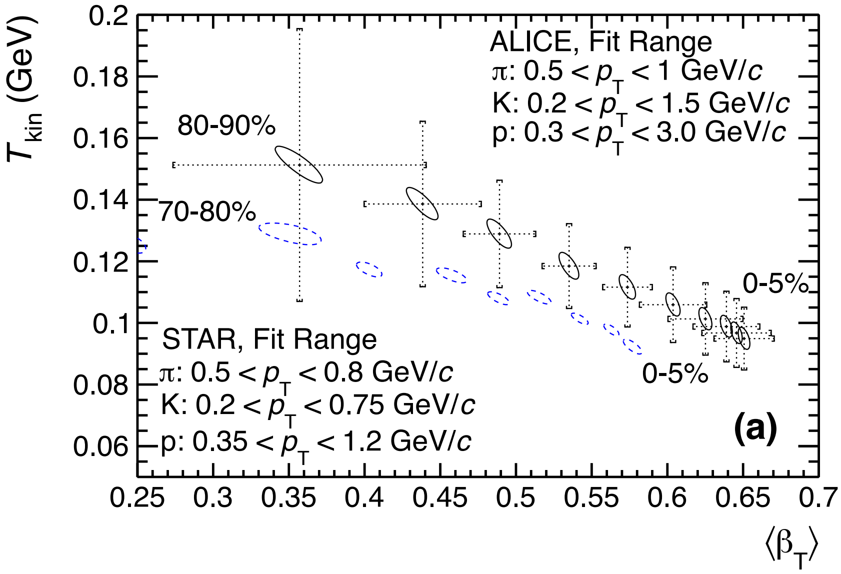

Figure 1.7: The correlation between the two extracted parameters, kinetic freeze-out temperature T_{kin} and average expansion velocity $\langle \beta_{\mathrm{T}} \rangle$ by Blast-wave fits in Pb-Pb collisions at $\sqrt{s_{\mathrm{NN}}}$ = 2.76 TeV (Black contours) and Au-Au collisions at $\sqrt{s_{\mathrm{NN}}}$ = 200 GeV (Blue contours) [9].

1.3.2 Azimuthal anisotropy

Azimuthal anisotropy of emitting particles gives us the key information on initial geometry and viscosity of Quark Gluon Plasma. In non-central nucleus-nucleus collisions, the overlap area of two nuclei has elliptic shape like an almond due to collision geometry which is sketched in Fig. 1.8. If the local thermal equilibrium is established at the overlap region, mean free path is much shorter than system size and system evolution can be described by hydrodynamics. In hydrodynamical picture, pressure gradient generates collective flow. Pressure gradient is considered to be steeper in the direction of reaction plane and collective flow is much more developed in this direction. Finally particle production is strongly biased with this collective motion, and more particles are produced along the short axis of the system than the long axis. Therefore azimuthal distribution at freeze-out is expected to be well reflected by an azimuthal anisotropy in the initial coordinate space (Fig. 1.8).

Azimuthal anisotropy of particle distribution can be extracted by Fourier expansion given by:

$$\frac{dN}{d\varphi} \propto 1 + \sum_{n=1}^{\infty} v_n \cos\left(n\left[\varphi - \Psi_n\right]\right), \tag{1.24}$$

where Ψ_n is n^{th}-order event plane determined by the azimuthal distribution of emitting particles in experiment, φ is azimuthal angle of particles, v_n represents the coefficients in the Fourier decomposition and indicates the magnitude of azimuthal anisotropy. Especially 2^{nd}-order Fourier coefficient is called elliptic flow and has been studied to probe the early stage of Quark Gluon Plasma.

If a huge number of nucleons exist in the nucleus and initial density distribution are smooth, the shape of initial overlap region would be perfectly elliptic shape. However the number of nucleons is finite and the density distribution of nucleons largely fluctuates event-by-event. This event by event participant fluctuation also generates pressure gradient and higher order flow coefficients.

Figure 1.9 shows azimuthal anisotropy v_2, v_3, v_4, and v_5 measured in Pb-Pb collisions at $\sqrt{s_{\text{NN}}}$ = 2.76 TeV. Left panel in Fig. 1.9 shows centrality dependence from ALICE. v_2 has large centrality dependence and v_2 significantly becomes larger from central to peripheral collisions. It is considered that the initial elliptic shape strongly contributes to this behaviour. On the other hand, higher order harmonic flow coefficients (v_3, v_4, and v_5) gently increase with increasing centrality percentile because fluctuation of the initial density distribution depends weakly on the centrality. Right panel in Fig. 1.9 shows p_{T} dependence of azimuthal anisotropy from ATLAS [11]. Both 2$^{\mathrm{nd}}$-order and higher order harmonic flow becomes larger from low p_{T} to high p_{T} , and ALICE and ATLAS data are compared with viscous hydrodynamical simulations depicted with bands, shear viscosity to entropy ratio η/s is set to 0.2 in this model. Hydrodynamical simulation fully reproduces the experimental results up to 5^{th}-order flow coefficients with very small viscosity, this results suggest that QGP is nearly perfect fluid with small viscosity.

Figure 1.10 shows p_{T}-integrated azimuthal anisotropy v_2, v_3 as a function of average $\mathrm{N_{part}}$ in Au-Au collisions at $\sqrt{s_{\mathrm{NN}}}$ = 200 GeV by PHENIX collaboration [12]. Experimental data are compared to hydrodynamical simulations with different initial state models and viscosity. For the results on v_2, almost all hydrodynamical models can successfully reproduce the data. However, MC-KLN model cannot describe v_3 well with the same parameter as that used for v_2, though Glauber model simulation can reproduce both v_2 and v_3. Therefore higher order flow harmonics give us stronger constraining power for the initial state.

Figure 1.11 shows p_{T} dependence of azimuthal anisotropy v_2, v_3, v_4, and v_5 for centrality 30-40% calculated with two particle correlation method in $\sqrt{s_{\mathrm{NN}}}$ = 2.76 TeV by ALICE collaboration [13]. Experimental data are compared with the models of ideal and viscous hydrodynamical simulations with $\eta/s = 0.0$ and $\eta/s = 0.08$, respectively. Theoretical calculation of viscous hydrodynamical model can describe experimental data up to p_{T} = 2.0GeV/c, and discrepancy between ideal and viscous hydrodynamic simulation is much larger for v_3 than v_2. Thus measurements of azimuthal anisotropy of emitting particle is powerful probe for initial geometry and hydrodynamical properties of Quark Gluon Plasma, and in particular higher harmonic flow (v_3) has a strong constraining power of not only the initial geometry but also the viscosity of the source.

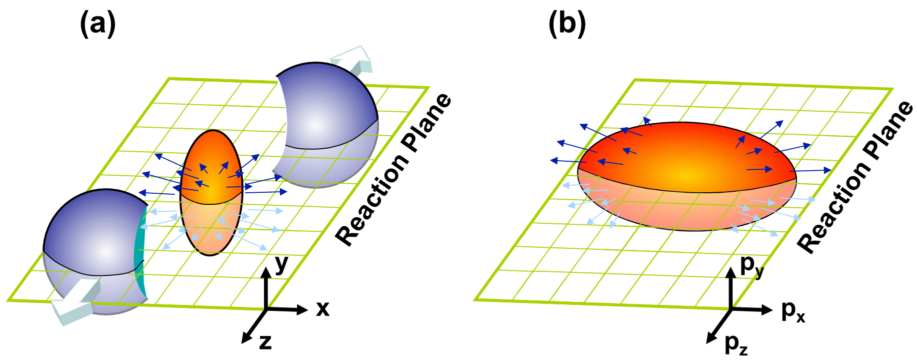

Figure 1.8: Illustrations of non-central relativistic heavy ion collisions in geometrical space (a) and momentum space (b)

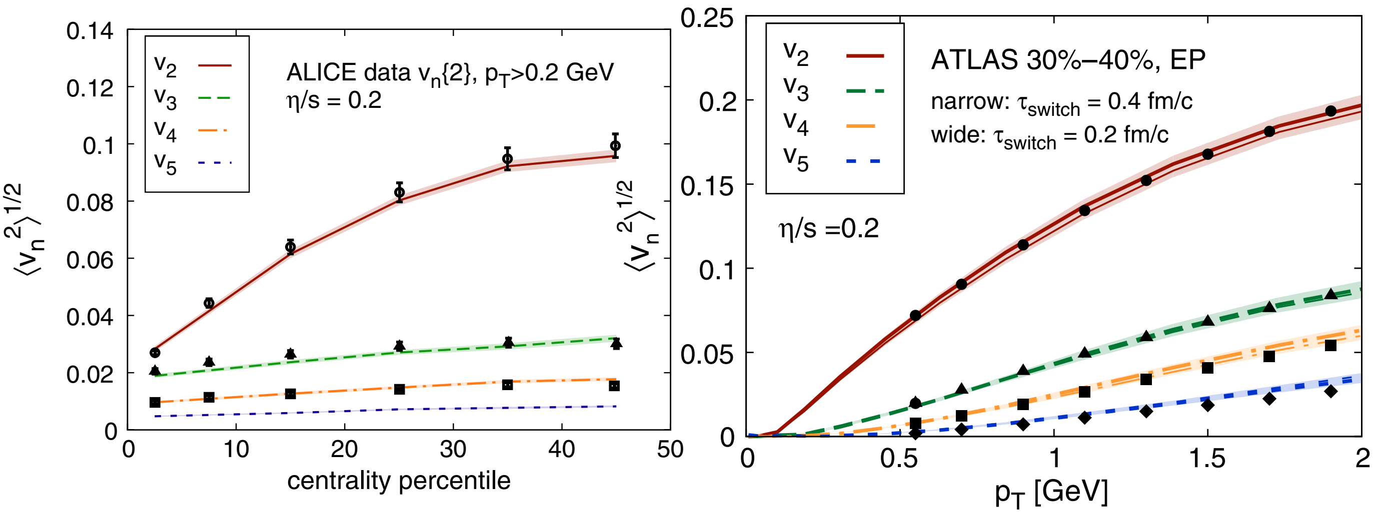

Figure 1.9: Azimuthal anisotropy v_2, v_3, v_4 and v_5 as a function of centrality percentile in $\sqrt{s_{\mathrm{NN}}}$ = 2.76 TeV Pb-Pb Collisions from ALICE. v_n is calculated with two particle correlation method using p_{T} > 0.2 GeV/$c$charged particles are integrated. ALICE data (black marker) is compared with viscous hydro dynamical calculation (solid and dashed lines) (left). p_{T} dependence of azimuthal anisotropy in centrality 30-40% via Event Plane method by ATLAS collaboration(right). For both hydrodynamical simulations, shear viscosity to entropy ratio η/s is set to 0.2 [11].

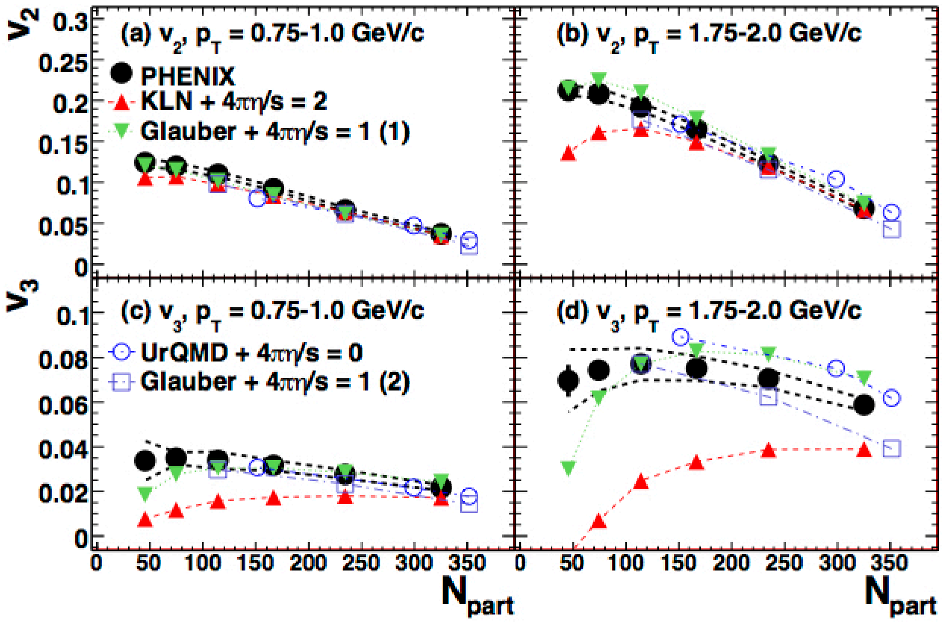

Figure 1.10: p_T integrated azimuthal anisotropy v_2 and v_3 as a function of number of participant with two different p_T ranges. in Au-Au collisions at $\sqrt{s_{NN}}$ = 200 GeV from PHENIX. Experimental data (black marker) are compared with theoretical predictions of two different initial state models MC-KLN and Glauber and different viscosity [12].

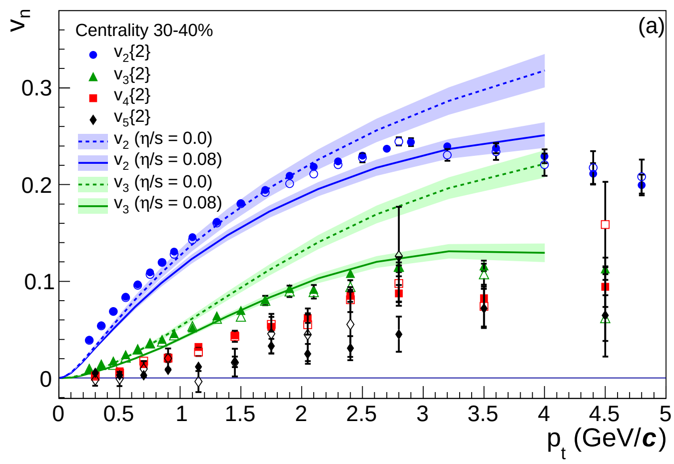

Figure 1.11: Azimuthal anisotropy v_2, v_3, v_4 and v_5 as a function of transverse momentum for centrality 30-40% measured with a two particle correlation method of two different rapidity gaps, $\Delta\eta > 0.2$ (open symbol) and $\Delta\eta > 1.0$ (closed symbol), in Pb-Pb collisions at $\sqrt{s_{NN}}$ = 2.76 TeV from ALICE. Data are compared with hydrodynamical simulations of ideal fluid and viscous fluid ($\eta/s = 0.08$).

1.3.3 Event Shape Engineering

For a further understanding of the spatio-temporal evolution of Quark Gluon Plasma, one of essential studies is initial collision geometry. In order to extract the initial collision geometry experimentally, collision centrality which is sensitive to impact parameter has been used until now. Recently, however, it is thought the initial geometry of nuclear overlap region largely fluctuates even at a fixed and narrow centrality window.

Figure 1.12 shows probability distributions of event-by-event v_2, v_3 and v_4 as a function of centrality measured in Pb-Pb collisions at $\sqrt{s_{\rm NN}}$ = 2.76 TeV from ATLAS collaboration [14]. The coefficients of azimuthal anisotropy v_n are largely fluctuated within a certain centrality bin and these fluctuations becomes larger from central to peripheral collisions. The azimuthal anisotropy is sensitive probe to the initial geometry, thus these fluctuations come mostly from the fluctuations of the initial geometry at initial stage of the collisions.

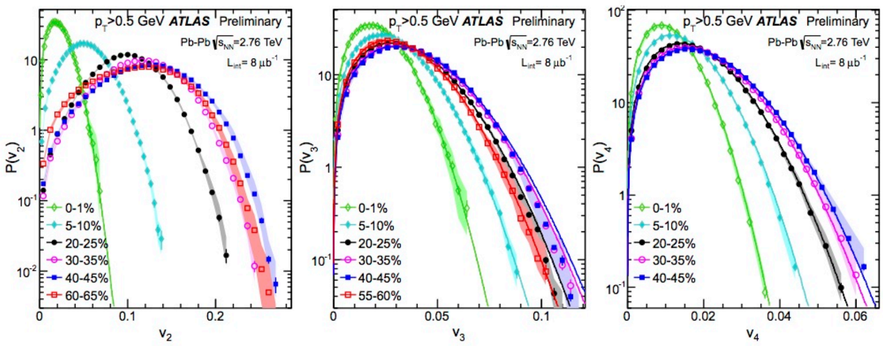

Figure 1.12: The probability distribution of event-by-event v_2 (left), v_3 (middle) and v_4 (right) in 5 or 6 centrality in Pb-Pb collisions at $\sqrt{s_{\rm NN}}$ = 2.76 TeV from ATLAS collaboration [14]. Error bars represent statistical uncertainties and Systematic uncertainties are shown as shaded bands. Solid line denotes the distributions assuming the v_n are radial projections of 2D Gaussian distributions.

Recently a new approach to select these event-by-event initial geometry fluctuations, so-called the Event Shape Engineering (ESE), was developed utilizing these large fluctuations of azimuthal anisotropy [15]. The ESE technique offers to select the initial geometrical source shape with the event-by-event flow vector q_n. The event-by-event flow vector q_n is given by:

$$Q_{n,x} = \sum_{i}^{M} \cos(n\phi_i), \tag{1.25}$$

$$Q_{y,x} = \sum_{i}^{M} \sin(n\phi_i), \tag{1.26}$$

$$q_n = \left(Q_{n,x}^2 + Q_{n,y}^2\right) / \sqrt{M}. \tag{1.27}$$

where n is the harmonics of Fourier coefficients, M is the multiplicity of an event, and ϕ_i is the azimuthal angles of emitting particles. The initial geometrical source shape can be calculated with n^{th}-order participant eccentricity ε_n which is given by:

$$\varepsilon_n = \sqrt{\varepsilon_{n,x}^2 + \varepsilon_{n,y}^2}, \tag{1.28}$$

$$\varepsilon_{n,x} = \langle r^n \cos(n\phi)\rangle, \tag{1.29}$$

$$\varepsilon_{n,y} = \langle r^n \sin(n\phi)\rangle, \tag{1.30}$$

where x and y represent space coordinates of nucleons and ϕ is an azimuthal angle of nucleons. By selecting the magnitude of an event-by-event flow vector q_n, we can control event-by-event initial geometrical source shape, i.e. larger (smaller) q_n tends to have larger (smaller) ε_n.

One of the big advantages on ESE technique is extracting how initial geometrical shape contributes to the other observables. Figure 1.13(left) shows azimuthal anisotropy v_2 as a function of p_{T} for various q_2 selections and no q_2 selection by ATLAS collaboration [17]. Elliptic flow coefficients v_2 largely changes with q_2 selection and this enhancement(suppression) does not depends on p_{T} . Right panel of Fig. 1.13 shows the correlation between low momentum v_2 (0.5 $< p_{\mathrm{T}} <$2 GeV/c) and high momentum v_2 ($3 < p_{\mathrm{T}} < 4$ GeV/c) in 7 centrality bins for 6 q_2 classes. The gray band represents a correlation between low p_{T} v_2 and high p_{T} v_2 without ESE selection, which shows the "boomerang-like" structure that can be understood by viscous-damping effects to different p_{T} ranges according to hydrodynamical model calculations [18]. For various q_2 selections, however, the correlation of v_2 in two different p_{T} ranges dramatically changes to a linear correlation. This linearity indicates that hydrodynamical viscous effects are determined by not the geometrical source shape but the source size.

Left(Right) panel in Fig. 1.14 shows the ratio of p_{T} distributions of $\pi^+ + \pi^-$, $K^+ + K^-$, and $p + \bar{p}$ with top (bottom) 10% q_2 selection to those without q_2 selection. Transverse momentum spectra of identified hadrons are enhanced (suppressed) with large (small) q_2 selection, and the ratio of p_{T} spectra becomes larger (smaller) from low p_{T} to high p_{T} with large (small) q_2 selection. Mass ordering can be explicitly found for the ratio of p_{T} spectra. Data are compared with the Blast-wave model and an average boost velocity can be extracted with this model. Large (small) q_2 selection enhances (suppresses) not only the azimuthal anisotropy v_2 but also the average boost velocity of the system.

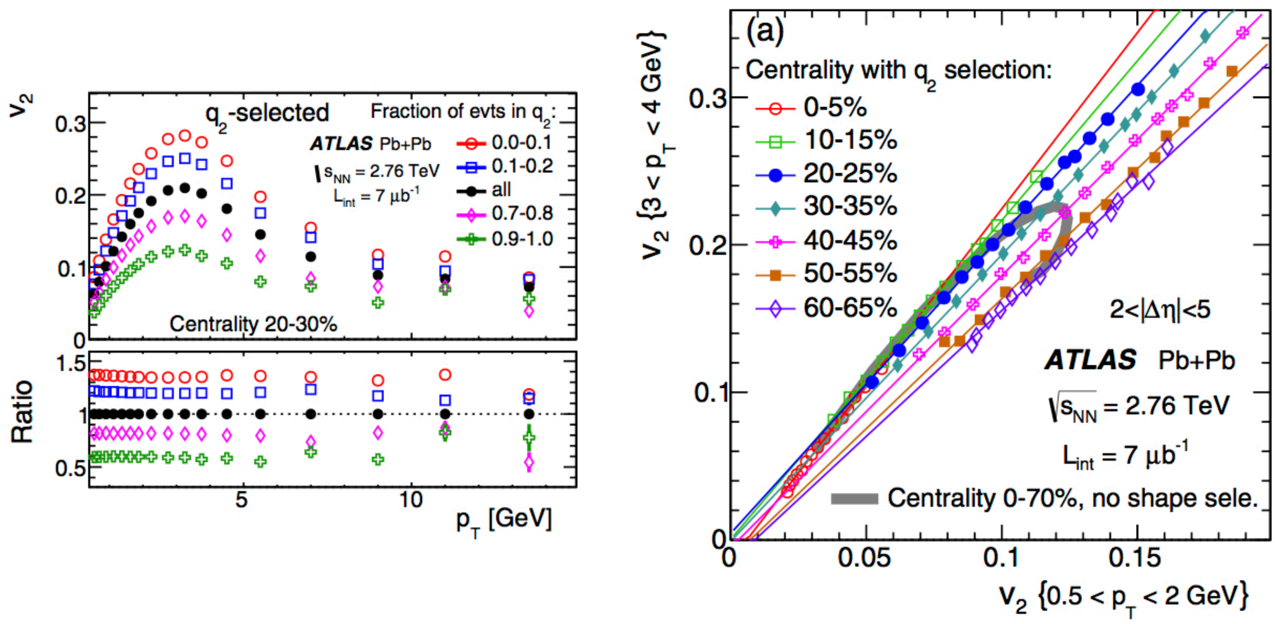

Figure 1.13: Azimuthal anisotropy v_2 as a function of transverse momentum in the centrality 20-30% (top left) for events selected on q_2 measured in Pb-Pb Collisions at $\sqrt{s_{\mathrm{NN}}}$ = 2.76 TeV from ATLAS. Bottom left panel shows the ratio of v_2 for q_2-selected to that without q_2 selection, and a correlation of v_2 between p_{T} :0.5-2GeV/c and p_{T} :3-4GeV/c in 7 centrality bins. Data points represent v_2 correlation in various q_2 selection and overlaid gray band denotes that without q_2 selection [17].

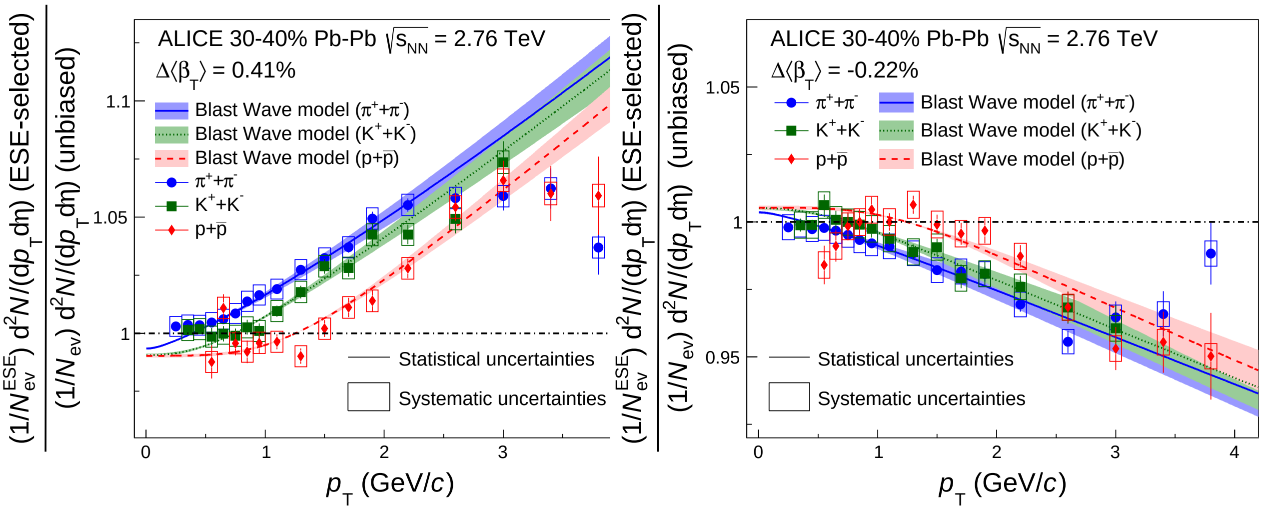

Figure 1.14: The ratio of p_T distributions of $\pi^+ + \pi^-$, $K^+ + K^-$, and $p + \bar{p}$ with large (small) q_2 selection to those without q_2 selection in centrality 30-40% are shown in left (right) panel. Results are measured in $\sqrt{s_{NN}} = 2.76$ TeV Pb-Pb Collisions from ALICE collaboration. Data are compared with the Blast-wave model which is the hydrodynamical inspired model. Based on the Blast-wave model, an average boost velocity $\langle\beta_T\rangle$ is 0.41% enhanced (0.22% suppressed) with ESE selection [19].

1.3.4 Hanbury-Brown and Twiss Interferometry

There are several parameters which describe the bulk properties of Quark Gluon Plasma, such as freeze-out temperature, boost velocity, viscosity, system size, freeze-out time, and emission duration. Basically the freeze-out temperature, boost velocity, and viscosity can be extracted with measurements of hadron spectra and azimuthal anisotropy. The other parameters (the system size, freeze-out time, and emission duration) can be extracted with Hanbury-Brown and Twiss interferometry (HBT interferometry). HBT measurement is an unique and essential method to address system size at freeze-out, emission duration, and system life time.

HBT is a method to measure the source size with two identical particles [20, 21]. Here we assume a simple model that two identical particles are emitted from a certain source, which is shown in Fig. 1.15. Emission points of two identical particles are defined r_1 and r_2, and two particles are observed by two detectors which are located at x_1 and x_2. We define r as the length from emission point to observed position, and R as the length from r_1 to r_2. Two particles can take two routes to two detectors, route1 and route2 which are depicted as red lines and blue lines in Fig. 1.15). If two particles are identical and L is much larger than R, quantum mechanics can be applied, then we cannot identify route. Hence, we can write the wave function of two identical particles in the from:

$$\begin{aligned} \Psi_{12} &= \frac{1}{\sqrt{2}} \left[\Psi_1(r_1)\Psi_2(r_2) \pm \Psi_2(r_1)\Psi_1(r_2) \right], \\ &= \frac{1}{\sqrt{2}} \left[A_1 A_2 e^{-ip_1(x_1-r_1)} e^{-ip_2(x_2-r_2)} \pm A_1 A_2 e^{-ip_1(x_2-r_1)} e^{-ip_2(x_1-r_2)} \right], \end{aligned} \tag{1.31}$$

where Ψ is a wave function of the signle particle with momentum p emitted from r, A is amplitude of wave function. The Sign of second term in Eq. 1.31 is determined with particle species. Bosons have positive and fermions have negative sign.Then the probability density is expressed by:

$$|\Psi_{12}|^2 = |A_1|^2 |A_2|^2 \left[1 \pm \cos(\Delta x \Delta p) \right] \tag{1.32}$$

where $\Delta x = x_1 - x_2$ and $\Delta p = p_1 - p_2$. The cosine term in Eq. 1.32 represents HBT correlation term. Therefore an effect of quantum interference are stronger in small Δx or Δp, and This correlation can be found as enhancement of probability density for bosons, thus HBT interference is also called Bose-Einstein enhancement.

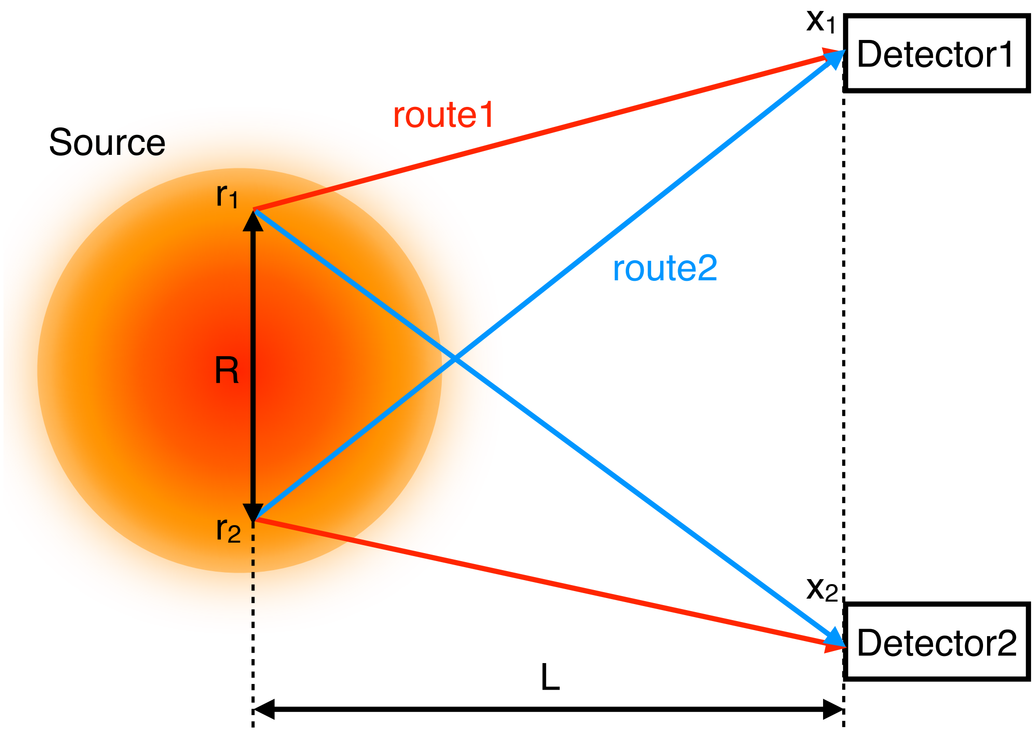

Figure 1.15: The schematic figure of HBT interferometry. Two identical particles emitted from a certain source. The emission points of each particles are defined as r_1 and r_2. A distance between r_1 and r_2 is expressed as R. Two particles are obserbed by detectors at x_1 and x_2. The distance between emission point and detected position is L. If R is much smaller than L, route 1 and route 2 can not be identified with quantum mechanics.

We define the correlation function C_2 with the following equation:

$$C_2 = \frac{P(p_1, p_2)}{P(p_1)P(p_2)} \tag{1.33}$$

where $P(p_1, p_2)$ denotes the probability to observe two particles with momentum p_1 and p_2 simultaneously, and $P(p_1)$ ($P(p_2)$) is the probability to observe single particle with momentum p_1 (p_2) indipendently. If we assume the density distribution of source as a Gaussian function, the correlation function C_2 of two identical particles are given by

$$C_2 = 1 \pm \lambda \exp\left(-R^2 q^2\right), \tag{1.34}$$

where λ is chaoticity (incoherence) parameter which is sensitive to incoherence of the system and resonance. The chaoticity parameter λ takes 0 to 1, and R is so-called "HBT radius" and indicates a standard deviation of the source distribution. The relative momentum of two identical particles is represented as $q = p_1 - p_2$.

Bertsch Pratt parametrization

For 1-dimensional HBT analysis, correlation function is given by

$$q_{inv} = \sqrt{q_x^2 + q_y^2 + q_z^2 + q_0^2}, \tag{1.35}$$

$$q_0 = E_1 - E_2. \tag{1.36}$$

Bertsch-Pratt parametrization are frequently utilized to extend the one dimensional to 3 dimensional HBT analysis [22, 23]. In this parametrization, one dimensional relative momentum q is decomposed into outward (q_{out}), sideward (q_{side}, and long (q_{long}). Long denotes a term along the direction of the beam axis and azimuthal plane is represented as outward and sideward, where outward is parallel to pair transverse momentum k_T and sideward is perpendicular to k_T. The pair transverse momentum k_T is given by:

$$k_T = \frac{\overrightarrow{p_{\mathrm{T1}}} + \overrightarrow{p_{\mathrm{T2}}}}{2}. \tag{1.37}$$

When we apply the Bertsch-Pratt parametrization in the Longitudinal Co-Moving System (LCMS) where $p_{z1} + p_{z2} = 0$, the correlation function C_2 is re-written as

$$\begin{aligned} C_2 &= 1 + \lambda \exp\left(-R^2 q^2\right), & (1.38)\\ &= 1 + \lambda \exp\left(-R_{\mathrm{x}}^2 q_x^2 - R_{\mathrm{y}}^2 q_y^2 - R_{\mathrm{z}}^2 q_z^2 - \sigma_t^2 q_0^2\right), & (1.39)\\ &= 1 + \lambda \exp\left(-R_{\mathrm{out}}^2 q_{out}^2 - R_{\mathrm{side}}^2 q_{side}^2 - R_{\mathrm{long}}^2 q_{long}^2\right), & (1.40) \end{aligned}$$

where σ_t represents an emission duration and σ_t is included in R_{out} in Eq. 1.40, therefore R_{side} is driven by a purely geometrical information on the system.

HBT measurements in dynamical system

In a static source, measured HBT radii represent a standard deviation of whole system size. In dynamically expanding source such as our universe (Hubble flow), however, HBT radii is equal not to a standard deviation of whole system size but the "length of homogeneity region" [24]. The length of homogeneity region depends on the expansion velocity of the source and pair transverse momentum k_T. HBT radii calculated with larger k_T pairs are corresponding to more surface part of the source.

Therefore, in order to understand the space time evolution of the dynamical source with HBT measurements, study of k_T dependence is important.

Extraction of geometrical source size and freeze-out time

Figure 1.16 shows the extracted 3D HBT radii (R_{side} , R_{out} and R_{long}) and λ as a function pair transverse mass $m_T = \sqrt{k_T^2 + m^2}$ for various centrality bins measured in Au-Au collisions at $\sqrt{s_{NN}}$ = 200 GeV from PHENIX collaboration [25]. All 3D HBT radii strongly decrease with increasing m_T. This explicit $m_T(k_T)$ dependence indicates the dynamical expansion of the system, and this m_T is qualitatively described with hydrodynamical model. If the difference in HBT radii between pions and kaons is due to particle mass, i.e. if the freeze-out time, emission duration, and subsequent system evolution are same, HBT radii of pions and kaons are scaled with m$_T$. However R_{out} and R_{long} of kaons are larger than that of pions, though R_{side} of kaon is comparable to those of pions. This behaviour can be also found in Pb-Pb collisions at $\sqrt{s_{NN}}$ 2.76 TeV from ALICE collaboration [26]. Based on the hydrodynamics, k_T dependence of R_{out} is sensitive to transverse velocity and that of R_{long} is sensitive to freeze-out time. The geometrical source size, system life time, and emission duration can be extracted with analytical formula [27]. It suggests that maximal emission time for kaons is larger than the one for pions. Therefore it could indicate that pions and kaons have different space-time correlations.

Azimuthal angle dependence of HBT radii with respect to Ψ_2

Basically HBT is the method to measure the source "size", but this technique is extended with combining the study of azimuthal anisotropy. Based on the hydrodynamical model, short axis of initial elliptic shape can be obtained with 2nd-order event plane Ψ_2 as described in detail in Sec. 3.2.2. Measurement of azimuthal angle dependence of HBT radii with respect to Ψ_2 gives us the information on "source elliptic shape" at freeze-out [28, 25, 29].

Left panel in Fig. 1.17 shows the azimuthal angle dependence of charged pion HBT radii with respect to Ψ_2 for 3 centralities measured in Au-Au collisions at $\sqrt{s_{NN}}$ = 200 GeV from STAR [28]. No significant oscillation can be found in R_{long} , but, in azimuthal plane, R_{out} , R_{side} and R_{os} have explicit oscillations. This indicates that final source has a finite eccentricity. Final

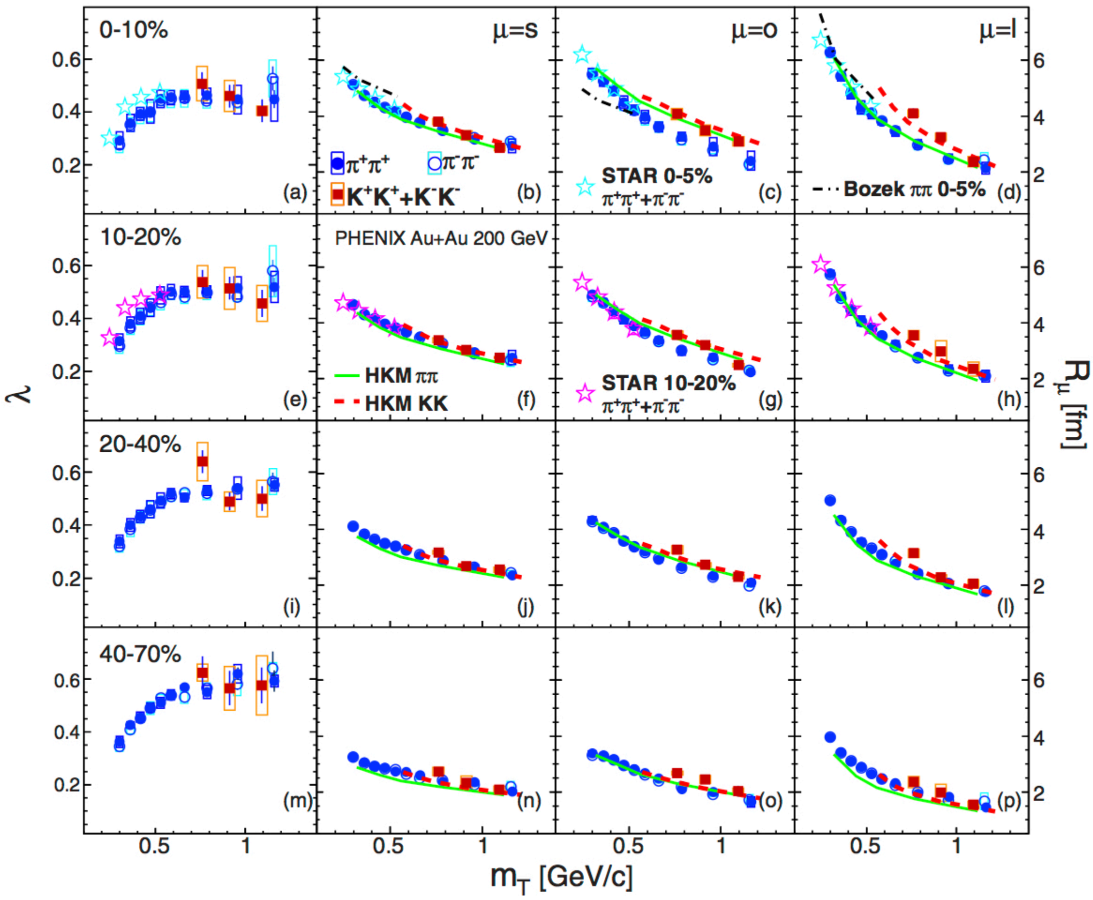

Figure 1.16: Extracted 3D HBT radii ($R_{\rm side}$, $R_{\rm out}$, and $R_{\rm long}$) and λ as a function of $m_{\rm T}$ for 4 centralities measured in Au-Au collisions at $\sqrt{s_{\rm NN}}$ = 200 GeV from PHENIX [25]. Data are compared with hydrokinetic simulation (HKM model) and viscous-hydrodynamic model (Bozek)

source eccentricity is calculated by fitting azimuthal angle dependence of HBT radii which is shown in left panel of Fig. 1.16. Right panel in Fig. 1.17 shows relation between initial eccentricity and final eccentricity. The dashed line in Fig. 1.17 indicates $\varepsilon_{initial} = \varepsilon_{final}$. One can find that final source eccentricity is much smaller than the dashed line. It indicates that initial elliptic shape is significantly diluted but out-plane elongated shape still remains at freeze-out. This information should constrain the space time evolution of the system.

Figure 1.18 shows hydrodynamic simulation of the azimuthal angle dependence of charged pion HBT radii with respect to Ψ_2 for 6 $k_{\rm T}$ calculated for LHC energy [30]. No significant oscillation can be found in $R_{\rm long}$ and the oscillation of $R_{\rm out}$ and $R_{\rm side}$ is out of phase ($R_{\rm out}$ is convex upward and $R_{\rm side}$ is concave up) in top 4 $k_{\rm T}$ classes, which is consistent to RHIC results.

However, in k_T : 0-0.2 GeV, a clearly different behaviour can be found, i.e. the oscillation of R_{out} is concave up and the one of R_{side} is convex upward in k_T = 0 GeV, but both the oscillation of R_{out} and R_{side} are convex upward in k_T = 0.2 GeV.

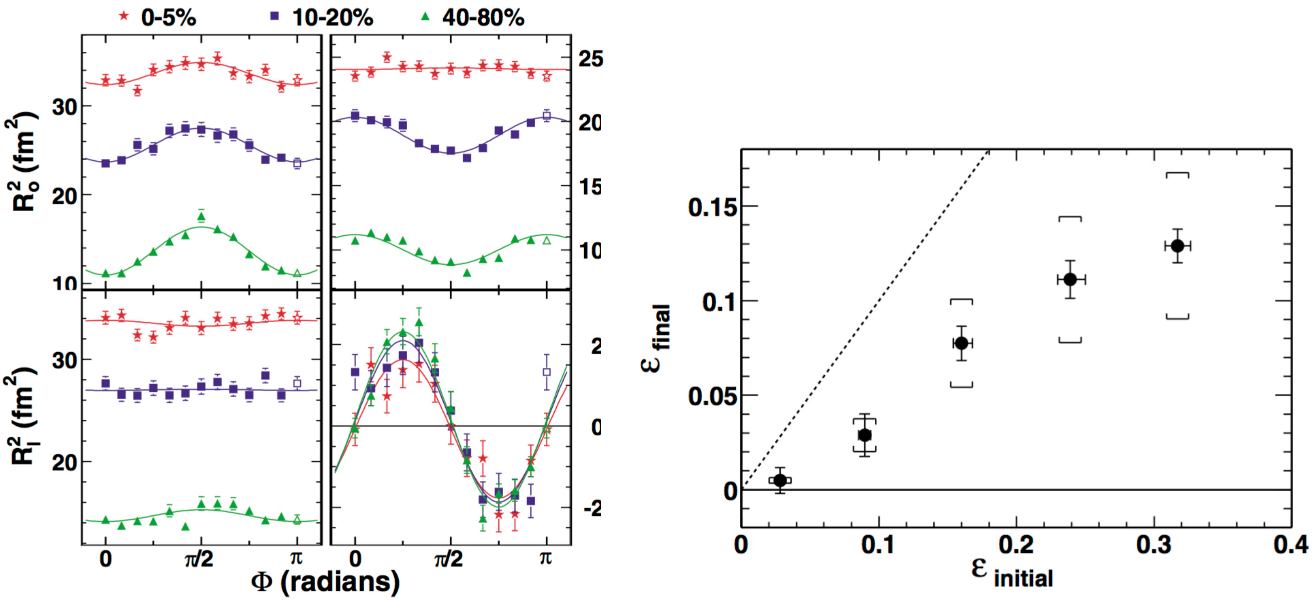

Figure 1.17: Azimuthal angle dependence of charged pion HBT radii (R_{out}, R_{side}, R_{long}, and R_{os}) with respect to Ψ_2 for 3 centralities measured in Au-Au collisions at $\sqrt{s_{NN}}$ = 200 GeV from STAR (left). Initial source eccentricity calculated with Glauber simulation v.s. source eccentricity at freeze-out obtained with azimuthal angle dependence of HBT radii (right) [28]. The dashed line indicates that $\varepsilon_{initial} = \varepsilon_{final}$.

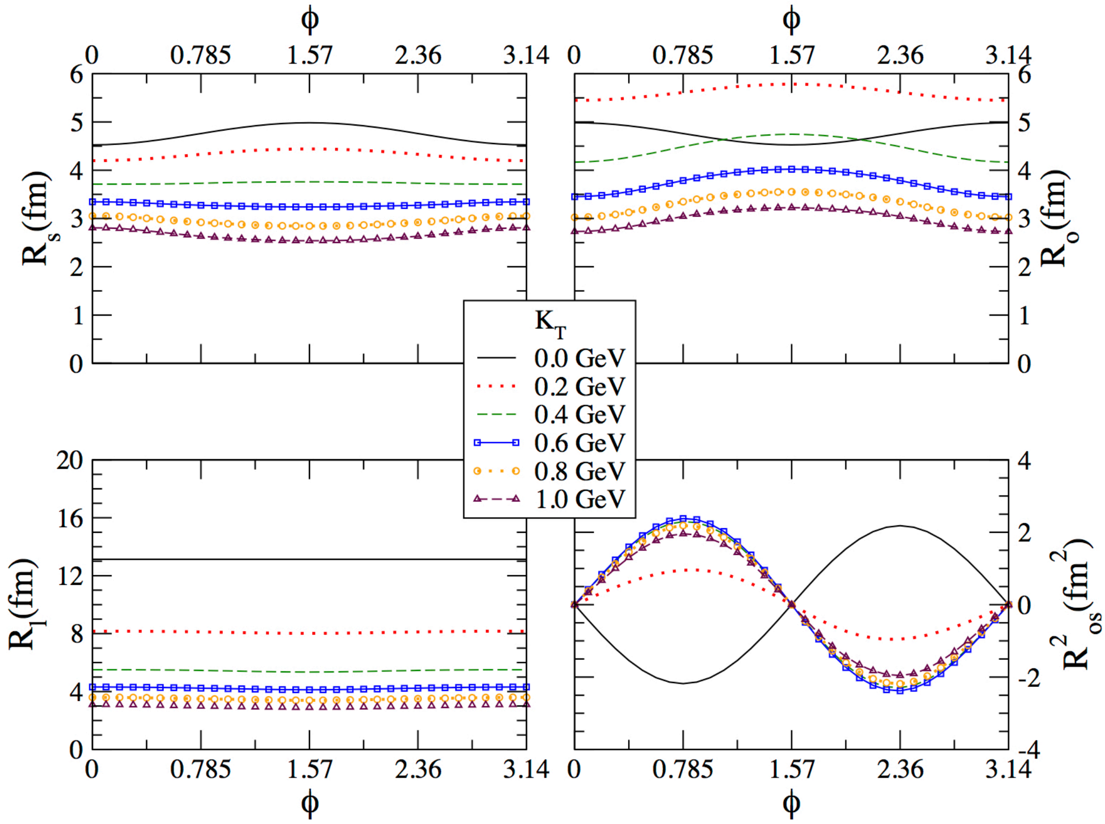

Figure 1.18: Azimuthal angle dependence of charged pion HBT radii (R_{out}, R_{side}, R_{long}, and R_{os}) with respect to Ψ_2 for 6 k_{T} classes in LHC energy, calculated with hydrodynamical model [30].

Azimuthal angle dependence of HBT radii with respect to Ψ_3

As mentioned in Sec. 1.3.2, the initial participant fluctuation makes higher order anisotropic flow, and recently higher order azimuthal anisotropy is actively measured to determine the initial geometry and the viscosity of the source.

Concerning HBT analysis, the possibility of 3$^{\text{rd}}$-order oscillation of HBT radii with respect to Ψ_3 is suggested with Blast-wave model calculation and AMPT simulation [31]. Measurement of azimuthal angle dependence of HBT radii with respect to Ψ_3 should be an unique and direct probe for triangular shape at freeze-out. In order to understand the space time evolution of hot dense matter, investigating not only the elliptic shape but also triangular shape at freeze-out is important.

Figure 1.19 shows the first measurement of the azimuthal angle dependence of charged pion HBT radii with respect to Ψ_3 (Ψ_2 dependence of HBT radii is plotted simultaneously) was performed in Au-Au collisions at $\sqrt{s_{\mathrm{NN}}}$ = 200 GeV. R_{side} oscillation relative to Ψ_3 is very weak, but R_{out} has a visible oscillation with respect to Ψ_3.

Figure 1.20 shows the relative amplitude of squared HBT radii with respect to Ψ_3(blue markers) and Ψ_2(red markers) obtained by Fig. 1.19. Contrary to relative amplitude of R_{side} with respect to Ψ_2, relative amplitude of R_{side} with respect to Ψ_3 has negative or zero value, whereas both relative amplitude of R_{out} with respect to Ψ_2 and Ψ_3 has positive value. Also relative amplitude of R_{os} with respect to Ψ_2 and Ψ_3 has positive value.

However triangular shape at freeze-out cannot be obtained directly from relative amplitude of HBT radii as is the case with eccentricity. In order to understand 3$^{\text{rd}}$ order oscillation of HBT radii, some of the model calculations (Gaussian toy model and hydrodynamical simulation) were performed [33, 34]. Figure 1.21 shows the relative amplitude of HBT radii with respect to Ψ_3 as a function of pair transverse momentum k_{T}, compared with two extreme case Gaussian model. Solid line indicates triangular flow dominated case which is spherical spatial distribution superimposed on an large triangular flow, and dashed line indicates triangular geometry dominated case which is the geometric triangular distribuion superimposed on an azimuthally symmetric radial flow. Data prefer flow dominated case, but relative amplitude of R_{side} in high k_{T} can not be described by this model. In order to constrain the ε_3 and v_3 in the model, more precise measurements of oscillation is important.

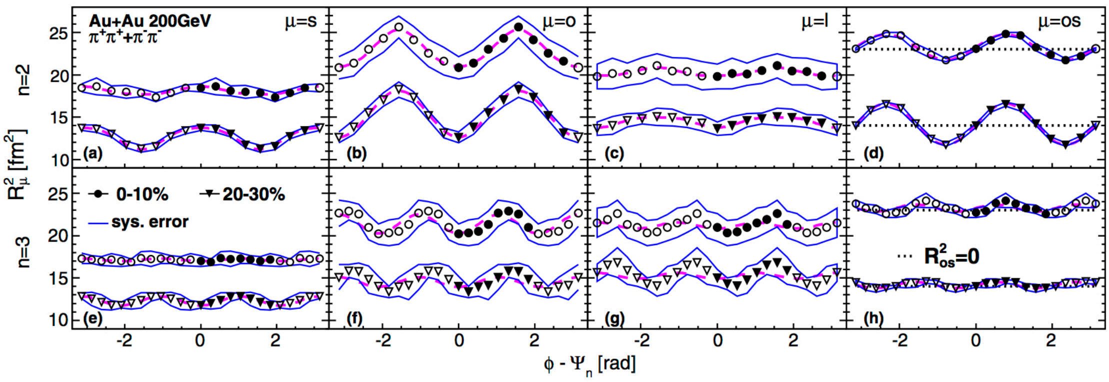

Figure 1.19: Azimuthal angle dependence of charged pion HBT radii (R_{out}, R_{side}, R_{long}, and R_{os}) with respect to Ψ_2 (top 4 panels) and Ψ_3 (bottom 4 panels) for 2 centralities measured in Au-Au collisions at $\sqrt{s_{\mathrm{NN}}}$ = 200 GeV from PHENIX [32]. First row from the left denotes R_{side} , second row is R_{out} , third row is R_{long} , and fourth row indicates R_{os} .

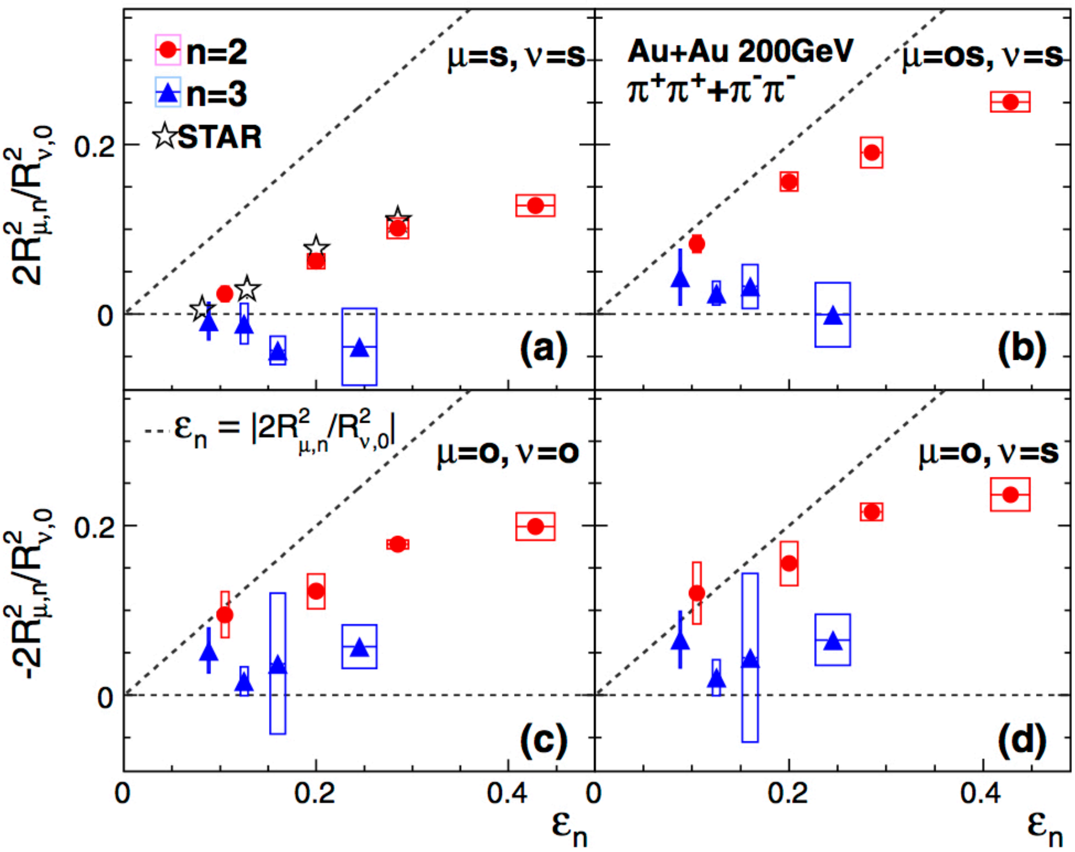

Figure 1.20: Relative amplitude of squared HBT radii (R_{out}, R_{side}, and R_{os}) with respect to Ψ_3 as a function of initial eccentricity which is calculated with Glauber model. The results are calculated with data in Au-Au collisions at $\sqrt{s_{\text{NN}}}$ = 200GeV from PHENIX [32]. Pair transverse momentum k_T is integrated from 0.2 to 2.0 GeV/c. Dashed line indicates relative amplitude of HBT radii = 0 and $\varepsilon_n = |2R^2_{\mu,n}/R^2_{\mu,0}|$. Boxes represent the systematic uncertainties.

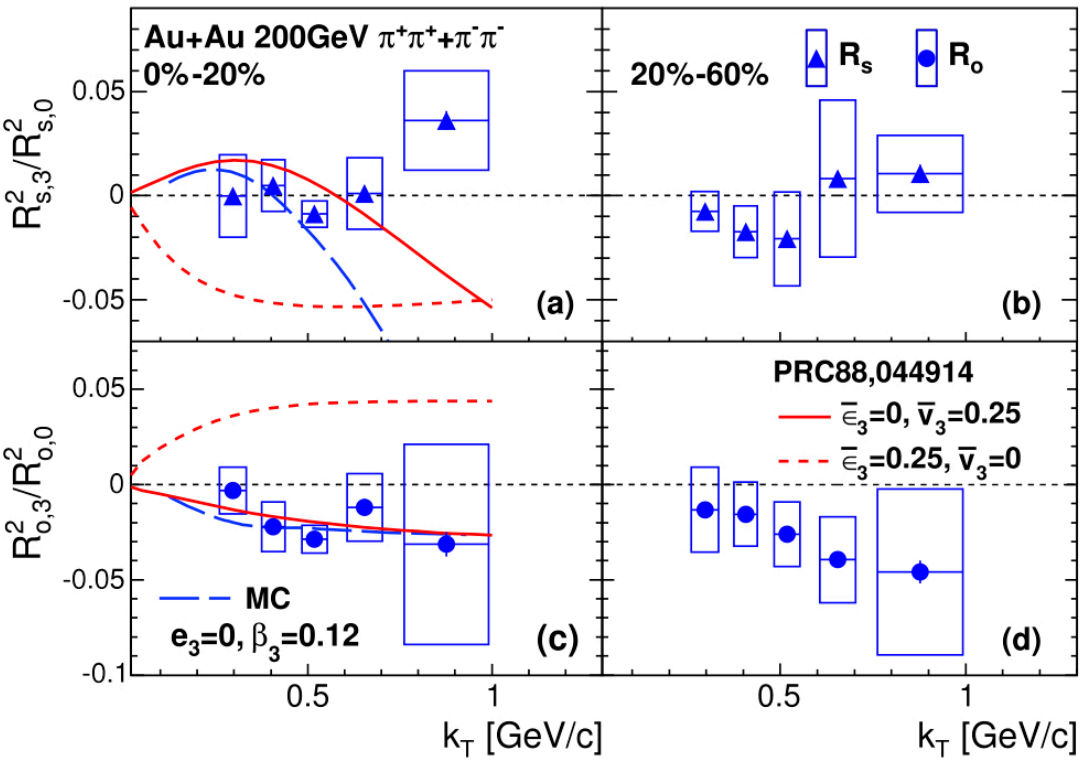

Figure 1.21: Relative amplitude of squared HBT radii(R_{out}, R_{side}, and R_{os}) for charged pion pairs with respect to Ψ_3 as a function of pair transverse momentum k_{T} for two centralities measured in Au-Au collisions at $\sqrt{s_{\mathrm{NN}}}$ = 200GeV from PHENIX [32]. Data is compared with two different Gaussian source distribution model. Solid line indicates that flow dominated case which is spherical spatial distribution superimposed on an large triangular flow, and dashed line shows geometry dominant case which is the geometric triangular distribuion superimposed on an azimuthally symmetric radial flow.

1.4 Thesis Motivation

Investigating a relation between initial and final source shape is quite important to understand the dynamics of the QGP and to provide feedbacks to theoretical models to further constrain the space time eveolution of heavy ion collisions. Azimuthal angle dependence of HBT radii is an unique and direct probe to access the final source shape. Measurements of azimuthal angle dependence of pions and kaons HBT radii with respect to Ψ_2 and Ψ_3 are extensively performed in Au-Au collisions at RHIC, but there is a remaining questions. Due to the large uncertainties, the oscillation sign of HBT radii relative to Ψ_3 is still not understood at this point. Furthermore, hydrodynamical model predicts the oscillaton of HBT radii with respect to Ψ_2 in LHC energy could be different to that in RHIC. Solving these problems will help to understand the scenarios of the system evolution.

In this thesis, measurements of azimuthal angle dependence of pion HBT radii with respect to Ψ_2 in Pb-Pb collisions at $\sqrt{s_{\rm NN}}$ = 2.76 TeV with ALICE detector is performed. Hydrodynamical model predicts oscillation of HBT radii relative to Ψ_2 shows the different behaviour to RHIC results due to extremely large collective flow [30]. Therefore we present the oscillation amplitude of HBT radii with respect to Ψ_2 and discuss the space time evolution of system with comparison of initial and final eccentricity.

Also measurements of azimuthal angle dependence of pion HBT radii with respect to Ψ_3 is performed. In LHC energy, large multiplicity and excellent event plane resolution allows us to measure azimuthal angle dependence of pion HBT radii with respect to Ψ_3 much more precisely to disentangle relative amplitude of HBT radii is positive or negative value to constrain the theoretical model.

Centrality is one of the probes for the initial geometry. However, when centrality changes from central to peripheral collisions, not only the initial geometry but also system size, freeze-out temperature, and flow velocity change simultaneously. Recently ESE technique is proposed to select the initial geometry within a certain centrality window, and it gives us the new insight of relation between the initial geometry and other observables separately from the system size. In this thesis, ESE q_2 and q_3 selection are applied to the measurements of azimuthal angle dependence of pion HBT radii with respect to Ψ_2 and Ψ_3. Relation between initial geometrical source shape and final source shape at freeze-out are discussed with Blast-wave model.

Chapter 2

Experiment

In this chapter, we introduce the performance of Large Hadron Collider where the hot and dense matter is created with relativistic heavy ion collisions and ALICE detector to measure the emitting particles. Also the method to accelerate the ions with LHC and to detect the particles with ALICE detector is described.

2.1 Large Hadron Collider (LHC)

Large Hadron Collider (LHC) is the world's largest particle accelerator, which is designed for proton-proton, proton-Lead and Lead-Lead collisions. LHC is built at European Organization of Nuclear Research (CERN) and located in French-Switzerland border. It consists of a 27-kilometer ring of superconducting magnets to boost the energy of the particles along the way. Inside the LHC beam pipe, particles circulate in the two tubes kept at ultrahigh vacuum (10^{-13}atm). They are manipulated with electromagnetic devices. Dipole magnets keep the beam to the circular orbits and quadrupole magnets focus the beam. Summary of the CERN's accelerator complex parameter is shown in Table2.1.

Table2.2 is beam parameters for LHC.The number of collision events per second ($\mathrm{N_{event}}$) is expressed with the following equation.

$$\mathrm{N_{event}} = \mathscr{L}\sigma_{event}, \tag{2.1}$$

where σ_{event} is the cross section and $\mathscr{L}$ is the machine luminosity which denotes the machine performance. Higher collision rate is the key for the precise understanding of high energy physics. $\mathscr{L}$ can be described under the Gaussian beam distribution by

$$\mathscr{L} = \frac{N_b^2 n_b f_{rev} \gamma}{4\pi \varepsilon_n \beta^*} F, \tag{2.2}$$

where N_b is the number of particles per bunch and n_b is the number of bunches per beam. f_{rev} is the number of bunch crossing per unit of time. γ is the relativistic gamma factor. ε_n is the normalized transverse beam emittance. β^* denotes the width of the beam F is the geometric luminosity reduction factor due to the crossing angle at the IP.

Table 2.1: Parameters for CERN's accelerator complex[35]

Quantity	unit	value
Circumference	m	26.659m
Dipole operating temperature	K	1.9K (-271.3^oC)
Peak magnetic dipole filed	T	8.33T
Number of magnets		9593
Number of main dipoles		1232
Number of main quadrupoles		392
Number of RF cavities		8 per beam

Table 2.2: Beam parameters for LHC[37]

Quantity	unit	Protons	Ions
Top collision energy	TeV (TeV/u for ions)	14	5.5
Design luminosity	$cm^{-2}s^{-1}$	1.0×10^{34}	1.0×10^{27}
Number of bunch		2808	592
Number of particles per bunch		1.15×10^{11}	7.0×10^{7}
RMS bunch length	cm	7.55	7.94

Figure2.1 shows the scenario of protons and lead ions acceleration[36]. Lead ions are accelerated to high energy with a succession of the machines : ECR (Electron Cyclotron Resonance source) , LINAC3 (LINear ACcelerator 3), LIEIR (Low Energy Ion Ring), PS (Proton Synchrotron), SPS (Super Proton Synchrotron) and LHC. At first, lead ions are produced with ECR ion source. A highly purified sample of solid lead (^{208}Pb) is heated to 550^{o}C, then solid lead (^{208}Pb) sample becomes a vapor. Evaporated lead (^{208}Pb) are injected into ECR. ECR is a plasma generator with solenoid magnets and Fe-Nd-B permanent magnet sextupole. The plasma electrons are confined with two magnet and accelerated with the electric field. Through the inelastic collisions between evaporated lead sample and hot electrons, lead sample are ionized (electron impact ionization)[38]. In this stage, Many different charge states are mixed

between Pb^{25+} and Pb^{29+}. Pb^{27+} at 2.5keV/u are selected and injected into LINIAC3. LINAC3 is the linear accelerator which consists of two machines, RFQ (Radio Frequency Quadrupole) and IH Linac. 100MHz RFQ accelerates the lead ions to 250keV/u and IH Linac increases the beam energy up to 4.2MeV/u. After the acceleration of Linac, lead (Pb^{27+}) ions are stripped by a 100 $\mu g/cm^2$ carbon foil and Pb^{53+} are provided to LEIR. LEIR also accelerates the ions, but the most important function of LEIR is electron cooling. Each long pulse from LINAC3 is split into 4 shorter bunches which contains 2.2×10^8 lead ions. Beam energy is accelerated to 72MeV/u in LEIR for 2.5 seconds. The nominal number of bunches per beam in LHC is 592, so it takes around 10 minutes for LEIR to fulfill this requirement. The beam in LEIR is transferred into the PS and accelerated to 5.9 MeV/u. Then Pb^{53+} beam is fully stripped by a thin 0.8 mm aluminum foil at the PS exit. Pb^{82+} beam is provided into SPS. The SPS accelerates it to 177GeV/u. Eventually ion beam is injected into LHC and accelerated up to 2.76 TeV/u.

Heavy ion collisions are provided at four interaction points in LHC and four experiments are investigating the physics of Quark Gluon Plasma : ALICE, ATLAS, CMS and LHCb which is installed in the huge underground caverns.

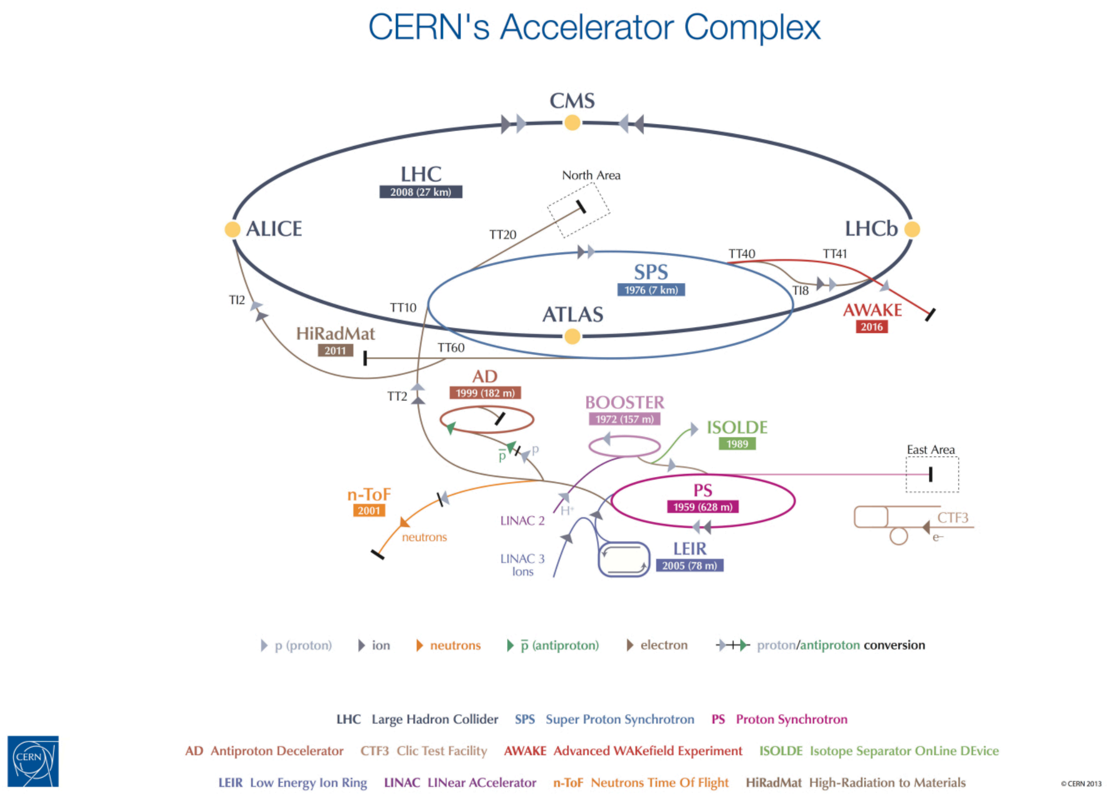

Figure 2.1: CERN accelerator complex

2.2 ALICE experiment

ALICE (A Large Ion Collider Experiment) is one of the large experiment at LHC-CERN. More than 1500 physicists, engineers from 41 countries are devoted to research into the property of Quark Gluon Plasma with heavy ion collisions at LHC. In heavy ion collisions, huge number of particles are produced which contains the clue of hot dense matter. ALICE detectors are optimized to measure the these particles with high granularity. In particular, charged particle can be reconstructed from low transverse momentum ($p_T^{min} \approx 0.15(GeV/c)$) and particle identification can be performed with wide momentum range up to 20 GeV/c.

Figure 2.2 is the 3D schematic of ALICE detector apparatus. Central barrel detectors are installed in the L3 solenoid magnet with 0.5T magnetic field and consist of 7 detectors - Inner Tracking system (ITS), Time Projection Chamber (TPC), Transition Radiation Detector (TRD), Time Of Flight (TOF), ElectroMagnetic CALorimeter (EMCAL), PHOton Spectrometer (PHOS) and High Momentum Particle Identification Detector (HMPID). Triggering and event characterization are performed with forward detectors (VZERO, TZERO, FMD, PMD and ZDC). ACORDE is located on the top of L3 magnet for triggering the cosmic-ray to collect high muon multiplicity events. In order to measure light vector mesons (ρ, ω) and quarkonium (J/ψ, Υ) with $\mu^+\mu^-$ decay channel, Muon Spectrometer are placed in the forward rapidity.

In this section, the detectors related to this thesis is introduced.

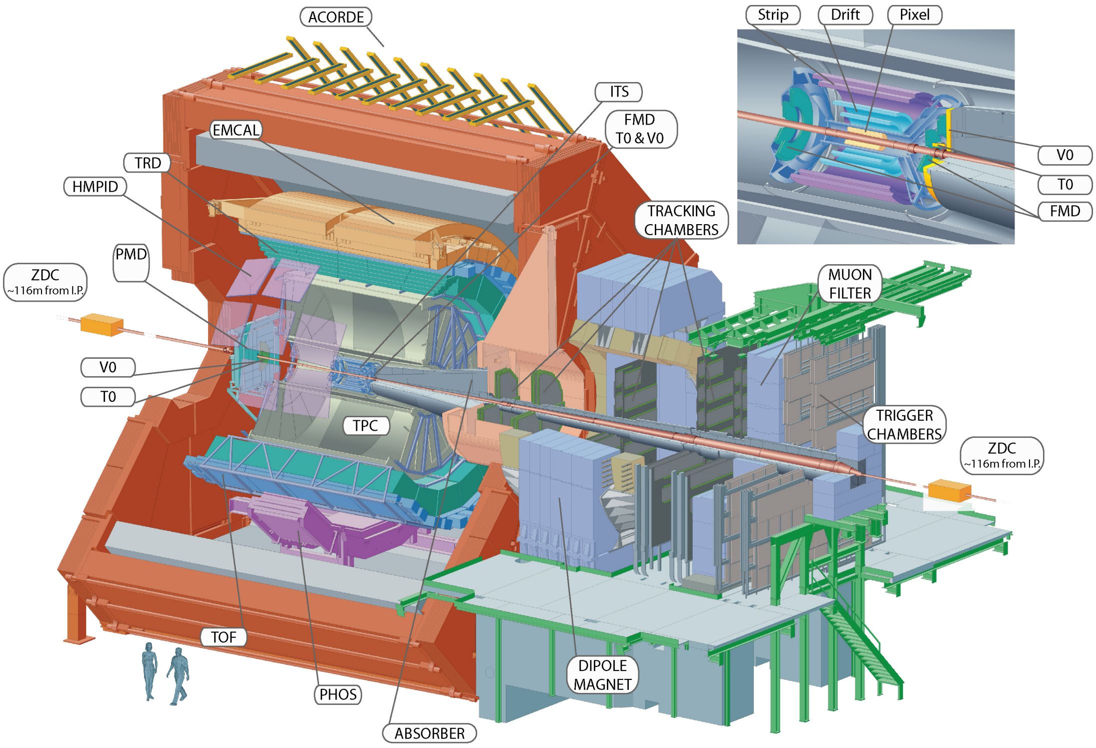

Figure 2.2: 3D schematic of ALICE experiment at the CERN LHC. ITS, TPC, TRD, TOF, EMCAL, PHOS and HMPID are installed in 0.5 Tesla magnetic field which is applied with solenoid magnet to measure the midrapidity particles. Forward detectors (VZERO, TZERO, FMD, PMD and ZDC) are also in the magnet and used for triggering and event characterization. In order to trigger the cosmic-ray, ACORDE is placed on the top of solenoid magnet. Muon arm which consists of Muon tracker (MCH) and Muon trigger (MTR) is located in the forward rapidity in the dipole magnet with $\int Bdz$=3Tm after the front absorber.

2.2.1 ALICE magnet system

ALICE is equipped with two large magnets (L3 magnet and dipole magnet) to measure the charged particle momentum and particle identification.

Figure2.3 shows the general layout of ALICE L3 magnet which is inherited from LEP-L3 experiment[39]. L3 magnet is a solenoid magnet consists of octagonal iron barrel yoke around the coil and two pole caps at the end of barrel. In order to make homogeneity magnetic field especially in TPC, it is important to limit the stray flux at the end of magnet. Two pole caps which is in the form of two semicircle per each side are build for it. Each sector is equipped as a hinged "door". the coil of L3 magnet consists of 168 octagonal turns constructed from 60 mm$\times$890 mm aluminum plates. typical current for the solenoid coil is 30 kA and each turns has a water cooling circuit. L3 magnets covers Central-barrel detectors and forward detectors except for ZDC and provide 0.5T magnetic filed in the direction of parallel to the beam.

Second magnet is dipole magnet for muon spectrometer located in the forward rapidity at 7m from interaction point. It's one of the biggest warm dipoles in the world. The schematic of dipole magnet assembly is denoted in Figure2.4. ALICE dipole magnet provide $0.7T$ nominal magnetic field (3 $T \cdot m$ field integral) in a perpendicular direction of beam axis and typical current is 6kA. A water cooling system is designed to manage the heat of joule effect in coil. This magnet consists of two semi-circular coils and the vertical poles of the rectangular yoke.

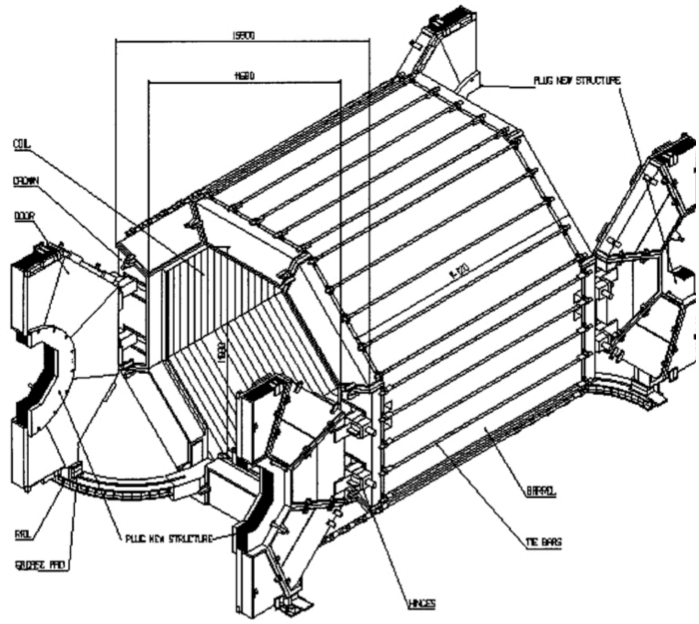

Figure 2.3: 3D schematic of L3 magnet

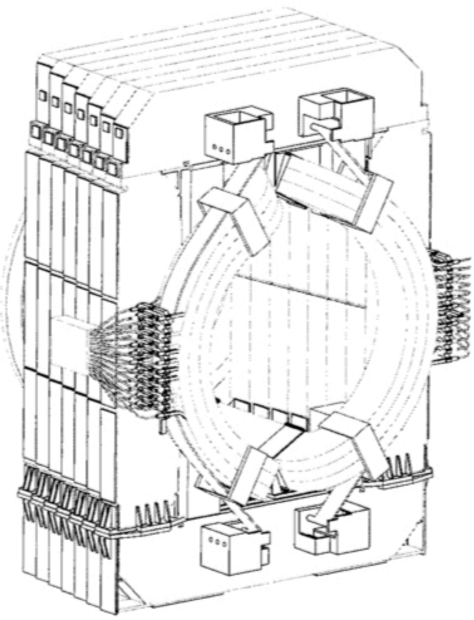

Figure 2.4: 3D schematic of Dipole magnet

2.2.2 Time Projection Chamber

Time Projection Chamber (TPC) is one of the main tracking detector for charged particles which covers mid rapidity. TPC has a lot of roles to provide the momentum of charged particles, particle identification with energy loss, collision vertex determination and two track separation (it's very important for this HBT correlation analysis. Because Bose-Einstein enhancement can be found in "closed" two pair).

This detector allows us to extract 3 dimensional trajectory of charged particles. ALICE TPC is designed of cylinder filled with Ne CO_2 (90:10) mixed gas. Inside of TPC, filed cage keeps the uniform electric filed in parallel direction to the beam axis. Charged particles traveling in the TPC ionize the gas and produce election-ion pairs along their trajectories. Electrons drift along electric field toward read-out pad due to the central high voltage electrode. Vicinity the grid of anode wire, drifting electrons make avalanche and their signals are amplified and read out from pad. x-y position of charged track can be obtained with their signal on the read-out pad and z axis coordinate can be extracted from the drift time of ionized electrons.

TPC acceptance is full azimuthal angle and $|\eta|<0.9$ (Though TPC drift volume covers much wider η acceptance, its acceptance is limited to combine the other detectors and to get good track reconstruction quality). The schematic of TPC is shown in Figure2.5. TPC inner and outer radius is about 80cm and 250cm respectively. Overall length in the beam direction is 510cm. Drift volume is 88m^3 and divided in two regions by the central electrode that applied HV is 100kV. Filed cage keeps uniform electric filed with the voltage gradients 400V/cm. TPC signals are obtained with readout chambers on the end cap of TPC. 18 readout chambers per each side are installed on the end cap. Each readout chambers are trapezoidal shape and each covers 20 degree in azimuthal angle. Figure 2.6 shows the schematic of wire planes in a TPC. Drifting electrons are amplified with avalanche around the anode wire (1450-1720V). A lot of ions are also produced with that avalanche and it cause a noticeable reduction in electron transmission. Cathode wire can collect these ions and separate the drift volume from the amplification region. Gating grid is power full tool to control the elections and ions go through with applied voltage and there are mainly two important roles. First one is to prevent ions created in the previous event from escaping to drift volume. escaping ions can cause distortions of the drift field. Second one is to prevent electrons from entering the avalanche region if there's no valid triggers.

In this analysis, two track resolution and dE/dx resolution are important. HIJING+GEANT study of two track separation is plotted in Figure2.7. Pericles are generated with HIJING in dN_{ch}/dy=8300. After the reconstruction with GEANT, two track efficiency is calculated as a ratio of the number of reconstructed pairs to that of generated ones. One can see that pair efficiency goes down if their momentum differs by less than $0.015 GeV/c$[40]. dE/dx resolution depends on particle density produced in the event. dE/dx resolution is 7.0% (dN_{ch}/dy=1300), 8.6% (dN_{ch}/dy=4300) and 17.3% (dN_{ch}/dy=8300).

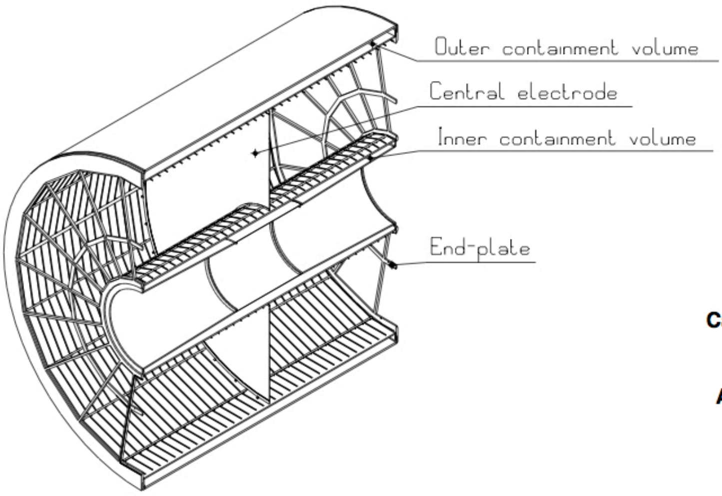

Figure 2.5: 3D schematic of TPC

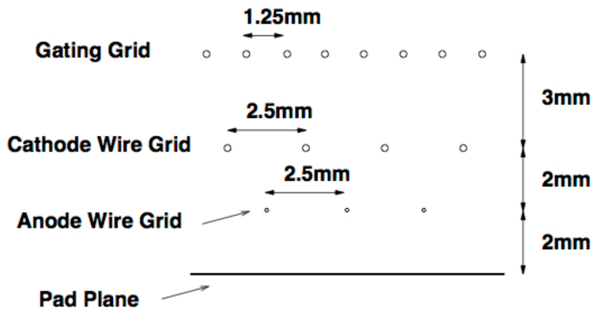

Figure 2.6: A cartoon illustrating of TPC wire in the readout chamber

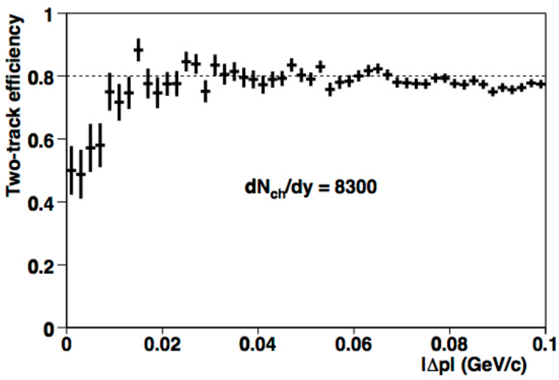

Figure 2.7: Two track efficiency for particle density dN_{ch}/dy=8300 as a function of absolute value of generated momentum difference of two particle with HIJING+GEANT simulation

2.2.3 Inner Tracking System

Precise vertex position determination and secondary vertices of charm and hyperon decay can be derived with Inner Tracking System (ITS). Also ITS improves momentum and angle measurement by TPC-ITS combined tracking. Particle identification of low momentum can be obtained with energy loss in ITS.

ITS is composed of six cylindrical layers of silicon detectors which is the surrounding the interaction point. The two innermost layers are Silicon Pixel Detectors (SPD), the middle two layers are Silicon Drift Detectors (SDD) and the two outermost layers are Silicon Strip Detectors (SSD). Figure 2.8 shows the front view of SPD layout (view from the beam axis). SPD consists of two silicon pixel detector modules at radius 3.9cm and 7.6cm. 6 staves (2 for inner and 4 for outer) are fixed on the each lightweight carbon-fiber sectors. Each stave has 4 ladders, each ladder consisting of 256×160 cell matrix silicon pixel sensor. In third and forth layers are SDD which is precise position resolution silicon detector. charged particles create electron hole-pair by ionization traveling inside the silicon. Electrons drifts with the constant speed towards n type silicon substrate by parallel drift cathodes. The drift time and read-out position allows us to unambiguous determination of both x-y coordinates with low readout channels and high position resolution. Figure2.10 shows the picture of SDD inner layer[42]. SDD consists of 14 ladders and 6 detectors for 3rd layer at radius 14.9cm and 22 ladders and 8 detectors for 4th layer at radius 23.8cm. 5th and 6th outermost layers SSD are double sided silicon strip detectors.Both p-side and n-side has strip structure and provides x-y coordinate with high position resolution and small dead time.SSD is composed of 34 ladders at radius 38.4cm and 38 ladders at radius 43.4cm. Each ladders have 23 and 26 silicon strip detector modules for 5 and 6 layers (Figure2.11).

The acceptance of ITS is full azimuthal angle and $|\eta| < 0.9$ except for the inner most pixel layer. In order to extend acceptance for multiplicity measurement, SPD first layer η acceptance is much wider $|\eta| < 1.75$. Position and angle resolution is written in Table2.3.

Figure2.12 shows primary vertex resolution in Pb-Pb collisions at 2.76 TeV as a function of half of the event tracklets multiplicity. Obtained vertex resolution is fitted with the equation spotted in the figure and extrapolated to most central collisions (0-5%) corresponding to orange region[44].

Table 2.3: Performance of ITS (position and two track resolution for azimuthal and beam directions).

Parameter	Unit	Silicon Pixel Detector	Silicon Drift Detector	Silicon Strip Detector
Spatial precision rϕ	μm	12	38	20
Spatial precision z	μm	70	28	830
Two track resolution rϕ	μm	100	200	300
Two track resolution z	μm	600	600	2400

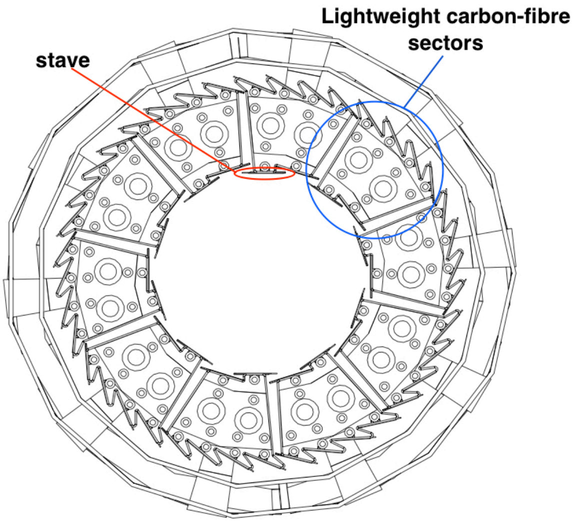

Figure 2.8: Front view of SPD layers layout. It is a modular structure with 10 sectors made of light carbon-fibre in φ. 6 staves (2 ladders and 4 ladders) are fixed on each carbon-fibre sectors. [41]

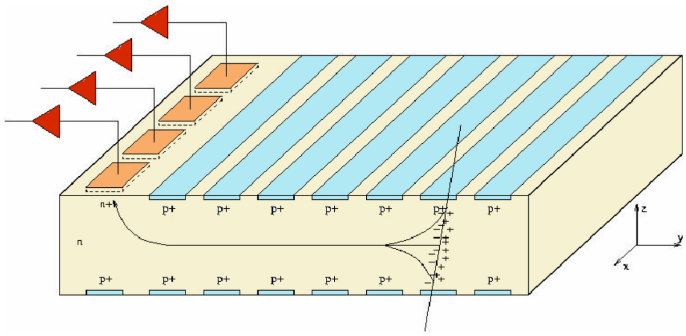

Figure 2.9: A cartoon illustrating of how to measure hit position of charged particles with SDD. Electrons created by charged particles drift in a silicon and signals are read in n type substrate

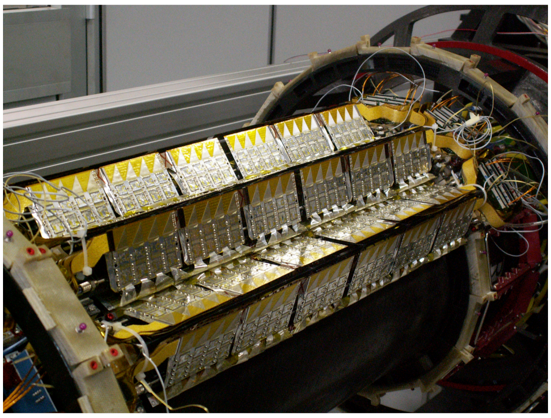

Figure 2.10: SDD (third layer) has 14 ladders and 6 detectors in each ladders for 3rd layer and 22 ladders and 8 detectors for 4th layer[42]

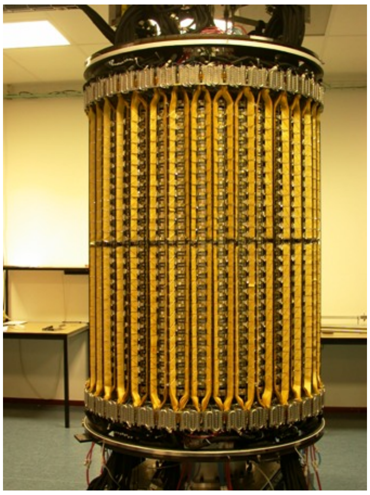

Figure 2.11: Side view of SSD. SSD has 34 and 38 ladders for layer5 and layer6, respectively. Each ladder in layer 5 and 6 is made of 38 and 26 SSD modules, respectively [43].

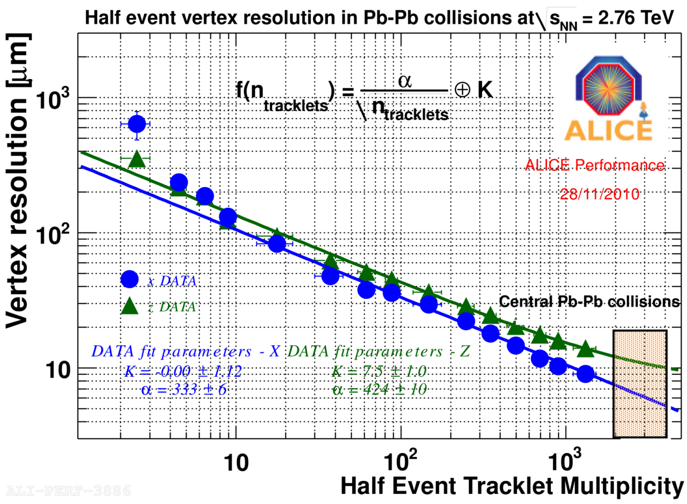

Figure 2.12: Primary vertex resolution in Pb-Pb collisions at $\sqrt{s_{NN}}$ = 2.76TeV as a function of half of the tracklets multiplicity of the event. In this figure, the resolution of X and Z coordinate primary vertex resolution are shown. The resolution is obtained dividing the tracks of the event in two random samples.[44]

2.2.4 Time Of Flight

ALICE Time Of Flight (TOF) detector is made of Multigap Resistive Plate Chamber (MRPC). Measuring time of flight of the emitting particle is important to identify particle species by the difference of its mass (Although PID can be applied with energy loss in TPC, π/K and K/p separation could not reach over 1 GeV/c and 2 GeV/c, respectively). The requirement for TOF is 3σ separation of π/K and K/p for momenta up to 2.5 GeV/c and 4 GeV/c, respectively. The time resolution of TOF should be better than 100ps to fulfill it[45]. Scintillates and phototubes are the representative of TOF detector with good time resolution and used in high energy physics frequently. But the cost we envisage is prohibitive to cover the large acceptance with scintillator/phototube type detector. Thus MRPC is selected in ALICE to offer the excellent time resolution and $\approx 176m^2$ coverage driving down producing cost. ALICE TOF is of 1593 double-stack MRPC covering full azimuthal angle and $|\eta| < 0.9$ acceptance. It is a modular structure called Super Module (SM) with 18 sectors in azimuthal angle and each of SM are divided into 5 modules (a central, 2 intermediate and 2 outer modules). 19 strips are installed in intermediate and outer modules. Central module is of 15 strips.

Figure 2.13 shows the schematic of a double-stack MRPC module. MRPC is a stuck of 4 highly resistive ($\approx 10^{13}\Omega$cm) soda-lime glass plates (400μm thick). These internal glasses are separated with fishing line to hold the width of gas gap to be 250μm. External glasses (550μm thick glass plate) are on the either side of internal glasses. High voltage are applied to specially developed acrylic paint loaded with metal oxides on the external glasses. Non-flammable gas are used in ALICE and it's mixture of 97% $C_2H_2F_4$ and 3% SF_6 Applied electric filed is greater than 100kV/cm^2 on the each gas gaps. Charged particles going through gas gaps makes the avalanche and image charge are readout by 2.5×3.5 cm^2 size cathode pick up pads (48×2 pads per strip).

The performance of TOF detector is shown in figure2.14. Time distribution with respect to start time defined with scintillator is plotted in left figure. Data is fitted with Gauss function and time resolution is 50.8ps. Right figure represents TOF efficiency, time resolution and the ratio of streamer as a function of applied voltage between 5 gas gaps. Efficiency becomes plateau from $\sim$11kV to reach 99.9%. time resolution doesn't have significant applied high voltage dependence and the value is 50ps.

Figure2.15 is distribution of difference between measured and expected time of flight for charged pions measured in Pb-Pb 2.76TeV collisions. It indicates TOF PID resolution. The width of this distribution contains time resolution of start counter. Obtained overall time resolution is 86 ps.

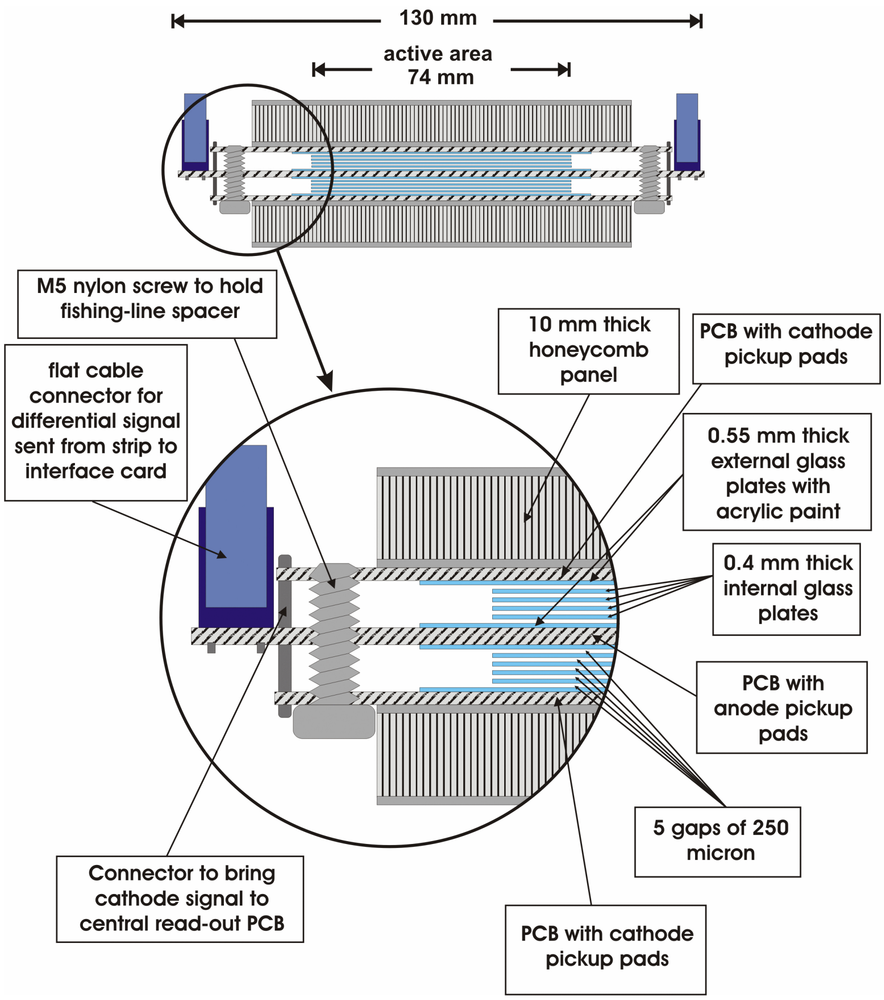

Figure 2.13: Construction details of a double-stack MRPC modules. 4 resistive inner glasses are inserted between external glass plate. Width of 5 gas Gaps are 250 μm, having fishing lines between the glass. High voltage are applied to the specially developed acrylic paint loaded on the external glass.[46]

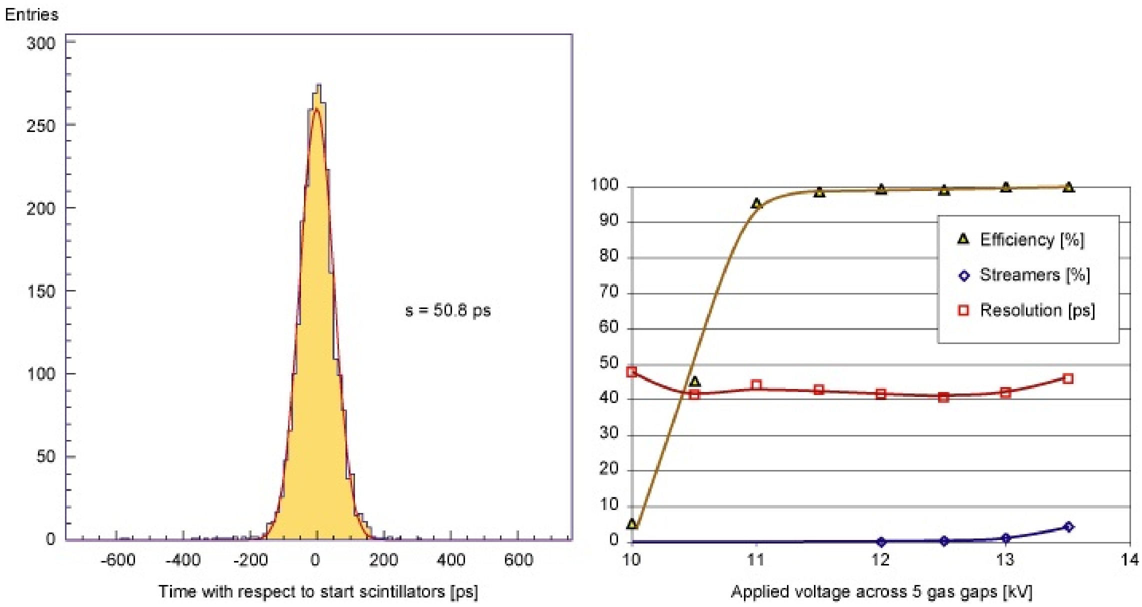

Figure 2.14: (Left) Time distribution of MRPC with respect to scintillator start time after the slewing calibration. Then 50.8ps time resolution can be obtained Gaussian fitting. (Right) Efficiency, time resolution and the ratio of streamer as a function of applied voltage across 5 gas gaps. Typical efficiency and time resolution flat as a function of applied high voltage is more than 11kV with 99.9% efficiency before the streamer is getting large.[47]

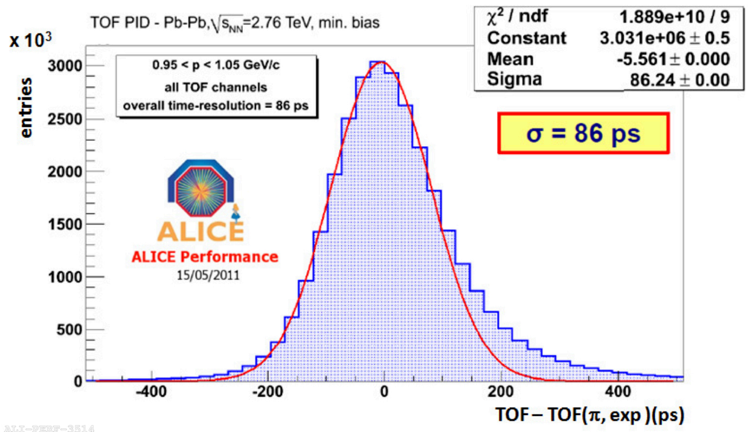

Figure 2.15: Distribution of the difference between measured and expected arrival time on TOF for selected pions (p:0.95-1.05GeV/c) in Pb-Pb collisions at 2.76 TeV. The width of the signal of charged pions at 1.5GeV/c. Red line shows the Gauss function to data.[48]

2.2.5 TZERO

TZERO (T0) detector is of two arrays detector composed by 24 Cherenkov counters depicted in figure2.16. Each cherenkov counters are of quartz + fine mesh photomultiplier. $FEU-187$ from Russian firm Electron is selected for photomultiplier as good timing resolution in magnetic field of 0.5T and large radiation dose (up to 500krad). Size of quartz radiator is 30mm diameter and 30mm long. charged particles passing through quartz radiator and if the speed of charged particles is greater than that of light in the medium, cherenkov light is emitted. Cherenkov light is amplified with photomultiplier. T0 detector provide multiplicity by measured number of photons with good time resolution. T0 detector two arrays (T0C and T0A) are on the opposite side of interaction point along with the beam axis. Each arrays are located at 0.7m and 3.6m from the IP for T0C (backward rapidity) and T0A (forward rapidity), respectively. So two arrays of T0 detector covers asymmetric rapidity coverage, T0A covers full azimuthal angle and 4.5 < η 5.0 and T0C covers backward rapidity -3.3 < η < -2.9. We can estimate approximate vertex position with the difference of signal arrival time between T0Aside and T0Cside.

Main roles of T0 detector are following.

- To provide the main signal for ALICE L0 trigger
- To give the start time for the Time Of Flight (TOF) detectors with good time resolution
- To supply the early "wake up" trigger for Transition Radiation Detector (TRD)

In order to fulfill the required performance, T0 must have 50ps time resolution (it indicates $\pm$1.5m vertex position resolution). Total dead time should be below the 25 ns.

Figure 2.17 shows the time of flight distribution obtained in the 2004 test run. Test beam was performed in CERN PS with 6GeV/c negative pion and kaon beams. Both start and stop time are determined with T0 detector. Obtained Time resolution of T0 detector is 28 ps with following equations (Eq. 2.4 and 2.4) where σ_{TOF} is sigma of Time of flight distribution and σ_{det} denotes time resolution of a detector.

$$\sigma_{TOF} \approx \frac{\text{FWHM}}{2.35}, \tag{2.3}$$

$$\sigma_{det} = \frac{\sigma_{\text{TOF}}}{\sqrt{2}}. \tag{2.4}$$

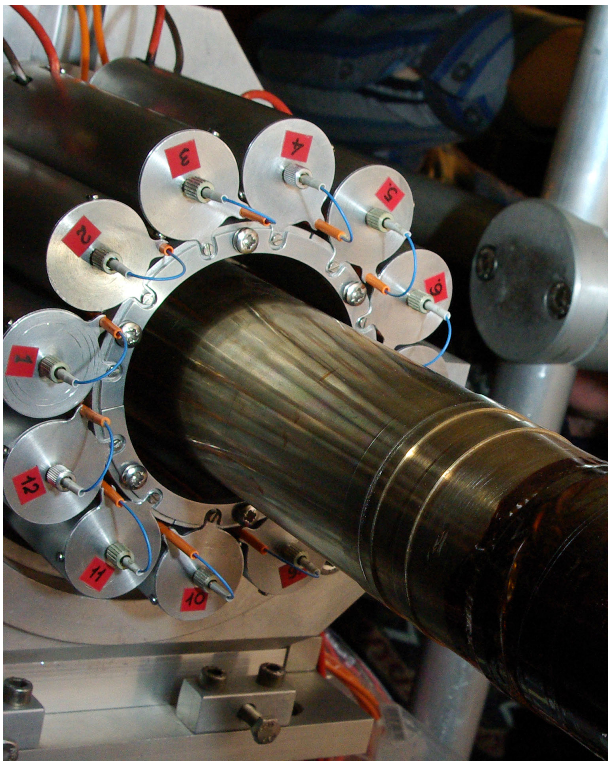

Figure 2.16: T0 detector C-side has 12 cherenkov counters made of fused cherenkov radiator (quartz) and photomultiplier located on the opposite side of IP.[47]

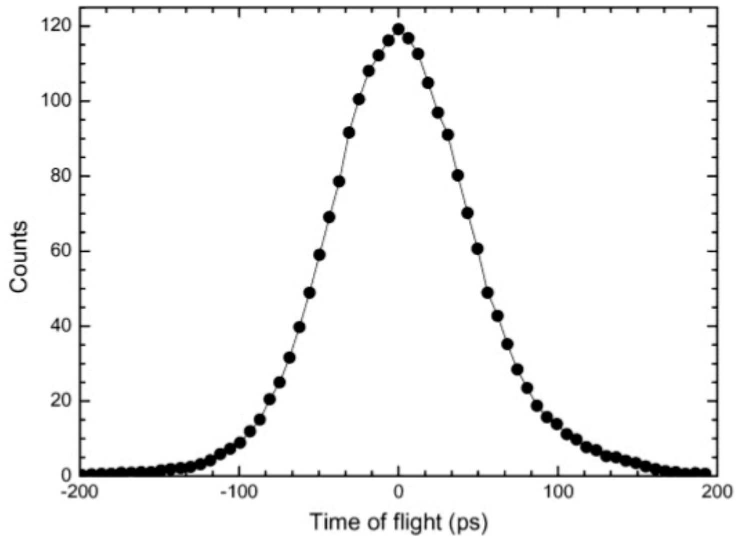

Figure 2.17: Time of flight distribution obtained in the 2004 test run with 6 GeV/c particles. Both start and stop time is measured with T0 (Cherenkov radiator+PMT) modules. The FWHM for this distribution is 94 ps which corresponds to 28 ps R.M.S. [49].

2.2.6 VZERO

VZERO (V0) detector is of two arrays scintillation counters installed on the opposite side of IP. Each arrays are called V0 Aside (V0A) and V0 Cside (V0C). V0 A side is located at 340cm from IP and covers forward rapidity ($2.8 < \eta < 5.1$). V0 C side is installed at the distance of 90cm from IP and covers backward rapidity ($-3.7 < \eta < -1.7$). Each array is composed of 32 segment scintillation detector distributed in 4 rings (Figure2.18). Each rings have 8 segments and 0.5 and 0.6 unit of pseudo-rapidity coverage for Aside and Cside, respectively. One segment of VZERO detector are made of photomultiplier tube (PMT) + BC404 plastic scintillator from Bicron with 2.5 and 2.0cm for V0A and V0C, respectively. Light from MIPs in scintillators are collected with WLS (WaveLength Shifter) fibre and transferred to fine mesh PMT R5946-70 from Hamamatsu which can be operated in 0.5T magnetic field. The different couplings of scintillator and WLS fibre is applied for V0A and V0C due to the limited space at C side (shown in Figure2.18, 2.19).

Number of charged particles traveling the each segment are measured with MIPs (Minimum Ionizing Particles). The difference of arrival time between V0A and V0C provide approximate vertex position.

V0 detector has several function written in the following.

- To provide Minimum Bias trigger for the central detectors in both pp and Pb-Pb collisions
- To give the centrality with the multiplicity by measuring MIPs in V0
- To reject p-gas events, caused by beams interacting with the residual gas in the beam pipe, in Minimum Bias pp collision
- Determination of Event plane with large rapidity coverage

In central Pb-Pb collisions total number of MIPs reaches 4000 (8000) for V0A (V0C) when secondary particles are included. Dynamic range of each segment in V0 is required to be at least 1-500 and 1-1000 for A and C side, respectively.

In Pb-Pb collisions, trigger efficiency depends on centrality. Except for very peripheral collisions, trigger efficiency is almost 100% and Pb-gas and Pb-halo collisions can be removed with V0 arrival time. Time resolution is about 450 ps and 350 ps for V0A and V0C.

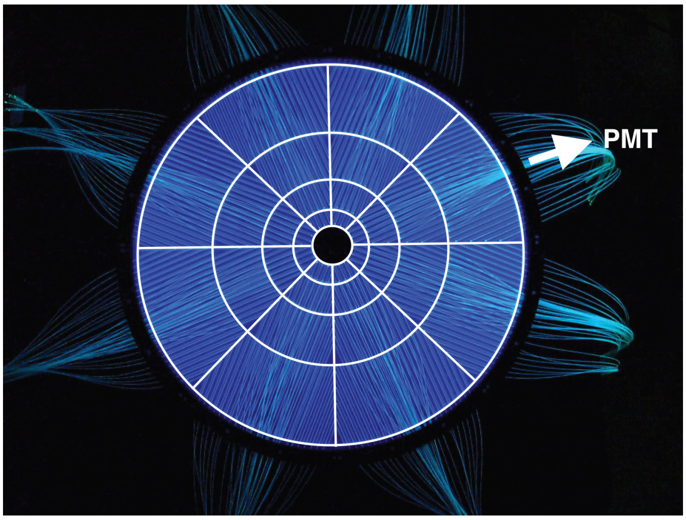

Figure 2.18: V0 detector Aside consists of 32 scintillator (4 rings and 8 segments of 45 degrees in φ) and WLS fibers. For V0A detector, WLS fibres are spaced by 1cm and each segments are divided with "magtile" construction method. Signals are collected with WLS fibres and sent to connected PMT. [47]

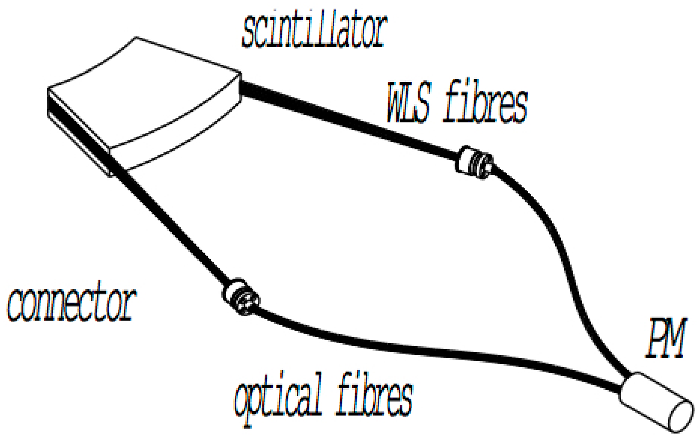

Figure 2.19: Schematic figure of coupling of the scintillator and WLS fibre for V0C. WLS fibre is embedded along the two radial edges of the scintillator piece. [49].

2.2.7 Forward Multiplicity Detector

Forward Multiplicity Detector (FMD) is silicon strip detector to measure charged particles. FMD is of 3 modules (FMD1, FMD2 and FMD3). Figure2.20 represents the location of overall FMD detector and ITS. FMD3 is located on the right side of ITS at the distance of 320cm. On the left side of ITS, two grey rings indicate FMD2 module located at 75.2 (83.4) cm from IP. Distantly located from ITS, FMD3 is located at 62.8 (75.2) cm from IP. FMD2, 3 is composed of two rings (inner and outer) geometry similar to PHOBOS experiment. FMD1, FMD2 inner and FMD3 inner rings consist of 40 segments silicon strip detector. each silicon sensor is subdivided into two azimuthal sectors and 512 strips. FMD2 outer and FMD3 outer rings are composed of 20 segments silicon strip detector. each silicon sensor is subdivided into two azimuthal sectors and 216 strips.

Location, segmentation and acceptance of FMD detector is summarized in table2.4.

Table 2.4: Table indicates nominal distance in z from the IP to the detector plane, pseudo-rapidity coverage of each detector modules, number of azimuthal sectors distributed in each ring and number of read out detector strip

Modules	z (cm)	η coverage	Azimuthal sectors	Radial strips
FMD1	320.0	$3.68 < \eta < 5.03$	12	512
FMD2 inner	83.4	$2.28 < \eta < 3.68$	20	512
FMD2 outer	75.2	$1.70 < \eta < 2.29$	40	256
FMD3 inner	-75.2	$-2.29 < \eta < -1.70$	20	512
FMD3 outer	-62.8	$-3.40 < \eta < -2.01$	40	256

FMD has several function written in the following. Especially 20 (40) segmentations in azimuthal angle allow us the precise measurement of event plane with excellent event plane resolution, in particular for higher order event plane resolution.

- To provide charged particle multiplicity distribution in large rapidity acceptance ($-3.4<\eta<-1.7$, $1.7<\eta<5.0$).
- To give precise determination of higher order event planes with 20 (40)segmentations in azimuthal angle

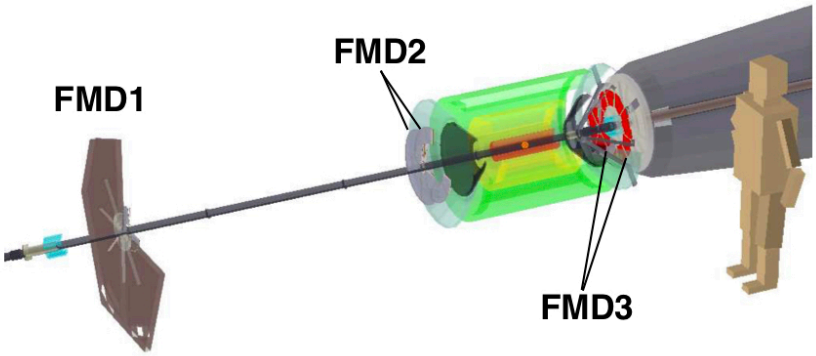

Figure 2.20: Location of overall FMD detector and ITS. Orange point denotes IP and ITS depicted yellow and green region surrounds the IP. On the right side of ITS, FMD3 module (two rings) is shown in red. Two rings on the left side of ITS indicate FMD2 module. Distantly located from ITS, FMD2 and FMD3, FMD1 module is represented as grey octagon. [49]

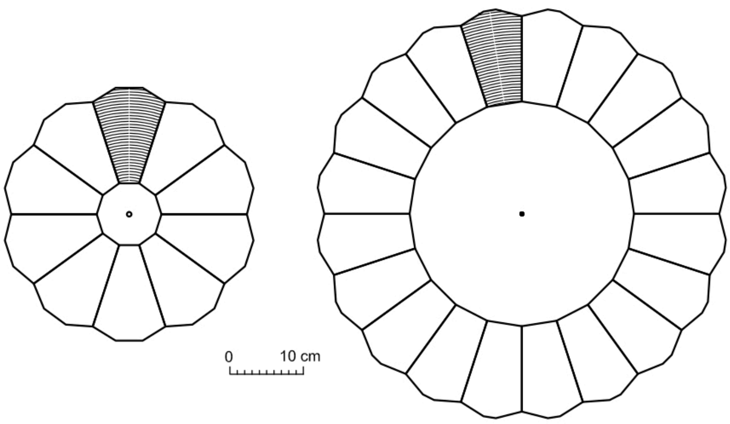

Figure 2.21: Assembly of FMD inner ring and FMD1 from 10 modules (left) and FMD outer ring from 20 modules (right). Each modules are subdivided into two segments in azimuthal angle. [49]

Chapter 3

Data Analysis

In this chapter, we introduce data set and analysis method which is event characterization, track selection, pair selection, particle identification of charged hadrons. Also fitting and correction for HBT analysis are described here.

3.1 Event characterization

The following event characterization method is written in this section.

- Event trigger and data set
- Centrality determination
- Event selection and track selection
- Event plane determination

3.1.1 Event trigger and data set

Event trigger is important to identify the beam-beam collisions in nuclear and particle physics using accelerator.

Minimum bias trigger is defined with V0 multiplicity that at least one signal can be found on the both V0A and V0C segment in coincidence with at least one beam at the ALICE IP. Multiplicity triggers (Central and Semi-central triggers) are also defined with V0 detector. V0A and V0C charge are integrated and compared with the defined threshold programmed in FPGA[49]. Central and Semi-central trigger are corresponding 0-10% and 10-50% online trigger, respectively.

In this analysis, 30 million events in $\sqrt{s_{\rm NN}}$ = 2.76 TeV Pb-Pb collisions collected with the ALICE detector in 2011 using Minimum Bias, Semi-central and Central trigger. Beam-gas and beam-halo collisions are the machine induced background of beam-beam collisions (about 10% of all triggered data[50]). These events can be rejected with offline event selection using particles arrival time on V0A and V0C. Figure 3.1 shows the geometry and time alignment of V0A and V0C. In beam-beam collisions, particles should be measured in 11ns and 3ns after the collision at V0A and V0C, respectively.

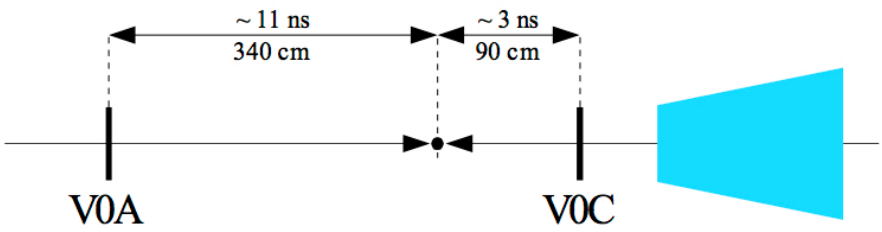

Figure 3.1: Geometry and time alignment of V0A, V0C and hadron absorber for muon spectrometer. Cyan trapezoid denotes hadron absorber. Interaction Point is shown in black full circle. [49]

3.1.2 Centrality determination

Initial volume and source shape are important probe for studying the hot dense matter and significantly correlated with impact parameter. But impact parameter can not be directly measured in experiment. So the concept of "centrality" which is defined as the overlap percentile of initial source is incorporated Initial source volume becomes larger when centrality becomes peripheral to central in participant-spectator model and the volume of the initial overlap region can be expressed via the number of participating nucleons(N_{part}) and the number of binary collisions(N_{coll}).

In this analysis, centrality is estimated via Glauber fitting with VZERO multiplicity distribution based on Negative Binomial Distribution(NBD)[50]. In this model, all emitting particles are generated with a given N_{part} and N_{coll} value and Both N_{part} and N_{coll} are defined as the concept of "ancestors" expressed by $N_{ancestors} = fN_{part} + (1-f)N_{coll}$. This is two component models that nucleus-nucleus collisions are decomposed into soft and hard interactions, where soft and hard interactions are proportional to N_{part} and N_{coll}, respectively. Each particles are produced based on negative binomial distribution. The probability of measuring n hists in each ancestor is expressed with the following equation.

$$P_{\mu,k}(n) = \frac{\Gamma(n+k)}{\Gamma(n+1)\Gamma(k)} \frac{(\mu/k)^n}{(\mu/k+1)^{n+k}} \tag{3.1}$$

where μ is the mean multiplicity in each ancestor and k denotes the width. Figure 3.2 shows the VZERO multiplicity distribution with 3-out-of-3 trigger which is defined by signals in V0A and V0C and at least two hits in the outer layer of SPD. Z-vertex cut $|V_z|$< 10cm is applied. The distribution is fitted with NBD Glauber shown in red line and centrality can be extracted with this model.

In ALICE, centrality can be extracted various detectors, V0A+C, V0A, V0C, SPD, TPC and ZDC. We can estimate the centrality resolution via 6 different centrality value with them. The average centrality value is calculated for each event.

$$\langle c \rangle = \frac{\sum_{i=0}^{N} c_i}{N} \tag{3.2}$$

where c_i is the centrality via each estimator and i denotes each estimator running over all detectors (N = 6). Here we define the difference between average and each centrality value via each estimator Δ_i = c_i - $\langle c \rangle$. Then average value is iteratively calculated with following equation, replacing $\langle c \rangle$ until $\langle c \rangle$ is converged.

$$\langle c \rangle = \frac{\sum_{i=0}^{N} c_i/\Delta_i^2}{\sum_{i=0}^{N} 1/\Delta_i^2} \tag{3.3}$$

Finally centrality resolution is obtained with the R.M.S. of Δ_i distribution via each detector. Figure 3.3 shows the centrality resolution of V0A+V0C, SPD($|\eta|$<1.4), TPC($|\eta|$<0.8), V0A, V0C, ZDC-ZEM. The best centrality resolution is achieved with V0A+C combined estimator. Centrality resolution via V0A and V0C combined is 0.5 to 2 % from most central to peripheral collisions.

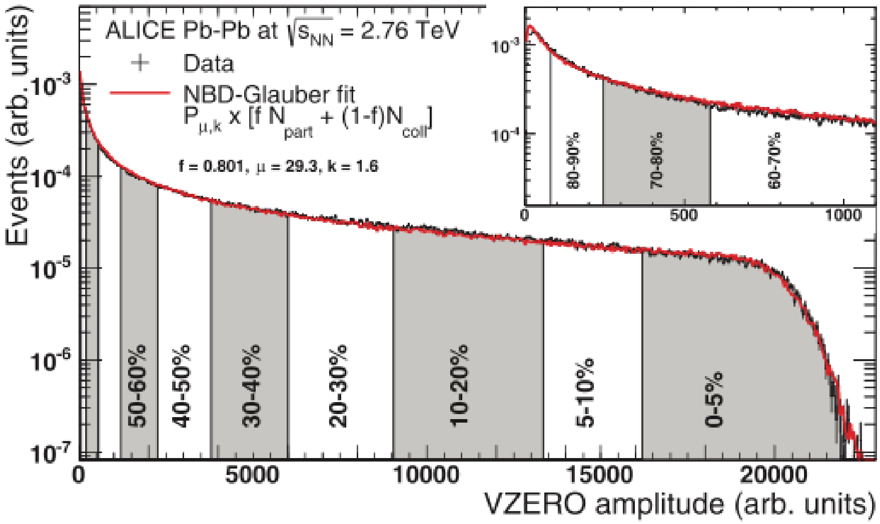

Figure 3.2: Distribution of sum of V0A+C amplitude. Data is fitted with NBD Glauber fit shown in red line. The centrality classes obtained by fitting are indicated with grey and white region. Inserted figure denotes a zoom of the most peripheral events. [50]

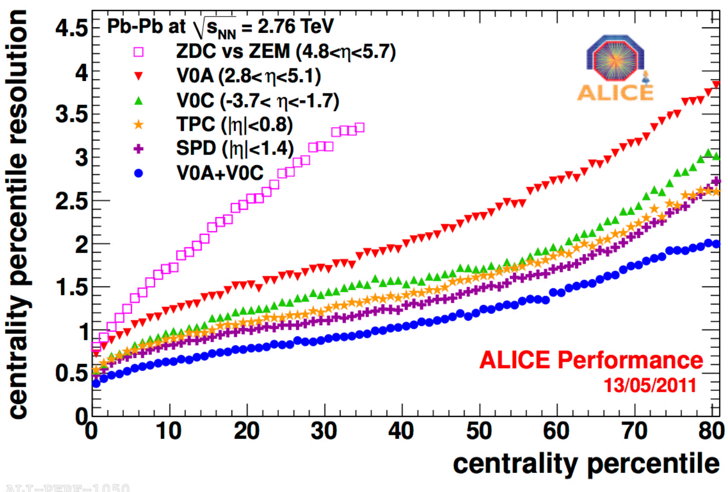

Figure 3.3: Centrality resolution with V0A, V0C, V0A+C, TPC($|\eta|$<0.8), SPD($|\eta|$<1.4) as a function of centrality percentile. resolution is calculated with 6 all estimation detectors. [50]

3.1.3 Event selection

Centrality is estimated with the amplitude of VZERO A and C side combined which has the best centrality resolution[50] and centrality 0-50% events are analyzed in this analysis. Minimum Bias trigger, Semi-central and Central triggers are required. Primary vertex is determined with SPD. Vertex position along the beam axis(z_{vtx}) is important because the detector acceptance largely changes if z vertex position shifts from the nominal interaction point. $|z_{vtx}| < 8.0$cm cut is applied.

3.1.4 Track selection

In this analysis, charged tracks are reconstructed with TPC, constrained with primary vertex via SPD. TPC clusters are fitted with Kalman filter algorithm[51]. Decay particles are also included and they are the background of this analysis. Thus the appropriate track selection is necessary to be applied. Fitting quality for track finding is provide with χ^2 per number of degree of freedom. There are 159 pad rows in TPC readout chamber and at most 159 TPC clusters are used for track reconstruction. In this analysis, χ^2/NDF is required to be below 4.0 and tracks which is reconstructed with at least 80 clusters are used. This selection allows us to remove the tracks which is not originated from primary vertex. In addition to this track selection, kink tracks are rejected. Kink structure is the feature of secondary particles. Moreover the contamination of daughter tracks from weak decay can be reduced with Distance of Closest Approach(DCA). tracks are extrapolated into primary vertex and then minimum distance between track and primary vertex is defined as DCA. DCA is divided into $\mathrm{DCA_{xy}}$(DCA in transverse direction) and $\mathrm{DCA_z}$(DCA in longitudinal direction). Absolute value of $\mathrm{DCA_{xy}}$ and $\mathrm{DCA_z}$ is constrained to be below 2.4cm and 3.2cm, respectively. Also two dimensional DCA cut $\mathrm{DCA_{xy}}^2/(2.4)^2 + \mathrm{DCA_z}^2(3.2)^2 < 1.0$ is applied. For HBT study, the selection of $0.15 < p_T < 1.5$ GeV/c is applied (HBT correlation in high p_T particles is too small). Tracks in $|\eta| < 0.8$ were used for both HBT and flow analysis.

3.2 Azimuthal anisotropy and Event plane

Azimuthal anisotropy of emitting particles and the method to extract event plane are described in this section.

3.2.1 Azimuthal anisotropy of emitting particles

The modulation of azimuthal angle of emitting particles are extracted with Fourier-expansion of the distribution in azimuthal angle ϕ.

$$
\begin{aligned}
r(\phi) &= \frac{x_0}{2\pi} + \frac{1}{\pi}\sum_{n=1}^{\infty}\left(x_n \cos(n\phi) + y_n \sin(n\phi)\right) && (3.4)\\
x_n &= \int_0^{2\pi} d\phi\, r(\phi)\cos(n\phi) && (3.5)\\
y_n &= \int_0^{2\pi} d\phi\, r(\phi)\sin(n\phi) && (3.6)
\end{aligned}
$$

where r and ϕ denote the azimuthal distribution and azimuthal angle of emitting particles. Harmonics of Fourier series is described as n. x_n and y_n are the nth oscillation components of $r(\phi)$ for x and y direction and calculated with integrated $r(\phi)$ over all particles. In experiments, number emitting particles are finite. So integral of x_n and y_n are expressed as sum:

$$
\begin{aligned}
x_n &= \sum_i r_i(\phi_i)\cos(n\phi_i) && (3.7)\\
y_n &= \sum_i r_i(\phi_i)\sin(n\phi_i) && (3.8)
\end{aligned}
$$

where i is the index of emitting particles and each cosine and sine of azimuthal angles ϕ_i weighted with azimuthal distribution r_i are summed over all particles. Here we define n-th order "Event plane"(Ψ_n^r) where each even plane angle is corresponding to the short axis of n-th order polygon(n = 2 : elliptic shape and n = 3 : triangular shape). Azimuthal distribution $r(\phi)$ is rewritten with respect to event planes:

$$
r(\phi) = \frac{x_0}{2\pi} + \frac{1}{\pi}\sum_{n=1}^{\infty}\left(x'_n \cos(n[\phi - \Psi_n^r]) + y'_n \sin(n[\phi - \Psi_n^r])\right) \tag{3.9}
$$

In symmetric nucleus-nucleus collisions, sine term of Fourier series should be zero. Therefore sine term is vanished :

$$
\begin{aligned}
r(\phi) &= \frac{x_0}{2\pi} + \frac{1}{\pi}\sum_{n=1}^{\infty}\left(x'_n \cos\left(n\left[\phi - \Psi_n^r\right]\right)\right) && (3.10)\\
&= \frac{x_0}{2\pi}\left(1 + 2\sum_{n=1}^{\infty}\left(\frac{x'_n}{x_0}\cos\left(n\left[\phi - \Psi_n^r\right]\right)\right)\right) && (3.11)\\
&= \frac{x_0}{2\pi}\left(1 + 2\sum_{n=1}^{\infty}\left(v_n \cos\left(n\left[\phi - \Psi_n^r\right]\right)\right)\right) && (3.12)
\end{aligned}
$$

where the strength of azimuthal anisotropy can be expressed with $v_n = \langle\cos\left(n\left[\phi - \Psi_n^r\right]\right)\rangle$. In this equation, $\langle\ \rangle$ denotes the average of running over all emitting particles. But "true" event plane (Ψ_n^r) cannot be directly measured in experiment. Measured event plane (Ψ_n) is defined based on the assumption of azimuthal anisotropy with respect to event plane.

$$
\begin{aligned}
v_n^{obs} &= \frac{\sqrt{x_n^2 + y_n^2}}{x_0} && (3.13)\\
\Psi_n &= \frac{1}{n}\tan^{-1}\left(\frac{y_n}{x_n}\right) \quad \left(0 \leq \Psi_n \leq \frac{2\pi}{n}\right) && (3.14)
\end{aligned}
$$

where v_n^{obs} is observed azimuthal anisotropy with respect to measured event plane (Ψ_n). Azimuthal distribution of emitting particles(Eq. 3.5) can be expressed with v_n^{obs} and Ψ_n :

$$
\begin{aligned}
r(\phi) &= \frac{x_0}{2\pi}\left(1 + 2\sum_{n=1}^{\infty}\frac{x_n}{x_0}\cos(n\phi) + \frac{x_n}{x_0}\sin(n\phi)\right) && (3.15)\\
&= \frac{x_0}{2\pi}\left(1 + 2\sum_{n=1}^{\infty}v_n^{obs}\cos(n\phi)\cos(n\Psi_n) + \frac{x_n}{x_0}\sin(n\phi)\sin(n\Psi_n)\right) && (3.16)\\
&= \frac{x_0}{2\pi}\left(1 + 2\sum_{n=1}^{\infty}v_n^{obs}\cos\left(n\left[\phi - \Psi_n\right]\right)\right) && (3.17)
\end{aligned}
$$

v_n^{obs} are rewritten with true event plane Ψ_n^r, measured event plane Ψ_n and azimuthal anisotropy v_n :

$$
\begin{aligned}
v_n^{obs} &= \langle \cos(n[\phi - \Psi_n]) \rangle & (3.18)\\
&= \langle \cos\{n[\phi - \Psi_n^r] - n[\Psi_n - \Psi_n^r]\} \rangle & (3.19)\\
&= \langle \cos(n[\phi - \Psi_n^r])\cos(n[\Psi_n - \Psi_n^r]) + \sin(n[\phi - \Psi_n^r])\sin(n[\Psi_n - \Psi_n^r]) \rangle & (3.20)\\
&= \langle \cos(n[\phi - \Psi_n^r])\cos(n[\Psi_n - \Psi_n^r]) & (3.21)\\
&= v_n \langle \cos(n[\Psi_n - \Psi_n^r]) & (3.22)\\
&= v_n \cdot \mathrm{Res}\{\Psi_n\} & (3.23)
\end{aligned}
$$

where the sine terms are vanished due to the symmetric distribution with respect to event planes. Here we define cosine of the difference between true and observed event plane as "resolution" of event plane ($\mathrm{Res}\{\Psi_n\}$).

3.2.2 Event plane determination

In experiment, event plane can be extracted with flow vector(Q vector) expressed by

$$
\begin{aligned}
M &= \sum_{i=0}^{N} w_i & (3.24)\\
Q_{x,n} &= \frac{\sum_{i=0}^{N} w_i \cos(n\phi_i)}{\sqrt{M}} & (3.25)\\
Q_{y,n} &= \frac{\sum_{i=0}^{N} w_i \sin(n\phi_i)}{\sqrt{M}} & (3.26)
\end{aligned}
$$

where w_i is weight. In this analysis, Event plane is determined via 3 detectors, FMD, VZERO and TPC.

For TPC event plane, weight w_i is p_{T} up to p_{T}=2.0GeV/c and w_i = 2.0 for the other particles (p_{T}>2.0). N denotes the number of charged particles reconstructed in TPC at one event and ϕ_i is the azimuthal angle of each particle.

For VZERO and FMD event plane, w_i denotes the multiplicity in each PMT and silicon strip channel and N is the total number of segment. Figure 3.4 shows the η-ϕ 2D distribution in FMD. The acceptance of FMD A + C side combined is -3.4<η<-1.7 and 1.7<η<5.1 and azimuthal angle divided into 20 silicon strip channel. Z axis denotes the multiplicity in each strip channel. azimuthal angle ϕ_i for FMD event plane is given by the center position of each strip channel. ϕ_i for VZERO event plane is represented as $\phi_i = \pi/4 \times (0.5 + n_{seg}\%8)$ where n_{seg} indicates the index of each segment(0-64 channel).

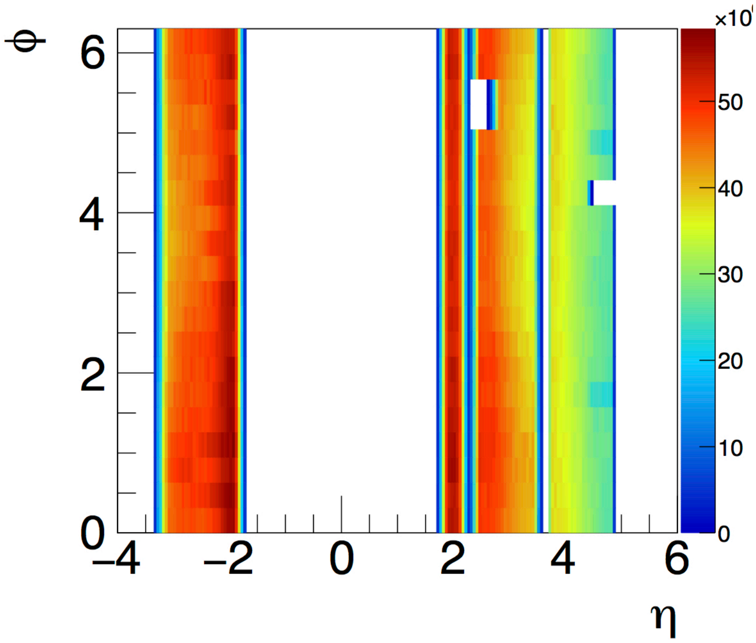

Figure 3.4: η v.s. ϕ 2D distribution measured via FMD. Z axis denotes multiplicity of each silicon strip channel.

Using nth order Q vector in Eq. 3.26, 3.26, event plane can be expressed by:

$$\Psi_n = \frac{1}{n} \tan^{-1} \left(\frac{Q_{x,n}}{Q_{y,n}} \right) \tag{3.27}$$

3.2.3 Event plane calibration

In nucleus-nucleus collisions, reaction planes and event planes are randomly determined because the collision geometry cannot be controlled by accelerator technique. Event plane distribution should be flat. But measured event plane distribution is in fact not flat. it's because event plane determination detectors have dead and non-uniform gain channels. Also non-central beam position can cause the non flat event planes. These effects are corrected with 2 step event plane calibrations, re-centering and flattening. Each calibration parameters are extracted in each run based on the assumption of stability during one run.

Re-centering calibration

Mean of $Q_{x,n}$, $Q_{y,n}$ vector distribution should be 0 and width of q vector in each x, y direction should have same value if event plane is flat. Re-centering calibration is the correction of mean and R.M.S. value of $Q_{x,n}$, $Q_{y,n}$ given as

$$Q^{corr}_{x,n} = \frac{Q_{x,n} - \langle Q_{x,n} \rangle}{\sigma_x} \tag{3.28}$$

$$Q^{corr}_{y,n} = \frac{Q_{y,n} - \langle Q_{y,n} \rangle}{\sigma_y} \tag{3.29}$$

$$\Psi^{rec}_{n} = \frac{1}{n}\tan^{-1}\left(\frac{Q^{corr}_{y,n}}{Q^{corr}_{x,n}}\right) \tag{3.30}$$

where $\langle Q_{x,n} \rangle$, $\langle Q_{y,n} \rangle$ denote the average of $Q_{x,n}$, $Q_{y,n}$ and σ_x, σ_y represent the width of $Q_{x,n}$, $Q_{y,n}$ in a certain run. Figure 3.5 shows 2nd, 3rd and 4th order harmonic Q_x vector before/after re-centering. Red, green solid line are raw $Q_{x,n}$, $Q_{y,n}$ distribution and blue solid, black dashed line denote re-centering $Q_{x,n}$, $Q_{y,n}$ distribution. After re-centering calibration, The mean value of Q vector distribution is zero and width is perfectly same.

In Figure 3.6, Blue and black line show the raw event plane and event plane after re-centering calibration. Event planes are largely flattened with this correction because the non-uniform detector channel and non-central beam position can be corrected with this calibration. Residual non-uniform components are corrected with flattening correction.

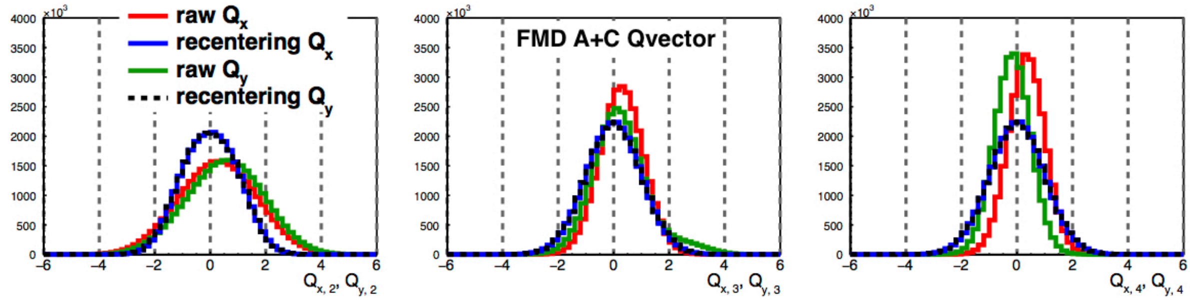

Figure 3.5: 2nd, 3rd and 4th harmonic q vector x distribution which is determined via FMD A side + C side combined in centrality 0-50%. Red line shows uncorrected distribution. Blue line indicates event plane distribution with recentering calibration.

Flattening calibration

Residual non-uniform components especially higher harmonics oscillations are corrected with Flattening calibration defined by

$$n\Psi_n^{flat} = n\Psi_n^{rec} + n\Delta\Psi_n \tag{3.31}$$

$$n\Delta\Psi_n = \sum_{k=1}^{N} A_k \cos\left(kn\Psi_n^{rec}\right) + B_k \sin\left(kn\Psi_n^{rec}\right) \tag{3.32}$$

where A_k, B_k represent the Fourier coefficients of event plane distribution. In flattening calibration, average cosine and sine of $n\Psi_n^{flat}$ are corrected to be zero. This calibration forces event planes to be flat distribution with Fourier expansion. A_k and B_k can be determined as

$$A_k = -\frac{2}{k}\langle\sin\left(nk\Psi_n^{rec}\right)\rangle \tag{3.33}$$

$$B_k = \frac{2}{k}\langle\cos\left(nk\Psi_n^{rec}\right)\rangle \tag{3.34}$$

In this analysis, flattening calibration was calculated up to 8th order Fourier coefficients. Eventually, flat event plane distribution can be obtained in orange line shown in Figure 3.6.

Event plane resolution

Analytically, nth harmonic event plane resolution can be expressed as the following equation :

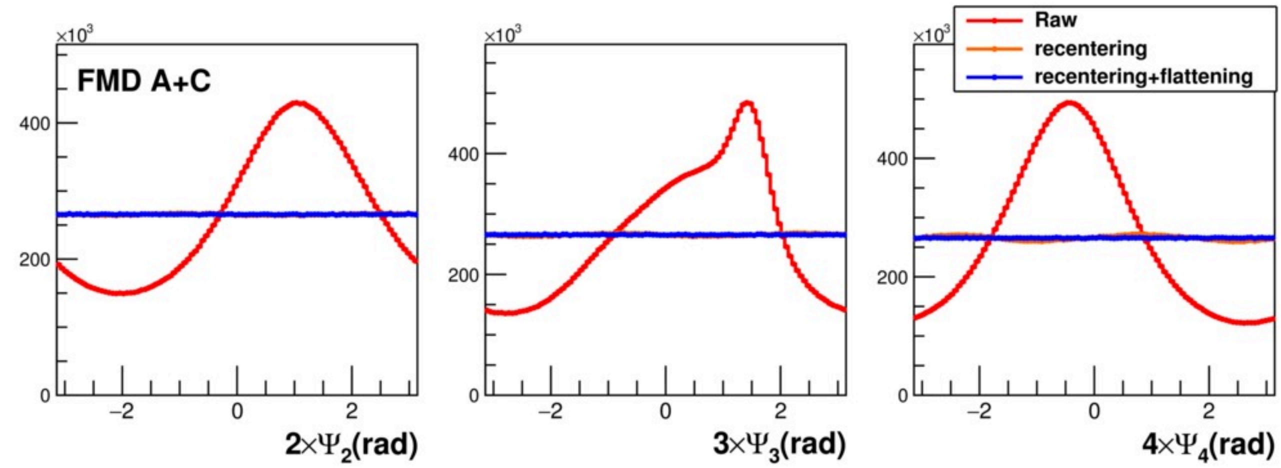

Figure 3.6: 2nd, 3rd and 4th harmonic event plane distribution which is determined via FMD A side + C side combined in centrality 0-50%. Red line shows uncorrected distribution. Orange line indicates event plane distribution with recentering calibration. Blue line represents recentering+flattening calibrated event plane distribution.

$$\langle\cos\left[km\left(\Psi_m-\Psi_r\right)\right]\rangle=\frac{\sqrt{\pi}}{2\sqrt{2}}\chi_m\exp\left(-\frac{\chi_m^2}{4}\right)\times\left[I_{(k-1)/2}\left(\frac{\chi_m^2}{4}\right)+I_{(k+1)/2}\left(\frac{\chi_m^2}{4}\right)\right] \tag{3.35}$$

where $\langle\cos\left[km\left(\Psi_m-\Psi_r\right)\right]\rangle$ represents event plane resolution and $\chi_m \equiv v_m\sqrt{2N}$. v_m is the Fourier coefficient of azimuthal anisotropy. N is the number of particles used for event plane calculation I_ν is the modified Bessel function of ν [52]. This equation represents event plane resolution is expressed with multiplicity and strength of azimuthal anisotropy. The more multiplicity is used to determine event plane and strength of anisotropic flow itself is larger, the better event plane resolution can be obtained.

The event plane correlation between detector A and B can be expressed as:

$$\begin{aligned}\langle\cos\left(n\left[\Psi_{n,A}-\Psi_{n,B}\right]\right)\rangle &= \langle\cos\left(n\left[\Psi_{n,A}-\Psi_{n,r}\right]-n\left[\Psi_{n,B}-\Psi_{n,r}\right]\right)\rangle && (3.36)\\ &= \langle\cos\left(n\left[\Psi_{n,A}-\Psi_{n,r}\right]\right)\rangle\langle\cos\left(n\left[\Psi_{n,B}-\Psi_{n,r}\right]\right)\rangle && (3.37)\\ &= \mathrm{Res}\left\{\Psi_{n,A}\right\}\mathrm{Res}\left\{\Psi_{n,B}\right\} && (3.38)\end{aligned}$$

When two detectors A and B cover symmetric rapidity acceptance and have same multiplicity, event plane resolution $\mathrm{Res}\left\{\Psi_{n,A}\right\}$ is equal to $\mathrm{Res}\left\{\Psi_{n,A}\right\}$ if we assume same v_n is measured at detector A and B. Because event plane resolution is determined with v_n value and multiplicity N. Therefore event plane resolution can be obtained by two sub-event method given as :

$$\mathrm{Res}\left\{\Psi_{n,A}\right\} = \mathrm{Res}\left\{\Psi_{n,B}\right\} = \sqrt{\left\langle \cos\left(n\left[\Psi_{n,A} - \Psi_{n,B}\right]\right)\right\rangle} \tag{3.39}$$

This method is used to calculate TPC event plane resolution in this analysis.

However ALICE forward detectors basically have "asymmetric" rapidity coverage. For asymmetric rapidity detectors, event plane resolution is usually calculated with "3-sub event method". Here we think 3 different rapidity detectors a, b and c. Event plane correlations can be expressed by :

$$\left\langle \cos\left(n\left[\Psi_{n,a} - \Psi_{n,b}\right]\right)\right\rangle = \mathrm{Res}\left\{\Psi_{n,a}\right\}\mathrm{Res}\left\{\Psi_{n,b}\right\} \tag{3.40}$$

$$\left\langle \cos\left(n\left[\Psi_{n,b} - \Psi_{n,c}\right]\right)\right\rangle = \mathrm{Res}\left\{\Psi_{n,b}\right\}\mathrm{Res}\left\{\Psi_{n,c}\right\} \tag{3.41}$$

$$\left\langle \cos\left(n\left[\Psi_{n,c} - \Psi_{n,a}\right]\right)\right\rangle = \mathrm{Res}\left\{\Psi_{n,c}\right\}\mathrm{Res}\left\{\Psi_{n,a}\right\} \tag{3.42}$$

Using Eq. 3.41, 3.42 and 3.42, event plane can be given as :

$$\mathrm{Res}\left\{\Psi_{n,a}\right\} = \sqrt{\frac{\left\langle \cos\left(n\left[\Psi_{n,a} - \Psi_{n,b}\right]\right)\right\rangle \left\langle \cos\left(n\left[\Psi_{n,c} - \Psi_{n,a}\right]\right)\right\rangle}{\left\langle \cos\left(n\left[\Psi_{n,b} - \Psi_{n,c}\right]\right)\right\rangle}} \tag{3.43}$$

In the same way, event plane resolution of b and c detectors can be obtained with Eq. 3.41, 3.42 and 3.42.

In this analysis, FMD A side, FMD C side, FMD A+C combined, V0 A side, V0 C side and V0 A+C combined event plane is calculated with 3-sub event method.

Figure 3.7 is 2nd, 3rd and 4th harmonic event plane resolution via VZERO, FMD and TPC. Blue and green markers represent event plane via VZERO and FMD. Black markers denote TPC event plane resolution. TPC rapidity is divided into 4 regions, -1.0 < η < -0.5, -0.5 < η < 0.0, 0.0 < η < 0.5 and 0.5 < η < 1.0. FMD(V0) A+C combined resolution can be extracted with TPC event plane resolution and event plane correlation between TPC and FMD A+C combined by :

$$\mathrm{Res}\left\{\Psi_{n,FMD\ A+C}\right\} = \frac{\left\langle \cos\left(n\left[\Psi_{n,TPC} - \Psi_{n,FMD\ A+C}\right]\right)\right\rangle}{\mathrm{Res}\left\{\Psi_{n,TPC}\right\}} \tag{3.44}$$

In this analysis, main event plane determination detector is FMD. The best resolution value is 0.87 at mid central collisions for 2nd harmonic event plane. Initial collision geometry and multiplicity distributions determine this structure. Third and fourth harmonic event plane has different behavior compared to 2nd order. The best resolution value for 3rd harmonic event plane is 0.5 at central collisions and resolution value becomes smaller from central to peripheral. Compared to VZERO event plane resolution, FMD performs better event plane resolution especially in higher harmonic orders owing to larger rapidity acceptance. This excellent resolution helps us to understand the detail structure in higher order harmonic anisotropy.

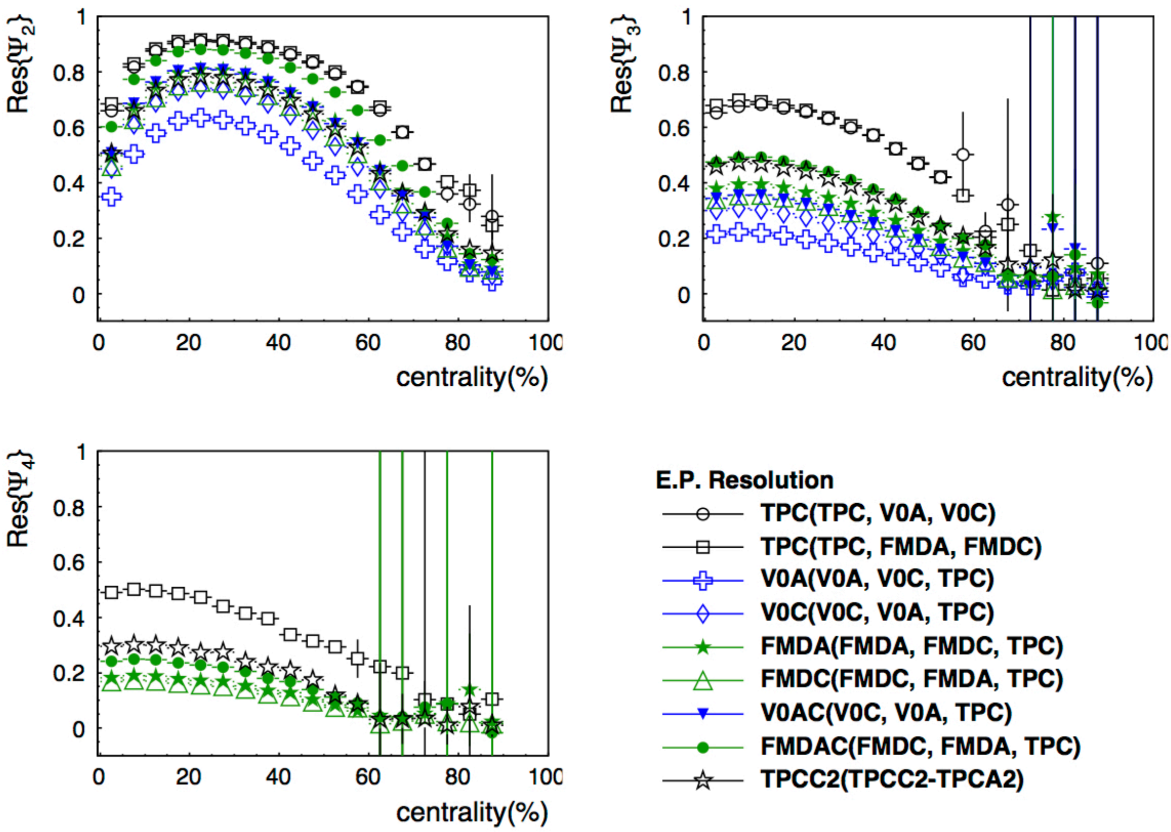

Figure 3.7: 2nd, 3rd and 4th harmonic event plane resolution which is determined via TPC($|\eta|$<1.0), V0 A side, V0 C side, V0 A+C combined, FMD A side, FMD C side, FMD A+C combined , TPC($0.5 < \eta < 1.0$) and TPC($-1.0 < \eta < -0.5$) as a function of centrality. Blue line indicates event plane distribution with recentering calibration. Since number of segments in V0 is not sufficient, 4 th harmonic event plane resolution via V0 is not shown.

3.2.4 Measurements of azimuthal anisotropy

Charged hadron v_n can be extracted with v_n^{obs} and event plane resolution $\mathrm{Res}\{\Psi_n\}$, using Eq. 3.23 :

$$v_n^{true} = \frac{v_n^{obs}}{\mathrm{Res}\{\Psi_n\}} \tag{3.45}$$

Figure 3.8 shows higher harmonic azimuthal anisotropy v_n as a function of collision centrality. Event planes are determined via 4 different detectors, V0 A+C combined, FMD A+C combined, TPC C2 and TPC A2. Here we define TPC C2 and TPC A2 as TPC(-1.0 < η < -0.5) and TPC(0.5 < η < 1.0), respectively. p_{T} is integrated from 0.2 to 2.0 GeV/c.

Rapidity gap between event plane and v_n measurement has to be at least 0.9, Since, for smaller rapidity gap, non flow effect such as resonance decay particles and jet enhance or suppress the measured v_n value.

Higher order anisotropy v_n via event plane method is compared with previous ALICE results for the purpose of consistency check[13]. Charged hadron v_n measured via two particle correlation method is also depicted as black marker in Figure 3.8. 2nd, 3rd and 4th order anisotropy via two different methods are fully consistent within the systematic uncertainty.

p_{T} dependence of higher harmonic anisotropy v_n for the 6 centrality classes is presented in Figure 3.9. Event plane is determined with 3 different detectors and the difference between them is so small. Previous ALICE results measured via event plane method are also shown in Figure 3.9 to check the consistency. Previous ALICE results and results in this analysis are consistent within the systematic uncertainty for all centralities.

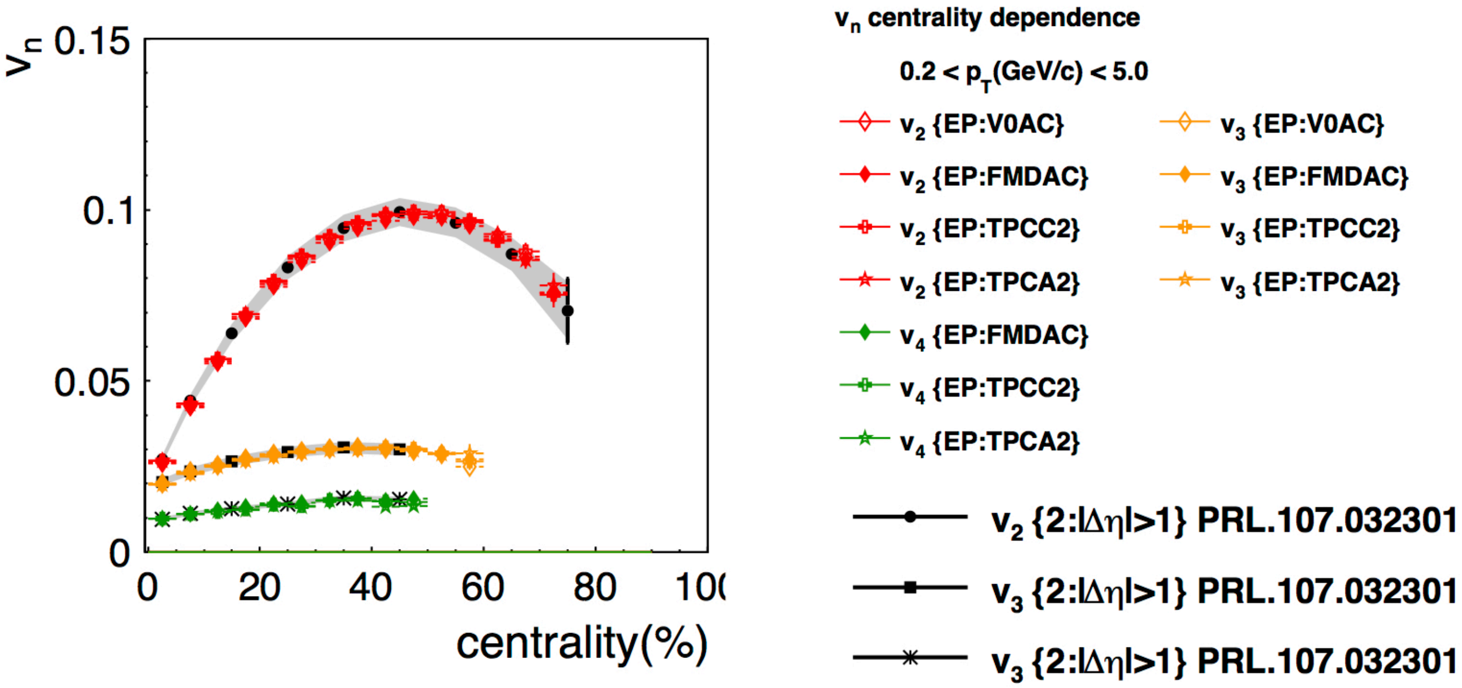

Figure 3.8: 2nd, 3rd and 4th harmonic anisotropy v_n as a function of centrality. v_n is measured via Event plane method and compared with previous ALICE results(two particle correlation). Event plane is determined with 4 different detectors.

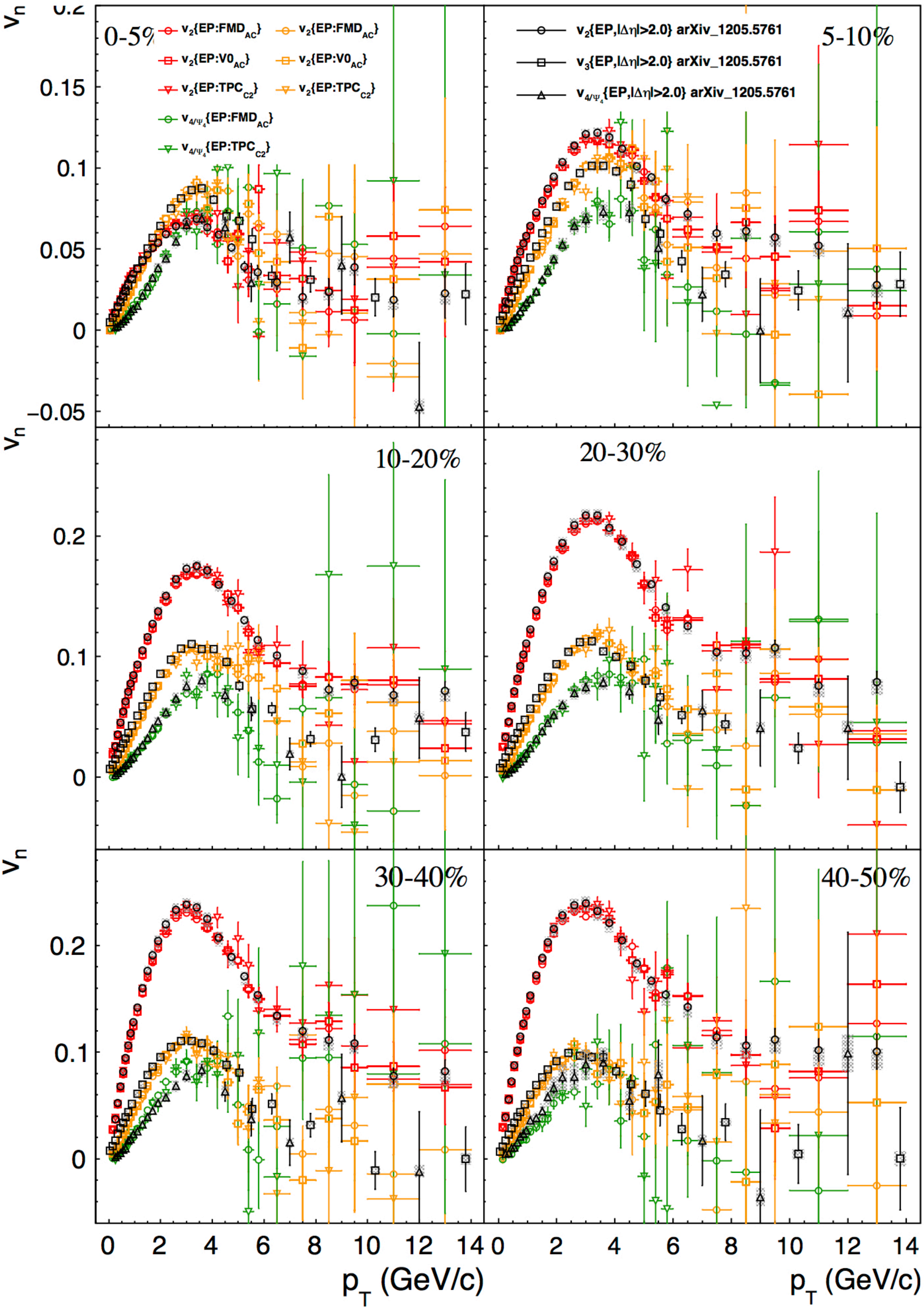

Figure 3.9: 2nd, 3rd and 4th harmonic anisotropy v_n as a function of p_T for the 6 centrality classes, measured via event plane method. Black markers are previous ALICE results via event plane method.

3.3 Event Shape Engineering

Event Shape Engineering (ESE) is method to select the event-by-event flow fluctuation by the magnitude of flow vector [15]. In this section, analysis method of ESE technique is described.

3.3.1 Event Shape Engineering

nth order flow vector is decomposed into x and y axis and represented as $Q_{x,n}$ and $Q_{y,n}$. These vectors are measured "event by event" and the length of them is sensitive to "event by event flow amplitude".

Here we describe the definition of Q vector again. Using $Q_{x,n}$ and $Q_{y,n}$ flow vectors, the magnitude of flow vector is given as :

$$M = \sum_{i=0} w_i \tag{3.46}$$

$$Q_{x,n} = \frac{\sum_{i=0} w_i \cos(n\phi_i)}{\sqrt{M}} \tag{3.47}$$

$$Q_{y,n} = \frac{\sum_{i=0} w_i \sin(n\phi_i)}{\sqrt{M}} \tag{3.48}$$

$$q_n = \sqrt{Q_{x,n}^2 + Q_{y,n}^2} \tag{3.49}$$

q_n indicates the length of nth harmonic flow vector. Figure 3.10 shows the length of 2nd and 3rd harmonic flow vector distributions in Pb-Pb 2.76 TeV collisions for 0-10% centrality. flow vector is determined with FMD A+C combined.

Left and right figure is 2nd and 3rd harmonic flow vector distribution, respectively. Mean value of q_2 is larger than that of q_3 and width of q_3 is slightly larger than that of q_2. Flow vector distribution is determined by 3 components.

- Event by event flow fluctuations
- Statistical fluctuations due to finite particle multiplicity used to determine flow vector
- Event plane resolution

The signal of event by event flow fluctuations are smeared with other two components. Statistical fluctuations and event plane resolution can broaden the q vector distribution.

One can obtain the event by event flow amplitude by dividing q_N distribution into flow vector event class. In order to determine the flow vector event class, cumulated q_N distribution as a function of centrality is measured in Figure 3.11. Cumulated q_n vector distribution is projected to Y axis for each 1% centrality. Spline fit is performed to each slice of cumulated q_n vector distribution. In this method, for each q_n vector value can be evaluated from the corresponding percentile.

For each 20 % of q_2 and q_3 classes are determined with FMD A+C combined q-vector in this thesis. q_n class 0 % means smallest v_n events and 100% denotes largest v_n events. Figure 3.13 shows q_2(left) and q_3(right) distribution for each q-vector classes in centrality 10-20%.

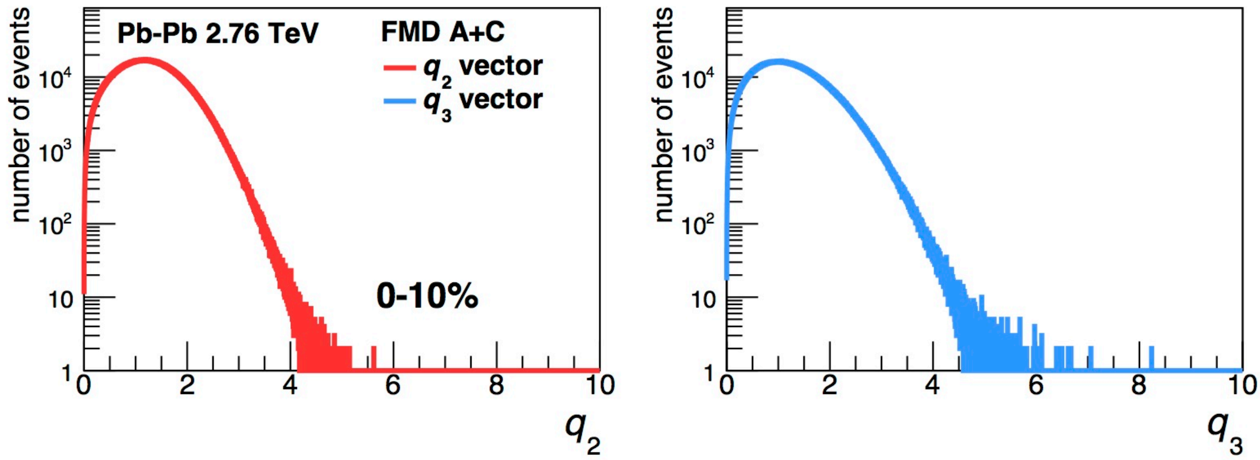

Figure 3.10: The magnitude of q_2(left) and q_3(right) flow vector distribution in centrality 0-10%. q_n is determined with FMD A+C combined.

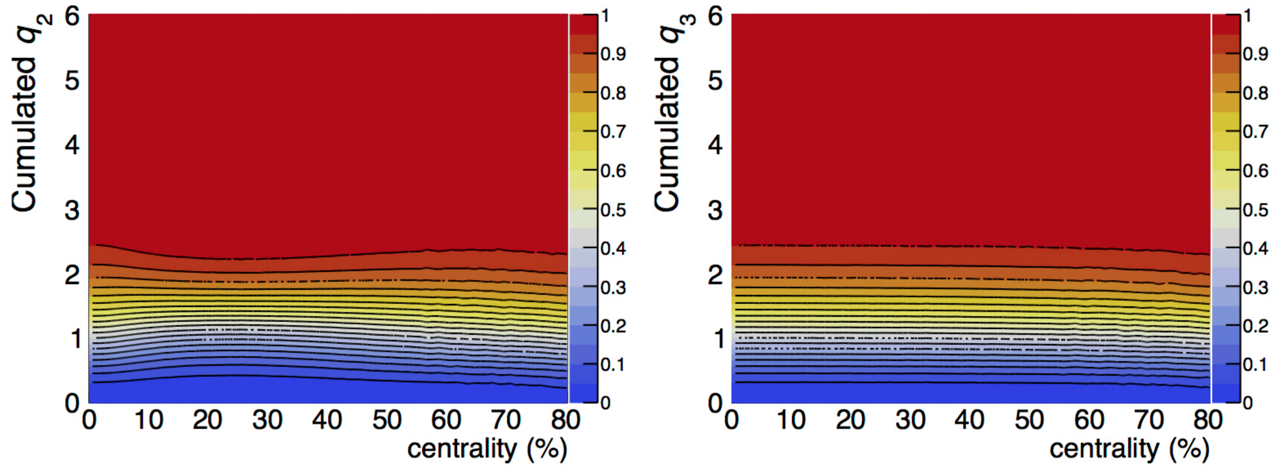

Figure 3.11: Cumulated q_2(left) and q_3(right) distribution as a function of centrality. flow vector q_n is determined via FMD A+C combined. Contour(5%) maps are plotted simultaneously.

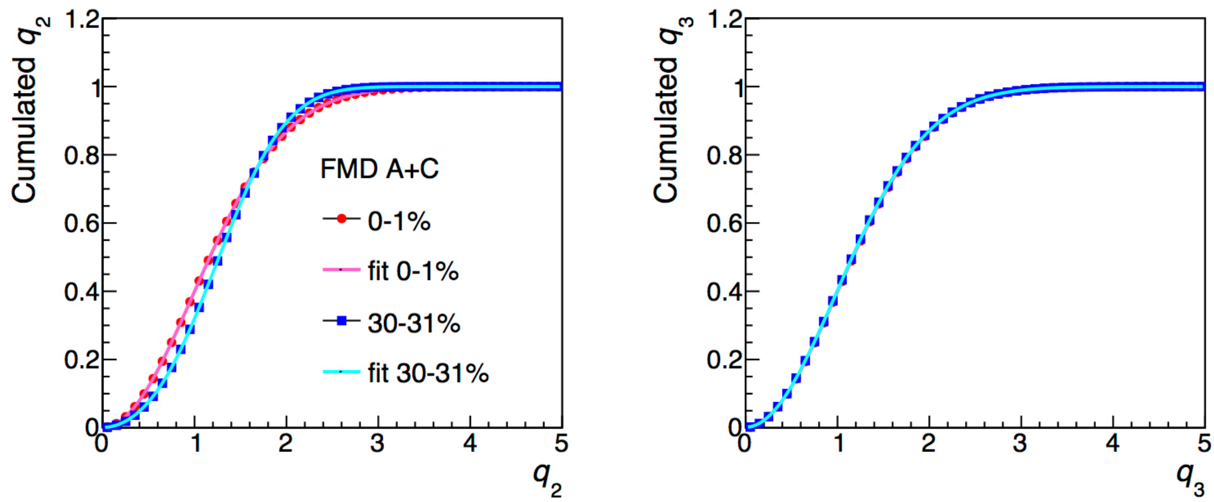

Figure 3.12: Cumulated q_2(left) and q_3 as a function of q_2(left) and q_3 distribution in centrality 0-1%(red) and 30-31%(blue). Spline fitting is performed to each slice of q_n distribution. Cumulated q-vector distribution is rebeined (merged 100 bins in one) for visibility.

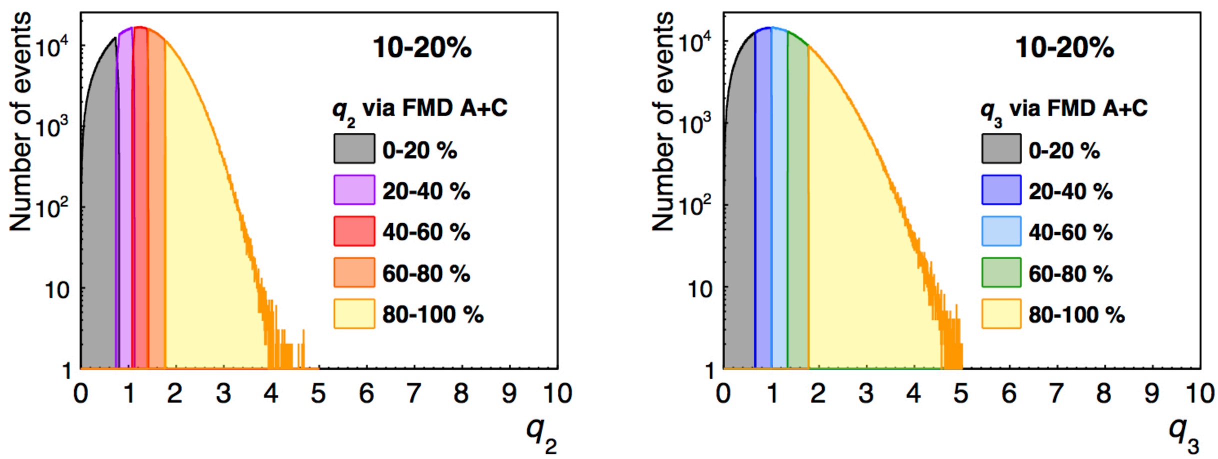

Figure 3.13: q_2(left) and q_3 distribution for each 20% q_2 and q_3 in centrality 10-20%. Both q_2 and q_3 are determined with FMD A+C combined.

3.3.2 Event plane resolution with ESE

nth order event plane resolution is determined with amplitude of v_n and multiplicity used to determine the event plane. ESE is the selection for event by event flow amplitude. Therefore amplitude of v_n changes in a same multiplicity(centrality) events and one can assume that larger(smaller) q_n selection makes event plane resolution better(worse).

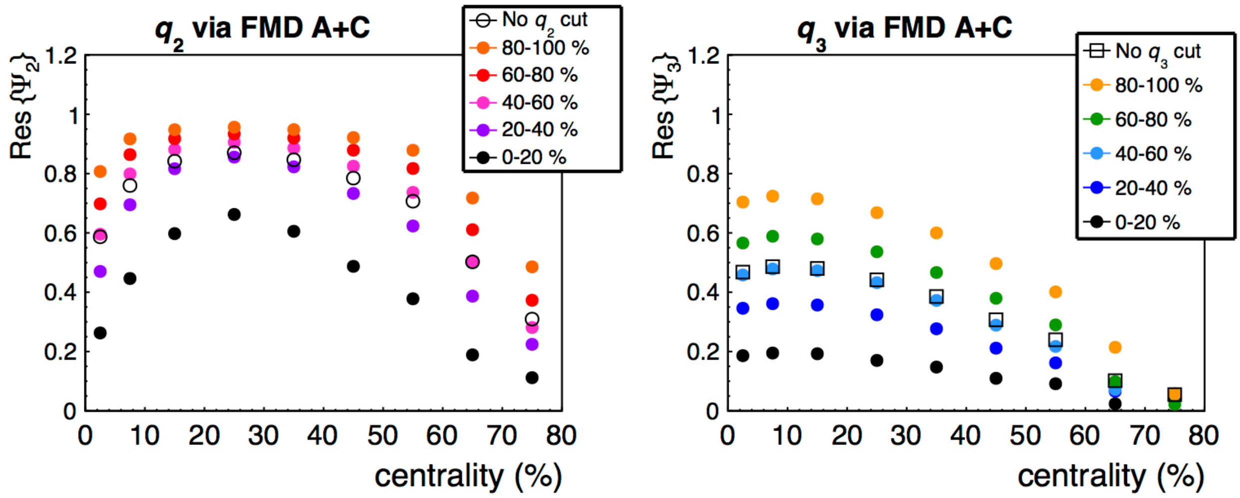

Figure 3.14: 2nd(left) and 3rd(right) harmonic event plane resolution as a function of centrality for each 20% q_2 and q_3 event classes. q_2 and q_3 selection and event plane are determined with FMD A+C combined. Inclusive(without q_2 and q_3 cut) event plane resolutions are also depicted as open marker. Event plane resolution is extracted with 3-sub event method and the combination is FMD A+C, TPC(-1.0<η<-0.5) and TPC(0.5<η<1.0).

Figure 3.14 shows the 2nd(left) and 3rd(right) order event plane resolution as a function of centrality for each 20% q_2 and q_3 event classes, respectively. q_2, q_3 selection and event planes(Ψ_2 and Ψ_3) are determined with FMD A+C combined. Inclusive(without q_2 and q_3 cuts) event plane resolutions are also shown as open marker. Event plane resolution is extracted with 3-sub event method that the combination is FMD A+C, TPC(-1.0<η<-0.5) and TPC(0.5<η<1.0). For both 2nd and 3rd harmonic event plane resolutions are explicitly enhanced(suppressed) with larger(smaller) q_n selection , compared to inclusive events. Ψ_2 resolution is about 0.25 to nearly 1.0 for centrality 0-50%, while Ψ_3 resolution is about 0.1 to nearly 0.73 for centrality 0-50%.

3.4 Particle identification(PID)

In ALICE, hadrons and leptons are identified with the combination of several detectors depending on the particle transverse momentum. Figure 3.15 shows π/K(left) and K/p(right) separation power with the ITS, TPC, TOF and HMPID. The separation power can be evaluated by the Gaussian width of σ for pions and kaons, respectively.

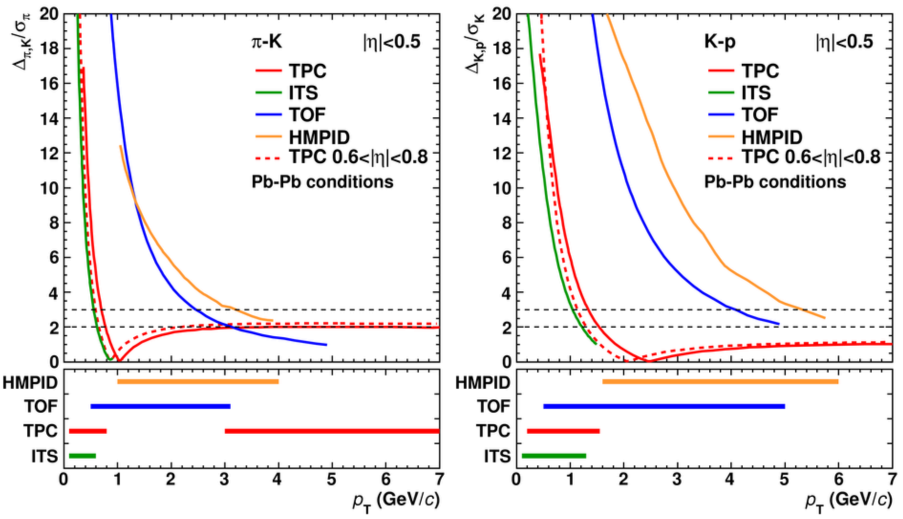

Figure 3.15: π/K(left) and K/p(right) separation power in the ITS, TPC, TOF and HMPID as a function of transverse momentum at mid rapidity. Y axis denotes the distance between the peaks divided by the resolution for the pion and the kaon, respectively. The left (right) panel shows the separation of pions and kaons (kaons and protons), expressed as the distance between the peaks divided by the resolution for the pion and the kaon, respectively. For the TPC, an additional dashed line is depicted in a edge of rapidity coverage. The lower panels show the range over which the different ALICE detector systems have a separation power of more than 2σ [55]. [54]

In this analysis, low momentum charged pions ($0.15 < p_{\mathrm{T}}$ (GeV/c) < 1.5) are used for HBT analysis and $\pi^{\pm}$, $K^{\pm}$ and $p+\bar{p}$ are analyzed for azimuthal anisotropy with ESE measurements. One can find that the identification of $\pi^{\pm}$, $K^{\pm}$ and $p+\bar{p}$ are covered with TPC and TOF in ALICE (Figure **??**). Thus TPC and TOF combined PID is applied to measure the particle species.

3.4.1 Energy loss(dE/dx) in TPC

As we introduced in section 2.2.2, TPC is the main tracking detector in ALICE. Particle identification information can be also extracted besides tracking. PID is performed by measuring specific energy loss(dE/dx) in gas, charge and momentum simultaneously. The energy loss of charged particle in material are described with Bethe-Bloch formula which is given as :

$$-\frac{dE}{dx} \approx \frac{z^2}{\beta^2} \ln \gamma \tag{3.50}$$

where z denotes the charge, β is the ratio of particle velocity to the speed of light and γ is the Lorentz factor. If the particle momentum is measured in TPC, difference of particle mass and charge makes the separation of dE/dx depending of its particle species.

Energy loss (dE/dx) distribution as a function of charge $z \times$ particle momentum are presented in Figure 3.16. In low momentum region, dE/dx distribution is definitely separated for different particle species. But, in p_{T} higher than 0.5 GeV/c, energy loss of pions and kaons is almost converged. Therefore, in this momentum range, TOF is the main PID detector.

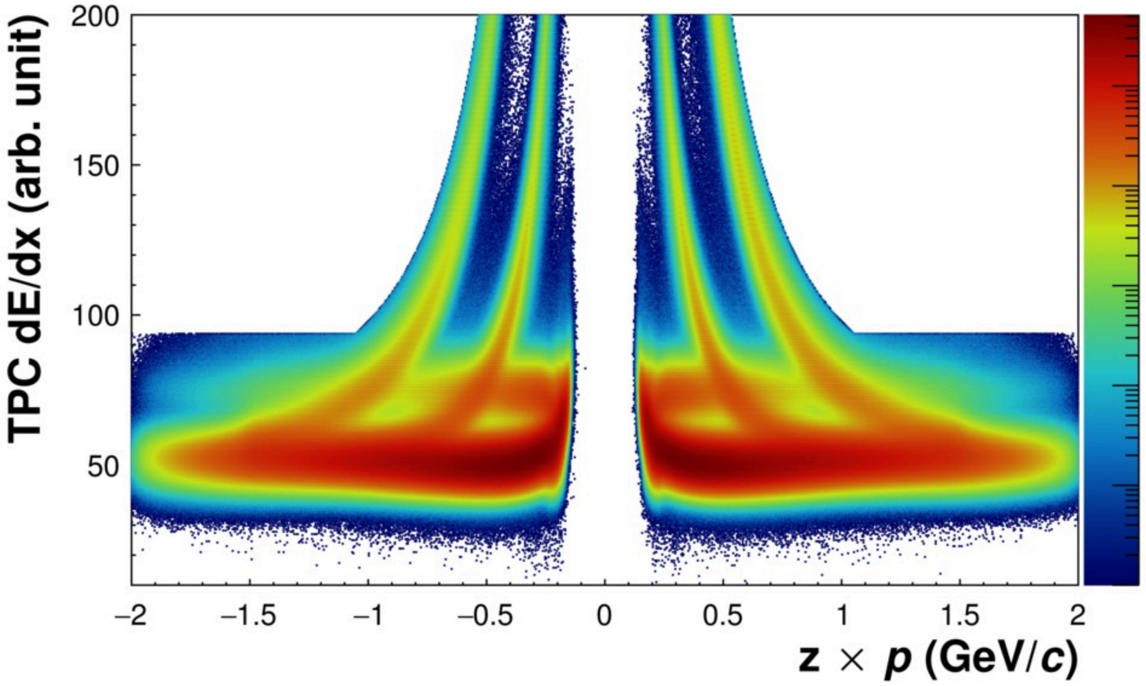

Figure 3.16: Energy loss (dE/dx) in TPC as a function of charge $z \times$ particle momentum in Pb-Pb 2.76 TeV collisions. pions, electrons, kaons and protons are identified with the difference of energy loss especially in low momentum region.

3.4.2 Particle identification in TOF

Time of Flight is a good probe to identify the particle species and measured with the difference between start time (which is mainly determined with TZERO detector in ALICE) and stop time with TOF. Particle velocity is given by :

$$\beta = \frac{L}{ct} \tag{3.51}$$

$$= \frac{p}{\sqrt{p^2+m^2}} \tag{3.52}$$

where L is the distance between start and stop counter, which can be extrapolated of reconstructed track in TPC, t represents time of flight and c denotes the speed of light in vacuum.

In addition β can be expressed with particle momentum p and mass m. In a given momentum p, velocity β is driven only from particle mass. Figure 3.17 is the distribution of TOF β as a function of a track momentum. each species are explicitly separated due to the difference of their mass. Combinatorial background comes from the miss-matched track of TPC-TOF in high multiplicity heavy ion collisions.

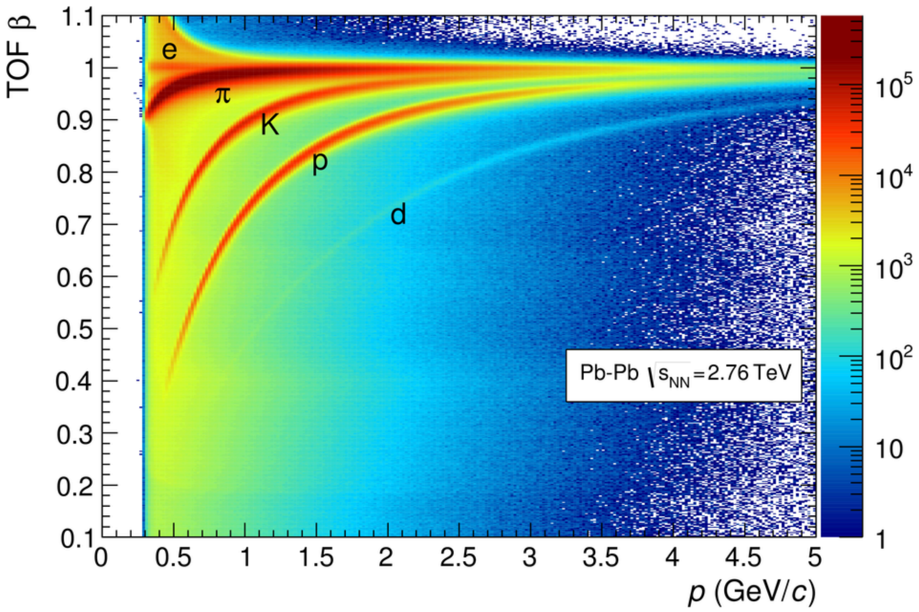

Figure 3.17: Distribution of β measured by TOF detector as a function of track momentum in Pb-Pb 2.76 TeV collisions

3.4.3 TPC-TOF combined PID

The separation power of π/K and K/p can be improved with the complementrarity of the different detector system. In this analysis 0.15-2.0 GeV/c pions, kaons and protons are used. Since TOF efficiency is not sufficient at low momentum(p_T < 0.5 MeV$/c$), TPC is the main PID detector for this p_{T} region. At intermediate p_{T} range, TOF performs more than 3 σ separation power up to 3.0GeV/c for π/K and 5GeV/c for K/p, respectively.

For HBT analysis, charged pion identification was performed with Nσ which is the Gaussian description of the response function of the detector given as :

$$n\sigma(\pi,\mathrm{TPC}) = \frac{dE/dx_{measured} - dE/dx^{\pi}_{expected}}{\sigma^{\pi}_{TPC}} \tag{3.53}$$

$$n\sigma(\pi,\mathrm{TOF}) = \frac{(time_{hit} - \mathrm{startTime}) - time^{\pi}_{expected}}{\sigma_{PID(TOF)}} \tag{3.54}$$

where $dE/dx_{measured}$ is measured dE/dx in TPC and energy loss expected as pion is represented as $dE/dx^{\pi}_{expected}$. Expected signal is calculated with Bethe-Bloch formula taking into account the η dependence and the multiplicity dependence. Distance to expected signal is divided by TPC dE/dx resolution(σ^{π}).

$time^{hit}$ denotes the hit time measured in TOF. $startTime$ is the collision time which is measured by means of the following (listed in order of priority) :

1. **TZERO detector (sum of the time signal from A and C side)**
2. TOF detector itself with a combinatorial algorithm based on χ^2 minimization
3. Average TOF start time for the run

TOF Expected time is measured from measured track length to reach the TOF and momentum in the pion mass hypothesis. The TOF PID resolution $\sigma_{PID(TOF)}$ is expressed with quadratic sum of intrinsic time resolution of TOF detector, time resolution of start counter and tracking capability of ALICE.

Figure 3.18 shows $n\sigma$ TPC(left) and TOF(right) for charged pions. Charged pions are identified with the following selection in Table 3.1.

Table 3.1: Pion selection for HBT analysis with TPC and TOF $n\sigma$

Momentum (GeV/c)	TOF enable	PID estimator
0.15-0.65	◯	$\lvert n\sigma(\pi,\mathrm{TPC})\rvert < 3.0 \cap \lvert n\sigma(\pi,\mathrm{TPC})\rvert < 3.0$
0.15-0.5	×	$\lvert n\sigma(\pi,\mathrm{TPC})\rvert < 3.0$
0.5-0.65	×	$\lvert n\sigma(\pi,\mathrm{TPC})\rvert < 2.0$
0.65-1.5	◯	$\lvert n\sigma(\pi,\mathrm{TPC})\rvert < 5.0 \cap \lvert n\sigma(\pi,\mathrm{TPC})\rvert < 3.0$

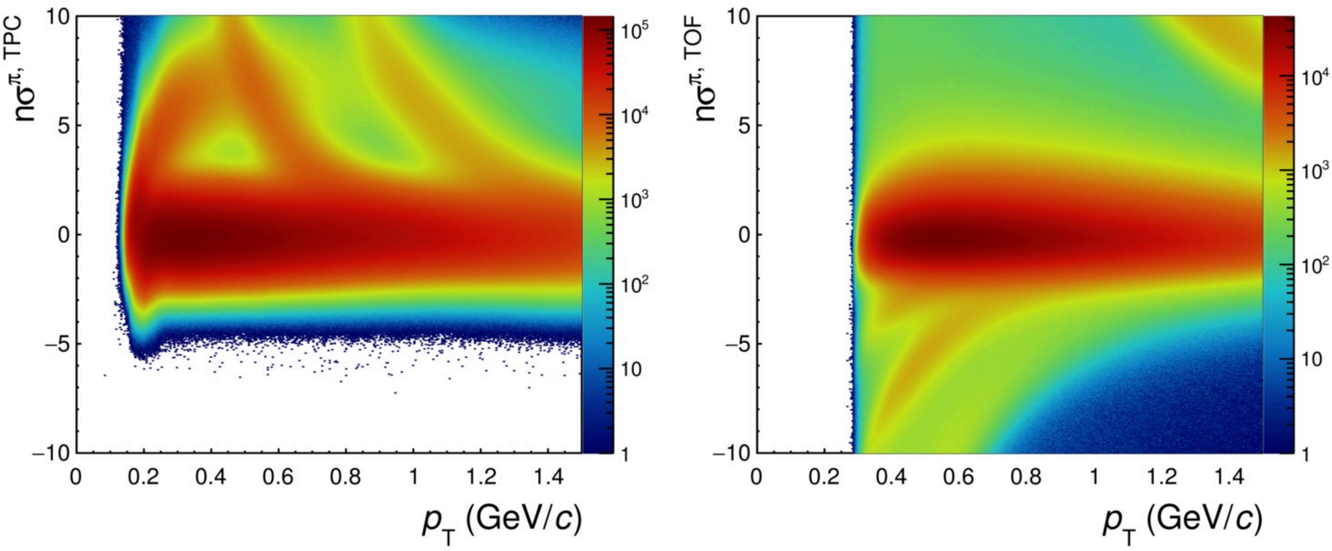

Figure 3.18: TPC dE/dx Nσ of $\pi^{\pm}$ as a function of particle transverse momentum shown in left and Right figure represents TOF Nσ for pion as a function of particle momentum transverse.

For azimuthal anisotropy with ESE study, charged pion, kaon and proton identified with is Bayesian approach[56]. In this analysis, the probability of π, K and p is estimated via TPC and TOF combined and required at least 90% for each species. Simultaneously TPC and TOF nσ are required within 1.0. PID purity of pions, kaons and protons is better than 95% where p_{T} up to 2.0GeV/c.

3.5 Pair selection

3.5.1 Two Track Resolution

HBT correlation is of the interference effect between two identical particles in low momentum range. Therefore in order to measure the HBT interferometry, precise selection of pairs in low relative momentum is necessary. However it's not easy to identify those pairs with tracking detector due to the high multiplicity in heavy ion collisions. Pairs where two tracks have similar momenta and small angular distance may have the following reconstruction effects due to the finite two track resolution of tracking detector.

- Track merging
- Track splitting

track merging

Track merging is when two track is falsely reconstructed as one track or one of them are not reconstructed shown in Figure 3.19(left). Horizontal lines denotes the TPC pad rows in read-out chamber. Suppose, for instance, two tracks are traveling spatially close in the tracking detectors. Due to the finite spatial resolution, two tracks can be falsely reconstructed as one track. This result in a depletion of close pairs and can cause the suppression of correlation function.

track splitting

Track splitting is when one track is falsely reconstructed as two tracks that are spatially close. Figure 3.19 (right) shows the cartoon illustrating of track splitting. Some of TPC clusters are shared between spatially close two tracks. These clusters, in particular, can cause track splitting effect, since it assumes as if two tracks makes shared clusters by tracking algorithm. This result in an enhancement of tracks with close pairs and correlation function. These tracks are also known as "ghost track".

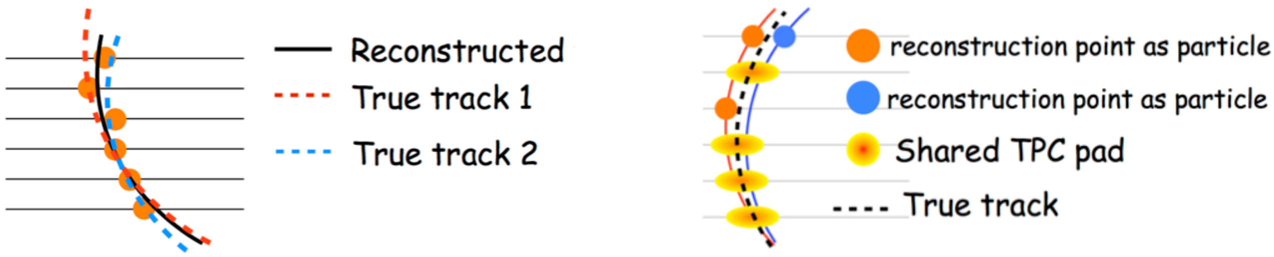

Figure 3.19: Cartoon illustrating of track merging and splitting effect. Horizontal lines denotes the TPC read-out pad rows. Two tracks shown in red and blue dashed lines are spatially close. Measured TPC clusters of these two tracks are shown as orange markers. Elliptic markers in yellow gradation denote the shared TPC clusters. Due to finite two track resolution, two tracks are falsely reconstructed as one track depicted as black solid line(left), while tracks composed of shared TPC clusters(black dashed line) can be falsely reconstructed as two tracks shown in orange and blue solid line(right).

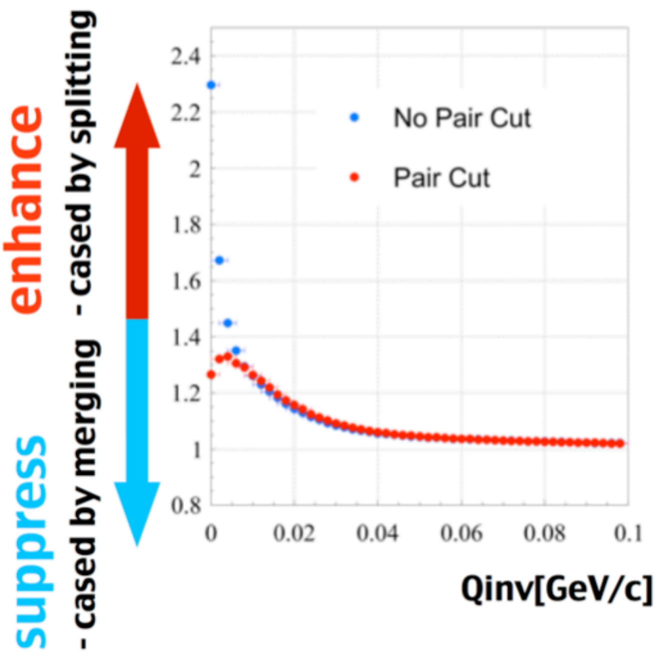

Figure 3.20: Track splitting & Track merging effect in correlation function C_2 as a function of one dimensional relative momentum(Q_{inv}). Blue marker indicates correlation function without any pair cut. Red marker denotes correlation function after pair cut.

Track merging and splitting on correlation function

Figure 3.20 shows the track merging and splitting effect on correlation function. in ideal case where only Bose-Einstein enhancement exists, correlation function is expressed as Gaussian and does not exceed two. Measured correlation function is a quit different shape from Gaussian and exceed two. These modification of correlation function can be removed by pair selection.

3.5.2 Pair Cut

In this analysis, pair selection is applied with Number of shared TPC clusters and angular distance in $\Delta\eta$ and $\Delta\phi^*$.

3.5.3 Fraction of shared TPC cluster

Due to high multiplicity events in Pb-Pb collisions, reconstructed tracks shares same TPC Pad channel in Figure 3.19. This leads to generate the ghost tracks. In order to remove this effect, Fraction of shared TPC clusters are used. Number of shared TPC clusters means the number of TPC pad row which is shared with other tracks shown. Fraction of shared TPC clusters are calculated with following equation.

$$F_{share} = \frac{N_{share}}{N_{hits}} \tag{3.55}$$

where F_{share} is fraction of shared TPC clusters and N_{hits} is the number of TPC clusters to reconstruct a certain track. N_{share} is the number of shared TPC clusters to reconstruct it. When the pair of the fraction of shared TPC cluster is larger than 5%, this pair is removed.

3.5.4 Angular distance in $\Delta\eta$-$\Delta\phi^*$

The other pair cut is Angular distance in $\Delta\eta$ and $\Delta\phi^*$. Two track resolution strongly depends on the distance of two tracks. the relative angle $\Delta\eta$ and $\Delta\phi$ in a certain radius of TPC is calculated in consideration of the magnetic fields. $\Delta\eta$ is not affected by magnetic filed. $\Delta\phi$ is extrapolated as following equation.

$$\Delta\phi^* = \phi_1 - \phi_2 + \sin^{-1}\left(\frac{-0.015 \cdot e \cdot B_z \cdot R}{p_{T1}}\right) - \sin^{-1}\left(\frac{-0.015 \cdot e \cdot B_z \cdot R}{p_{T2}}\right) \tag{3.56}$$

where $\Delta\phi^*$ is extrapolated azimuthal angle of the tracks in a certain radius R. B_z[T] is the magnetic field in z direction and e is the elementary charge. phi_1 and phi_2 are the azimuthal angle of the tracks at the vertex and p_{T1} and p_{T2} are the transverse momentum of the tracks. The angular distance in $\Delta\eta$ and $\Delta\phi^*$ distribution can be calculated various TPC radii R and pair transverse momentum k_T.

In order to optimize the cut value of $\Delta\eta$ and $\Delta\phi^*$. $\Delta\eta$ v.s. $\Delta\phi^*$ distribution are calculated with TPC radii R bin (R = 0.8, 1.0, 1.1, 1.2, 1.3, 1.4$[m]$) and k_T bin (0.2-0.3, 0.3-0.4, 0.4-0.5, 0.5-0.6, 0.6-0.7, 0.7-1.0$[GeV/c]$).

Figure 3.21 illustrates the ratio of real and mixed two dimensional distribution in $\Delta\eta$ and $\Delta\phi^*$ of each k_T bin. Y-axis is the extrapolated $\Delta\phi^*$ at the TPC radii($R = 1.1[m]$). The acceptance and efficiency effect are corrected by event mixing. So the ratio of real and mixed event should be unity, if there is no physics correlation in this $\Delta\eta$ and $\Delta\phi^*$ region. But a depletion can be seen near $\Delta\eta = 0$ and $\Delta\phi^* = 0$. This depletion is coming from the inefficiency effect by track merging. This track merging effect is getting stronger with increasing the pair transverse momentum k_T.

In order to study this effect in detail, we projected this two dimensional distribution to $\Delta\eta$ direction in Figure 3.22 and $\Delta\phi^*$ in Figure 3.23. Projected histograms are fitted with double Gaussian function as dashed line in order to quantify the width of this depletion. The mean value of fit function is fixed to 0.

The sigma of narrower Gaussian as a function of extrapolated TPC radius R is shown in Figure 3.24 and 3.25. 3.24 is $\Delta\eta$ direction and 3.25 is $\Delta\phi^*$ direction. Both $\Delta\eta$ and $\Delta\phi^*$ direction, $\sigma_{\Delta\eta}$ takes a minimum value at $R = 1.0[m]$ and $R = 1.1[m]$ for $\sigma_{\Delta\phi*}$. The extrapolated radius dependence of σ is larger in $\Delta\phi^*$ direction. We determined to use the extrapolated radius $R = 1.1[m]$. Eventually the following $\Delta\eta$ and $\Delta\phi^*$ cut is applied for my analysis.

- $\Delta\phi^* < 0.066$ ($R = 1.1[m]$)
- $\Delta\eta < 0.018$

This values are determined by the fit result (3σ of narrower Gaussian in lowest k_T range which has widest Gaussian σ).

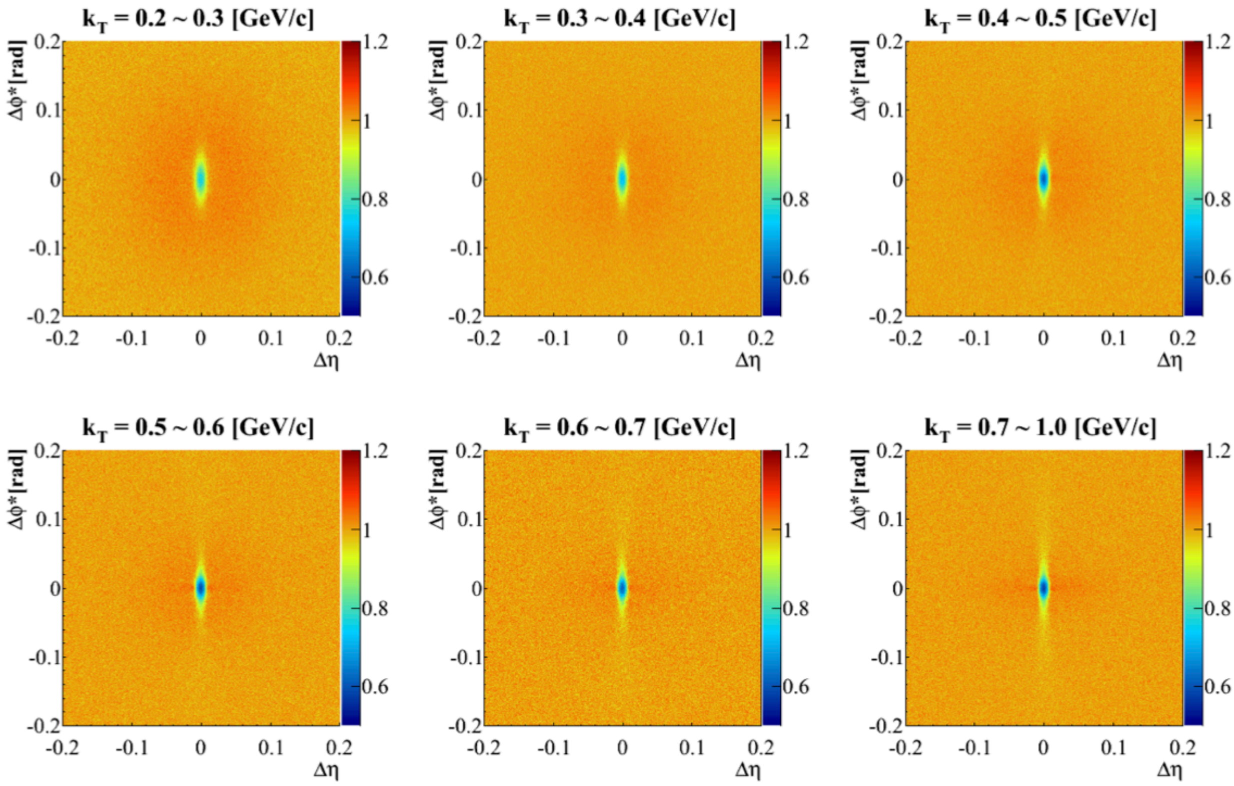

Figure 3.21: Two dimensional ratio in $\Delta\eta$-$\Delta\phi^*$ in different k_T at the TPC radii(R=1.1). k_T ranges are 0.2-0.3, 0.3-0.4, 0.4-0.5, 0.5-0.6, 0.6-0.7, 0.7-1.0 GeV/c. In all k_T ranges, one can find the broad peak and narrow dip at small $\Delta\eta$-$\Delta\phi^*$.

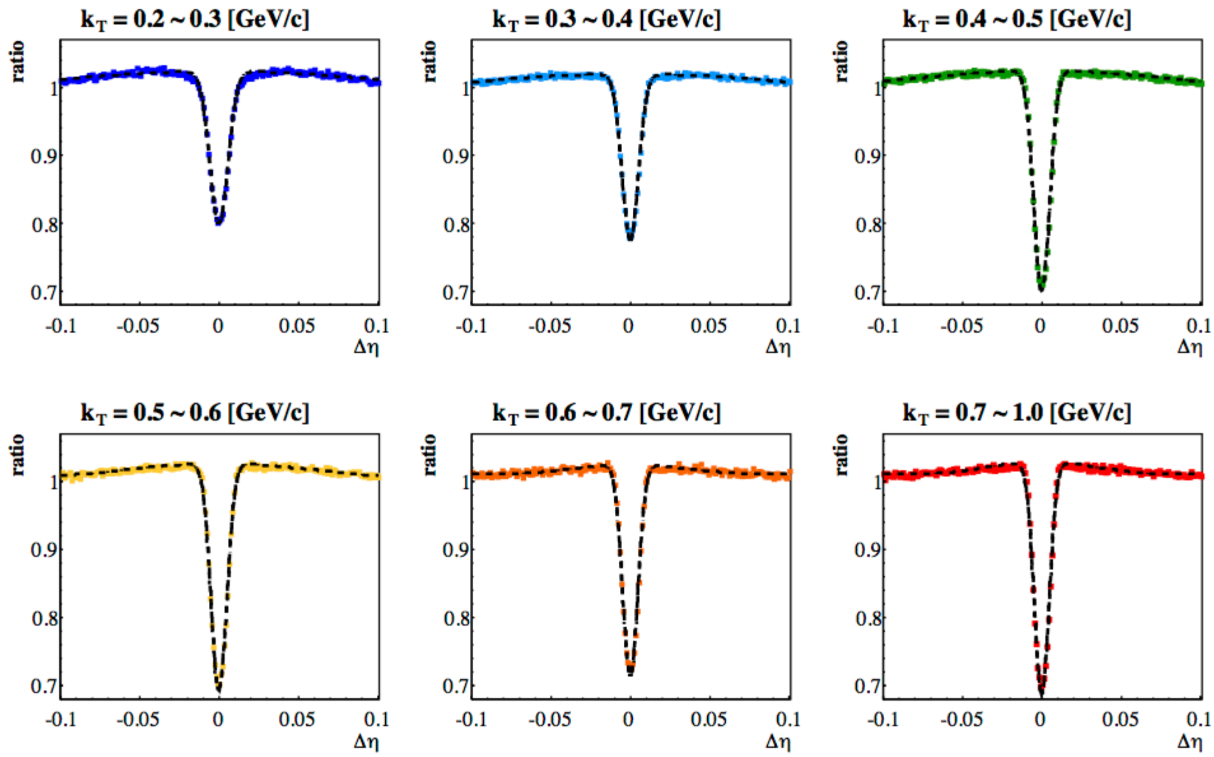

Figure 3.22: $\Delta\eta$ projection of the $\Delta\eta$-$\Delta\phi^*$ 2D ratio for each k_T range, at R = 1.1m Projected $\Delta\eta$ distributions are fitted with double Gaussian function shown in black dashed lines.

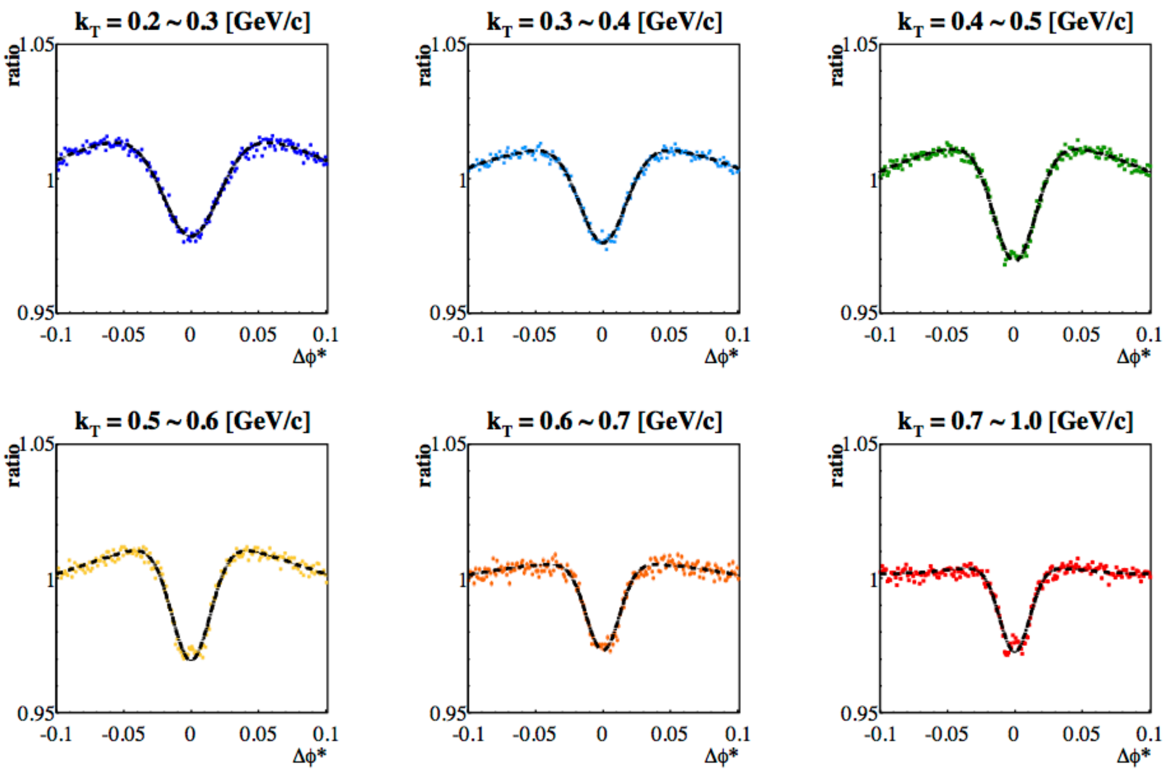

Figure 3.23: $\Delta\phi^*$ projection of two dimensional ration in $\Delta\eta$-$\Delta\phi^*$ at R = 1.1m. Double Gaussian fitting is performed to all distributions.

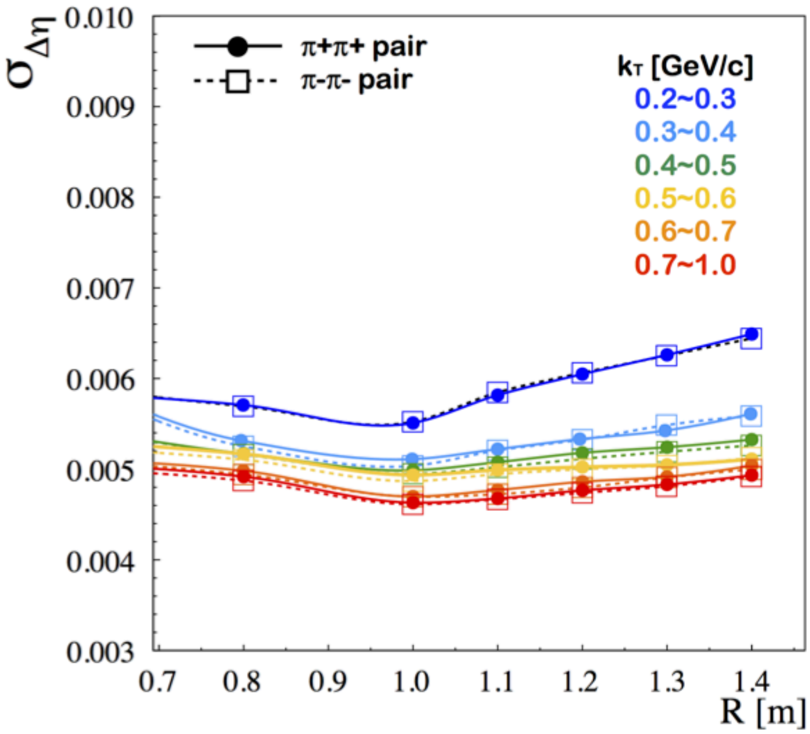

Figure 3.24: Width of Gaussian fit function(narrow dip) to $\Delta\eta$ distribution as a function of extrapolated TPC radius R for each k_T bins in centrality 0-50%. Closed circle and open square

low k_T to high k_T.

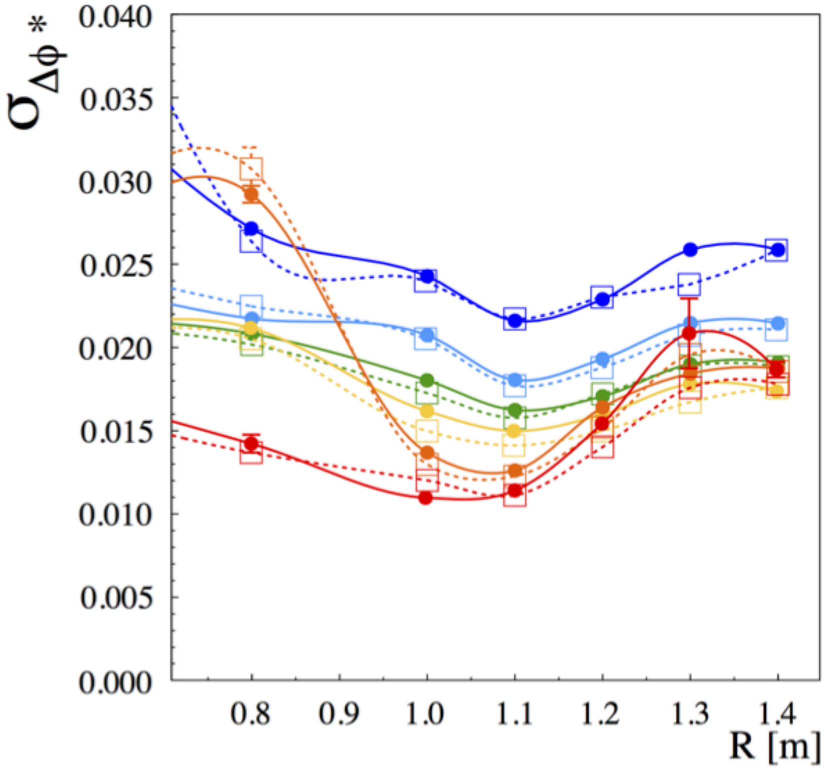

Figure 3.25: Width of Gaussian fit function(narrow dip) to $\Delta\phi^*$ distribution as a function of extrapolated TPC radius R. Closed circle and open square marker denote $\pi^+\pi^+$ and $\pi^-\pi^-$ pairs, respectively. Width grows from low k_T to high k_T.

3.6 HBT analysis method

Theoretically correlation of Bose-Einstein enhancement can be extracted with the ratio of two particles probability distribution to single particle probability distribution. Basically pairs in same events (real pair) contain the physical correlation such as HBT and flow correlation. However, in experiment, pair distribution is biased by the limited detector acceptance and finite particle efficiency. These effects are corrected with event mixing technique.

In event mixing technique, one dimensional correlation function is given by :

$$C_2(q) = \frac{q^{real}}{q_{mix}} \tag{3.57}$$

where the numerator q^{real} is the relative momentum distribution of real pairs and denominator q^{mix} denotes the relative momentum distribution of mixed pairs which mean pair distribution in different events. Mixed pairs have no physical correlations. But mixed pairs are also affected with similar acceptance and efficiency effect. when mixed event have similar event properties centrality and z vertex position.

As a consequence, the detector effect is canceled out and correlation function C_2 is driven from only the physical correlations.

In order to subtract the detector effect correctly, we define event class(Table 3.2 of event mixing technique. The classification of event plane angle Ψ_2 and Ψ_3 is only applied for study of HBT w.r.t. Ψ_2 and Ψ_3, respectively.

Relative momentum distribution of real pairs and mixed pairs are simultaneously shown in Figure 3.26, 3.27 (top panel). Shape of these distributions mainly comes from p_{T} distribution and detector effect. The small difference between real and mixed pairs at low relative momentum region is the HBT correlation. Correlation function is calculated with event mixing method in the bottom panel of Figure 3.26, 3.27.

Table 3.2: Event classification of event mixing

Class name	Range	Bin width
Centrality	0-50%	5%
z vertex	$\|z_{vertex}\| < 8.0$ cm	2 cm
Ψ_2	$\Psi_2 < \pi/2$ rad	$\pi/30$ rad
Ψ_3	$\Psi_3 < \pi/3$ rad	$\pi/30$ rad

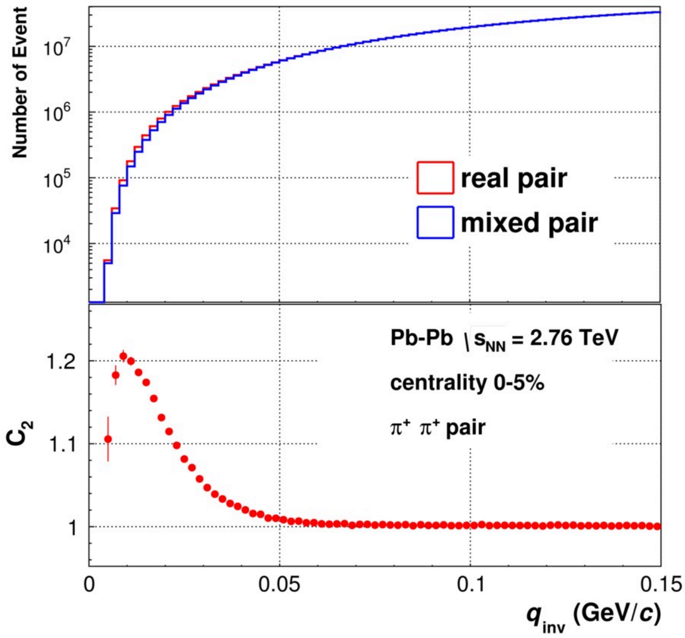

Figure 3.26: Relative momentum distribution of real pairs(red) and mixed pairs(blue) are simultaneously depicted in top panel. Mixed pair distribution is scaled to the real pair in q_{inv} range 0.17-0.34 (GeV/c). Correlation function is extracted with event mixing technique and shown in red marker on the bottom panel.

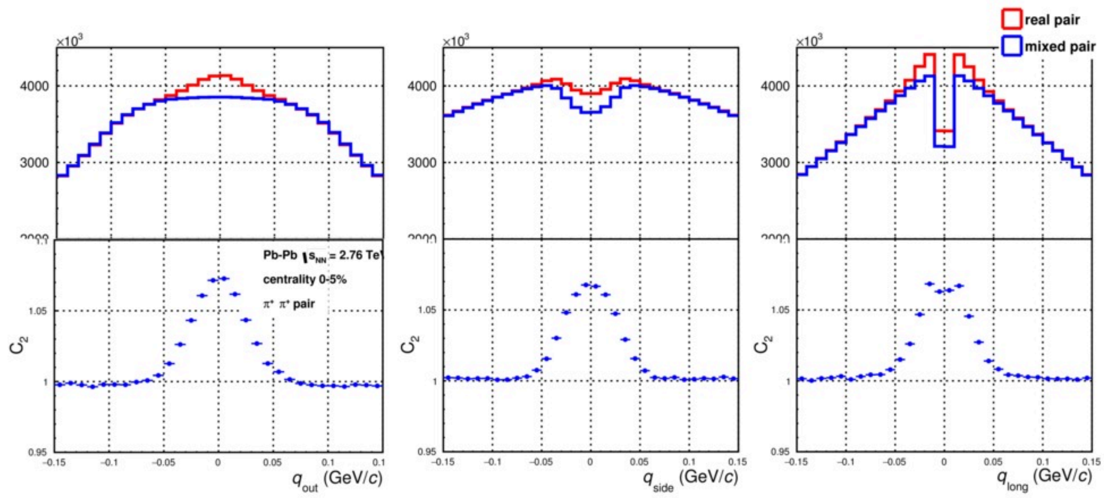

Figure 3.27: 1D projection of 3D Relative momentum distribution of real pairs(red) and mixed pairs(blue) are simultaneously depicted in top three panels. Left, Middle and Right panel are out, side and long direction, respectively. Mixed pair distribution is scaled to the real pair in $q_{\mathrm{out,side,long}}$ range 0.15-0.30 (GeV/c). Correlation function is extracted with event mixing technique and shown in blue marker on the bottom panel.

3.6.1 Fitting

χ^2 test is commonly used to examine the goodness-of-fit test. Suppose a histogram of the observed x values with N bins and the number of entries in bin i is n_i. When we perform fit to this histogram with function $f(x)$. Goodness-of-fit test is examined based on Pearson's χ^2 statistic,

$$\chi^2 = \sum_{i=1}^{N} \frac{(n_i - f(x))^2}{f(x)} \tag{3.58}$$

This statistical test works if the data n_i (i = 1, 2, 3,..., N) are Poisson distributions and the number of entries in each bin is not too small(e.g. $n_i \geq 5$). But measured correlation function which is expressed by the ratio of two Poisson distribution is not itself Poisson distributed, especially when taking the ratio of small numbers. Simple χ^2 examination is inappropriate for fitting the correlation function. As a consequence, maximum log-likelihood is used to examine the goodness-of-fit. A log-likelihood minimization function is given by :

$$\chi^2_{PML} = -2\left[A\ln\left(\frac{C(A+B)}{A(C+1)}\right) + B\ln\left(\frac{A+B}{B(C+1)}\right)\right] \tag{3.59}$$

where A and B are relative momentum distribution for real and mixed pairs, respectively. C is the ratio of A to B. This maximum log-likelihood equation assumes that Both real and mixed are distributed as Poisson.

3.6.2 Corrections

Compared to the ideal case where the correlation function C_2 can be simply expressed by Bose-Einstein enhancement, analyzing experimentally measured correlation function is more complicated. We have to perform appropriate corrections for measured correlation functions in order to extract correct source radii. In this analysis, applied corrections to the correlation functions fall into three categories, Coulomb interaction, momentum resolution correction and event plane resolution correction.

Coulomb Interaction

First correction concerns Coulomb interaction for charged particles. One dimensional Correlation function (Figure 3.26) is not simple Gauss function. There is dip structure at small q_{inv}. This is Coulomb-induced correlations. In order to extract HBT correlation, Coulomb correlation must be analyzed at small q_{inv}, where HBT correlation can be also found as well.

Experimentally we have two correction method of Coulomb interaction. First one is Gamow correction, where the correlation function itself is corrected with Gamow factor[57]. Gamow factor is given by :

$$G(\eta) = \frac{2\pi\eta}{e^{2\pi\eta} - 1} \tag{3.60}$$

$$\eta \equiv \frac{\mu e^2}{\hbar q} Z_1 Z_2 \tag{3.61}$$

where μ is reduced mass and $Z_1 e$, $Z_2 e$ are charge. For realistic source, however, Gamow factor procedure over-corrects the correlation function due to the very long-lived-resonances such as η and ω.

Second one is Bowler-Sinyukov fit, where Coulomb interaction is included in the fit function[58]. In this method, Core-Halo picture is employed. Correlation function is decomposed into Core and Halo term. Long-lived-resonances and misidentified particles are referred to as Halo which has neither Femtoscopic correlation nor Coulomb induced correlation. The other pion pairs which directly emanates from the source are described as Core. The ratio of Core to Halo is determined with the empirical parameter λ. In this analysis Bowler Sinyukov fit is used. Fit function of Bowler Sinyukov fit can be expressed as :

$$C_2(q) = C_2^{Core}(q) + C_2^{Halo} \tag{3.62}$$

$$= N\left[\lambda\left\{1+G(q)F(q)\right\}+(1-\lambda)\right] \tag{3.63}$$

where $C_2^{Core}(q)$ and $C_2^{Halo}(q)$ are Core and Halo term of correlation function, respectively. N is normalization factor, $F(q)$ is Coulomb component, $G(q)$ is Gaussian estimated HBT correlation component. For one dimensional HBT analysis, $G(q)$ is described as :

$$G(q_{\mathrm{inv}}) = \exp\left(-R_{\mathrm{inv}}^2 q_{\mathrm{inv}}^2\right) \tag{3.64}$$

and for three dimensional out-side-long coordinates, $G(q)$ is expressed by :

$$G\left(q_{\mathrm{out}}, q_{\mathrm{side}}, q_{\mathrm{long}}\right) = \exp\left(-R_{\mathrm{out}}^2 q_{\mathrm{out}}^2 - R_{\mathrm{side}}^2 q_{\mathrm{side}}^2 - R_{\mathrm{long}}^2 q_{\mathrm{long}}^2 - 2R_{\mathrm{os}}^2 q_{\mathrm{out}} q_{\mathrm{side}} - 2R_{\mathrm{ol}}^2 q_{\mathrm{out}} q_{\mathrm{long}} - 2R_{\mathrm{sl}}^2 q_{\mathrm{side}} q_{\mathrm{long}}\right) \tag{3.65}$$

Coulomb component $F(q)$ is given by Coulomb wave function given by :

$$F_c = \frac{P_c(\overrightarrow{p_1}, \overrightarrow{p_2})}{P_{12}(\overrightarrow{p_1}, \overrightarrow{p_2})} \tag{3.66}$$

$$P_c(\overrightarrow{p_1}, \overrightarrow{p_2}) = \int d^3 r \rho(\vec{r}) \left|\Psi_{c,\mathrm{sym}}\right|^2 \tag{3.67}$$

where F_c is the strength of Coulomb interaction, $\Psi_{c,\mathrm{sym}}$ denotes the symmetrized Coulomb wave function, $P_c(\overrightarrow{p_1}, \overrightarrow{p_2})$ is the probability to observe two particles with coulomb interaction, $P_c(\overrightarrow{p_1}, \overrightarrow{p_2})$ is the probability to observe two particles without coulomb interaction and $\rho(r)$ is the spatial distribution of the distance between two particles.

Since Eq.3.67 requires the spatial coordinate of two particles, We have to assume the particle distribution of source. In this analysis, source distribution is assumed to be Gaussian. For each pion pairs, 20 particles are randomly distributed according to Gaussian whose width is σ_{input}. and Coulomb-induced correlation is calculated by the average of 361 pairs(from 20 particles).

In order to calculate the correct Coulomb correlation strength, the determination of σ_{input} is important. We performed the second times iteration procedure and input source size for iteration is shown in Table 3.3.

Table 3.3: Input source size of Coulomb interaction

Centrality	Source size
0-5%	11 fm
5-10%	10 fm
10-20%	9 fm
20-30%	8 fm
30-40%	7 fm
40-50%	6 fm

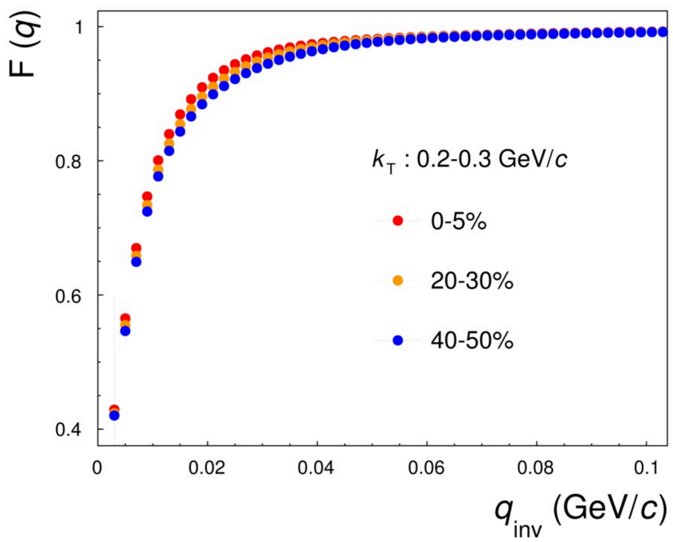

Figure 3.28: Coulomb correction factor $F(q)$ calculated by Coulomb wave function assuming Gaussian distribution at pair transverse momentum k_T:0.2-0.3GeV/c for 3 centralities as a function of one dimensional relative momentum $q_{\rm inv}$

Figure 3.28 shows Coulomb correction factor $F(q)$ calculated by Coulomb wave function assuming Gaussian distribution at pair transverse momentum k_T:0.2-0.3GeV/c for 3 centralities as a function of one dimensional relative momentum $q_{\rm inv}$.

Momentum Resolution Correction

Second correction is momentum resolution correction. Finite resolution effects in the relative momentum artificially smear the correlation function especially at small relative momentum, where quantum interference becomes important. The effect of momentum resolution is estimated by using Monte Carlo event generator HIJING[59] and full simulation of the ALICE detectors with GEANT. Correction factor is calculated by the double ratio of the ideal correlation function divided by smeared correlation function. Here we define the correction factor $CF\left(q_{\mathrm{inv}}\right)$ given by :

$$CF\left(q\right) = \frac{C_2\left(q^{gen}\right)}{C_2\left(q^{rec}\right)} \tag{3.68}$$

where $C_2\left(q^{gen}\right)$ denotes correlation function generated from HIJING with perfect momentum resolution. Generated particles are propagated through detector simulation GEANT and smeared correlation function is described as $C_2\left(q^{rec}\right)$. Each correlation function is expressed as

$$C_2\left(q_{\mathrm{inv}}^{gen}\right) = \frac{A\left(q^{gen}\right)}{B\left(q^{gen}\right)} \tag{3.69}$$

$$C_2\left(q_{\mathrm{inv}}^{rec}\right) = \frac{A\left(q^{rec}\right)}{B\left(q^{rec}\right)} \tag{3.70}$$

where A and B are real and mixed relative momentum distribution obtained by event mixing technique. Event, track and pair selections are exactly same condition to experimental analysis and resonance decay particles are rejected to exclude these effect on correlation function. Pair selection such as fraction of shared TPC clusters and angular distance in $\Delta\phi^*$-$\Delta\eta$ cut is applied on both generated and reconstructed particles. For generated particles, corresponding reconstructed track information was used to these selections. But geometrical information is not included in HIJING. Therefore HBT correlation is inserted into real pair distribution as the weight iteratively until the extracted HBT radii converge.

Figure 3.29 shows the comparison of the generated correlation function and reconstructed correlation function (left panel) and the correction factor $CF\left(q_{\mathrm{inv}}\right)$ (right panel).

Obtained correction factor are included in the fitting function expressed by

$$C\left(q\right) = N\left[\lambda\left\{1+G\left(q\right)F\left(q\right)\right\}+\left(1-\lambda\right)\right]/CF\left(q\right) \tag{3.71}$$

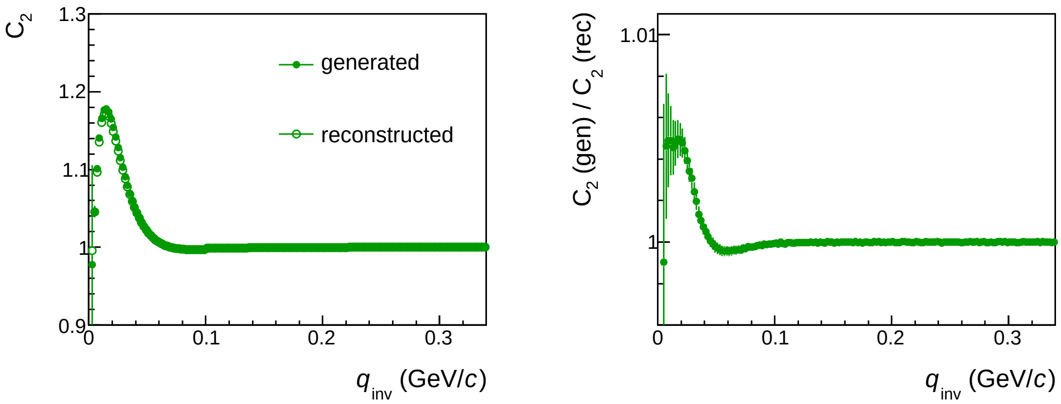

Figure 3.29: Correlation function of pure pions for centrality 20-30% calculated with HIJING + GEANT (left panel). Correlation function of generated pions that detector effect is not included is shown in closed marker and Correlation function of reconstructed pions that detector effects are included is plotted in open marker. (open marker). Ratio of generated correlation function to reconstructed correction function shown in right panel.

3.6.3 Event Plane Resolution Correction

Finite event plane resolution smears the oscillation of azimuthally sensitive HBT with respect to event plane. A model independent correction is applied in this analysis. Real and mixed q-distribution are corrected with the following equation.

$$N(q,\Psi_j) = N_{exp}(q,\Psi_j) + \sum_{n=m,2m,...}^{n_{bin}/2} \zeta_{n,m}(\Delta)\left[N_{c,n}^{exp}(q)\cos(n\Psi_j) + N_{s,n}^{exp}(q)\sin(n\Psi_j)\right] \quad (3.72)$$

where $N(q,\Psi_j)$ is the measured relative momentum distribution of real and mixed pairs, n_{bin} is the number of azimuthal bins and m is the order of the measured event plane. Ψ_j denotes the center of j_{th} azimuthal bin which corresponds to azimuthal pair angle with respect to the measured event plane. $N_{c,n}^{exp}(q)$, $N_{s,n}^{exp}(q)$ and $\zeta_{n,m}(\Delta)$ are expressed as

$$N_{c,n}^{exp}(q) = \left\langle N_{exp}(q,\Psi)\cos(n\Psi)\right\rangle = \frac{1}{n_{bin}}\sum_{j=1}^{n_{bin}} N_{exp}(q,\Psi)\cos(n\Psi_j), \quad (3.73)$$

$$N_{s,n}^{exp}(q) = \left\langle N_{exp}(q,\Psi)\sin(n\Psi)\right\rangle = \frac{1}{n_{bin}}\sum_{j=1}^{n_{bin}} N_{exp}(q,\Psi)\sin(n\Psi_j), \quad (3.74)$$

$$\zeta_{n,m}(\Delta) = \frac{n\Delta/2}{\sin(n\Delta/2)\left\langle\cos(n(\Psi_m-\Psi_R))\right\rangle} - 1, \quad (3.75)$$

where $\langle\cos(n(\Psi_m-\Psi_R))\rangle$ is well known correction factors as event plane resolution. Ψ_m and Ψ_R are measured and real event plane. Δ denotes the width of azimuthal angular bins. When we calculate the pairs relative to 3^{rd}-order event plane, only odd value of $n = 3$ and above are summed over. In this analysis, only $n = 3$ case are calculated.

Equation 3.73 correct the smeared oscillation amplitude which is affected by finite event plane resolution and event plane binning.

Figure 3.30 shows the comparison between event plane resolution corrected and uncorrected result of extracted 3D HBT radii of charged pions as a function of $\phi_{pair}-\Psi_3$. Event plane is determined with FMD AC. As can be seen, event plane resolution correction does not change the average value of azimuthal angle dependence. But the oscillation amplitude became a little larger due to the event plane resolution correction. Figure 3.31 illustrates comparison of the cross term before and after the event plane resolution correction. Due to the average values of cross term are almost zero, All data points are shifted along the y-axis for visibility. R_{os} shows the clear sine curve in all centrality.

Solid lines shows the fit function by cosine function. Both corrected and uncorrected fit functions are plotted as red and black lines, respectively.

There is an another method to correct the oscillation amplitude of azimuthal HBT radii with respect to event plane. This method is much more simple one compared with bin-by-bin method, which is expressed as

$$R^2_{\mu,n,true} = R^2_{\mu,n,measured} / \langle \cos(n(\Psi_m - \Psi_R)) \rangle \frac{n\Delta/2}{\sin(n\Delta/2)}, \tag{3.76}$$

where $R^2_{\mu,n,measured}$ denotes the measured oscillation amplitude of squared HBT radii. $R^2_{\mu,n,true}$ is the corrected oscillation amplitude of squared HBT radii. $\langle \cos(n(\Psi_m - \Psi_R)) \rangle$ is n_{th} order event plane resolution. Pair angle with respect to Ψ_n are divided into n_{bins} classes and each bins can be expressed as $\Delta = \pi/n_{bins}$. The term $\frac{n\Delta/2}{\sin(n\Delta/2)}$ represents finite azimuthal bin width correction. Oscillaion amplitude of HBT radii are smeared with finite number of divisions in pair angles with respect to event plane.

For QA of event plane resolution correction, corrected oscillation functions are compared with results with different correction method with Equation 3.76 in Figure 3.30. Red solid line is fit function of bin-by-bin event plane correction and Blue line is obtained by applying Equation 3.76 to uncorrected black line. Two different method is fully consistent (the difference is about 0.1%).

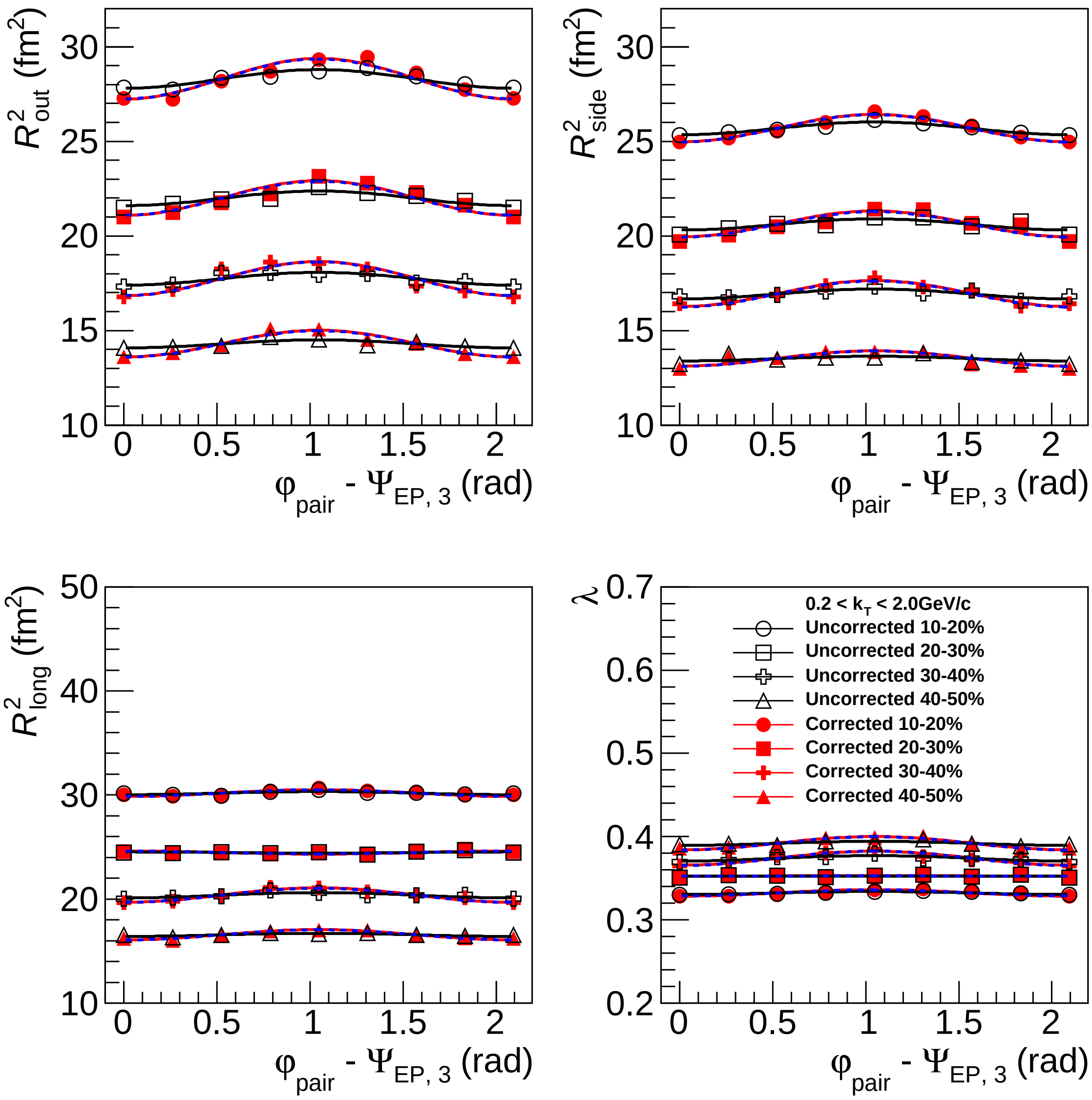

Figure 3.30: Extracted 3D HBT radii of charged pions as a function of azimuthal pair angle with respect to Ψ_3. Comparison of before and after the event plane resolution correction,

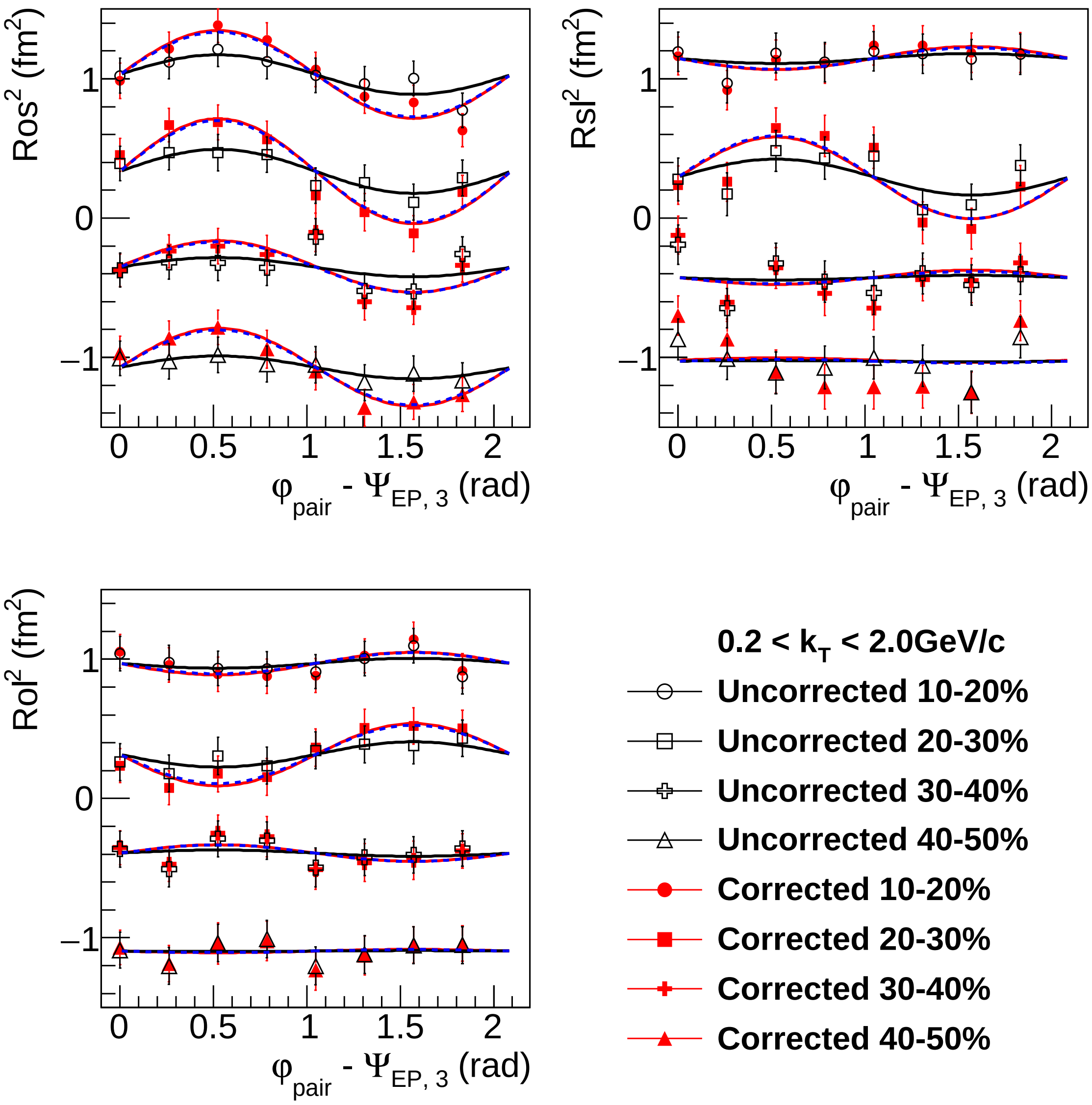

Figure 3.31: Extracted 3D HBT cross term of charged pions as a function of azimuthal pair angle with respect to Ψ_3. Comparison of before and after the event plane resolution correction. All points are shifted along the y-axis for visibility

3.7 Systematic Uncertainties

In this section, the effect of various source systematic uncertainties on HBT analysis and v_n analysis are presented.

3.7.1 Systematic Uncertainties for HBT analysis

Systematic uncertainties related to HBT analysis are listed as following.

- Systematic difference of positive pion pairs and negative pion pairs
- Effect of magnetic field polarity
- Various fitting range of relative momentum
- Effect of different pair selection
- Effect of different event plane determination detector

Systematic Uncertainties of Charge

Positive and negative pions are combined for this analysis. The difference of each positive and negative pion pairs for Azimuthally sensitive HBT studies are estimated as systematic uncertainty. Since $R_{\rm os}$ significantly changes with respect to charge difference, which comes from the difference of pair selection effect to positive and negative particles. More positive pairs are subtracted in $q_{\rm out}\,q_{\rm side} > 0$, while more negative pairs are subtracted in $q_{\rm out}\,q_{\rm side} < 0$. This effect can be canceled out by summing positive and negative charged particles. Therefore the difference of charged pion pairs are excluded from systematic uncertainties for $R_{\rm os}$. Figure 3.32 shows the azimuthal angle dependence of squared HBT radii relative to Ψ_2 in 0-5, 5-10% centrality with positively and negatively charged pions and combined of them.

Systematic uncertainty of different charge is defined by the standard deviation of HBT radii R in each azimuthal angle bins given by:

$$\sigma_{\mu}^{charge} = \sqrt{\left(\sum_{i}^{2} R_{\mu,i} - R_{\mu,combined}\right)/2} \tag{3.77}$$

where μ denotes the HBT radii in each directions at Bertsch-Pratt frame, namely $R_\mu = R_{\rm out}$, $R_{\rm side}$, $R_{\rm long}$, λ, $R_{\rm ol}$ and $R_{\rm sl}$.

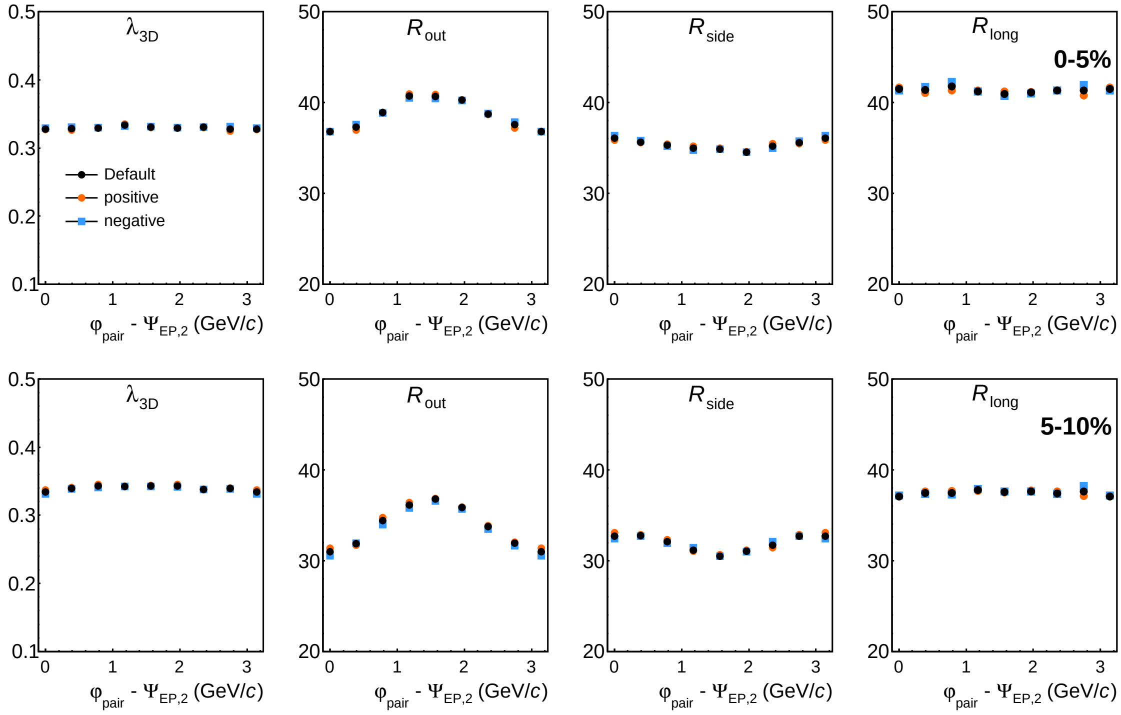

Figure 3.32: Extracted 3D HBT radii (λ, R^2_{out} , R^2_{side} , R^2_{long}) of charged pions as a function of azimuthal pair angle relative to Ψ_2. Figures in top rows represents centrality 0-5%, while 5-10% are shown in bottom panels. Default value is positive and negative pions combined results shown in black marker. Comparison with positive and negative charged pion pairs are depicted as orange circle and blue square, respectively.

Systematic Uncertainties of Charge and Magnetic Field Polarity

In ALICE, two different polarity of the solenoid magnetic field are applied. This analysis was performed in both positive and negative magnetic field combined results. The difference in two magnetic field polarity is analyzed separately.

Figure 3.34 shows the azimuthal angle dependence of squared HBT radii relative to second harmonic event plane in centrality 0-5, 5-10% with three patterns of magnetic field polarity, positive, negative and combined them.

Systematic uncertainty of different magnetic field polarity is defined by the standard deviation of HBT radii R in each azimuthal angle bins given by:

$$\sigma_{\mu}^{mag} = \sqrt{\left(\sum_{i}^{2} R_{\mu,i} - R_{\mu,combined}\right)/2} \tag{3.78}$$

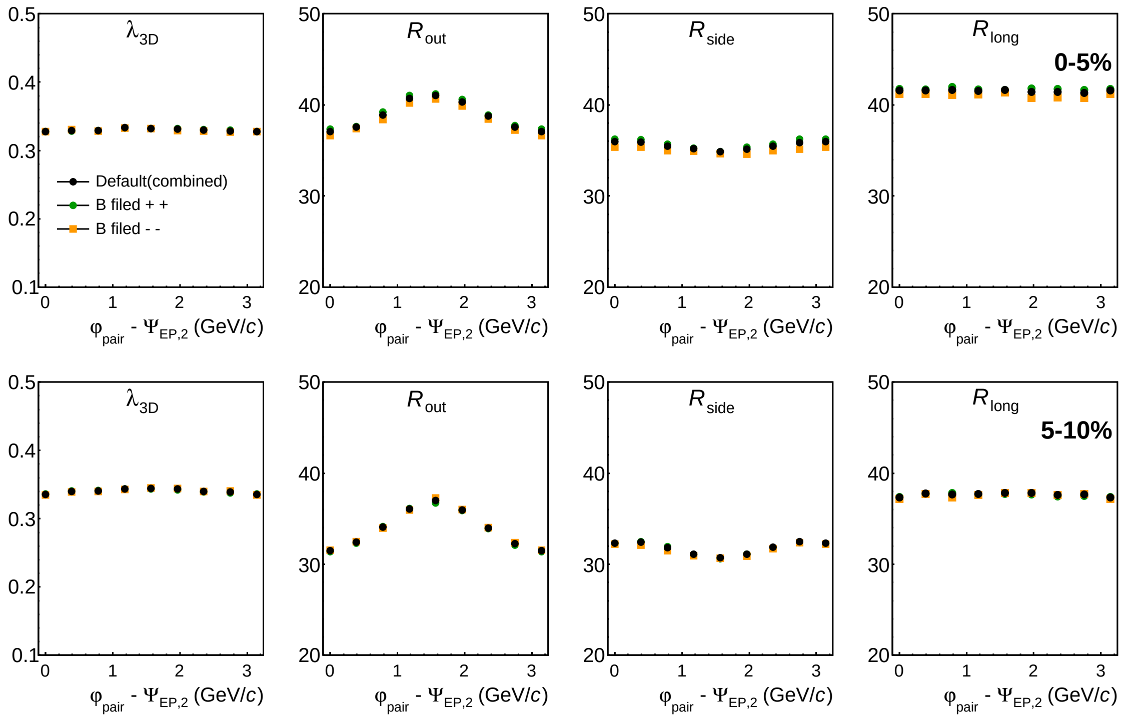

Figure 3.33: Extracted 3D HBT radii (λ, $R^2_{\rm out}$, $R^2_{\rm side}$, $R^2_{\rm long}$) of charged pions as a function of azimuthal pair angle relative to Ψ_2. Figures in top rows represents centrality 0-5%, while 5-10% are shown in bottom panels. Default value is positive and negative B field combined results shown in black marker. Positive and negative B field results are separately analyzed and depicted in green circle and yellow square, respectively.

Systematic Uncertainties of Fit Range

3 dimensional fit is performed to correlation function at the relative momentum range 0-150 GeV/c . Systematic difference with varying the fitting range is studied for each 10 GeV/c bin up to 200 GeV/c .

Figure 3.34 shows the azimuthal angle dependence of squared HBT radii relative to second harmonic event plane in centrality 0-5, 5-10% with three patterns of magnetic field polarity, positive, negative and combined them.

Systematic uncertainty of different magnetic field polarity is defined by the standard deviation of HBT radii R in each azimuthal angle bins given by:

$$\sigma_\mu^{range} = \sqrt{\left(\sum_i^5 R_{\mu,i} - R_{\mu,150\mathrm{MeV}/c}\right)/5} \tag{3.79}$$

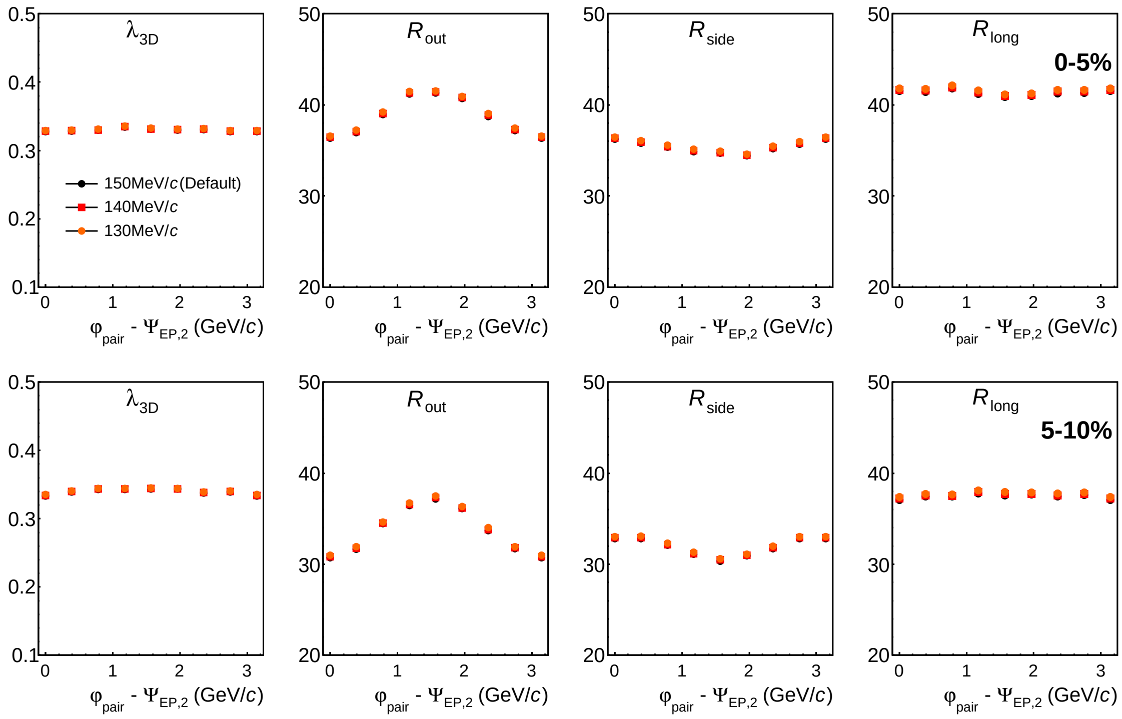

Figure 3.34: Extracted 3D HBT radii (λ, R^2_{out} , R^2_{side} , R^2_{long}) as a function of azimuthal pair angle relative to Ψ_2, varying fit range from 150GeV/c (Default) to 200GeV/c for each 10GeV/c bin. Figures in top rows represents centrality 0-5%, while 5-10% are shown in bottom panels. Default fit range is 150GeV/c shown in black marker. Comparison with positive and negative charged pion pairs are depicted as orange circle and blue square, respectively.

Systematic Uncertainties of Pair Cut

The analysis is repeated at tighter Pair Cut selection definition with angular distance in $\Delta\phi^*\Delta\eta$. Default cut value is determined by fitting $\Delta\phi^*\Delta\eta$ with double Gaussian and 3 σ of narrower Gauss function. Effect of tighter pair selection with 3.5 σ is studied as shown in the following list.

- $\Delta\phi^*$: 0.066(default), 0.077(tight)
- $\Delta\eta$: 0.018(default), 0.021(tight)

Figure 3.35 shows the azimuthal angle dependence of squared HBT radii relative to second harmonic event plane in centrality 0-5, 5-10% with two different pair selection.

Systematic uncertainty of pair selection is defined by the absolute value of HBT radii R in each azimuthal angle bins given by:

$$\sigma_{\mu}^{pair} = |R_{\mu,tight} - R_{\mu,default}| \tag{3.80}$$

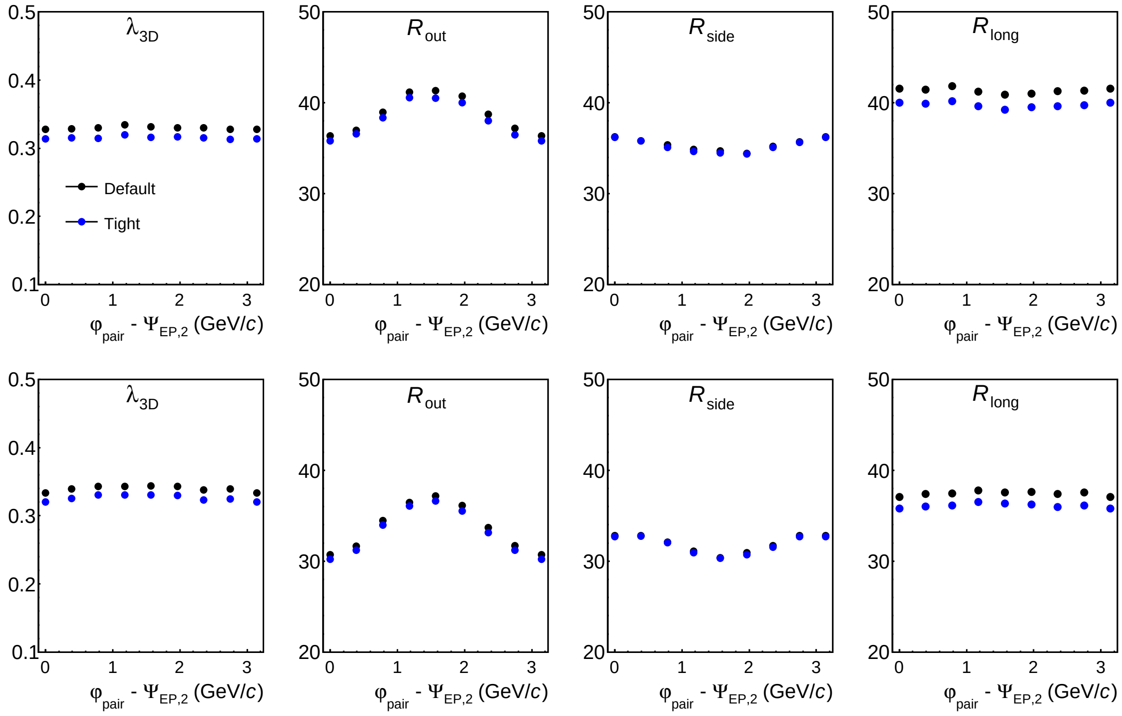

Figure 3.35: Extracted 3D HBT radii (λ, R^2_{out} , R^2_{side} , R^2_{long}) as a function of azimuthal pair angle relative to Ψ_2 with two different pair selection. Figures in top rows represents centrality 0-5%, while 5-10% are shown in bottom panels. Default pair selection is plotted in black marker. Comparison with the result in tighter pair selection are depicted as orange circle.

Systematic Uncertainties of Event Plane Determination Detector

Systematic study of different event plane is performed with VZERO detector which has different event plane resolution and rapidity gap between HBT measurements. Estimation of systematic uncertainty is evaluated via VZERO A+C combined event plane.

Figure 3.36 shows the azimuthal angle dependence of squared HBT radii relative to second harmonic event plane in centrality 0-5, 5-10% with two different event plane, FMD A+C combined and VZERO A+C combined.

Systematic uncertainty of different event plane is defined by the absolute value of HBT radii R in each azimuthal angle bins given by:

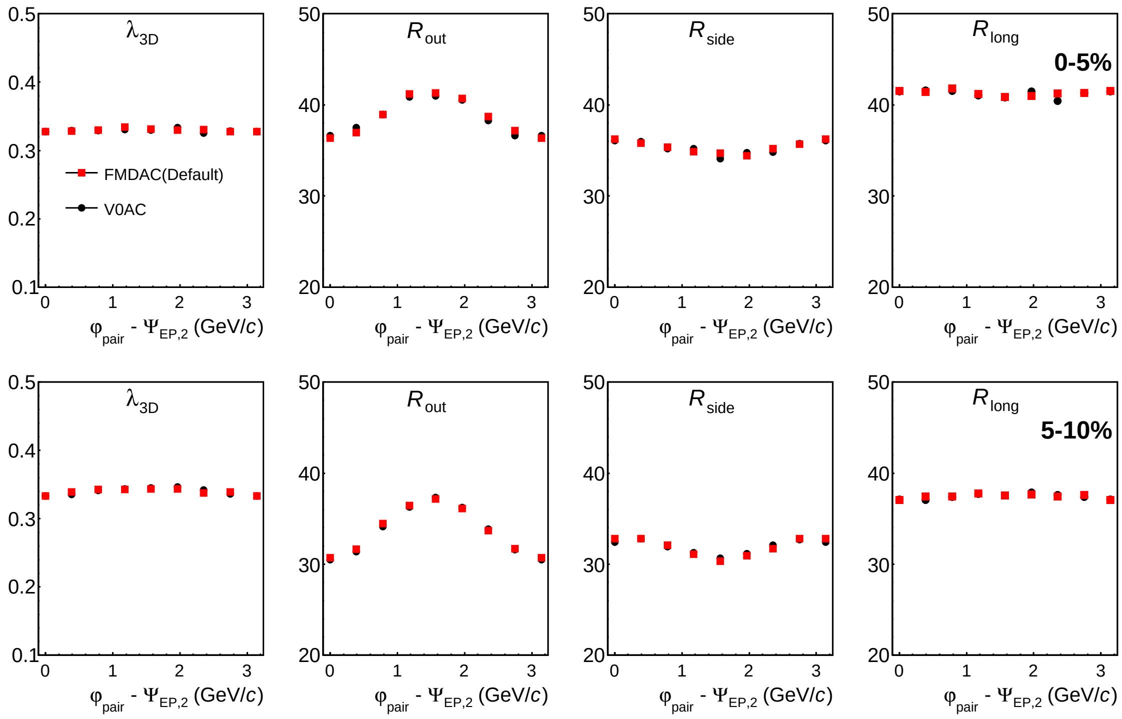

Figure 3.36: Extracted 3D HBT radii (λ, $R^2_{\rm out}$, $R^2_{\rm side}$, $R^2_{\rm long}$) as a function of azimuthal pair angle relative to Ψ_2 with two different event plane via FMD A+C and VZERO A+C. Figures in top rows represents centrality 0-5%, while 5-10% are shown in bottom panels. FMD A+C combined results is plotted in black marker. VZERO A+C combined results is plotted in blue marker.

$$\sigma_\mu^{EP} = |R_{\mu,tight} - R_{\mu,default}| \tag{3.81}$$

Total systematic uncertainty is calculated by quadratic sum of each systematic error given by :

$$\sigma_\mu^{tot} = \sqrt{\left(\sigma^{charge}\right)^2 + (\sigma^{mag})^2 + (\sigma^{range})^2 + (\sigma^{pair})^2 + (\sigma^{EP})^2 +} \tag{3.82}$$

Ratio of total systematic uncertainty to HBT radii (or relative amplitude of squared HBT radii) is shown in Table 3.43.53.63.7.

Table 3.4: Systematic table for λ w.r.t. Ψ_2 unbiased(No q_2 selection)

centrality 0-5%								
$\Delta\phi$	0	$\pi/8$	$\pi/4$	$3\pi/8$	$\pi/2$	$5\pi/8$	$3\pi/4$	$7\pi/8$
charge(%)	0.03	0.66	0.48	0.02	0.03	0.27	0.02	0.19
B field(%)	0.09	0.24	0.21	0.05	0.05	0.49	0.39	0.54
Event plane(%)	0.41	0.15	0.57	0.07	0.37	1.13	0.37	0.60
Pair cut(%)	3.96	3.87	4.08	4.15	3.89	3.95	3.97	3.71
Fit range(%)	1.72	1.79	1.76	1.82	1.76	1.69	1.76	1.74
Quadratic sum (%)	4.34	4.33	4.51	4.53	4.29	4.48	4.37	4.19
centrality 5-10%								
charge(%)	0.09	0.38	0.03	0.40	0.25	0.34	0.07	0.10
B field(%)	0.16	0.14	0.25	0.14	0.27	0.22	0.11	0.39
Event plane(%)	0.44	0.52	0.22	0.11	0.11	0.35	0.61	0.00
Pair cut(%)	3.99	3.88	4.05	3.90	3.67	3.87	3.92	4.02
Fit range(%)	1.25	1.24	1.28	1.33	1.31	1.22	1.29	1.26
Quadratic sum (%)	4.21	4.13	4.26	4.15	3.92	4.10	4.18	4.23
centrality 10-20%								
charge(%)	0.31	0.2	0.16	0.81	0.18	0.36	0.64	0.24
B field(%)	0.84	0.76	0.54	1.01	0.76	0.23	0.22	0.18
Event plane(%)	0.65	0.29	0.37	0.31	0.12	0.00	0.56	0.17
Pair cut(%)	3.54	3.67	3.29	3.47	3.20	4.01	3.54	3.66
Fit range(%)	0.79	0.84	0.83	0.94	0.87	0.94	0.90	0.84
Quadratic sum (%)	3.79	3.86	3.46	3.84	3.41	4.14	3.76	3.77
centrality 20-30%								
charge(%)	0.18	0.12	0.19	0.56	0.29	0.46	0.33	0.26
B field(%)	0.14	0.68	0.67	0.03	0.63	0.48	0.53	0.41
Event plane(%)	0.06	0.16	0.36	0.63	0.47	0.08	0.68	0.40
Pair cut(%)	2.95	3.33	2.68	2.62	3.39	2.78	2.45	3.19
Fit range(%)	1.02	0.97	1.06	1.05	1.06	0.95	1.02	0.98
Quadratic sum (%)	3.13	3.54	2.99	2.95	3.65	3.02	2.81	3.40
centrality 30-40%								
charge(%)	0.51	1.15	0.25	1.49	0.24	1.31	0.55	1.66
B field(%)	0.68	0.13	1.01	0.25	1.09	1.04	0.35	0.24
Event plane(%)	0.91	0.80	0.98	0.39	1.63	0.62	0.43	1.19
Pair cut(%)	2.27	2.32	1.84	2.34	2.11	2.17	2.11	2.32
Fit range(%)	1.14	1.09	1.00	0.97	1.12	0.94	1.12	1.15
Quadratic sum (%)	2.83	2.92	2.54	2.98	3.10	2.96	2.51	3.31
centrality 40-50%								
charge(%)	0.29	0.10	1.15	0.08	0.27	0.13	0.61	1.45
B field(%)	2.03	0.49	0.72	0.68	1.26	0.61	2.22	1.51
Event plane(%)	1.68	0.92	0.45	0.18	0.21	0.99	0.52	0.00
Pair cut(%)	1.78	1.78	2.26	2.21	1.89	1.67	2.57	1.47
Fit range(%)	1.26	1.09	1.14	1.27	1.31	1.44	1.37	1.38
Quadratic sum (%)	3.43	2.33	2.91	2.64	2.65	2.50	3.75	2.90

Table 3.5: Systematic table for R_{out} w.r.t. Ψ_2 unbiased(No q_2 selection)

centrality 0-5%								
$\Delta\phi$	0	$\pi/8$	$\pi/4$	$3\pi/8$	$\pi/2$	$5\pi/8$	$3\pi/4$	$7\pi/8$
charge(%)	0.38	0.27	0.11	0.09	0.21	0.18	0.22	0.07
B field(%)	0.94	0.37	1.11	0.97	0.67	0.86	0.58	0.67
Event plane(%)	0.13	0.30	0.14	1.03	0.39	0.26	0.14	0.45
Pair cut(%)	1.75	1.59	1.67	1.83	1.69	1.91	1.87	1.70
Fit range(%)	1.12	1.18	1.15	1.17	1.11	1.02	1.11	1.12
Quadratic sum (%)	2.31	2.06	2.32	2.59	2.17	2.35	2.27	2.19
centrality 5-10%								
charge(%)	0.69	0.32	0.37	0.64	0.60	0.62	0.54	0.54
B field(%)	0.21	0.24	0.20	0.16	0.70	0.13	0.11	0.33
Event plane(%)	0.00	0.50	0.36	0.48	0.11	0.00	0.45	0.23
Pair cut(%)	1.41	1.36	1.45	1.30	1.22	1.36	1.33	1.40
Fit range(%)	1.36	1.30	1.32	1.37	1.36	1.30	1.39	1.38
Quadratic sum (%)	2.09	1.99	2.04	2.06	2.05	1.99	2.05	2.08
centrality 10-20%								
charge(%)	0.47	0.35	0.75	1.15	0.27	0.31	0.59	0.36
B field(%)	1.47	1.41	1.21	2.54	1.74	1.88	1.03	0.87
Event plane(%)	1.05	0.03	0.08	0.04	0.34	1.24	0.58	0.19
Pair cut(%)	1.32	0.99	1.33	1.54	1.37	1.94	1.25	1.61
Fit range(%)	0.94	1.00	0.97	1.06	0.99	1.10	1.05	1.02
Quadratic sum (%)	2.48	2.03	2.18	3.35	2.47	3.19	2.10	2.13
centrality 20-30%								
charge(%)	0.45	0.32	0.12	0.51	0.34	0.21	0.56	0.19
B field(%)	0.91	0.70	0.29	0.19	0.70	0.78	0.24	0.92
Event plane(%)	0.10	0.76	0.81	0.19	0.12	1.48	0.26	0.46
Pair cut(%)	0.70	1.59	0.87	1.67	2.12	1.05	0.83	1.36
Fit range(%)	1.60	1.52	1.61	1.48	1.46	1.41	1.51	1.50
Quadratic sum (%)	2.02	2.45	2.02	2.31	2.69	2.44	1.85	2.28
centrality 30-40%								
charge(%)	0.50	1.10	0.15	0.22	0.05	0.36	0.84	1.59
B field(%)	0.50	0.28	0.64	0.16	0.38	0.42	1.13	0.43
Event plane(%)	1.20	0.53	0.83	0.39	1.76	1.41	0.31	0.40
Pair cut(%)	0.93	1.20	0.96	0.90	1.18	0.48	0.77	0.50
Fit range(%)	2.04	1.91	1.73	1.64	1.89	1.55	1.95	2.00
Quadratic sum (%)	2.64	2.58	2.24	1.93	2.87	2.22	2.55	2.67
centrality 40-50%								
charge(%)	0.84	1.09	0.71	0.16	0.50	1.67	1.17	1.38
B field(%)	2.81	1.67	1.69	0.40	0.57	2.45	2.80	1.30
Event plane(%)	1.16	0.52	2.81	0.86	0.51	0.20	3.41	1.30
Pair cut(%)	0.93	0.90	1.63	0.39	0.12	1.42	1.06	0.64
Fit range(%)	2.63	2.23	2.23	2.42	2.56	2.80	2.72	2.82
Quadratic sum (%)	4.21	3.16	4.35	2.63	2.72	4.32	5.42	3.69

Table 3.6: Systematic table for R_{side} w.r.t. Ψ_2 unbiased(No q_2 selection)

centrality 0-5%								
$\Delta\phi$	0	$\pi/8$	$\pi/4$	$3\pi/8$	$\pi/2$	$5\pi/8$	$3\pi/4$	$7\pi/8$
charge(%)	0.08	0.30	0.47	0.18	0.06	0.60	0.20	0.17
B field(%)	1.27	1.23	1.15	0.58	0.49	1.21	1.08	1.61
Event plane(%)	0.56	0.29	0.34	0.12	0.12	0.37	0.06	0.16
Pair cut(%)	0.13	0.05	0.09	0.09	0.03	0.03	0.05	0.01
Fit range(%)	1.72	1.79	1.78	1.86	1.81	1.70	1.76	1.74
Quadratic sum (%)	2.21	2.21	2.20	1.96	1.88	2.20	2.07	2.38
centrality 5-10%								
charge(%)	0.21	0.47	0.20	0.31	0.17	0.35	0.87	0.45
B field(%)	0.32	0.60	0.75	0.35	0.32	0.47	0.38	0.29
Event plane(%)	0.90	0.06	0.26	0.31	0.43	0.50	0.53	0.23
Pair cut(%)	0.20	0.23	0.36	0.43	0.15	0.31	0.13	0.11
Fit range(%)	1.44	1.40	1.44	1.51	1.49	1.40	1.48	1.46
Quadratic sum (%)	1.75	1.61	1.69	1.67	1.60	1.63	1.84	1.57
centrality 10-20%								
charge(%)	0.60	0.54	0.46	0.47	0.45	0.46	1.49	0.54
B field(%)	0.56	0.47	0.73	0.28	1.13	0.36	0.28	0.56
Event plane(%)	0.41	1.06	0.16	1.07	0.62	0.82	0.64	0.51
Pair cut(%)	0.14	0.31	0.07	0.56	0.69	0.69	0.35	0.34
Fit range(%)	0.96	1.03	1.03	1.18	1.12	1.21	1.13	1.04
Quadratic sum (%)	1.33	1.67	1.36	1.78	1.90	1.72	2.03	1.44
centrality 20-30%								
charge(%)	0.16	0.14	0.90	0.80	1.03	0.23	1.44	0.61
B field(%)	1.06	0.14	0.56	0.29	0.20	0.74	0.58	0.49
Event plane(%)	0.36	0.73	0.53	0.07	0.57	0.38	0.01	0.75
Pair cut(%)	0.60	0.53	0.56	0.70	1.00	0.16	0.59	0.52
Fit range(%)	1.54	1.46	1.62	1.60	1.61	1.50	1.56	1.47
Quadratic sum (%)	2.00	1.73	2.08	1.94	2.24	1.74	2.28	1.90
centrality 30-40%								
charge(%)	1.61	0.89	0.28	2.29	1.57	0.91	0.55	2.05
B field(%)	1.11	0.29	0.74	1.81	0.84	1.17	0.59	0.34
Event plane(%)	0.24	1.20	2.28	0.15	1.01	0.20	0.78	1.57
Pair cut(%)	0.33	0.04	0.18	0.87	1.32	0.84	0.63	0.30
Fit range(%)	1.86	1.74	1.70	1.71	2.00	1.63	1.94	1.84
Quadratic sum (%)	2.73	2.31	2.96	3.49	3.15	2.36	2.33	3.20
centrality 40-50%								
charge(%)	0.23	1.05	0.60	0.41	0.59	0.54	1.91	0.34
B field(%)	1.63	0.12	0.21	1.44	0.88	0.68	0.92	0.51
Event plane(%)	0.27	0.31	0.10	1.85	0.89	2.79	0.22	0.80
Pair cut(%)	0.51	0.20	1.45	1.61	1.29	1.43	1.33	0.17
Fit range(%)	2.29	1.99	2.13	2.47	2.64	2.79	2.55	2.50
Quadratic sum (%)	2.88	2.28	2.65	3.79	3.25	4.28	3.58	2.70

Table 3.7: Systematic table for R_{long} w.r.t. Ψ_2 unbiased(No q_2 selection)

centrality 0-5%								
$\Delta\phi$	0	$\pi/8$	$\pi/4$	$3\pi/8$	$\pi/2$	$5\pi/8$	$3\pi/4$	$7\pi/8$
charge(%)	0.10	0.60	0.29	0.17	0.11	0.39	0.05	0.27
B field(%)	0.77	0.62	1.19	0.66	0.42	1.31	1.15	1.14
Event plane(%)	0.41	0.41	0.12	0.24	0.16	0.81	0.45	1.04
Pair cut(%)	3.28	3.25	3.40	3.44	3.17	3.24	3.29	3.08
Fit range(%)	2.15	2.22	2.16	2.24	2.18	2.10	2.21	2.18
Quadratic sum (%)	4.01	4.05	4.21	4.17	3.88	4.17	4.15	4.09
centrality 5-10%								
charge(%)	0.55	0.56	0.14	0.26	0.14	0.36	0.27	0.63
B field(%)	0.34	0.16	0.69	0.17	0.26	0.24	0.23	0.29
Event plane(%)	0.13	0.72	0.19	0.28	0.39	0.35	0.45	0.19
Pair cut(%)	3.57	3.59	3.68	3.56	3.29	3.49	3.55	3.58
Fit range(%)	1.46	1.43	1.48	1.53	1.47	1.37	1.46	1.45
Quadratic sum (%)	3.92	3.97	4.04	3.90	3.64	3.79	3.88	3.93
centrality 10-20%								
charge(%)	0.75	0.35	1.55	0.42	0.63	0.61	0.84	0.52
B field(%)	0.66	1.59	0.19	2.18	1.00	0.50	0.69	2.37
Event plane(%)	0.66	0.33	0.44	0.63	0.32	0.23	1.01	0.60
Pair cut(%)	3.25	3.34	3.09	3.20	2.64	3.30	3.49	3.59
Fit range(%)	1.08	1.16	1.14	1.28	1.20	1.32	1.25	1.18
Quadratic sum (%)	3.63	3.91	3.67	4.15	3.15	3.65	4.00	4.53
centrality 20-30%								
charge(%)	0.56	1.19	0.17	0.87	1.75	0.08	0.85	0.19
B field(%)	0.10	1.61	0.40	0.29	1.98	0.10	0.31	1.19
Event plane(%)	0.29	0.04	0.61	0.03	1.68	0.91	0.15	0.89
Pair cut(%)	2.92	3.18	2.84	2.80	3.14	2.67	2.73	3.31
Fit range(%)	1.76	1.67	1.81	1.76	1.74	1.65	1.73	1.68
Quadratic sum (%)	3.47	4.11	3.45	3.43	4.77	3.27	3.36	4.00
centrality 30-40%								
charge(%)	1.19	1.20	1.85	0.15	0.13	1.01	0.66	0.17
B field(%)	0.60	0.73	0.21	1.21	0.53	0.59	0.09	0.12
Event plane(%)	0.26	1.54	0.04	1.60	0.69	1.70	1.32	1.07
Pair cut(%)	2.05	2.54	1.88	1.67	2.17	2.49	1.89	2.50
Fit range(%)	2.21	2.09	1.93	1.88	2.18	1.76	2.20	2.21
Quadratic sum (%)	3.31	3.89	3.28	3.22	3.20	3.68	3.25	3.51
centrality 40-50%								
charge(%)	0.25	1.18	1.42	0.40	0.97	0.50	0.88	1.57
B field(%)	2.05	0.96	2.38	0.98	1.78	0.40	0.97	2.00
Event plane(%)	1.33	1.79	1.84	1.84	3.30	0.98	1.89	0.75
Pair cut(%)	2.01	1.64	2.74	1.81	2.10	1.97	2.24	1.74
Fit range(%)	2.72	2.32	2.50	2.73	2.86	3.16	3.01	2.98
Quadratic sum (%)	4.18	3.69	4.98	3.90	5.25	3.90	4.40	4.35

3.7.2 Systematic Uncertainties for v_n analysis

In this analysis 6 variables are considered for the systematic uncertainties and they are listed as following.

- Effect of number of TPC clusters
- Systematic uncertainties of centrality estimator
- Various track reconstruction mode
- Effect of primary vertex position in the direction of beam axis
- Systematic uncertainties of Event Plane determination detectors
- Systematic uncertainties related to particle identification selection with TPC and TOF

Effect of number of TPC clusters

For track reconstruction of charged particles, at least 80 TPC clusters are required in this analysis. 2 different number of TPC cluster 50 (loose) and 90 (tight) selection are considered for estimation of systematic uncertainties (Total number of TPC pad rows are 159, therefore this TPC cluster selection is corresponding to 30-56% of all TPC pad rows).

Figure 3.37 are centrality dependence of charged pion, kaon and proton(anti-proton) v_2 with two different number of TPC clusters for track reconstruction.

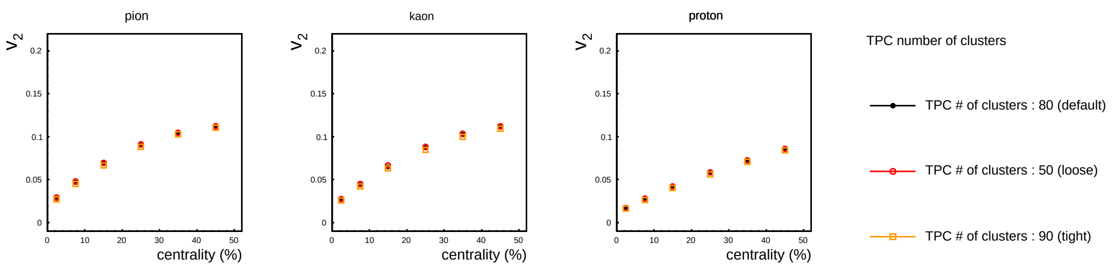

Figure 3.37: charged pion, kaon and proton(anti-proton) p_{T} integrated v_2 as a function of centrality with two different TPC number of clusters for track reconstruction. p_{T} is integrated from 0.15-1.5 GeV/$c$which is corresponding to same selection for HBT analysis.

Systematic Uncertainties of Tracking mode

In this analysis, TPC clusters and primary vertex determined with ITS are used for track reconstruction. However we have several different track reconstruction algorithms. Uncertainties originating from two different tracking modes (Global track and hybrid track). Global track and Hybrid track are defined by track reconstruction with the combination of TPC and ITS.

Figure 3.38 are azimuthal anisotropy of charged pion, kaon and proton(anti-proton) v_2 as a function of centrality with two different tracking mode using TPC and ITS combined. Compared to pions and kaons, the systematic difference of protons and anti-protons are larger especially in peripheral collisions.

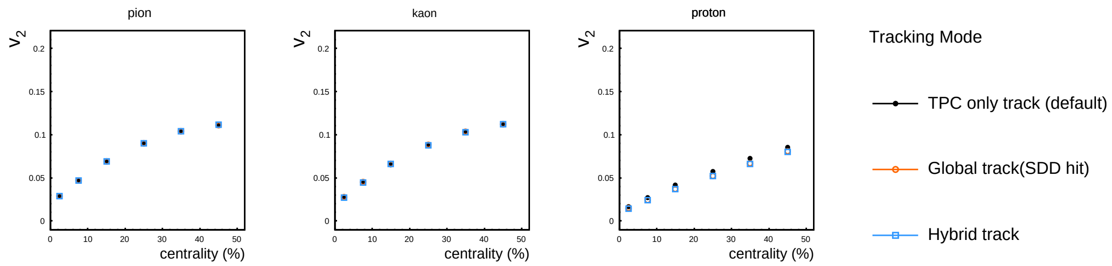

Figure 3.38: charged pion, kaon and proton(anti-proton) p_T integrated v_2 as a function of centrality with two different tracking modes using TPC and ITS. p_T is integrated from 0.15-1.5 GeV/$c$which is corresponding to same selection for HBT analysis.

Systematic Uncertainties of Centrality Estimator

The contribution from centrality estimator is estimated with changing centrality determination detector from VZERO signal to the number of clusters in SPD outer layer.

Figure 3.39 are azimuthal anisotropy of charged pion, kaon and proton(anti-proton) v_2 as a function of centrality with different centrality estimator using second layer in SPD.

Effect of primary vertex position in the direction of beam axis

Primary vertex position affects the detector acceptance in particular to the direction of beam axis. The effect of primary vertex position in the direction of beam axis($zvtx$) is studied by varying the different z-vertex selection, $|zvtx| < 5$cm (tight) and $|zvtx| < 10$cm (loose) event selection.

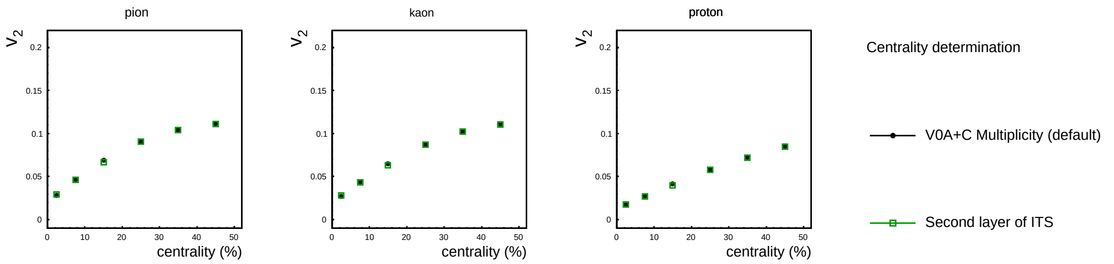

Figure 3.39: Systematic difference of centrality determination detectors V0 amplitude and number of clusters in second layer of SPD for charged pion, kaon and proton(anti-proton) p_T integrated v_2 as a function of centrality. p_T is integrated from 0.15-1.5 GeV/$c$which is corresponding to same selection for HBT analysis.

Figure 3.40 are azimuthal anisotropy of charged pion, kaon and proton(anti-proton) v_2 as a function of centrality with two different Z vertex selection (tight and loose).

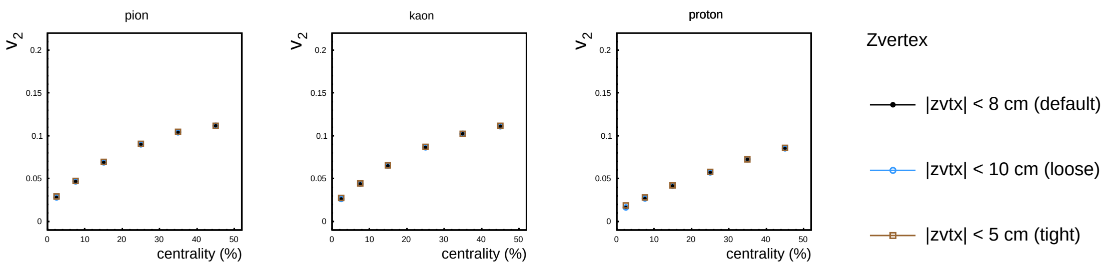

Figure 3.40: Systematic difference of primary vertex position along the beam axis tight($|zvtx|$<5cm) and loose($|zvtx|$<10cm) for charged pion, kaon and proton(anti-proton) p_T integrated v_2 as a function of centrality. p_T is integrated from 0.15-1.5 GeV/$c$which is corresponding to same selection for HBT analysis.

Systematic Uncertainties of Event Plane Determination Detector

In this thesis, azimuthal anisotropy is calculated with Event plane method and default event plane determination detector is FMD A+C combined which covers wide rapidity range with rapidity gap $|\Delta\eta| > 0.9$ between FMD and TPC. Systematic uncertainties of event plane determination detector is estimated with 7 different Event plane determination detector, V0C, V0A, V0AC, FMDC, FMDA, FMDAC, TPCC2(-1.0 < η < -0.5), TPCA2(0.5 < η < 1.0). When Event plane is determined with TPCC2(TPCA2), tracks in 0.5 < η < 1.0(-1.0 < η < -0.5) are used to calculate v_n with $|\Delta\eta| > 1.0$.

Figure 3.41 are azimuthal anisotropy of charged pion, kaon and proton(anti-proton) v_2 as a function of centrality with 7 different Event plane determination detectors.

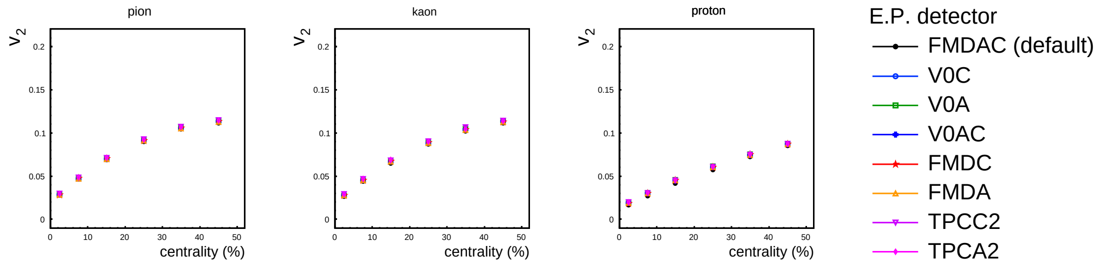

Figure 3.41: Systematic difference of Event plane determination detector for charged pion, kaon and proton(anti-proton) p_T integrated v_2 as a function of centrality. p_T is integrated from 0.15-1.5 GeV/$c$which is corresponding to same selection for HBT analysis.

Systematic Uncertainties related to particle identification selection with TPC and TOF

Charged pions, kaons and protons are identified with the probability of Bayesian approaches with TPC and TOF. Systematic uncertainties associated with particle identification is studied with changing the value of minimum probability of Bayesian approaches.

Figure 3.42 are azimuthal anisotropy of charged pion, kaon and proton(anti-proton) v_2 as a function of centrality. In this study, two different PID selection are estimated with minimum probability of Bayesian approaches 75%(loose) and 90%(tight).

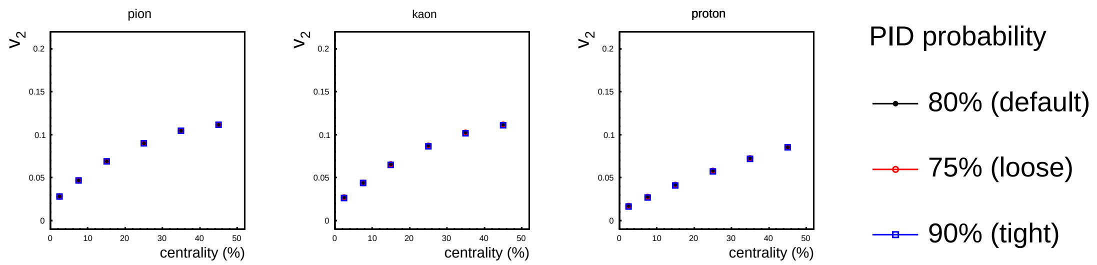

Figure 3.42: Systematic difference of probability of Bayesian approaches 75% loose cut (red open circle) and tight (blue open square) for charged pion, kaon and proton(anti-proton) p_T integrated v_2 as a function of centrality. p_T is integrated from 0.15-1.5 GeV/$c$which is corresponding to same selection for HBT analysis.

Table 3.8: Systematic table for the identified charged hadron v_2 as a function of centrality

π^+ and π^-						
centrality(%)	0-5	5-10	10-20	20-30	30-40	40-50
TPC ncls	3.99	3.23	2.36	1.68	1.23	0.95
Centrality estimator	3.99	0.84	3.25	0.16	0.25	0.43
Tracking Mode	0.99	0.56	0.09	0.28	0.35	0.44
Primary vertex position	2.79	0.92	0.40	0.25	0.15	0.15
Event plane detector	2.99	2.37	2.34	1.80	1.84	1.83
PID selection	0.21	0.16	0.08	0.03	0.02	0.04
Quadratic sum	7.04	4.24	4.66	2.50	2.26	2.17
K^+ and K^-						
TPC ncls	4.20	3.55	2.75	2.17	1.68	1.40
Centrality estimator	4.59	1.05	3.42	0.01	0.14	0.58
Tracking Mode	2.30	2.03	1.50	1.19	0.80	0.56
Primary vertex position	2.78	0.82	0.31	0.21	0.07	0.10
Event plane detector	5.13	4.19	3.80	2.73	2.42	2.01
PID selection	0.63	0.60	0.41	0.30	0.24	0.20
Quadratic sum	8.86	6.04	6.02	3.70	3.07	2.59
p and $\bar{p}$						
TPC ncls	2.93	2.71	2.19	1.69	1.35	1.12
Centrality estimator	6.25	1.17	4.51	0.13	0.23	0.92
Tracking Mode	12.57	11.21	10.70	9.45	8.10	6.26
Primary vertex position	7.44	2.41	1.06	0.42	0.47	0.46
Event plane detector	13.79	11.27	9.19	5.22	3.81	1.84
PID selection	1.96	1.57	1.05	0.59	0.29	0.17
Quadratic sum	21.33	16.42	15.04	10.95	9.07	6.71

Chapter 4

Results

In this chapter, the results of extracted 3D HBT radii for charged pions as a function of azimuthal pair angle with respect to 2$^{\text{nd}}$-order and 3$^{\text{rd}}$-order event plane measured in Pb-Pb collisions at $\sqrt{s_{\text{NN}}}$ = 2.76 TeV are presented. We also report on the results obtained with the Event Shape Engineering technique (q_2 and q_3 cut) applied to azimuthal anisotropy v_2 and v_3 and azimuthal angle dependence of HBT radii with respect to 2$^{\text{nd}}$-order and 3$^{\text{rd}}$-order event plane which is sensitive to source shape at freeze-out.

4.1 Azimuthal angle dependence of HBT radii with respect to Ψ_2

4.1.1 1D projection of 3D Correlation functions

Azimuthal pair angle of pions with respect to 2$^{\text{nd}}$-order event plane is divided into 8 bins. Each azimuthal angle bin width is $\pi/8(rad)$.

Figure 4.1 shows correlation functions of charged pions measured in $0.2 < k_T < 1.5$ GeV/c for two azimuthal bins ($|\varphi_{pair} - \Psi_2| < \pi/16$ and $7\pi/16 < |\varphi_{pair} - \Psi_2| < \pi/2$) corresponding to in-plane and out-plane directions of Ψ_2 angle, respectively) in centrality 0-50% after the bin-by-bin correction on the event plane resolution. Three-dimensional correlation functions are projected along to each axis (out, side, long). When making the projection of the 3D correlation function to a specific q direction, the projections over the other q components was performed within 50 GeV/c for each numerator and denominator in Eq. 3.65. Left columns show the C_2 projected into the outward direction, middle columns for the sideward direction, and right columns for the longitudinal direction. Top to bottom panels are corresponding to the projected correlation function in central (0-5%) to peripheral (40-50%) collisions. Black and red solid lines represent fit functions to the projected correlation functions measured in in-plane and out-plane directions.

The 3D fitting to correlation function for all centrality and both azimuthal angle are well succeeded (chi^2/NDF is smaller than 1.0). For longitudinal axis, correlation functions at in-plane and out-plane directions are almost same in all centrality. In most central collisions 0-5% and 5-10%, there is no significant difference between correlation function measured in in-plane and out-plane of Ψ_2 directions. On the other hand, difference of correlation functions between in-plane and out-plane grows from central to peripheral collisions. Width of correlation function for outward in in-plane is explicitly larger than that in out-plane in centrality 30-40%. In addition to that, this behaviour is opposite in sideward. Width of correlation function indicates extracted HBT radii. Therefore, the significant difference of HBT radii in outward and sideward can be seen and becomes larger in particular at peripheral collisions.

This difference of source size is discussed in detail with centrality dependence of extracted HBT radii with respect to Ψ_2 in the next section.

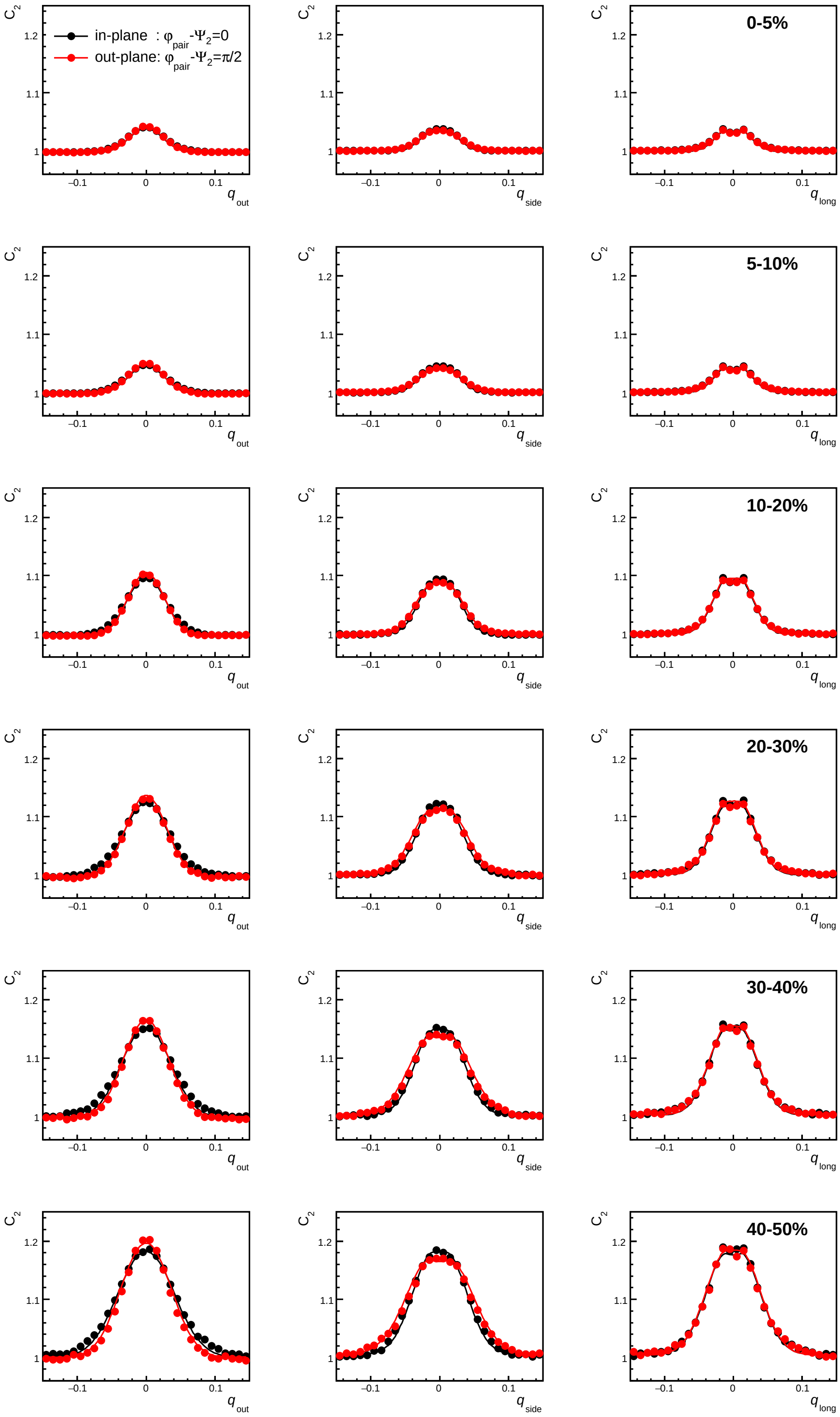

Figure 4.1: Projection of 3D correlation function to 1D (outward, sideward, and longitudinal axis) of charged pions in $0.2 < k_T < 1.5$ GeV/c for two azimuthal bins ($|\varphi_{pair} - \Psi_2| < \pi/16$ (Black marker) and $7\pi/16 < |\varphi_{pair} - \Psi_2| < \pi/2$ (Red marker)) at centrality 0-50%. The projection range of other q components are within 50 GeV/c . Solid lines denote the fitting function of 3D correlation function.

4.1.2 Centrality dependence of HBT radii with respect to Ψ_2

Figure 4.2 shows the extracted 3D HBT radii for charged pions as a function of azimuthal pair angle with respect to 2nd-order event plane Ψ_2 for 6 different centralities. Data points at $\varphi_{pair} - \Psi_2 = \pi$ is same value to those at $\varphi_{pair} - \Psi_2 = 0$ for symmetry with respect to the event plane. Charged pions for HBT analysis is measured in mid rapidity ($|\eta| < 0.8$) and event plane Ψ_2 is determined via FMD A+C combined at forward rapidity ($1.7 < \eta < 5.0$ and $-3.4 < \eta < -1.7$). Smeared oscillation of HBT radii due to finite event plane resolution is corrected with model independent bin-by-bin event plane resolution correction [63]. Systematic uncertainties are plotted as transparent band and statistical uncertainties are smaller than marker size.

For boost-invariant system, the azimuthal angle dependence of HBT radii should be described with cosine and sine series functions [63].

$$R^2_{\mu}(\Delta\phi) = R^2_{\mu,0} + 2\sum_n R^2_{\mu,n}(\Delta\phi)\cos(n\Delta\phi), \tag{4.1}$$

$$R^2_{os}(\Delta\phi) = 2\sum_n R^2_{os,n}(\Delta\phi)\sin(n\Delta\phi), \tag{4.2}$$

where $R^2_{\mu,n}$ is the n^{th}-order Fourier coefficients, μ is each direction in the Bertsch-Pratt parametrization (μ = out, side and long). $\Delta\phi = \varphi - \Psi_n$. In this thesis, the summation over n takes $n = 2$ for the case of 2nd-order event plane dependence. The parameter $R^2_{\mu,0}$ indicates the average of squared HBT radii, while $R^2_{\mu,2}$ represents the oscillation of azimuthal angle dependence of HBT radii. Azimuthal angle dependence of HBT radii are fitted with Eq.4.1. To extract the parameters, the azimuthal angle dependence of HBT radii shown in Fig. 4.2 are fitted with Eq. 4.2, 4.2.

As can be seen in Fig. 4.2, $R_{\rm out}$ and $R_{\rm side}$ have the explicit oscillations with respect to Ψ_2 and the oscillations in outward are out of phase with the one in sideward by $\pi/2$ radian. Compared to the oscillation amplitude of $R_{\rm out}$, $R_{\rm side}$ oscillation amplitude is much smaller for all centralities. The out-side cross term $R_{\rm os}$ shows sine oscillation and its oscillation amplitude grows from central to peripheral collisions. The average HBT radii become smaller from central to peripheral collisions due to the geometry of initial overlap region. Contrary to average HBT radii, oscillation amplitude of $R_{\rm out}$ and $R_{\rm side}$ increase from central to peripheral collisions. λ, $R_{\rm long}$, $R_{\rm ol}$, and $R_{\rm sl}$ have no significant oscillation.

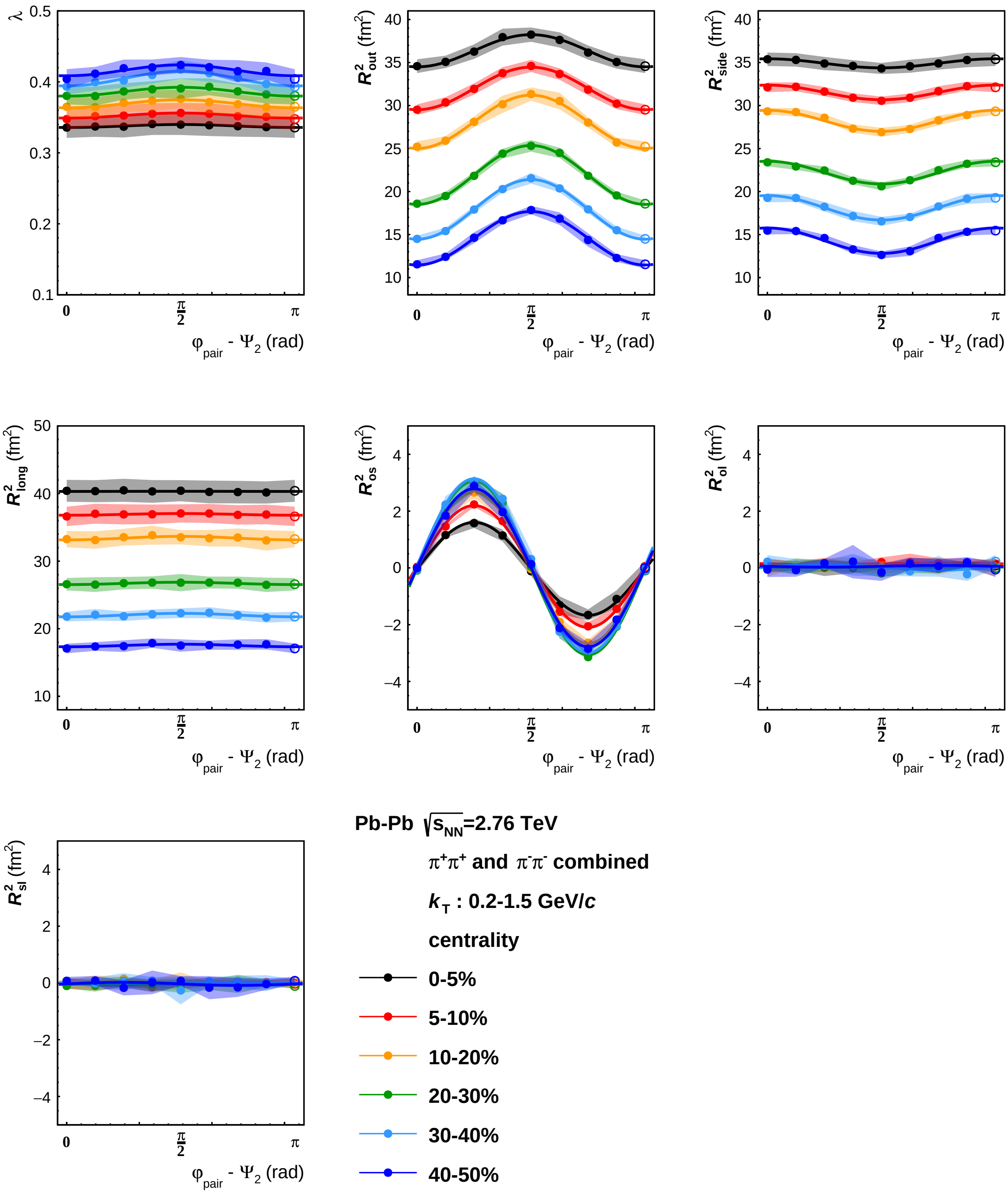

Figure 4.2: Extracted HBT parameters (R_{out}, R_{side}, R_{long} λ, R_{os}, R_{ol}, and R_{sl}) of charged pions in $0.2 < k_T < 1.5$ GeV/c as a function of azimuthal pair angle with respect to 2$^{\text{nd}}$-order event plane for 6 different centrality bins. The data points at $\varphi_{pair} - \Psi_2 = \pi$ are same value at $\varphi_{pair} - \Psi_2 = 0$. Systematic uncertainties are shown with transparent bands.

4.2 Azimuthal anisotropy of charged hadrons

In this section, at first, event shape engineering technique is applied to azimuthal anisotropy measurements which is sensitive to initial geometry.

4.2.1 Second order azimuthal anisotropy and Event Shape Engineering (q_2) selection

Event shape engineering technique is the selection of event-by-event flow amplitude with the magnitude of flow vector q_n described in Eq. 3.49 [15]. Based on the model simulation, it could be one of the methods to select initial source shape [16]. Since ESE is the selection of event-by event flow amplitude, large or small q_2 selection should affect to azimuthal anisotropy of momentum space, and measured v_2 should become large (small) with large (small) q_2 selection

Figure 4.3 shows charged pions, charged kaons, proton (anti-proton) and charged particle v_2 measured with event plane method as a function of centrality with each 20% q_2 selection. Both event plane and q_2 vector are determined via FMD A+Ci and rapidity gap between flow measurement and event plane determination is $|\Delta\eta| > 0.9$. Transverse momentum (p_T) is integrated from 0.15-1.5GeV/c which is corresponding to same p_T range to HBT measurements.

For three particle species, larger (smaller) azimuthal anisotropy v_2 can be selected with ESE selection. Unbiased v_2 is comparable to v_2 with 40-60% q_2 selection. Difference between ESE selected v_2 and unbiased v_2 increases from central to peripheral collisions.

In order to qualitatively estimate the ESE effect, the ratio of v_2 with and without q_2 selection is calculated as shown in Fig. 4.4. For all three particle species, azimuthal anisotropy v_2 is enhanced (suppressed) with q_2 selection. One can find that v_2 ratio does not show significant centrality dependence. However, in most central collisions 0-5%, the effect of ESE selection is smaller than that in the other centrality classes. This behaviour is consistent to previous results [19], and it could be due to smaller v_2 signal and Ψ_2 resolution in most central collisions. By applying q_2 selection, azimuthal anisotropy v_2 is enhanced by 26% for q_2:80-100%, 8% for q_2:60-80%, and suppressed by 3% for q_2:40-60%, 14% for q_2:20-40%, and 26% for q_2:0-20%.

Figure 4.5, 4.6 and 4.7 shows p_T dependence of charged pions, charged kaons and protons (anti-protons) as a function of centrality(0-50%). Each 20% q_2 selection is applied to flow measurements up to p_T 4GeV/c. As is the case of p_T integrated v_2 measurements (Fig. **??**), ESE q_2 selection effect (enhancement and suppression) of v_2 can be found for all three particle species. Difference of v_2 with and without q_2 selection can be seen up to p_T 4 GeV/c, and it depends on the value of v_2.

Transeverse momentum dependence of the ratio of q_2 selected to no q_2 selected v_2 are shown in Fig. 4.8, 4.9 and 4.10. Effect of q_2 selection does not have explicit p_T dependence for pions, kaons, and protons. However, in the largest q_2 class at centrality 5-40%, the ratio of v_2 with and without q_2 selection slightly decreases with increasing p_T, and this behaviour is also found for the v_2 ratio in the smallest q_2. But p_T dependence of v_2 ratio is opposite to the one in the largest q_2 selection. The ratio of v_2 in the smallest q_2 selection becomes larger from low p_T to high p_T). This small p_T dependence might be interpreted that anisotropic flow mostly originates from low momentum particles and also indicates that the magnitude of q_2 vector is a global property of the event which is not biased by jet.

Figure 4.11 denotes the comparison of the v_2 ratios with and without q_2 selection amang three particle species in centrality 0-50%. In all centrality and all q_2 classes, the enhancement and suppression with q_2 selection does not depends on the particle species.

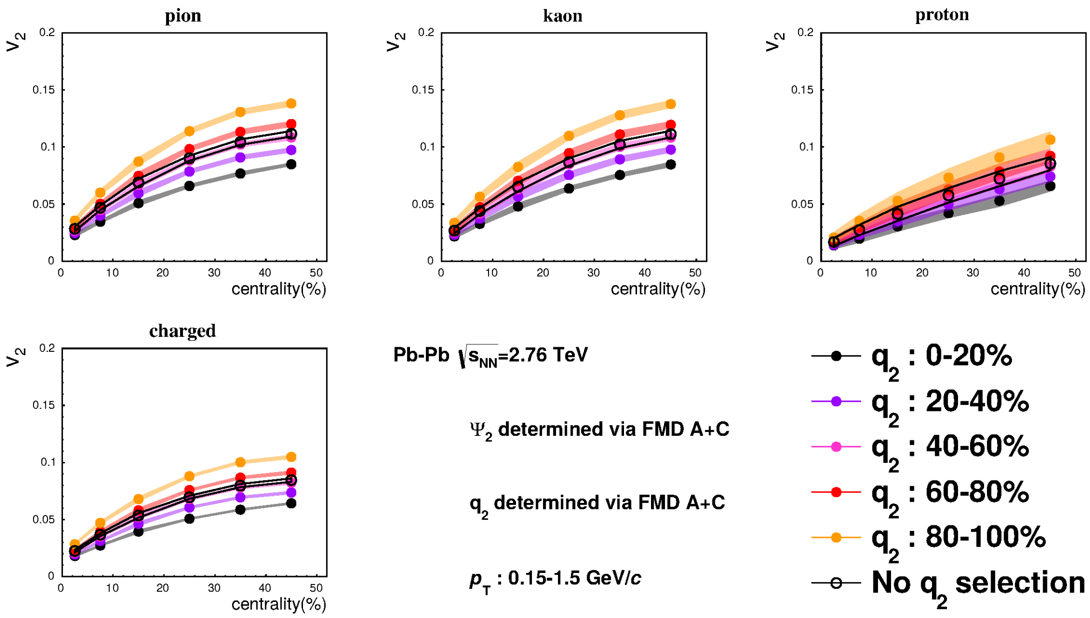

Figure 4.3: Charged hadron and identified hadron (π, K and p) p_T integrated v_2 as a function of centrality. Both Ψ_2 and q_2 are determined via FMD A+C and p_T are integrated from 0.15 to 1.5GeV/c. Each 20% ESE q_2 selection is applied to flow measurements(closed markers). Open black markers denote no ESE selected v_2. Systematic uncertainties are depicted as transparent bands.

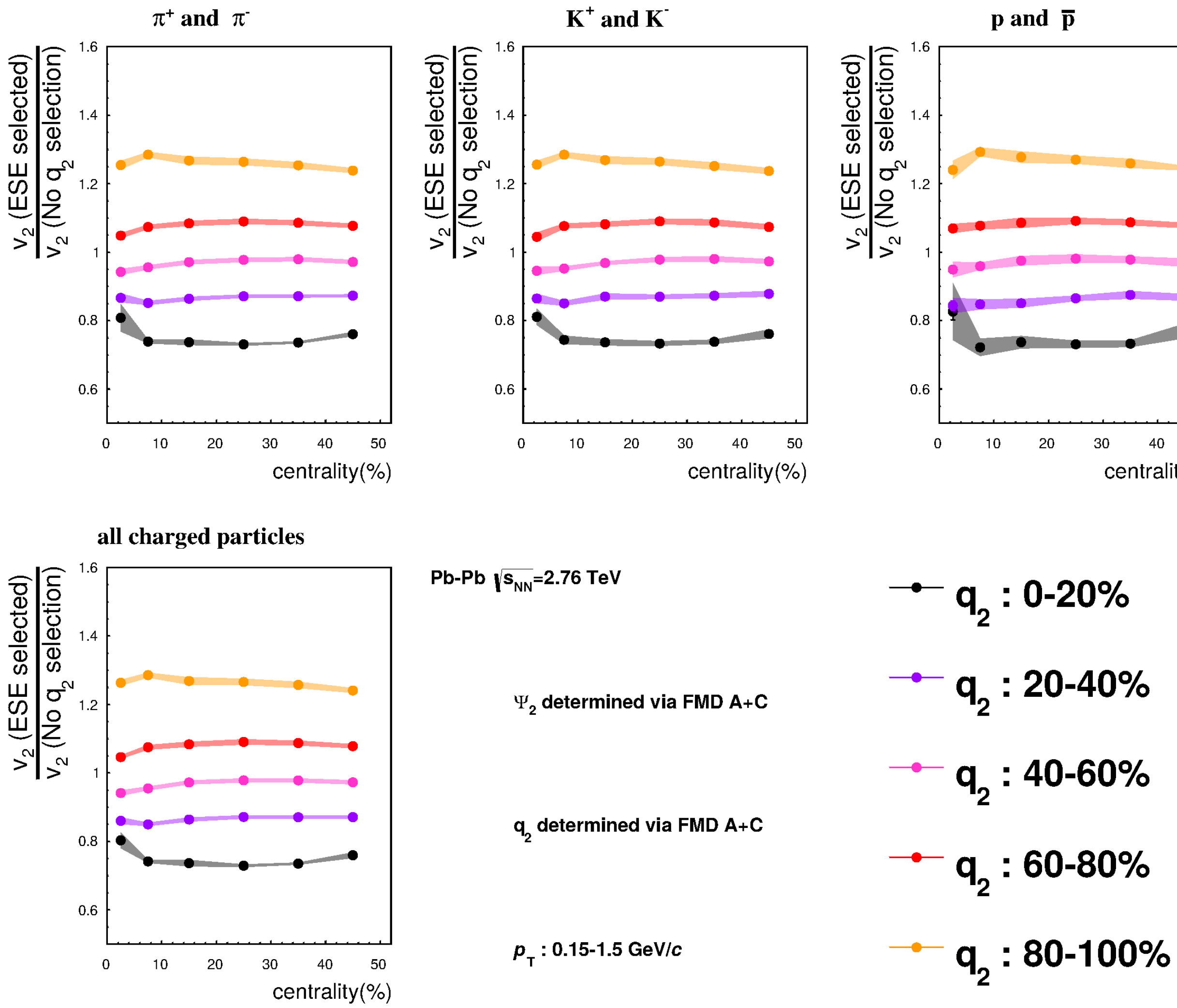

Figure 4.4: Ratio of v_2 with each 20% q_2 selection to without q_2 selection (unbiased sample) for unidentified and identified charged hadrons (π, K and p). Both Ψ_2 and q_2 vector are determined via FMD A+C and p_{T} are integrated from 0.15 to 1.5GeV/c. Systematic uncertainties are depicted as transparent bands.

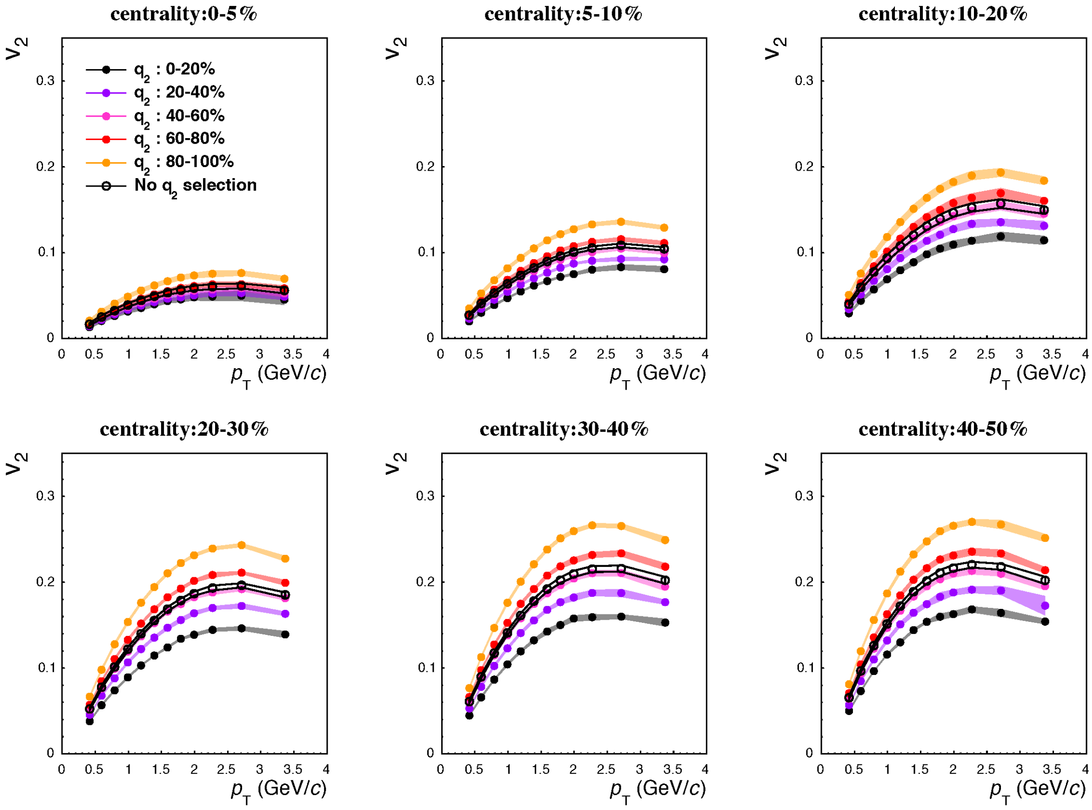

Figure 4.5: Measurement of charged pion v_2 as a function of p_T for 6 centrality classes with each 20% q_2 selection and no q_2 selected samples. Systematic uncertainties are plotted as transparent bands.

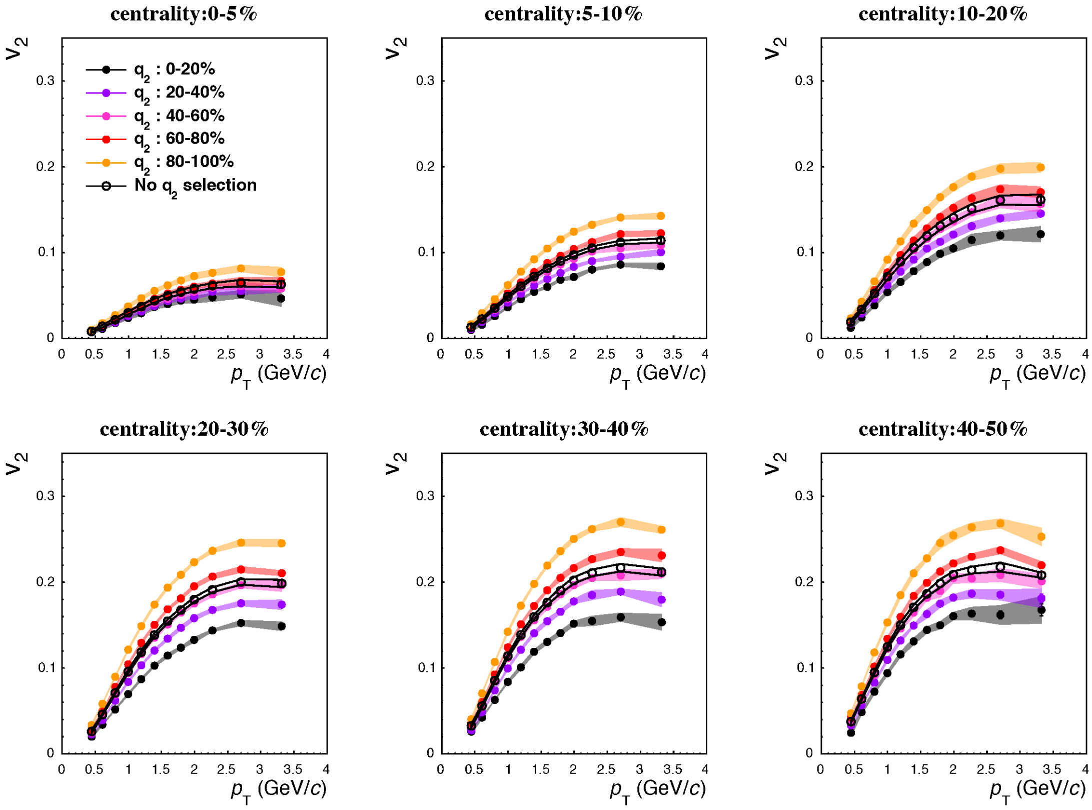

Figure 4.6: Measurement of charged kaon v_2 as a function of p_T for 6 centrality classes with each 20% q_2 selection and no q_2 selected samples. Systematic uncertainties are plotted as transparent bands.

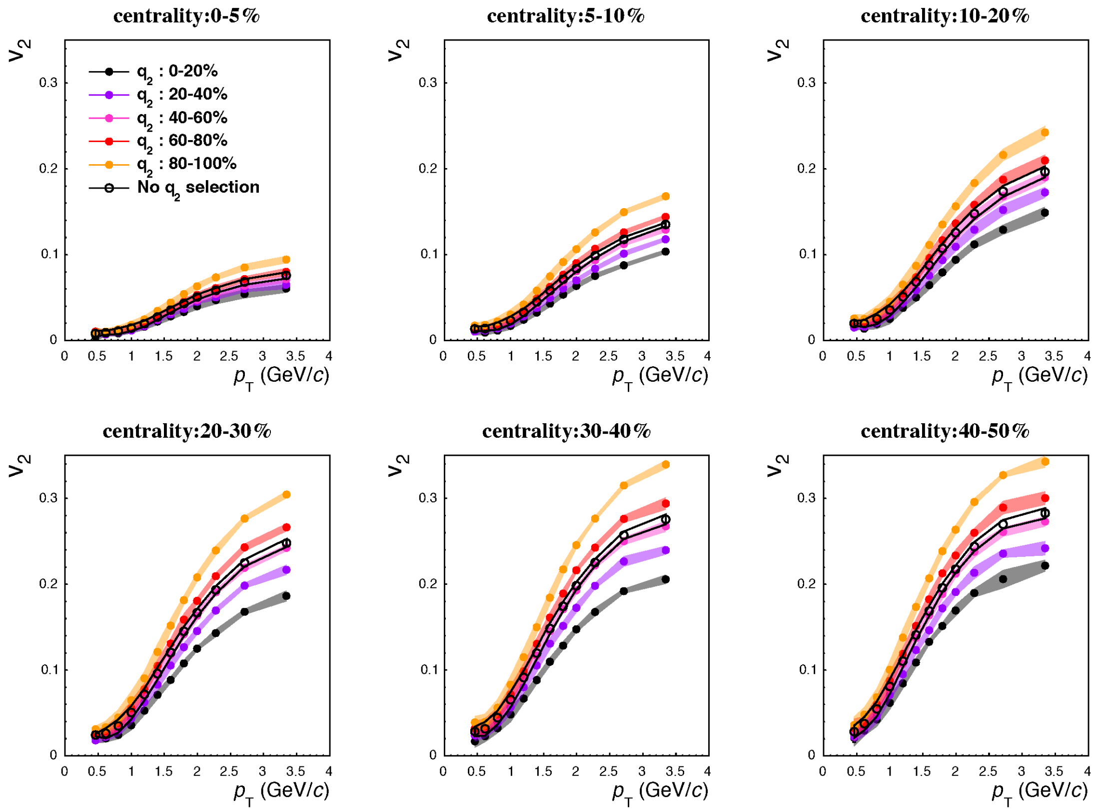

Figure 4.7: Measurement of protons and anti-protons v_2 as a function of p_T for 6 centrality classes with each 20% q_2 selection and no q_2 selected samples. Systematic uncertainties are plotted as transparent bands.

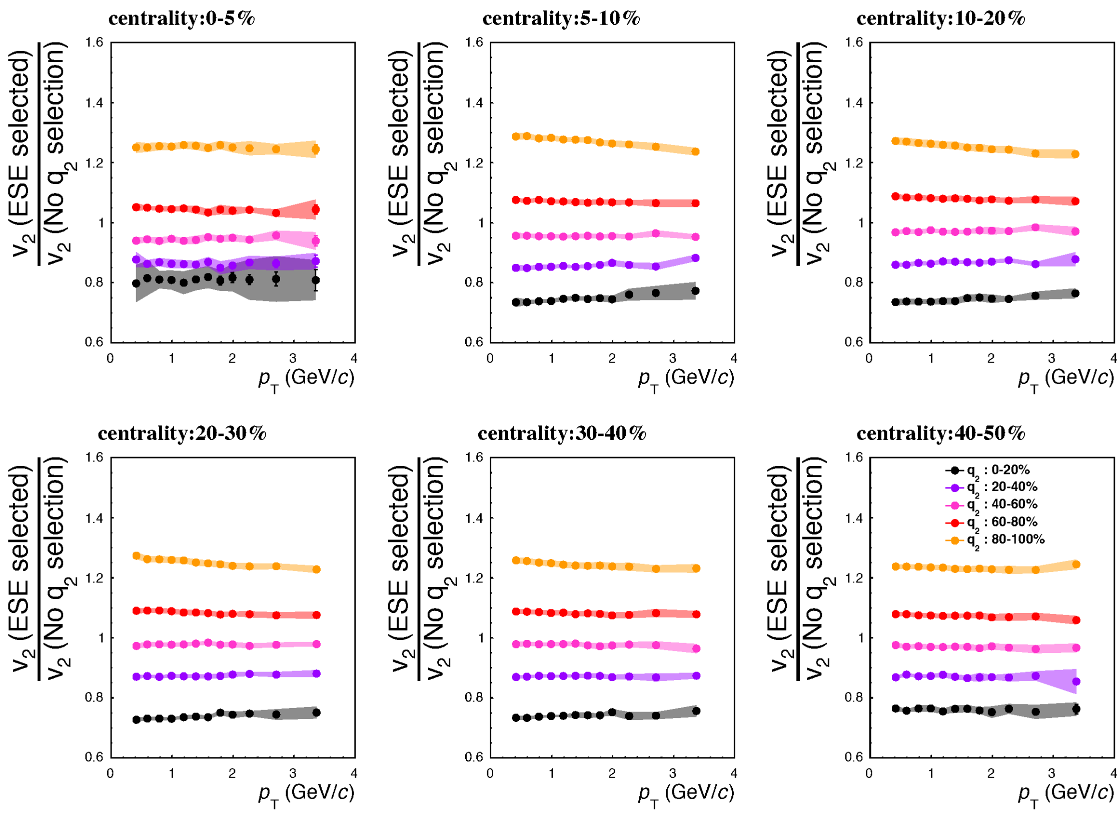

Figure 4.8: Ratio of v_2 with each 20% q_2 selection to without q_2 selection (unbiased sample) for charged pions.

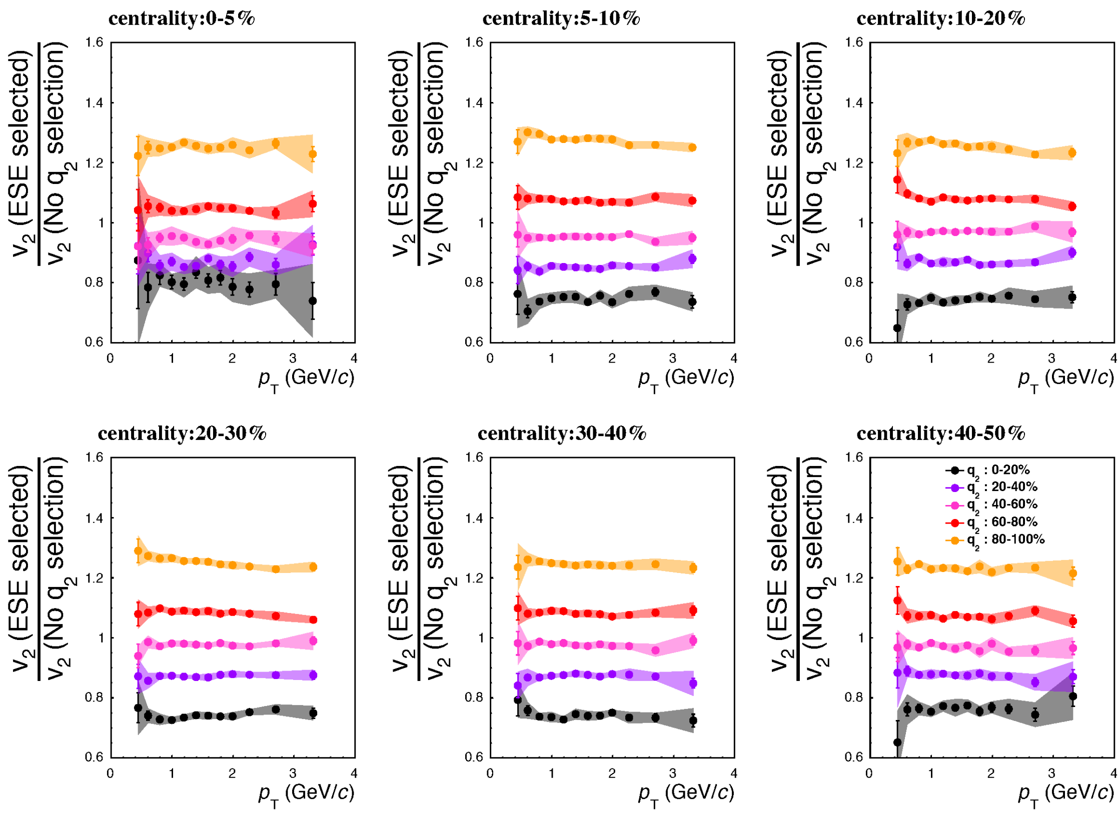

Figure 4.9: Ratio of v_2 with each 20% q_2 selection to without q_2 selection (unbiased sample) for charged kaons.

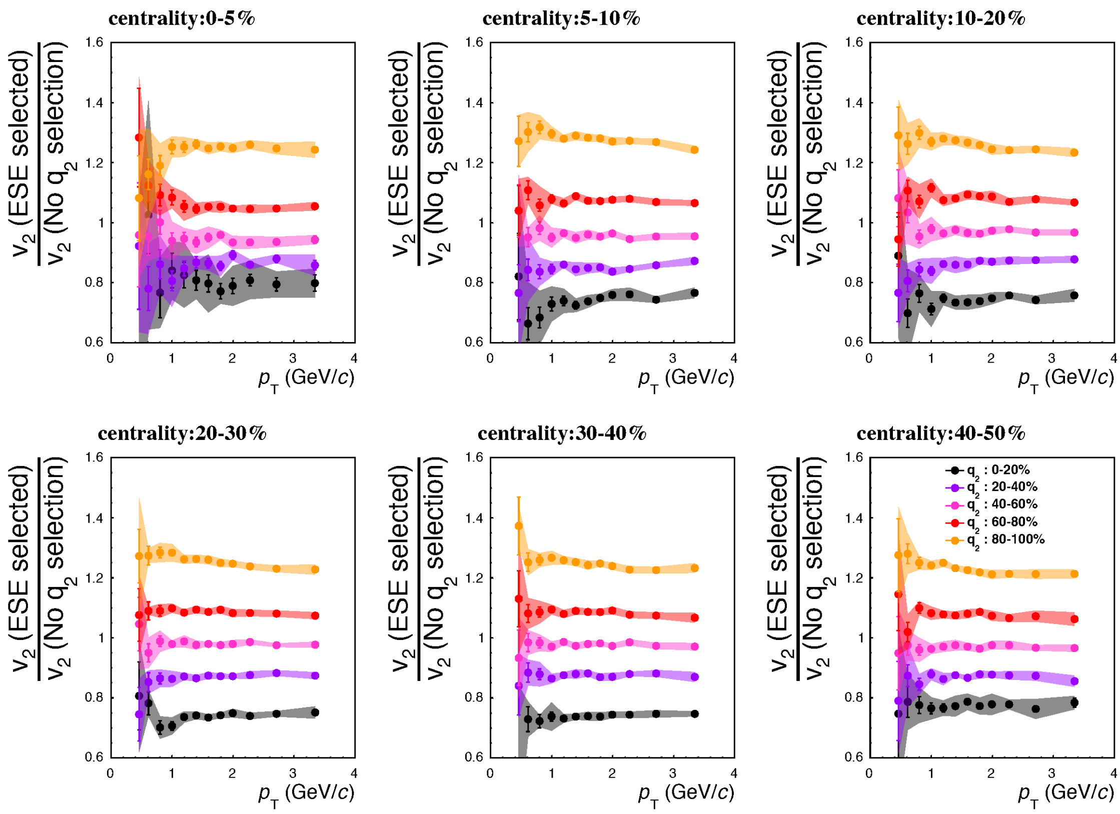

Figure 4.10: Ratio of v_2 with each 20% q_2 selection to without q_2 selection (unbiased sample) for protons.

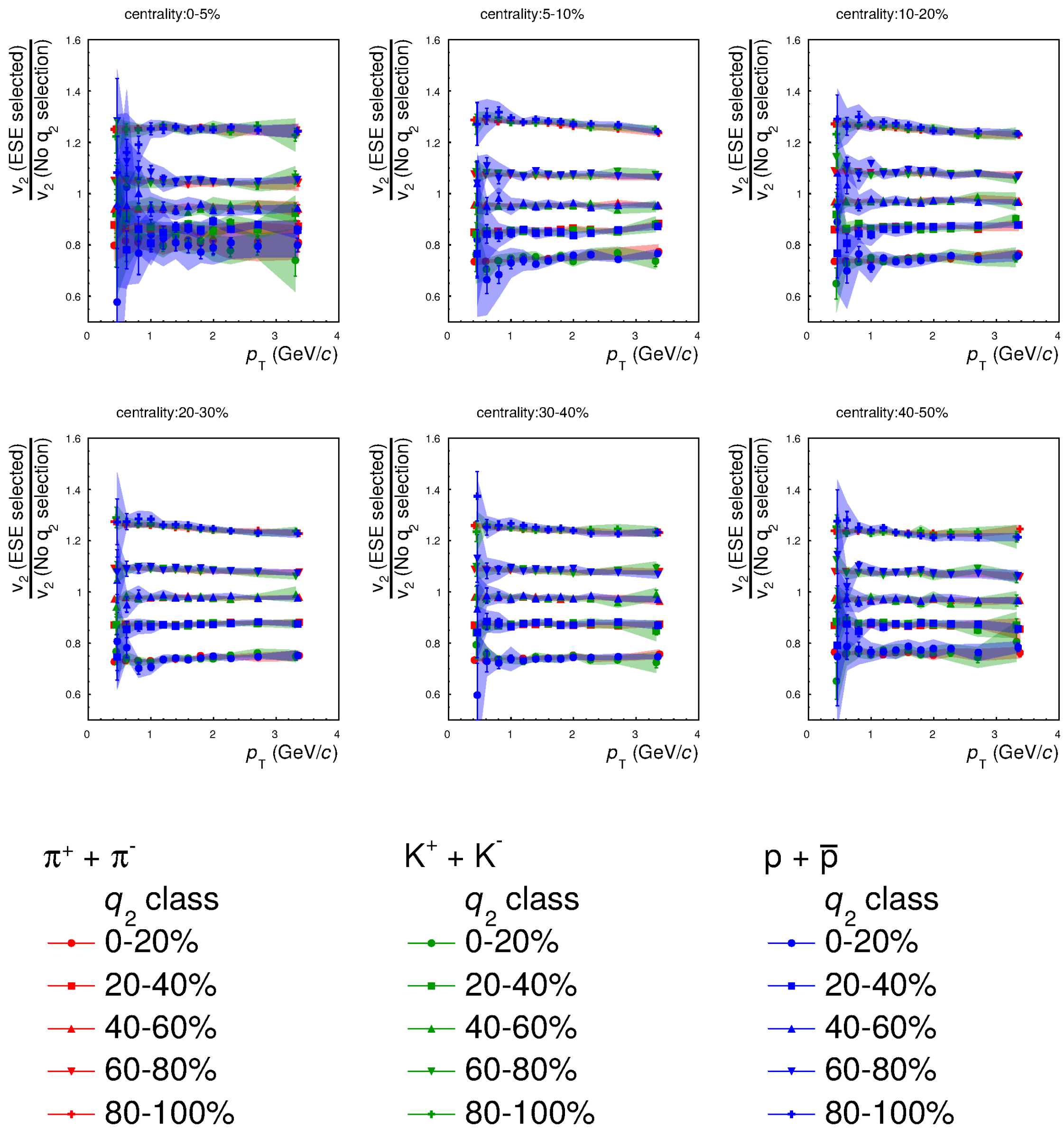

Figure 4.11: Transverse momentum dependence of v_2 ratio with each 20% q_2 selection to without q_2 selection (unbiased sample) for unidentified and identified charged hadrons (π, K and p) for 6 centrality bins.

4.2.2 Third-order azimuthal anisotropy and Event Shape Engineering (q_3) selection

If higher-order azimuthal anisotropy (such as v_3, v_4 and so on) originates from the initial density fluctuations and subsequent hydrodynamical evolution, Event Shape Engineering technique applied to the higher-orders to possibly study a response of such initial density fluctuations to the hydrodynamic evolution and an effect to final state spatial anisotropies. In this thesis, we study a sensitivity of 3$^{\mathrm{rd}}$-order azimuthal anisotropy v_3 to q_3.

Figure 4.12 shows v_3 of charged pions, charged kaons, proton(anti-proton) and charged particle which are measured with event plane method as a function of centrality with each 20% q_3 selection. In the same way to q_2 study, event plane and q_3 vector are determined via FMD A+C and a gap of pseudorapidity for v_3 measurements and event plane reconstruction is $|\Delta\eta|$ > 0.9. Transverse momentum is integrated from 0.15-1.5 GeV/c which is the same p_{T} range as that for HBT measurements.

For charged pions, charged kaons, and protons (anti-protons), v_3 is enhanced (suppressed) by q_3 selection. Triangular flow v_3 without q_3 selection is comparable to the one with 60-80% q_3 selection. Contrary to q_2 selection to v_2, the difference of v_3 with and without q_3 selection seems to slightly depend on centrality.

For the qualitative estimation of ESE effect, ratio of v_3 with q_3 selection to the one without q_3 selection is shown in Fig. 4.13. In top 20 % q_3 selection, v_3 ratio explicitly depends on centrality. The ratio of v_3 is enhanced 20% in most central collisions (0-5%) , but it decreases down to 9% in peripheral collisions (40-50%). On the other hand, no significant centrality dependence can be seen in the ratio of v_3 for the other q_3 classes.

Basically, selectivity of large (small) q_3 selection depends on the Ψ_3 resolution and Ψ_3 resolution is worse than Ψ_2 resolution and it decreases from central to peripheral collisions, this centrality dependence in the q_3 selection could be explained by the worse Ψ_3 resolution. However not only Ψ_3 resolution but also Ψ_3 resolution depends on centrality. Therefore, if the correlation of event plane resolution and ESE selectivity is linear, centrality dependence should be also seen in the ratio of v_2. it might be explained by the correlation of event plane resolution and ESE selectivity is "non-linear" and selectivity rapidly decreases in smaller event plane resolution.

Figure 4.13 is fitted with 0^{th}-order polynomial function to extract the value of enhancement (suppression) of v_3 ratio. The ratio of v_3 is enhanced by 2% for q_3:60-80% and suppressed by 5% for q_3:40-60%, 10% for q_3:20-40%, and 13% for q_3:0-20%.

Figure 4.14, 4.15, and 4.16 shows p_T dependence of charged pions, charged kaons, and protons (anti-protons) for 6 different centrality bins. Each 20% q_3 selection is applied to v_3 measurements up to p_T 4GeV/c. The enhancement (suppression) can be found for π^+ (π^-), K^+ (K^-), and p ($\bar{p}$). The defference of the v_3 ratio with and without q_3 selection depends on v_3 signal size.

Transverse momentum dependence of the ratios of v_3 with and without q_3 selection are shown in Fig. 4.17, 4.18, and 4.19. Similarly to v_2 ratio, no significant p_T dependence can be seen in v_3 ratio with and without q_3 selection.

Figure 4.20 shows the comparison of v_3 ratio of charged pions, kaons, and protons (anti-protons) for 6 different centrality bins and two q_3 classes (60-80% and 80-100%). As well as q_2 selection, an effect of q_3 selection to v_3 does not depend on the particle species.

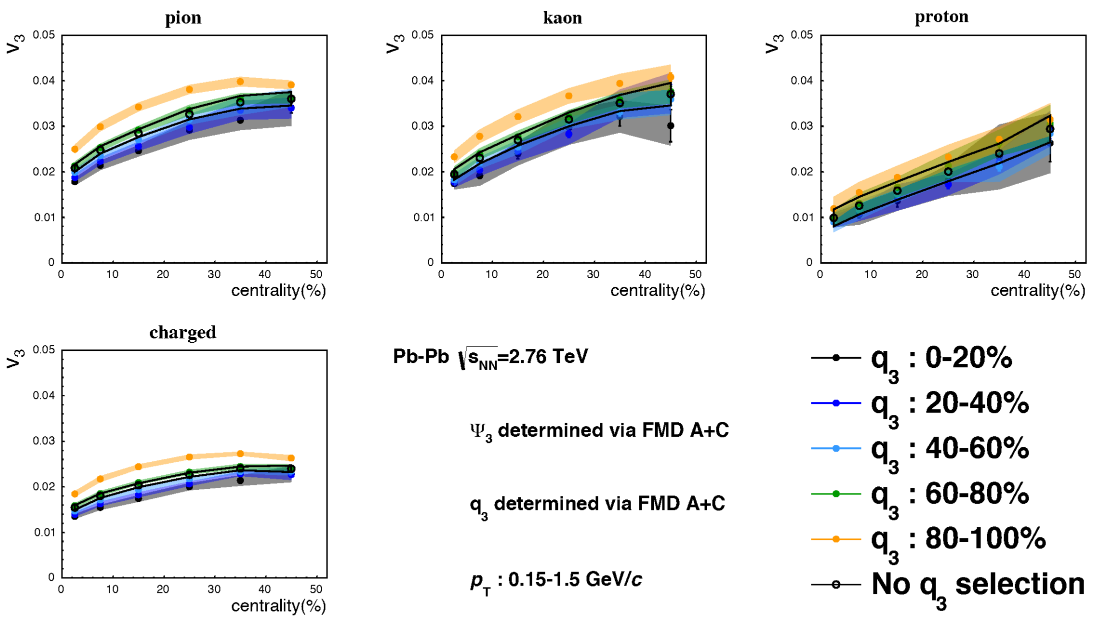

Figure 4.12: Centrality dependence of v_3 for unidentified and identified charged hadrons (π, K and p) with and without q_3 selection. Results for each 20% q_3 selection are shown and p_T are integrated from 0.15 to 1.5. Systematic uncertainties are plotted as transparent bands.

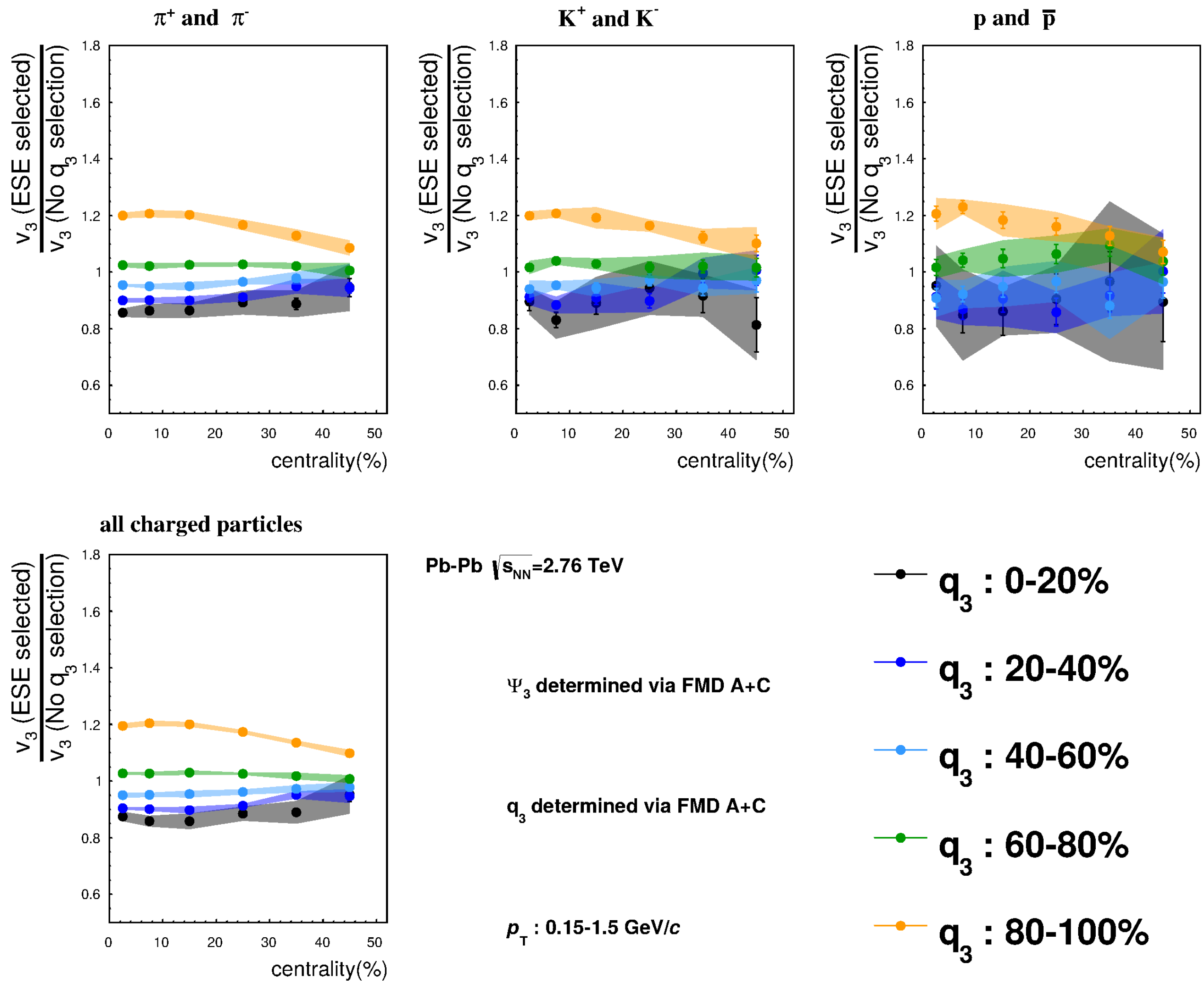

Figure 4.13: Ratio of v_3 with each 20% q_3 selection to without q_3 selection (unbiased sample) for unidentified and identified charged hadrons (π, K and p). Both Ψ_3 and q_3 vector are determined via FMD A+C and p_T are integrated from 0.15 to 1.5GeV/c. Systematic uncertainties are depicted as transparent bands.

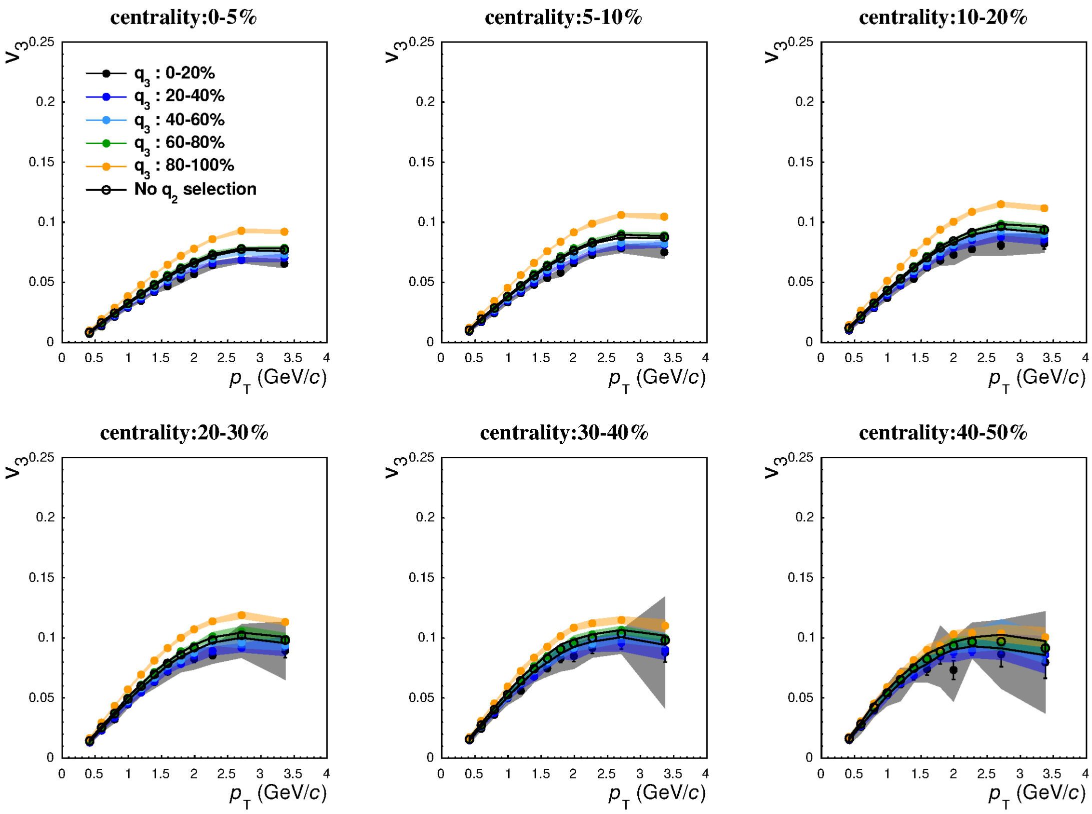

Figure 4.14: Measurement of charged pion v_3 as a function of p_T for 6 centrality classes with each 20% q_3 selection and no q_3 selected samples. Systematic uncertainties are plotted as transparent bands.

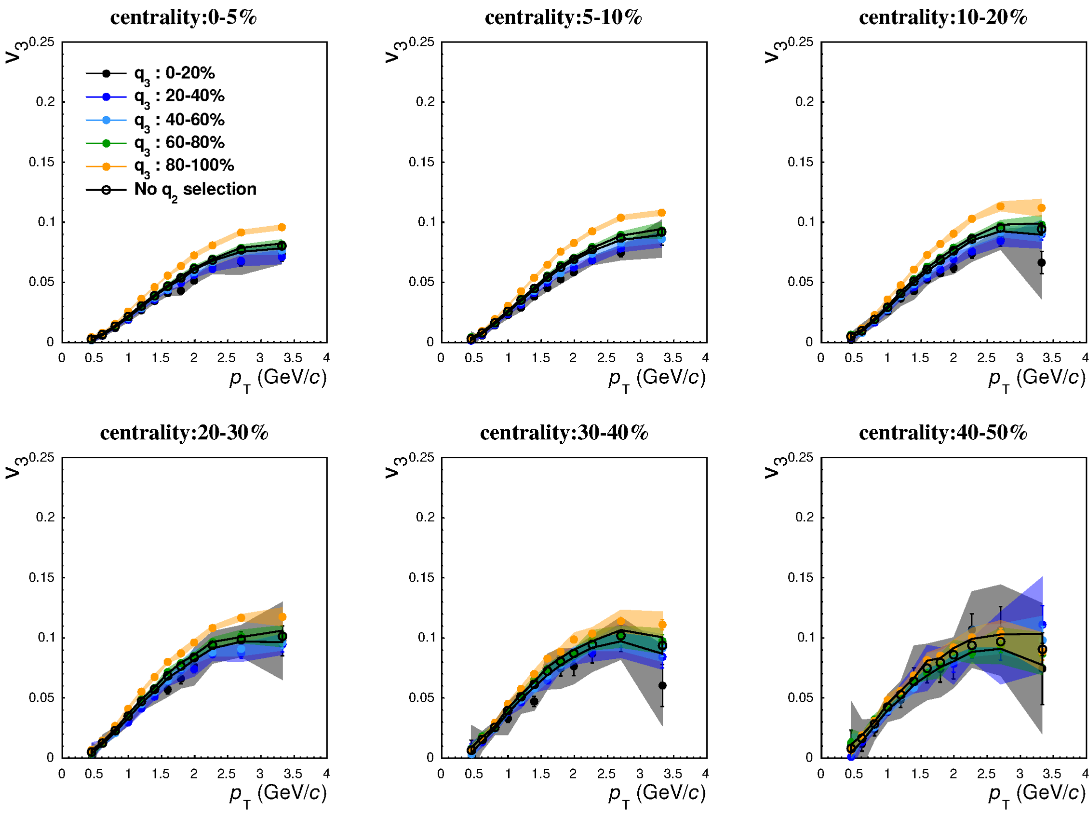

Figure 4.15: Measurement of charged kaon v_3 as a function of p_T for 6 centrality classes with each 20% q_3 selection and no q_3 selected samples. Systematic uncertainties are plotted as transparent bands.

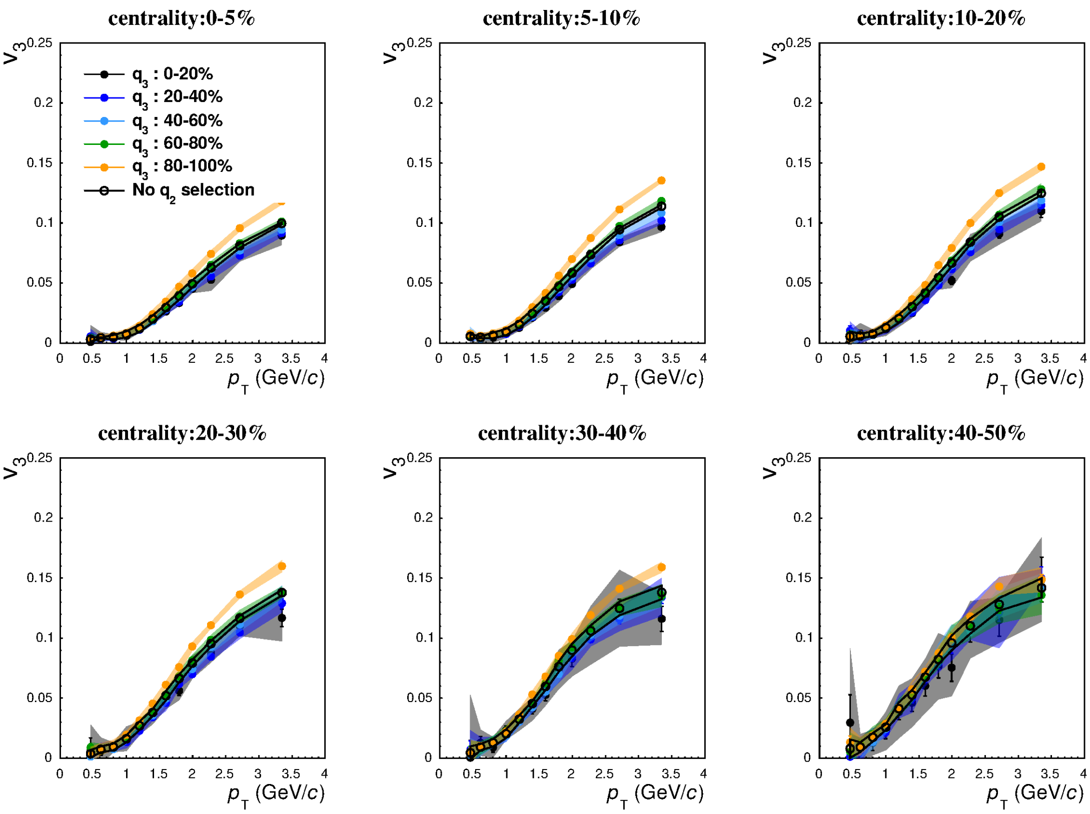

Figure 4.16: Measurement of protons and anti-protons v_3 as a function of p_T for 6 centrality classes with each 20% q_3 selection and no q_3 selected samples. Systematic uncertainties are plotted as transparent bands.

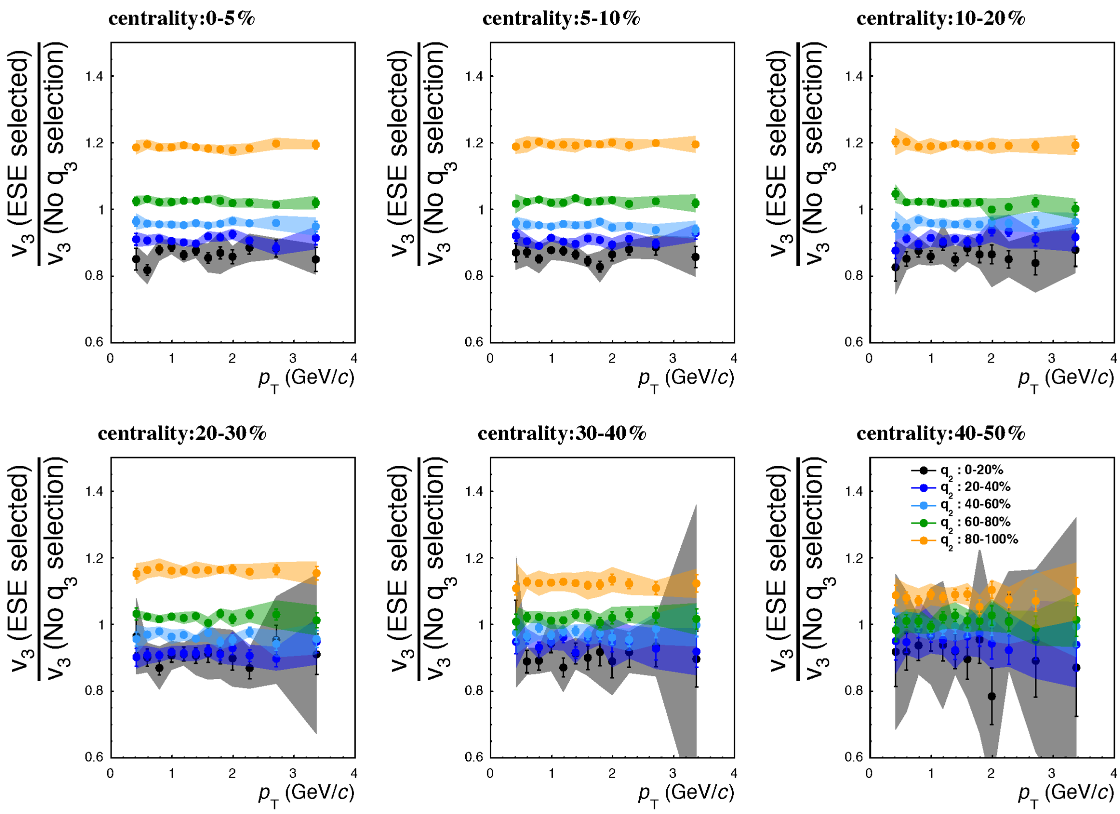

Figure 4.17: Ratio of v_3 with each 20% q_3 selection to without q_3 selection (unbiased sample) for charged pions.

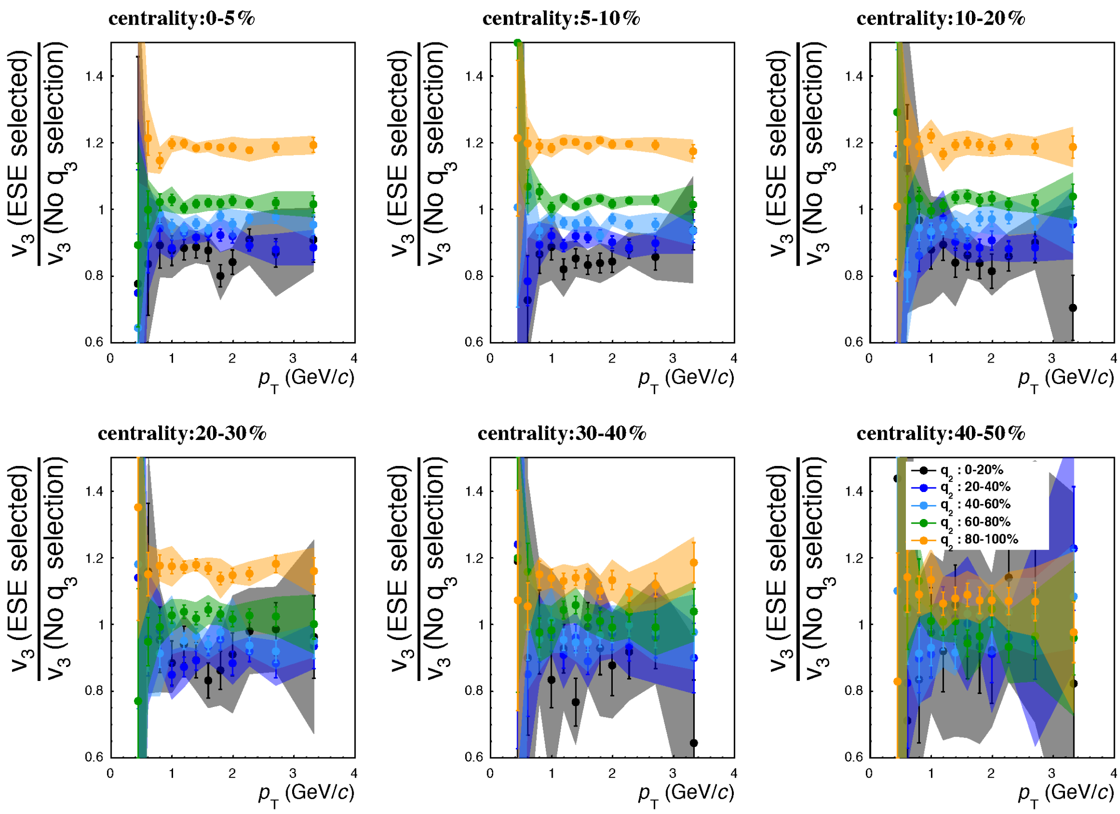

Figure 4.18: Ratio of v_3 with each 20% q_3 selection to without q_3 selection (unbiased sample) for charged kaons.

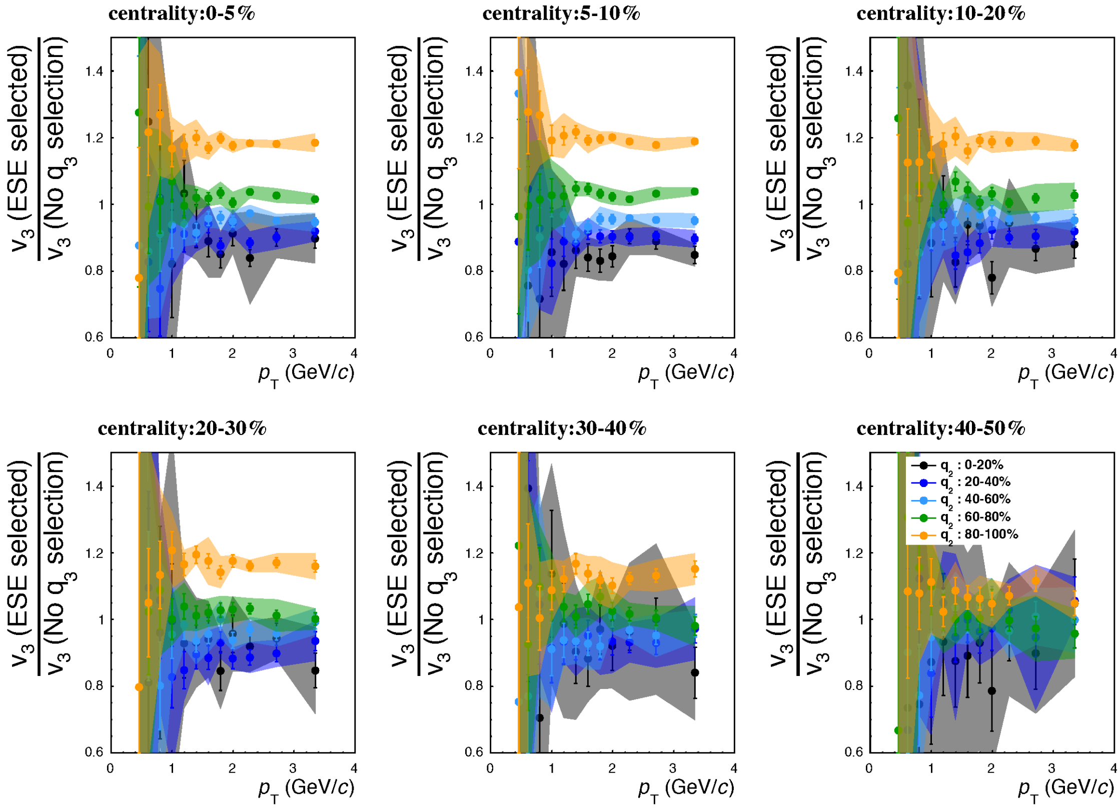

Figure 4.19: Ratio of v_3 with each 20% q_3 selection to without q_3 selection (unbiased sample) for protons.

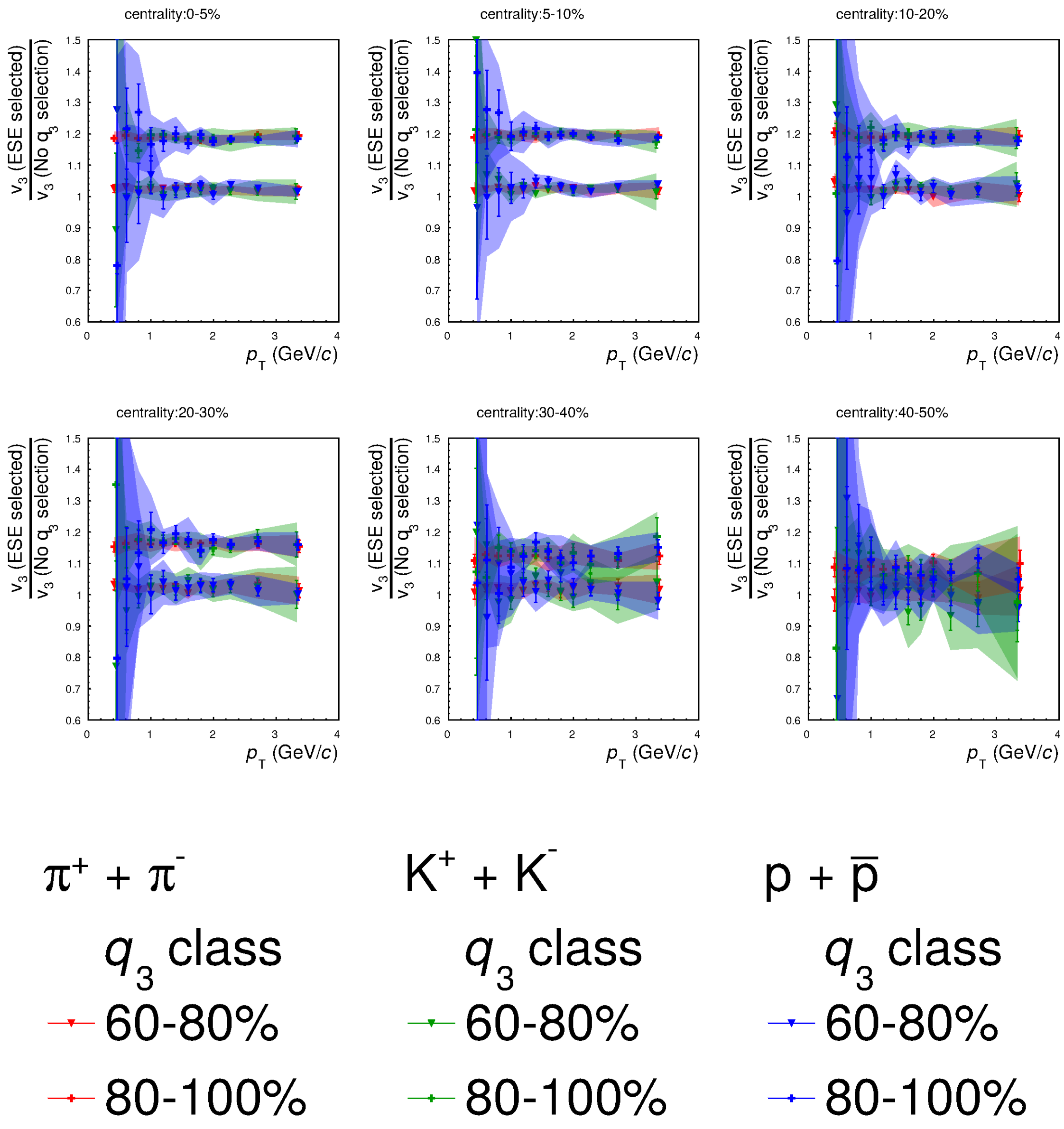

Figure 4.20: Transverse momentum dependence of v_3 ratio with each 20% q_3 selection to without q_3 selection (unbiased sample) for unidentified and identified charged hadrons (π, K and p) for 6 centrality bins.

4.3 Azimuthal angle dependence of HBT radii with respect to Ψ_2 with Event Shape Engineering q_2 selection

Study of pion, kaon and proton v_2 and v_3 measurement with Event Shape Engineering technique gives us the results that larger and smaller v_2 and v_3 can be selected.

Study on v_2 and v_3 of unidentified and identified hadrons (π, K and p) with ESE shows that event-by-event v_2 and v_3 can be selected, though the enhancement (suppression) varies from small to large.

In order to investigate the correlation between initial and final source shape, Event Shape Engineering q_2 selection is applied to azimuthal angle dependence of HBT radii.

Figure 4.21, 4.22, 4.23, 4.24, and 4.25 shows the extracted 3D HBT radii for charged pions as a function of azimuthal pair angle with respect to Ψ_2 for 6 different centrality bins with 0-20%, 20-40%, 40-60%, 60-80%, and 80-100% q_2 selection, respectively. Azimuthal angle dependence of HBT radii with respect to Ψ_2 without q_2 selection are simultaneously plotted as open circles.

In Fig. 4.25, no significant modification can be found in λ, $R_{\rm long}$, $R_{\rm ol}$, and $R_{\rm sl}$with q_2 selection. But oscillation amplitudes of HBT radii in $R_{\rm out}$ and $R_{\rm os}$ are explicitly enhanced, as is the case with large q_2 selected v_2. Also the oscillation amplitude of $R_{\rm side}$ is slightly enhanced with this q_2 selection.

In Fig. 4.22, 4.23 and 4.23, oscillation amplitudes of $R_{\rm out}$, $R_{\rm side}$, and $R_{\rm os}$ are slightly modified with 20-40%, 40-60%, and 60-80% q_2 selections, respectively.

In Fig. 4.21, oscillation amplitudes of $R_{\rm out}$ and $R_{\rm os}$ are slightly suppressed with 0-20% q_2 selection. Although q_2 selection modifies the oscillation amplitudes of $R_{\rm out}$ and $R_{\rm os}$, sign of their oscillations does not change. The oscillation amplitude of $R_{\rm side}$ are also slightly suppressed with 0-20% q_2 selection. However, in most central 0-5% collisions, $R_{\rm side}$ has changed oscillation sign from concave up to convex up with 0-20% q_2 selection. Therefore, in this q_2 range, $R_{\rm out}$ and $R_{\rm side}$ has same oscillation sign (convex up).

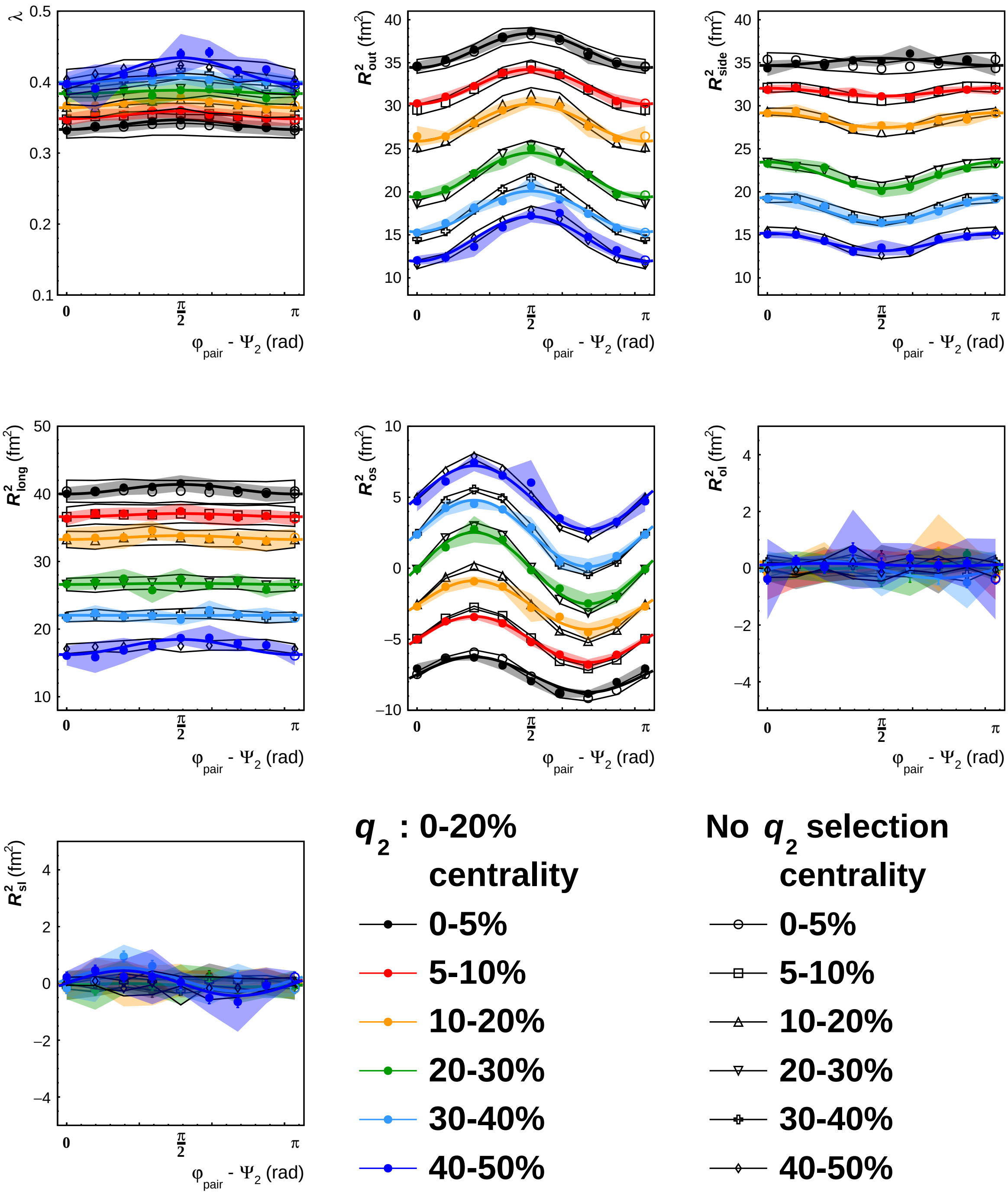

Figure 4.21: Extracted HBT parameters (R_{out}, R_{side}, R_{long}, λ, R_{os}, R_{ol}, and R_{sl}) of charged pions in $0.2 < k_T < 1.5$ GeV/c as a function of azimuthal pair angle with respect to 2$^{\mathrm{nd}}$-order event plane for 6 different centrality bins. Bottom 20% q_2 selection is applied to HBT measurements. The data points at $\varphi_{pair} - \Psi_2 = \pi$ are same value at $\varphi_{pair} - \Psi_2 = 0$. Systematic uncertainties are plotted as transparent bands. All points of R_{os} are shifted along the y-axis for visibility.

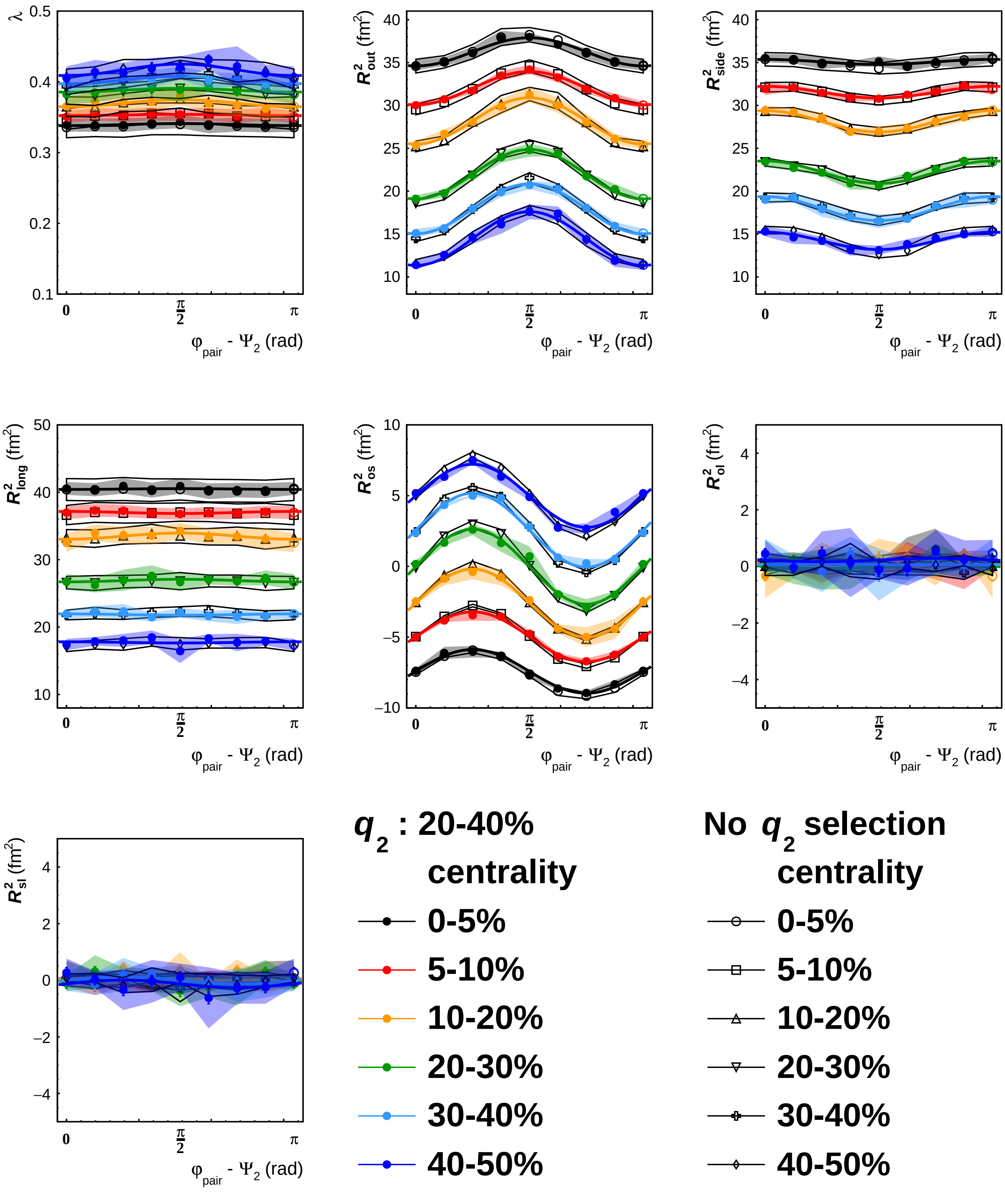

Figure 4.22: Extracted HBT parameters ($R_{\rm out}$, $R_{\rm side}$, $R_{\rm long}$, λ, $R_{\rm os}$, $R_{\rm ol}$, and $R_{\rm sl}$) of charged pions in $0.2 < k_T < 1.5$ GeV/c as a function of azimuthal pair angle with respect to 2$^{\rm nd}$-order event plane for 6 different centrality bins. 20-40% q_2 selection is applied to HBT measurements. The data points at $\varphi_{pair} - \Psi_2 = \pi$ are same value at $\varphi_{pair} - \Psi_2 = 0$. Systematic uncertainties are plotted as transparent bands. All points of $R_{\rm os}$ are shifted along the y-axis for visibility.

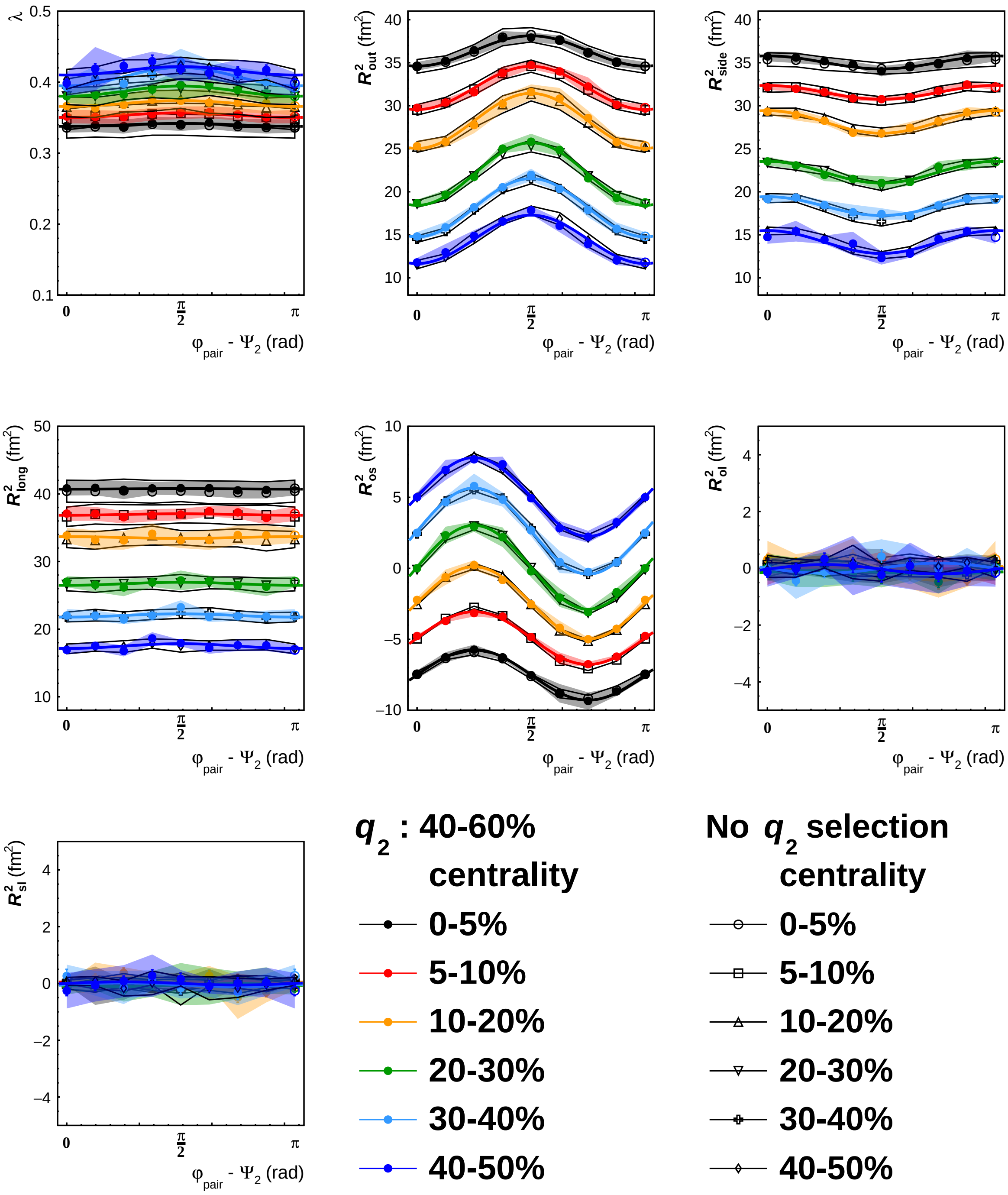

Figure 4.23: Extracted HBT parameters (R_{out}, R_{side}, R_{long}, λ, R_{os}, R_{ol}, and R_{sl}) of charged pions in $0.2 < k_T < 1.5$ GeV/c as a function of azimuthal pair angle with respect to 2$^{\text{nd}}$-order event plane for 6 different centrality bins. 40-60% q_2 selection is applied to HBT measurements. The data points at $\varphi_{pair} - \Psi_2 = \pi$ are same value at $\varphi_{pair} - \Psi_2 = 0$. Systematic uncertainties are plotted as transparent bands. All points of R_{os} are shifted along the y-axis for visibility.

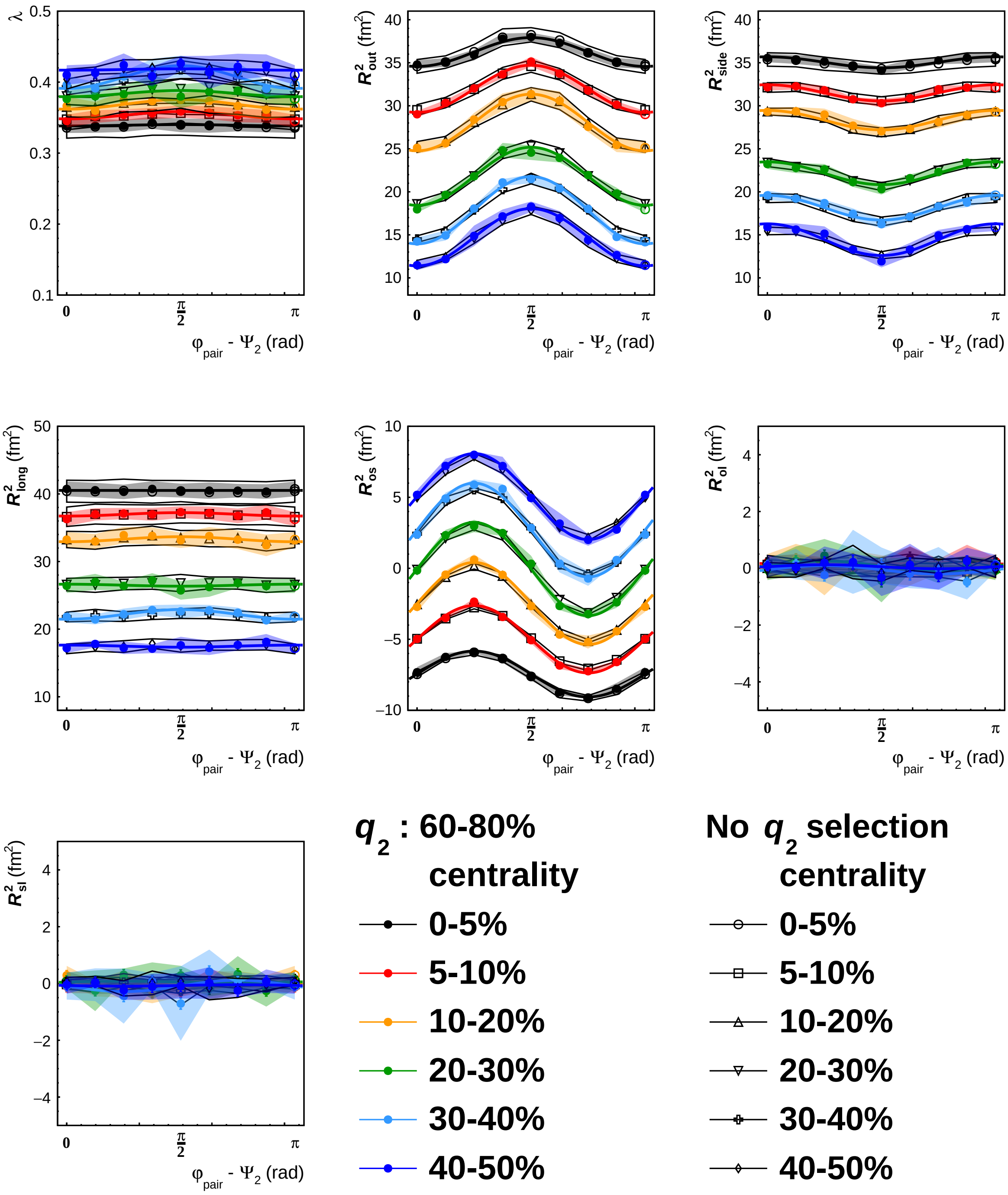

Figure 4.24: Extracted HBT parameters (R_{out}, R_{side}, R_{long}, λ, R_{os}, R_{ol}, and R_{sl}) of charged pions in $0.2 < k_T < 1.5$ GeV/c as a function of azimuthal pair angle with respect to 2$^{\mathrm{nd}}$-order event plane for 6 different centrality bins. 60-80% q_2 selection is applied to HBT measurements. The data points at $\varphi_{pair} - \Psi_2 = \pi$ are same value at $\varphi_{pair} - \Psi_2 = 0$. Systematic uncertainties are plotted as transparent bands. All points of R_{os} are shifted along the y-axis for visibility.

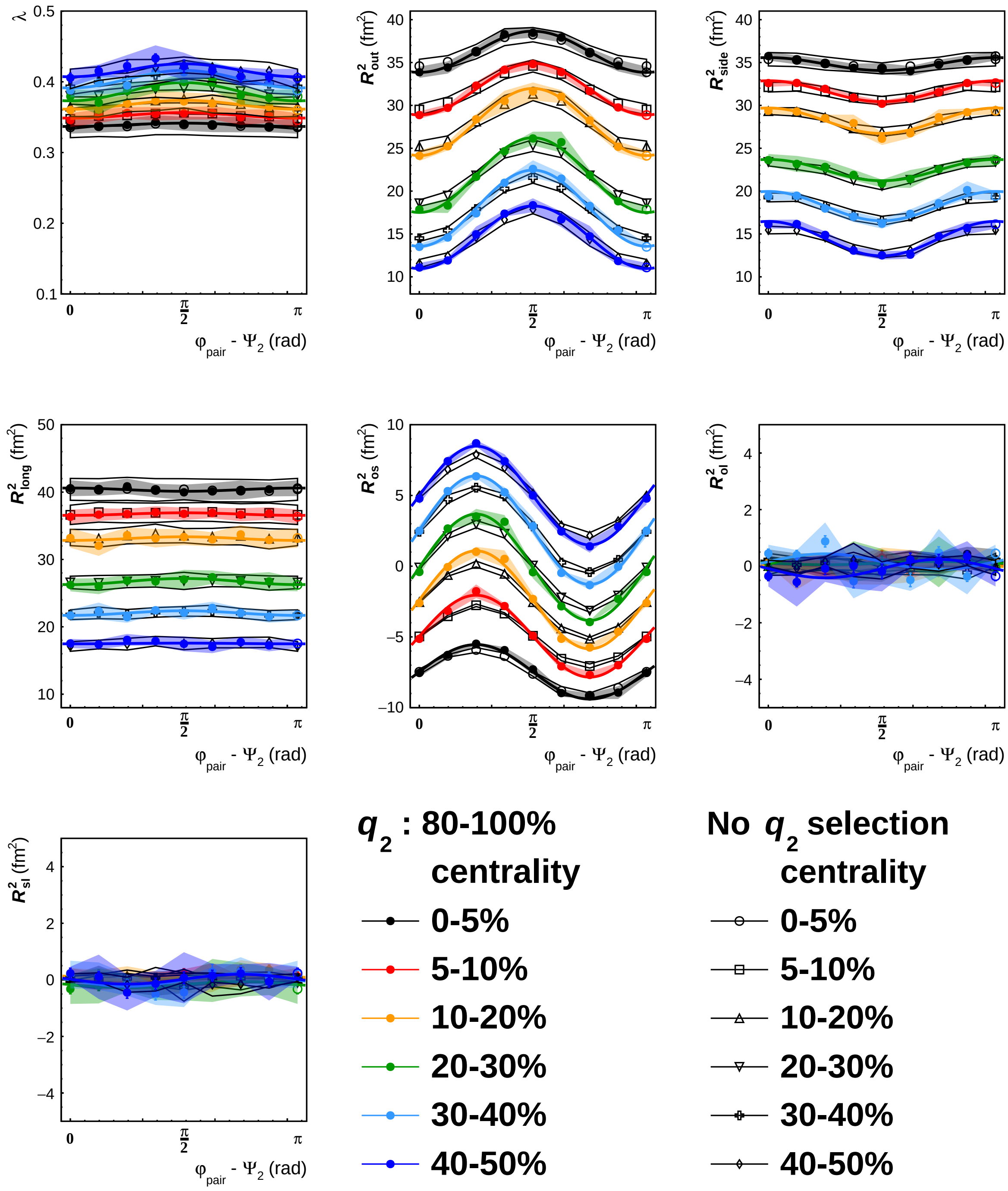

Figure 4.25: Extracted HBT parameters (R_{out}, R_{side}, R_{long}, λ, R_{os}, R_{ol}, and R_{sl}) of charged pions in $0.2 < k_T < 1.5$ GeV/c as a function of azimuthal pair angle with respect to 2$^{\mathrm{nd}}$-order event plane for 6 different centrality bins. Top 20% q_2 selection is applied to HBT measurements. The data points at $\varphi_{pair} - \Psi_2 = \pi$ are same value at $\varphi_{pair} - \Psi_2 = 0$. Systematic uncertainties are plotted as transparent bands. All points of R_{os} are shifted along the y-axis for visibility.

4.4 Azimuthal angle dependence of HBT radii with respect to Ψ_3

4.4.1 1D projection of 3D Correlation functions

Azimuthal pair angle of pions with respect to 3^{rd}-order event plane is divided into 8 bins. Each bin width is $\pi/12(rad)$.

Figure 4.26 shows the correlation function of charged pions measured for $0.2 < k_T < 1.5$ GeV/$c$for two azimuthal bins ($|\varphi_{pair} - \Psi_3| < \pi/24$ and $7\pi/24 < |\varphi_{pair} - \Psi_3| < \pi/3$) corresponding to in-plane and out-plane directions of Ψ_3 angle, respectively) at centrality 0-50% after the bin-by-bin correction on the event plane resolution. As is the case with azimuthal angle dependence of HBT radii with respect to Ψ_2, three-dimensional correlation functions are projected along to each axis (outward, sideward, and longitudinal directions). The other q components within 50 MeV/c are projected. To make the projection of the 3D correlation function to a specific q direction, the projections over the other q components was performed within 50 GeV/c for each numerator and denominator in Eq. 3.65. Left columns show the correlation function C_2 in the outward direction, middle columns for C_2 in the sideward directions, and right columns for C_2 in the longitudinal directions. Difference of row is centrality (top row figures are central (0-5%) and bottom row figures indicate peripheral (40-50%) collisions). Dashed lines are fit function which is also projected to each directions. Top to bottom panels show the projected correlation function in central (0-5%) to peripheral (40-50%) collisions. Black and red solid lines represent fit functions to the projected correlation functions measured in in-plane and out-plane of the Ψ_3 directions.

Contrary to 2^{nd}-order event plane dependence of HBT correlation function, no significant difference between correlation function in-plane and out-plane directions with respect to Ψ_3 in all centrality for outward, sideward, and longitudinal axis.

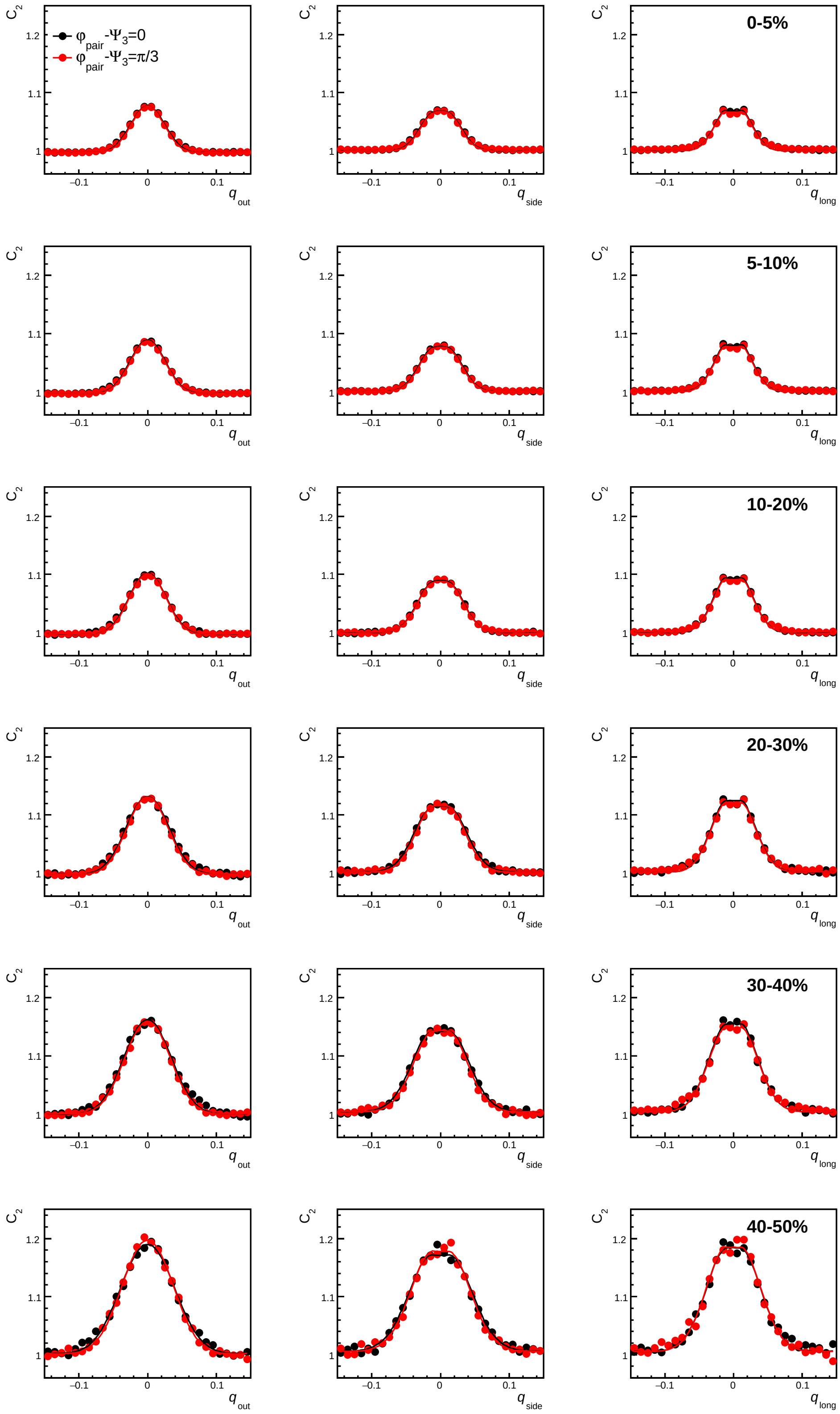

Figure 4.26: Projection of 3D correlation function to 1D (outward, sideward, and longitudinal directions) of charged pions in $0.2 < k_T < 1.5$ GeV/c for two different azimuthal angle classes, $|\varphi_{pair} - \Psi_3| < \pi/24$ (Black marker) and $7\pi/24 < |\varphi_{pair} - \Psi_3| < \pi/3$ (Red marker) in centrality 0-50%. The projection range of the other q components are within 50 GeV/c . Solid line denotes the fitting function of 3D correlation function.

4.4.2 Centrality dependence of HBT radii with respect to Ψ_3

Figure 4.27 shows the extracted 3D HBT radii for charged pions as a function of azimuthal pair angle with respect to 3rd-order event plane Ψ_3 for 6 different centralities. The data points at $\varphi_{pair} - \Psi_3 = \pi/3$ are same value to those at $\varphi_{pair} - \Psi_3 = 0$ based on the symmetry with respect to event plane. Charged pions for HBT analysis are measured at mid rapidity and event plane Ψ_3 is determined via FMD A+C combined. Systematic uncertainties are plotted as transparent bands and statistical uncertainties are smaller than marker size.

The azimuthal angle dependence of HBT radii is fitted with Eq.4.1. But, in 3rd order event plane case, the summation over n takes $n = 3$ in Eq.4.1.

As is the case with azimuthal angle dependence of HBT radii with respect to Ψ_2, λ, $R_{\rm long}$, $R_{\rm ol}$, and $R_{\rm sl}$ have no explicit oscillation in all centrality. On the other hand, $R_{\rm out}$ and $R_{\rm side}$ have finite oscillations. For Ψ_2 case, oscillations of $R_{\rm out}$ are convex upward and those of $R_{\rm side}$ are concave upward. However, for Ψ_3 case, both $R_{\rm out}$ and $R_{\rm side}$ are convex upward. This behaviour of the azimuthal angle dependence $R_{\rm side}$ in Ψ_3 is explicitly different to Ψ_2. However, as we mentioned in Sec. 4.3, in bottom 20% q_2 and most central 0-5% collisions, oscillation signs of $R_{\rm out}$ and $R_{\rm side}$ are same and concave up. Two different analysises are quit similar at the point of same oscillation signs in outward and sideward. Contrary to Ψ_2 case, no significant oscillation relative to Ψ_3 in $R_{\rm os}$ can be found.

4.5 Azimuthal angle dependence of HBT radii with respect to Ψ_3 with Event Shape Engineering q_3 selection

Figure 4.28, 4.29, 4.30, 4.31, and 4.32 shows the extracted 3D HBT radii for charged pions as a function of azimuthal pair angle with respect to 3rd-order event plane Ψ_3 for 6 different centralities with each 20% q_3 selection. The results without q_3 selection are simultaneously plotted as open circles.

For v_3 measurement with q_3 selection, measured v_3 is enhanced (suppressed) with large (small) q_3 selection and the difference between q_3 selected v_3 and inclusive v_3 is remarkable at central collisions.

But there is no significant difference in azimuthal angle dependence of HBT radii with respect to Ψ_3 between with and without q_3 selection even in top 20% and bottom 20% q_3

selection, while the explicit differences can be found in azimuthal angle dependence of HBT radii with respect to Ψ_2 with q_2 selection.

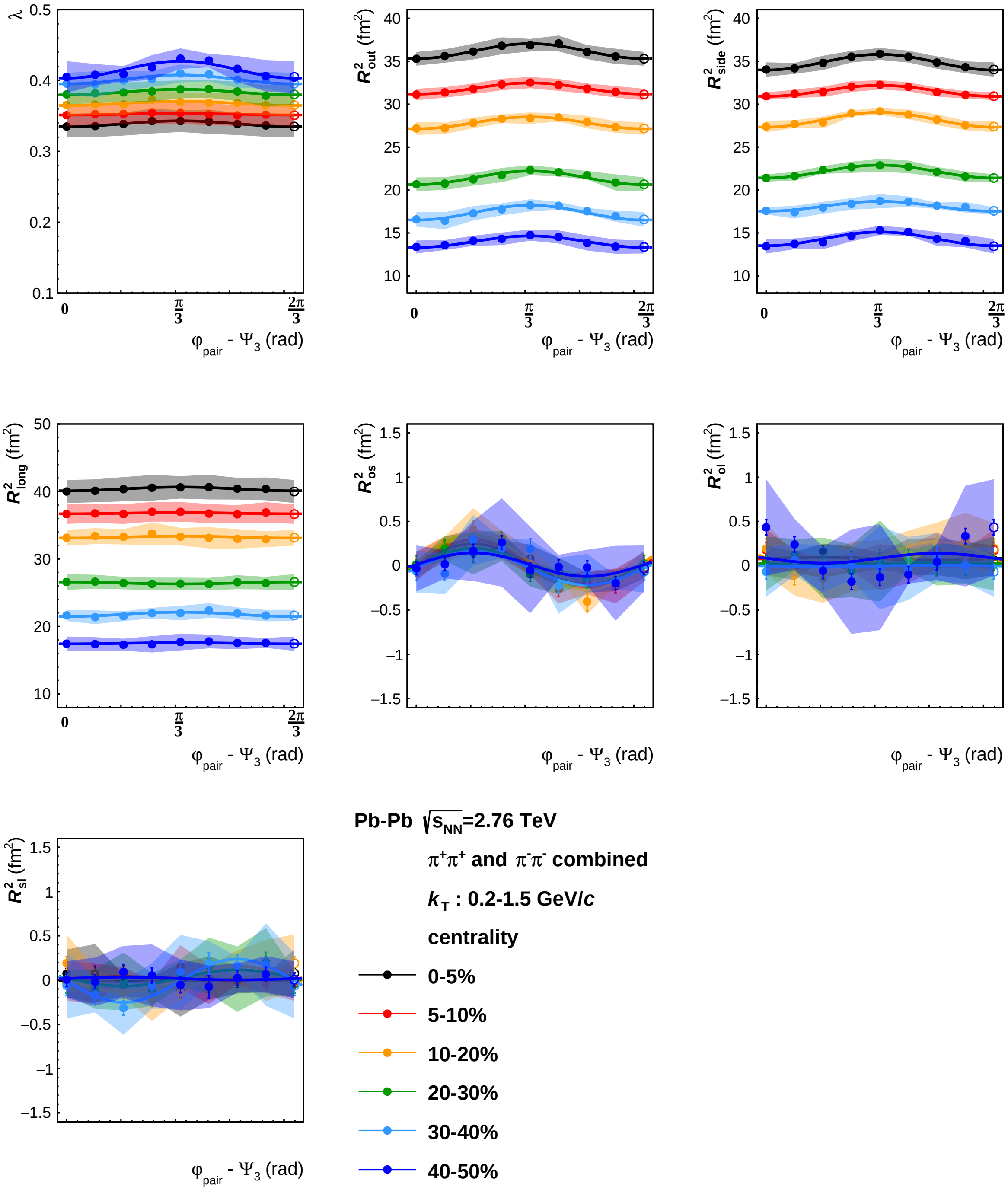

Figure 4.27: Extracted HBT parameters (R_{out}, R_{side}, R_{long}, λ, R_{os}, R_{ol}, and R_{sl}) of charged pions in $0.2 < k_T < 1.5$ GeV/$c$as a function of azimuthal pair angle with respect to 3rd-order event plane for 6 different centrality bins. The data points at $\varphi_{pair} - \Psi_3 = 2\pi/3$ is same value to those at $\varphi_{pair} - \Psi_3 = 0$. Systematic uncertainties are shown as transparent bands.

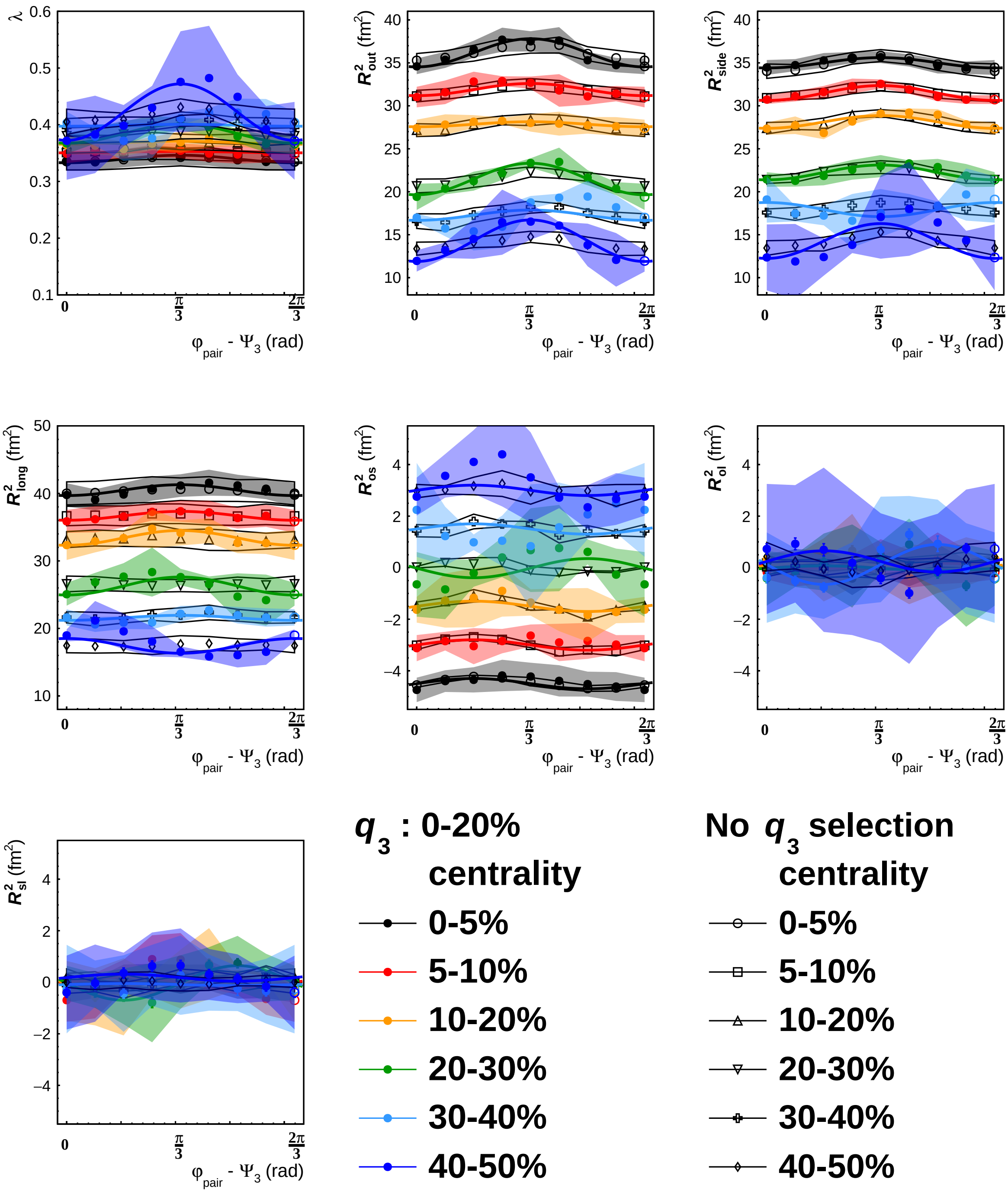

Figure 4.28: Extracted HBT parameters (R_{out}, R_{side}, R_{long}, λ, R_{os}, R_{ol}, and R_{sl}) of charged pions in $0.2 < k_T < 1.5$ GeV/c as a function of azimuthal pair angle with respect to 3$^{\mathrm{rd}}$-order event plane for 6 different centrality bins. Bottom 20 % q_3 selection is applied to HBT measurements. The data points at $\varphi_{pair} - \Psi_3 = 2\pi/3$ is same value to those at $\varphi_{pair} - \Psi_3 = 0$. Systematic uncertainties are plotted as transparent bands. All points of R_{os} are shifted along the y-axis for visibility.

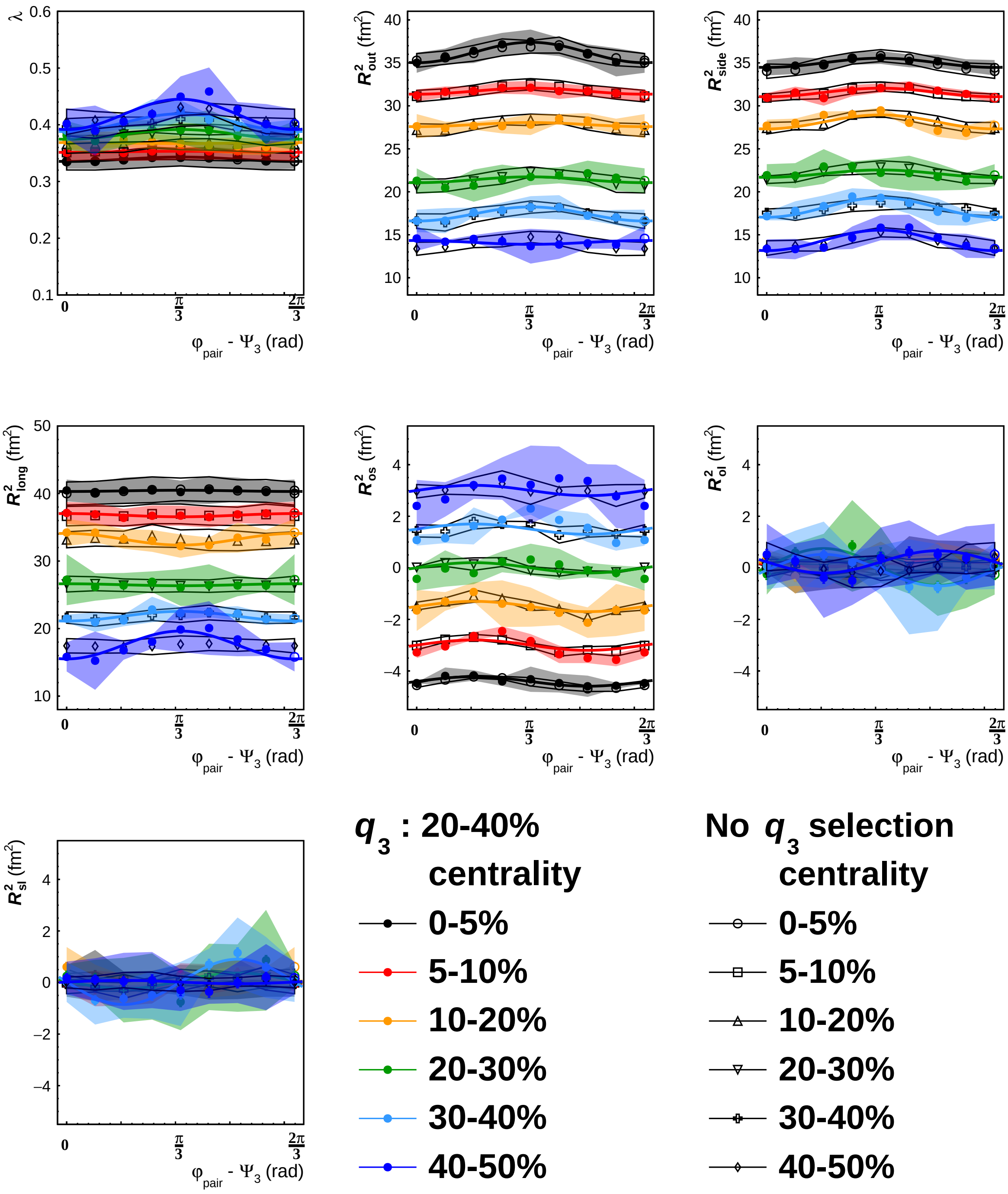

Figure 4.29: Extracted HBT parameters (R_{out}, R_{side}, R_{long}, λ, R_{os}, R_{ol}, and R_{sl}) of charged pions in $0.2 < k_T < 1.5$ GeV/c as a function of azimuthal pair angle with respect to 3rd-order event plane for 6 different centrality bins. 20-40% q_3 selection is applied to HBT measurements. The data points at $\varphi_{pair} - \Psi_3 = 2\pi/3$ is same value to those at $\varphi_{pair} - \Psi_3 = 0$. Systematic uncertainties are plotted as transparent bands. All points of R_{os} are shifted along the y-axis for visibility.

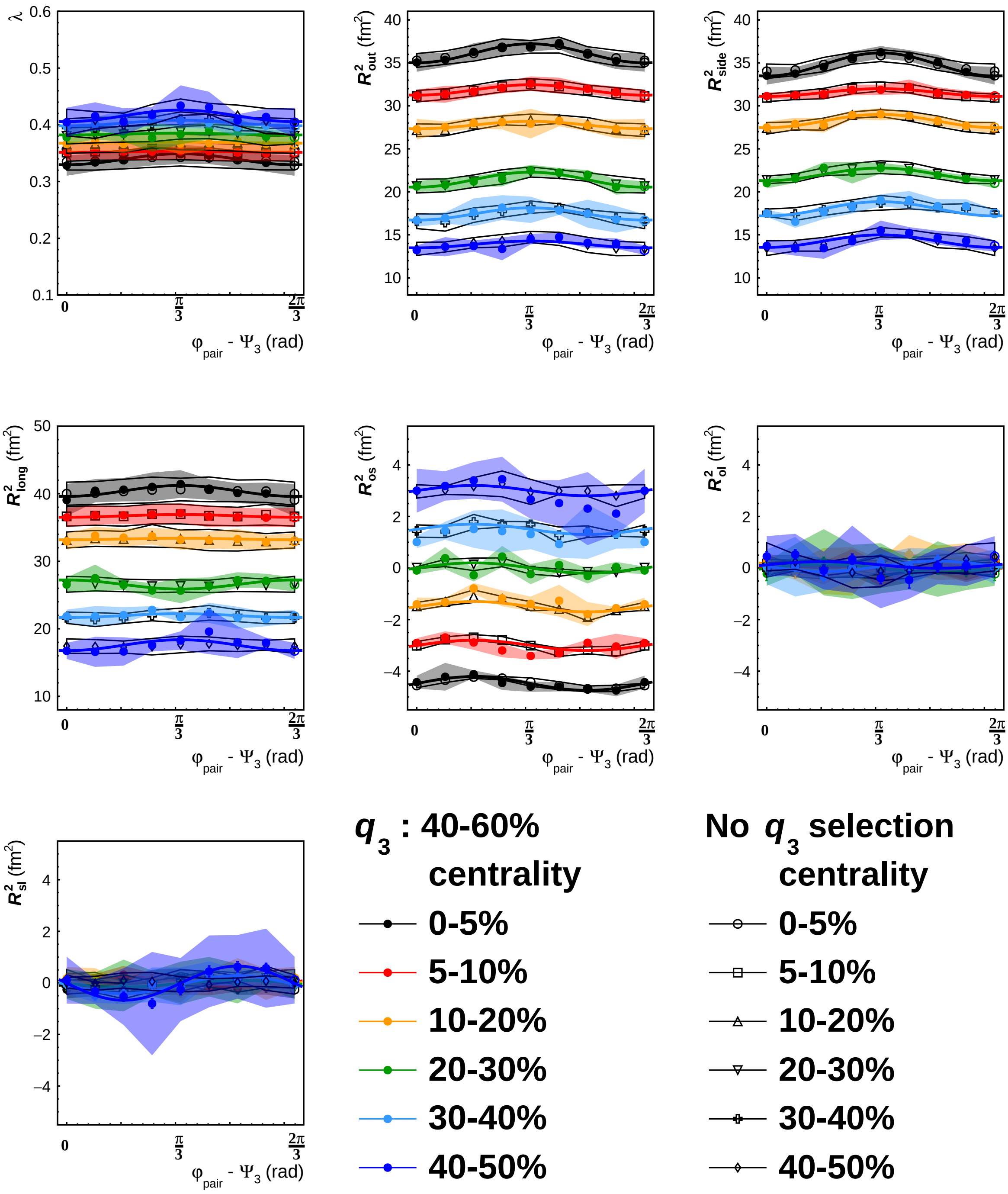

Figure 4.30: Extracted HBT parameters (R_{out}, R_{side}, R_{long}, λ, R_{os}, R_{ol}, and R_{sl}) of charged pions in $0.2 < k_T < 1.5$ GeV/c as a function of azimuthal pair angle with respect to 3rd-order event plane for 6 different centrality bins. 40-60% q_3 selection is applied to HBT measurements. The data points at $\varphi_{pair} - \Psi_3 = 2\pi/3$ is same value to those at $\varphi_{pair} - \Psi_3 = 0$. Systematic uncertainties are plotted as transparent bands. All points of R_{os} are shifted along the y-axis for visibility.

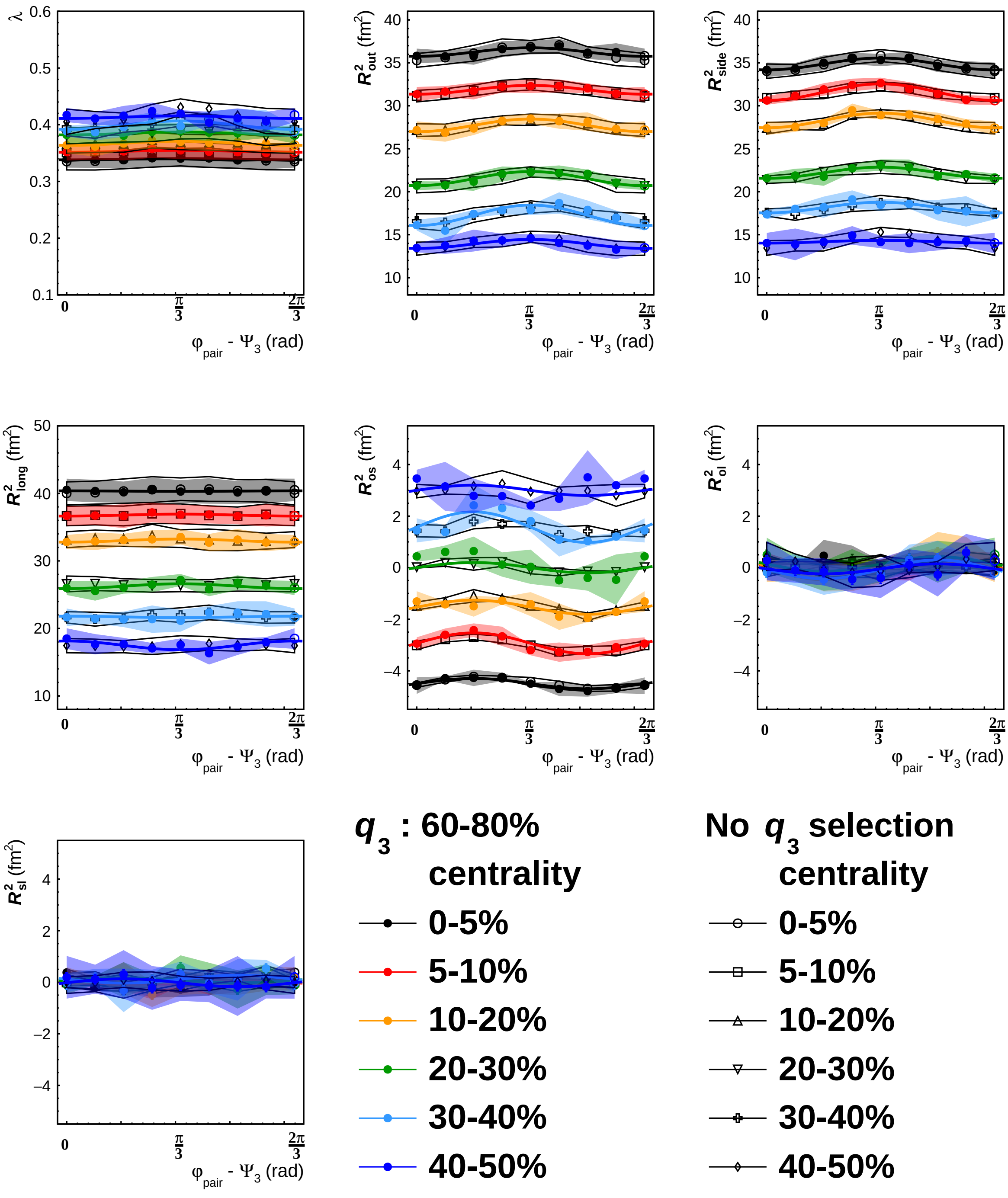

Figure 4.31: Extracted HBT parameters ($R_{\rm out}$, $R_{\rm side}$, $R_{\rm long}$, λ, $R_{\rm os}$, $R_{\rm ol}$, and $R_{\rm sl}$) of charged pions in $0.2 < k_T < 1.5$ GeV/c as a function of azimuthal pair angle with respect to 3rd-order event plane for 6 different centrality bins. 60-80% q_3 selection is applied to HBT measurements. The data points at $\varphi_{pair} - \Psi_3 = 2\pi/3$ is same value to those at $\varphi_{pair} - \Psi_3 = 0$. Systematic uncertainties are plotted as transparent bands. All points of $R_{\rm os}$ are shifted along the y-axis for visibility.

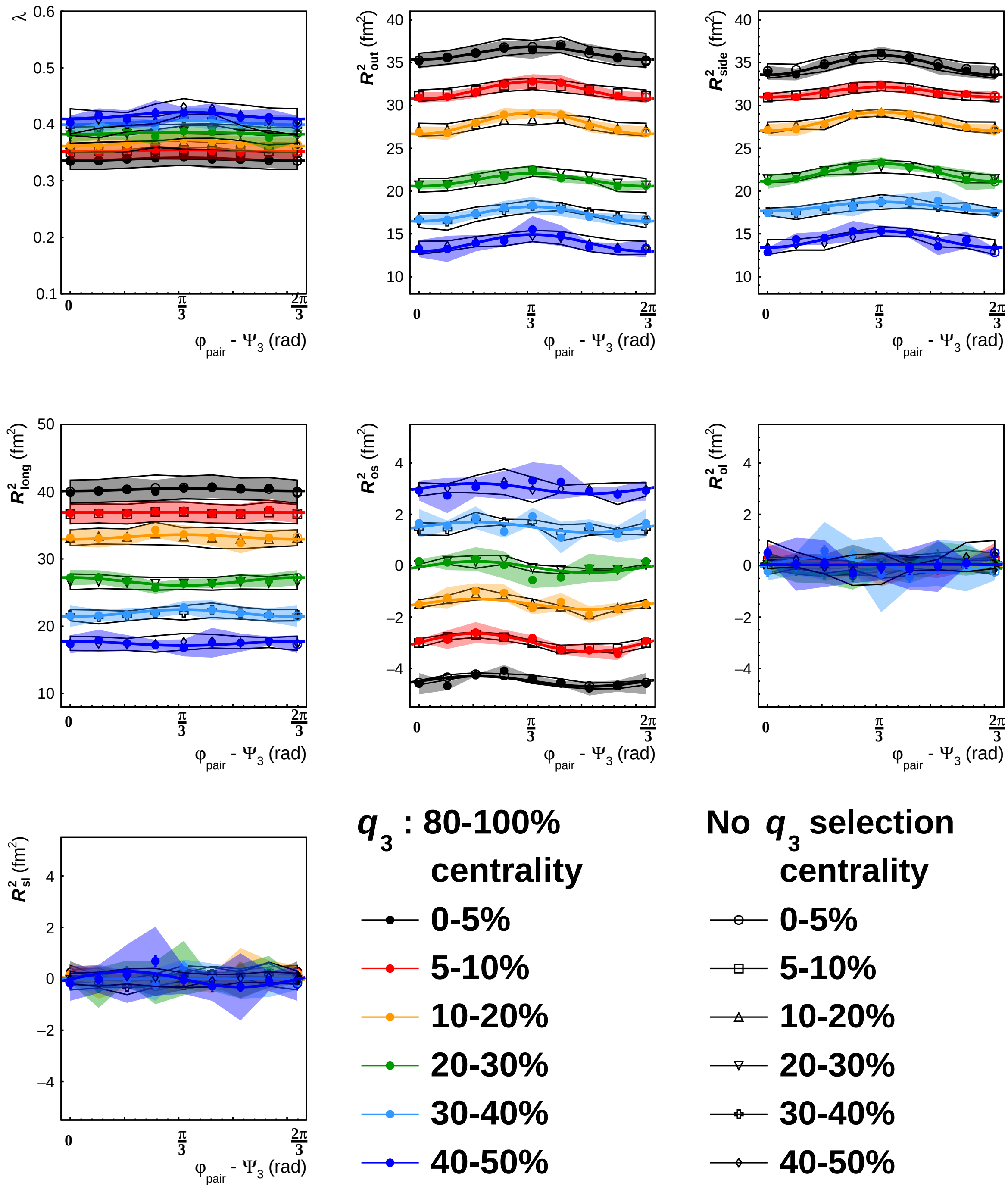

Figure 4.32: Extracted HBT parameters (R_{out}, R_{side}, R_{long}, λ, R_{os}, R_{ol}, and R_{sl}) of charged pions in $0.2 < k_T < 1.5$ GeV/c as a function of azimuthal pair angle with respect to 3[rd]-order event plane for 6 different centrality bins. Top 20% q_3 selection is applied to HBT measurements. The data points at $\varphi_{pair} - \Psi_3 = 2\pi/3$ is same value to those at $\varphi_{pair} - \Psi_3 = 0$. Systematic uncertainties are plotted as transparent bands. All points of R_{os} are shifted along the y-axis for visibility.

4.6 Consistency check of HBT radii with the previous results from ALICE

Figure 4.33, 4.34, and 4.34 shows 3D HBT radii (R_{out}, R_{side}, and R_{long}) of charged pions as a function of pair transverse momentum k_{T} for 6 centrality bins. My results are plotted as closed circles which is obtained with azimuthal dependence of HBT radii with respect to Ψ_3. Open squared markers are results of azimuthal differential pion HBT with respect to Ψ_2 [60]. Open circle markers are results of azimuthal integrated pion HBT analysis [61]. Error bars of my analysis and open squared markers are quadratic sum of sytematic and statistical uncertainties. Shaded bands are systematic uncertainties of open circles. All three results are calculated with data measured in Pb-Pb collisions at $\sqrt{s_{\mathrm{NN}}}$ = 2.76 TeV collisions.

R_{out} of my calculations are fully consistent to two published results within systematic uncertainties for all centralities and k_{T} . R_{side} of my calculations in central 0-10% collisions are slightly smaller than the other calculations. But all results are consistent within systematic uncertainties. R_{long} of my calculations in k_{T} 0.3-0.5 GeV/c are slightly smaller than the other calculations. But all results are consistent within systematic uncertainties.

4.7 Consistency check of v_2 and v_3 with the previous results from ALICE

Figure 4.36 and 4.37 show Identified hadron (π, K and p) v_2 and v_3 as a function of p_{T} for 6 centrality classes. My results are compared with previous results from ALICE.

Charged pion and kaon v_2 and v_3 are fully consistent with published results. Proton v_2 and v_3 of my calculation are systematically smaller than published results in especially smaller p_{T} . But both results are consistent within systematic uncertainties.

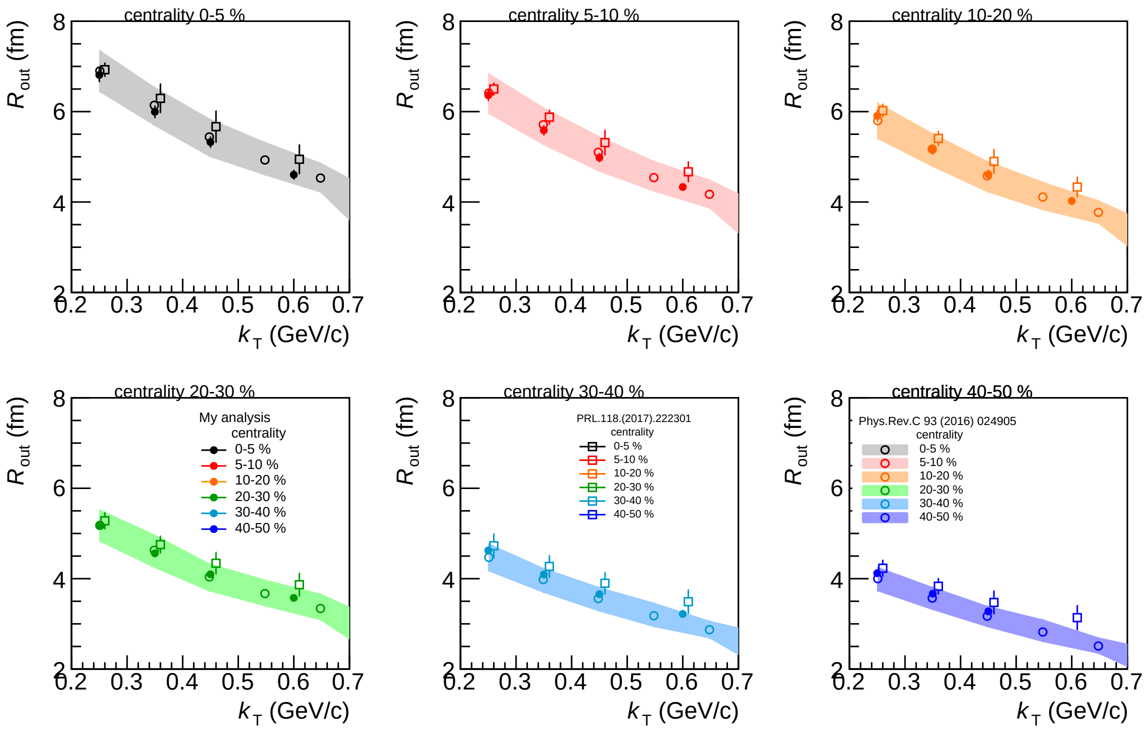

Figure 4.33: 3D HBT radii (R_{out}) of charged pions as a function of pair transverse momentum k_T for 6 centrality bins. My results are plotted as closed circles which is obtained with azimuthal dependence of HBT radii with respect to Ψ_3. Open squared markers are results of azimuthal differential pion HBT with respect to Ψ_2 [60]. Open circle markers are results of azimuthal integrated pion HBT analysis [61].

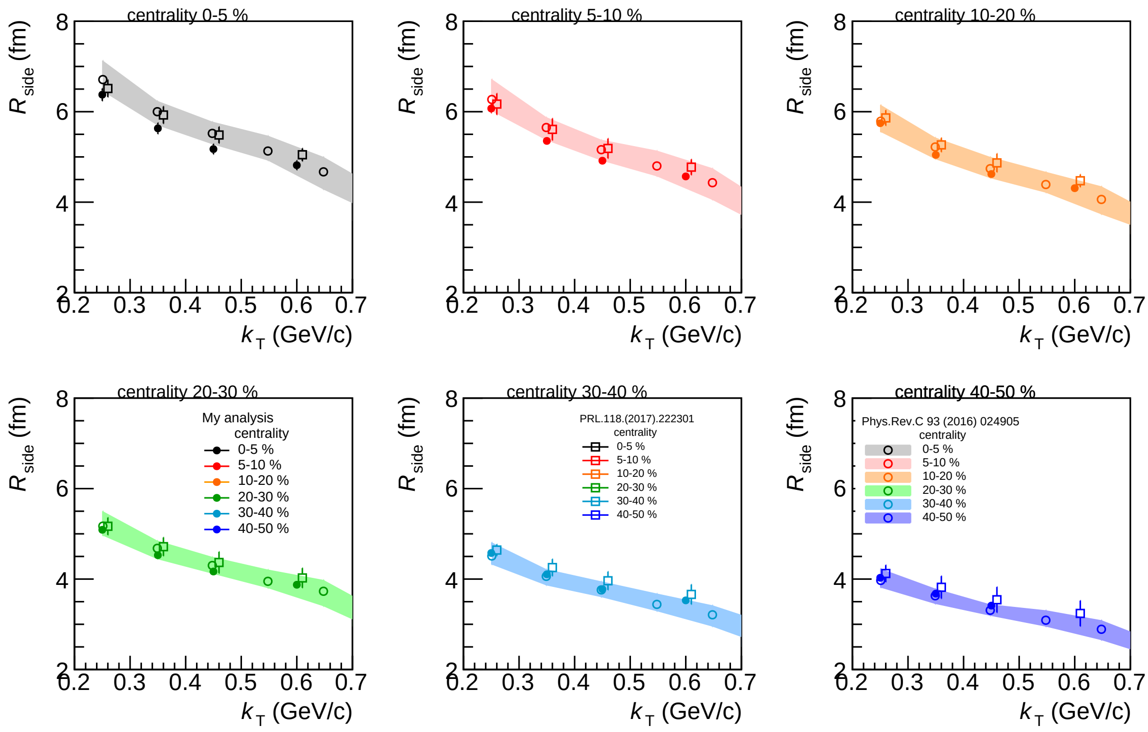

Figure 4.34: 3D HBT radii (R_{side}) of charged pions as a function of pair transverse momentum k_{T} for 6 centrality bins. My results are plotted as closed circles which is obtained with azimuthal dependence of HBT radii with respect to Ψ_3. Open squared markers are results of azimuthal differential pion HBT with respect to Ψ_2 [60]. Open circle markers are results of azimuthal integrated pion HBT analysis [61].

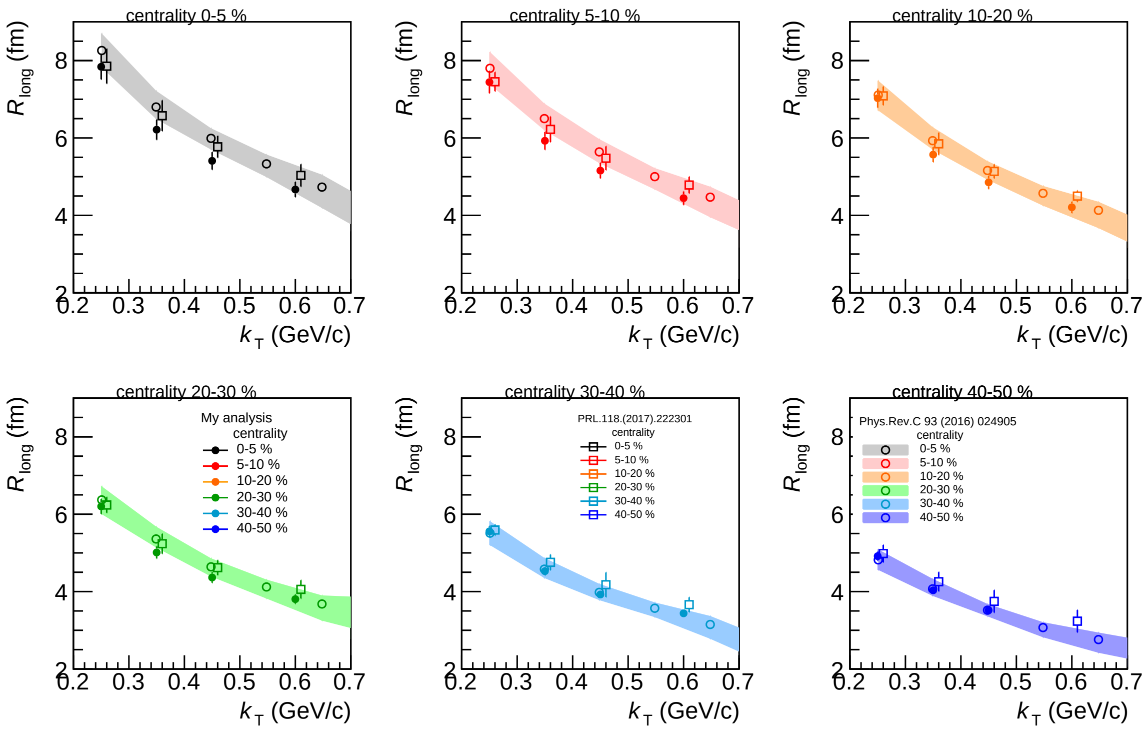

Figure 4.35: 3D HBT radii (R_{side}) of charged pions as a function of pair transverse momentum k_{T} for 6 centrality bins. My results are plotted as closed circles which is obtained with azimuthal dependence of HBT radii with respect to Ψ_3. Open squared markers are results of azimuthal differential pion HBT with respect to Ψ_2 [60]. Open circle markers are results of azimuthal integrated pion HBT analysis [61].

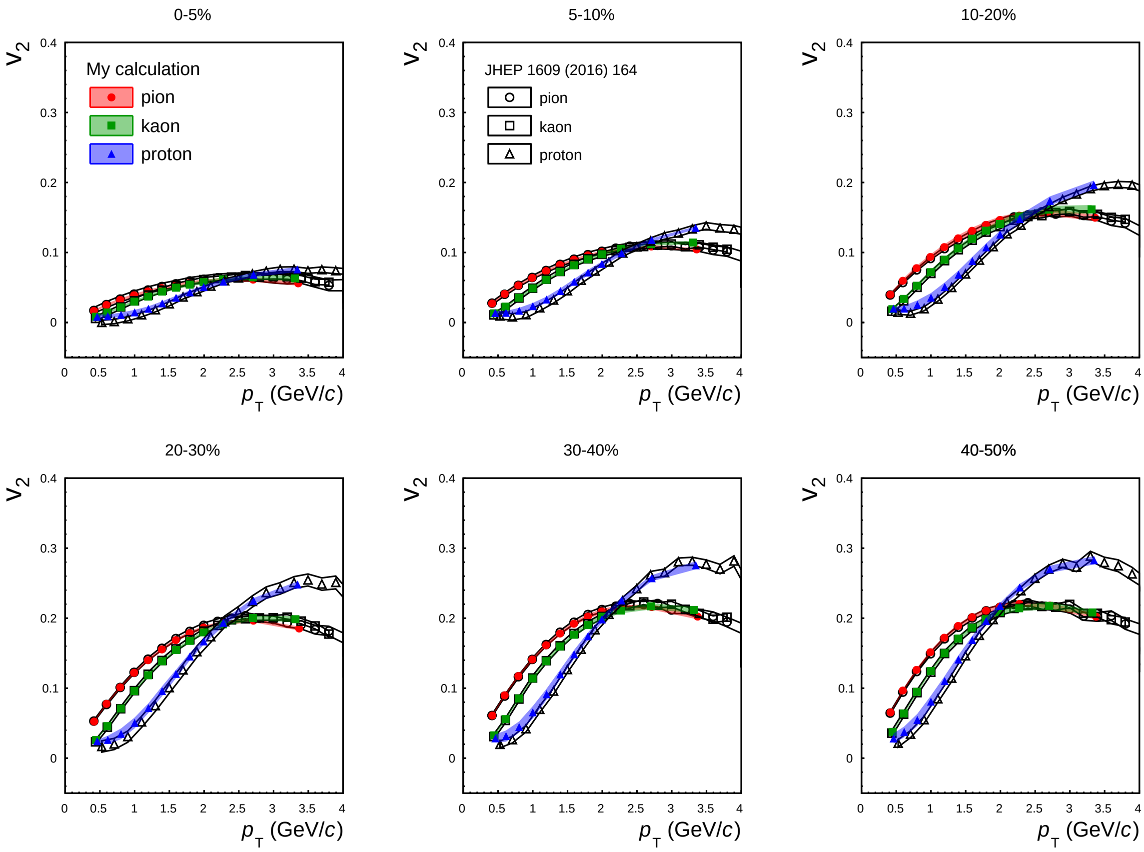

Figure 4.36: Identified hadron (π, K and p) v_2 as a function of p_T for 6 centrality classes. Ψ_2 is determined via FMD A+C. My results are plotted as closed markers and systematic uncertainties of my calculation are depicted as transparent bands. Published results are plotted as opened markers [62].

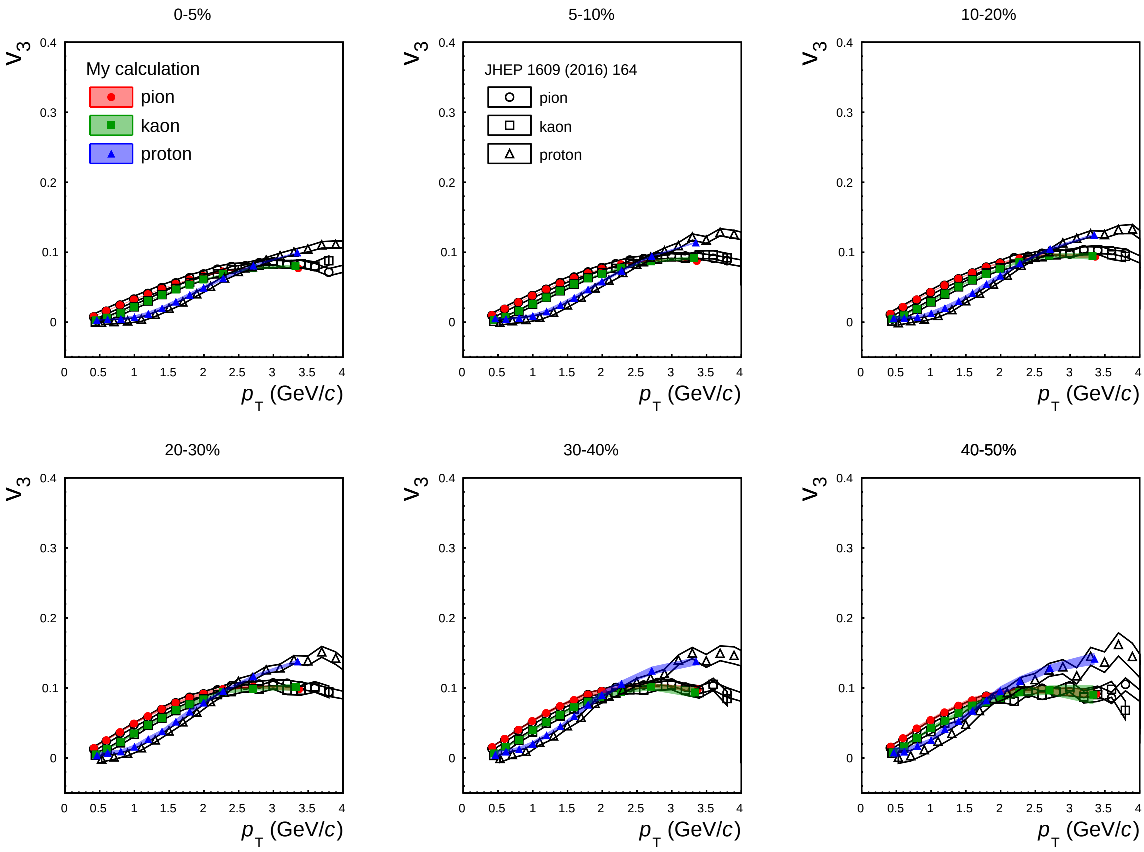

Figure 4.37: Identified hadron (π, K and p) v_3 as a function of p_T for 6 centrality classes. Ψ_2 is determined via FMD A+C. My results are plotted as closed markers and systematic uncertainties of my calculation are depicted as transparent bands. Published results are plotted as opened markers [62].

Chapter 5

Discussion

5.1 Final source Eccentricity

In order to understand space-time evolution of the system, one of the important probes is a relation between the initial geometrical shape and final source shape at the time of kinetic freeze-out. Blast wave model suggests that an eccentricity at the freeze-out can be extracted with relative amplitude of azimuthal angle dependence of HBT radii with respect to Ψ_2 at the limit of $k_T = 0$ [63]. Based on the assumption of Blast wave approach, a final source eccentricity is given by

$$\varepsilon_{final} = 2\frac{R^2_{side,2}}{R^2_{side,0}} = -2\frac{R^2_{out,2}}{R^2_{side,0}} = 2\frac{R^2_{os,2}}{R^2_{side,0}}. \tag{5.1}$$

where $R^2_{\mu,2}$ denotes the second-order oscillation amplitude of HBT radii with respect to Ψ_2, and $R^2_{\mu,0}$ represents average HBT radii. Both two parameters $R^2_{\mu,2}$ and $R^2_{\mu,0}$ are obtained by fitting azimuthal angle dependence of HBT radii with respect to Ψ_2 using Eq.(4.1). It should be noted that the parameters $R_{\rm out}$ and $R_{\rm os}$ terms include temporal information and thus relative amplitude of $R_{\rm out}$ and $R_{\rm os}$ tends to be much affected by radial and anisotropic flow than that in $R_{\rm side}$. Therefore, in order to extract geometrical source shape, the relative amplitude of $R_{\rm side}$ is more suitable to study a geometrical shape of the source.

5.1.1 Centrality dependence of final source eccentricity

Figure 5.1 shows relative amplitudes of squared HBT radii for charged pion pairs with respect to Ψ_2 as a function of centrality obtained by fitting Figure 4.2 with Eq.(4.1). Pair transverse momentum k_T is integrated from 0.2 to 1.5 GeV/c, where the mean $k_{\rm T}$ is $\sim$ 0.4 GeV/c. The relative amplitudes of R_{long} , R_{ol} and R_{sl} are almost zero for all centrality. On the other hand, the relative amplitudes of R_{out} , R_{side} and R_{os} have explicitly non-zero value and they grow from central to peripheral collisions. This behaviour is similar to centrality dependence of v_2 which is sensitive to the initial eccentricity. Therefore it is likely that centrality dependence of initial eccentricity still remains at the freeze-out. The relative amplitudes of R_{out} and R_{os} are larger than that of R_{side} . It indicates that R_{out} and R_{os} oscillations include the temporal term, thus they are biased by collective flow and enhaced compared to geometrical term R_{side} .

In order to study the relation between the initial eccentricity and the final eccentricity, Final source eccentricity (relative amplitude of squared HBT radii) as a function of initial eccentricity obtained with Glauber model simulation[13] is shown in Figure 5.2. Dashed line represents $\varepsilon^{\mathrm{final}}(2R^2_{\mathrm{side},2}/R^2_{\mathrm{side},0}) = 0$ and dotted lined indicates $\varepsilon^{\mathrm{initial}} = \varepsilon^{\mathrm{final}}$ which means that the initial out-plane elongated elliptic shape remains even if the source size enlarges with the system evolution.

The final source eccentricity is much smaller than dotted line. This indecates that the initial elliptic shape is strongly diluted in the final state throuhg the system evolution because of large radial and elliptic flow. However initial elliptic shape can not be reversed by collective expansion even in LHC energy.

The final source eccentricity almost linearly increases with increasing centrality, which means centrality dependence of initial overlap region still remains at freeze-out.

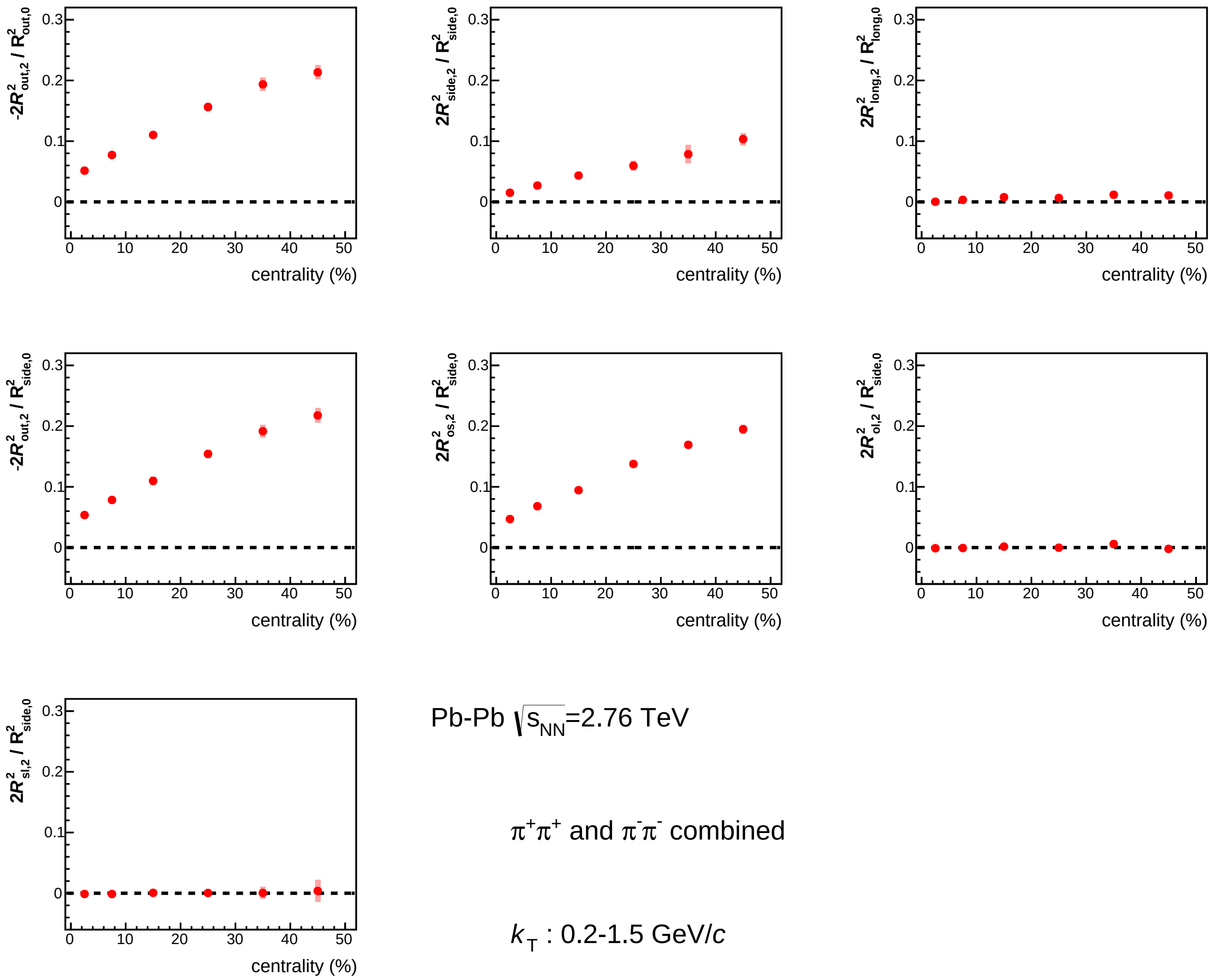

Figure 5.1: Relative amplitudes of squared HBT radii (R_{out} , R_{side} , R_{long} , R_{os} , R_{ol} and R_{sl}) for charged pion pairs with respect to Ψ_2 as a function of centrality measured in Pb-Pb collisions at $\sqrt{s_{NN}} = 2.76$ TeV. Pair transverse momentum k_T is integrated from 0.2 to 1.5 GeV/c. Dashed line indicates relative amplitude of HBT radii = 0. Transparent red boxes represent the systematic uncertainties.

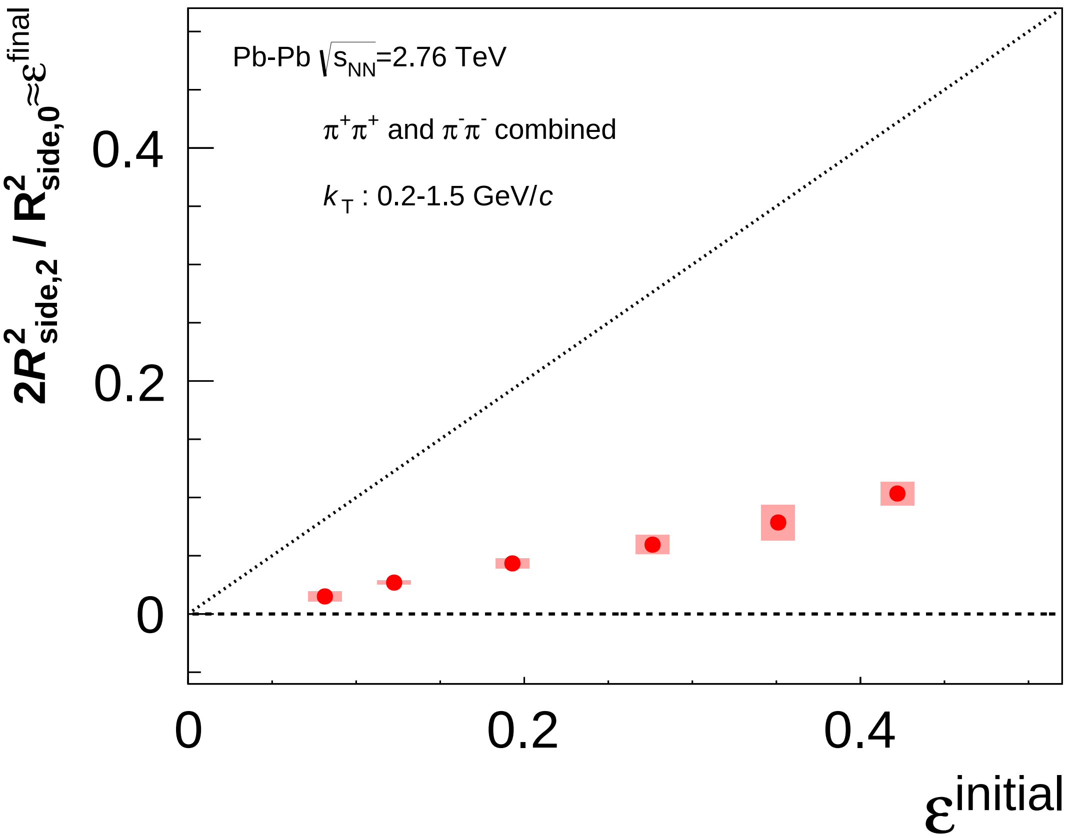

Figure 5.2: Relation between initial source eccentricity(Glauber Model Calculation[13]) and final source eccentricity extracted with azimuthal angle dependence of charged pion HBT radii ($2R^2_{side,2}/R^2_{side,0}$) in Pb-Pb 2.76 TeV. k_T is integrated from 0.2 to 1.5 GeV/c. Dashed line is $2R^2_{side,2}/R^2_{side,0}$=0 and dotted line denotes $\varepsilon^{initial} = \varepsilon^{final}$. Boxes represent the systematic uncertainties and statistical uncertainties are smaller than marker size

5.1.2 k_T dependence of final source eccentricity

Figure 5.3 shows relative amplitudes of squared HBT radii for charged pions with respect to Ψ_2 as a function of pair pair transverse momentum k_{T}. Pair transverse momentum is divided for 3 bins (0.2-0.3, 0.3-0.4, 0.4-1.5GeV/c).

Relative amplitude of R_{side} , R_{out} , and R_{os} ($2R^2_{\mathrm{side},2}/R^2_{\mathrm{side},0}$, $-2R^2_{\mathrm{out},2}/R^2_{\mathrm{out},0}$, $-2R^2_{\mathrm{out},2}/R^2_{\mathrm{side},0}$, $2R^2_{\mathrm{os},2}/R^2_{\mathrm{side},0}$) increases with increasing pair transverce momentum k_{T} for all 3 centrality bins and slope of k_{T} dependence of $2R^2_{\mathrm{side},3}/R^2_{\mathrm{side},0}$ becomes slightly larger from central to peripheral.

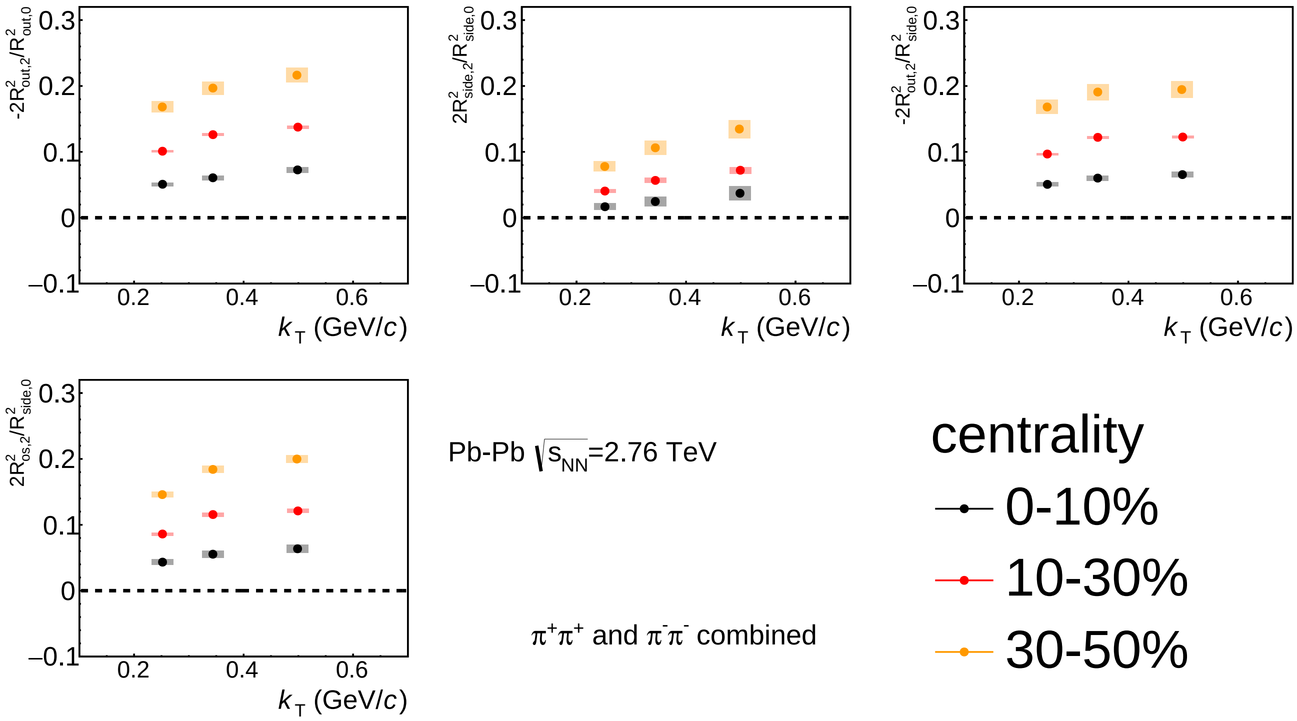

Figure 5.3: Relative amplitudes of squared HBT radii (R_{out}, R_{side}, and R_{os}) for charged pion pairs with respect to Ψ_2 as a function of pair transverse momentum k_T for 3 centrality bins measured in Pb-Pb collisions at $\sqrt{s_{\mathrm{NN}}}$ = 2.76 TeV. Dashed line indicates relative amplitude of HBT radii = 0. Transparent boxes represent the systematic uncertainties.

5.1.3 Relative amplitude of HBT radii with respect to Ψ_2 with ESE q_2 selection

Studying the centrality dependence of relative amplitude of HBT radii gives us the relation between initial and final source eccentricity. However when the centrality changes from central to peripheral collisions, not only the eccentricity but also a volume size, freeze-out temperature, and flow velocity change simultaneously. Event Shape Engineering technique, i.e. q_2 selection allows us to select the events which have more elliptical shape in the initial state within a certain centrality window. When we apply ESE selection to azimuthal angle dependence of HBT radii with respect to Ψ_2, more details study of the relation between initial and final source eccentricity can be expected.

Figure 5.4 shows relative amplitude of charged pion HBT radii (R_{out}, R_{side}, R_{long}, R_{os}, R_{ol} and R_{sl}) with respect to Ψ_2 with each 20% q_2 selection as a function of centrality , where 0-20% (80-100%) corresponds to the smallest (largest) q_2 bin. No significant modification with q_2 selection is found in relative amplitude of R_{long}, $R_{\mathrm{ol}}$and R_{sl}. The Relative amplitudes of R_{long}, $R_{\mathrm{ol}}$and R_{sl} don't depend on centrality and initial eccentricity. On the other hand, relative amplitude of R_{out} and R_{os} significantly changes with q_2 selection. Relative amplitude of R_{out} and R_{os} becomes larger from small q_2 to large q_2 and the variation by q_2 selection becomes largest at 30-40% centrality bin.

Also the relative amplitude of R_{side}, which is most sensitive to final source shape, shows a similar trend to that of R_{out} and R_{os}. But in most central 0-5% and smallest q_2 event selection, relative amplitude of R_{side} seems to show a negative value although it is consistent with zero within the systematic uncertainties. It might be a hint that the small elliptical shape by the smallest q_2 selection has vanished or even has been reversed with strong radial flow and elliptic flow.

Another interesting feature of q_2 dependence can be found in R_{side} oscillation in mid central collisions. The q_2 dependence of the relative amplitude of R_{side} shows a smilar behaviour to those of R_{out} and R_{os} except 20-40% centrality. Results for 20-40% centrality show a slight different trend although the uncertainties are large.

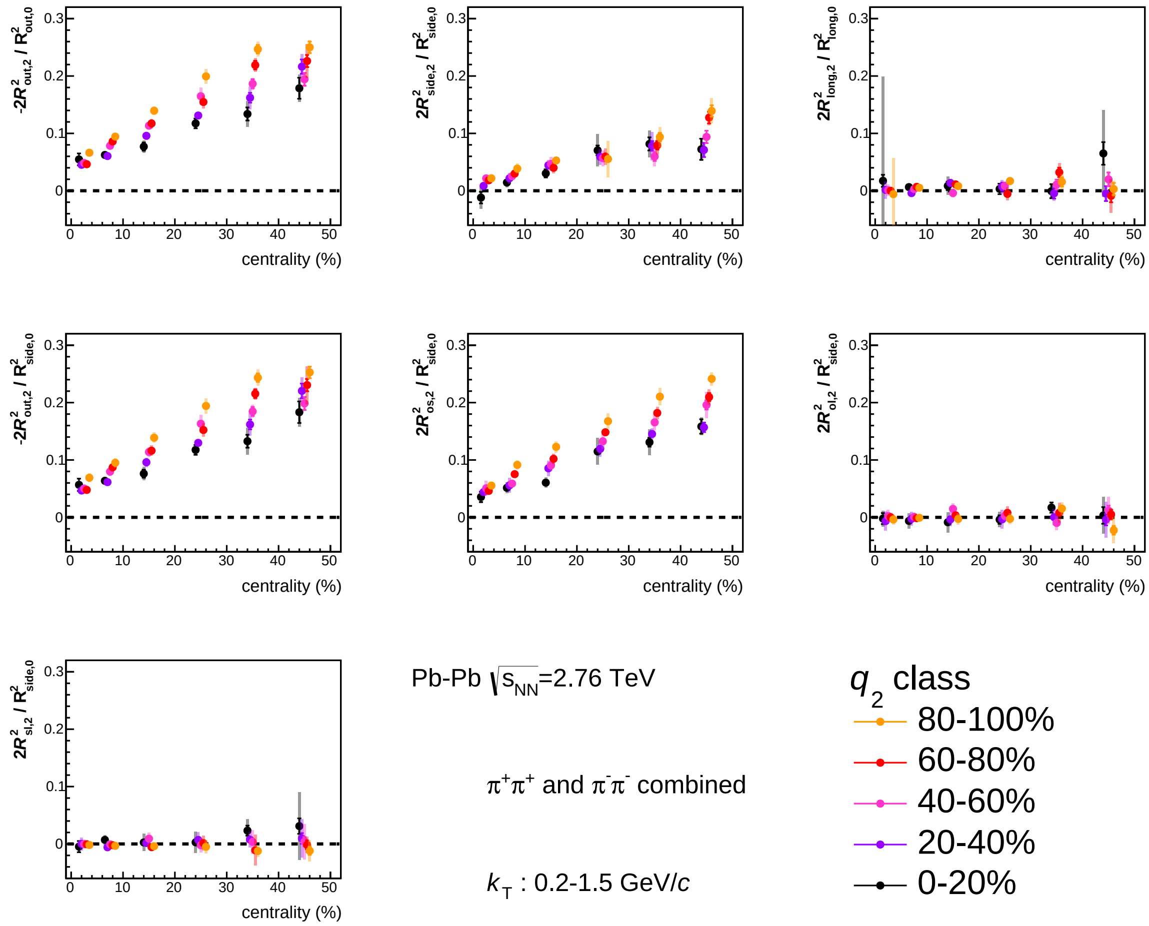

Figure 5.4: Each 20% q_2 selection is applied to relative amplitude of squared HBT radii (R_{out}, R_{side}, R_{long}, R_{os}, R_{ol} and R_{sl}) for charged pion pairs with respect to Ψ_2 as a function of centrality measured in Pb-Pb 2.76TeV collisions. Pair transverse momentum k_T is integrated from 0.2 to 1.5 GeV/c. Dashed line indicates relative amplitude of HBT radii = 0. Transparent boxes represent the systematic uncertainties. All points are shifted along the x-axis for visibility.

5.1.4 k_{T} dependence of relative amplitude of HBT radii with respect to Ψ_2 with ESE q_2 selection

In dynamically expanding source, study of k_{T} dependence of HBT radii is important to understand the system evolution.

Figure 5.5, 5.6, and 5.6 shows relative amplitudes of squared HBT radii (R_{out}, R_{side}, and R_{os}) of charged pion pairs with respect to Ψ_2 as a function of centrality measured in Pb-Pb 2.76TeV collisions for k_{T} 0.2-0.3, 0.3-0.4, and 0.4-1.5 GeV/c, respectively.

One can find that relative amplitude of R_{out} and R_{os} explicitly changes with q_2 selection. For all centrality bins and all k_{T} bins, relative amplitudes of R_{out} and R_{os} becomes larger from small

q_2 to large q_2 and the sensitivity to q_2 selection is largest at results of highest k_T .

In centrality 0-10 and 30-50%, relative amplitude of R_{side} shows the similar q_2 dependence to those of R_{out} and R_{os} . As is the case with Sec. 5.1.3, relative amplitude of R_{side} does not change with q_2 selection in mid-central collisions (10-30%) in low k_T 0.2-0.4 GeV/c. However relative amplitude of R_{side} of largest k_T becomes larger from small q_2 to large q_2 even in mid-central collisions.

Based on the Blast-wave model study, final source eccentricity can be extracted with relative amplitude of R_{side} at the limit as k_T approaches 0, which means that HBT radii in larger k_T becomes smaller with system expansion, and the obtained results shows that no q_2 dependence was found in smallest k_T . Therefore, in mid-central collisions (10-30%), it might indicate that final source eccentricity does not depend on the initial eccentricity due to the correlation between initial eccentricity and radial and elliptic flow.

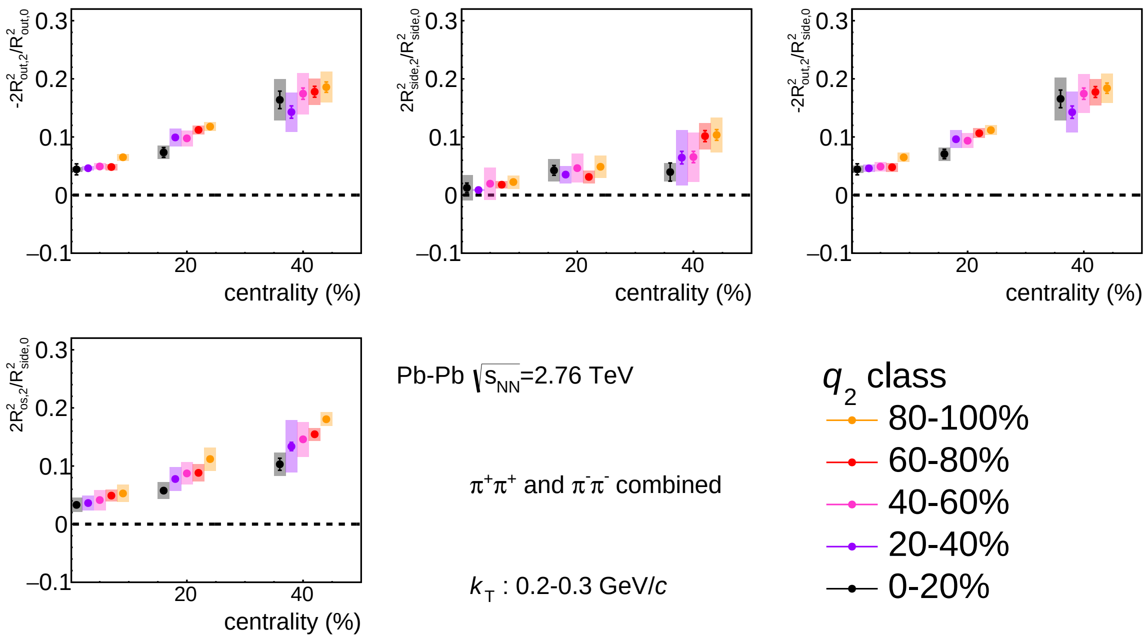

Figure 5.5: Each 20% q_2 selection is applied to relative amplitudes of squared HBT radii (R_{out}, R_{side}, and R_{os}) of charged pion pairs with respect to Ψ_2 for k_T 0.2-0.3 GeV/$c$as a function of centrality measured in Pb-Pb 2.76TeV collisions. Dashed line indicates relative amplitude of HBT radii = 0. Transparent boxes represent the systematic uncertainties. All points are shifted along the x-axis for visibility.

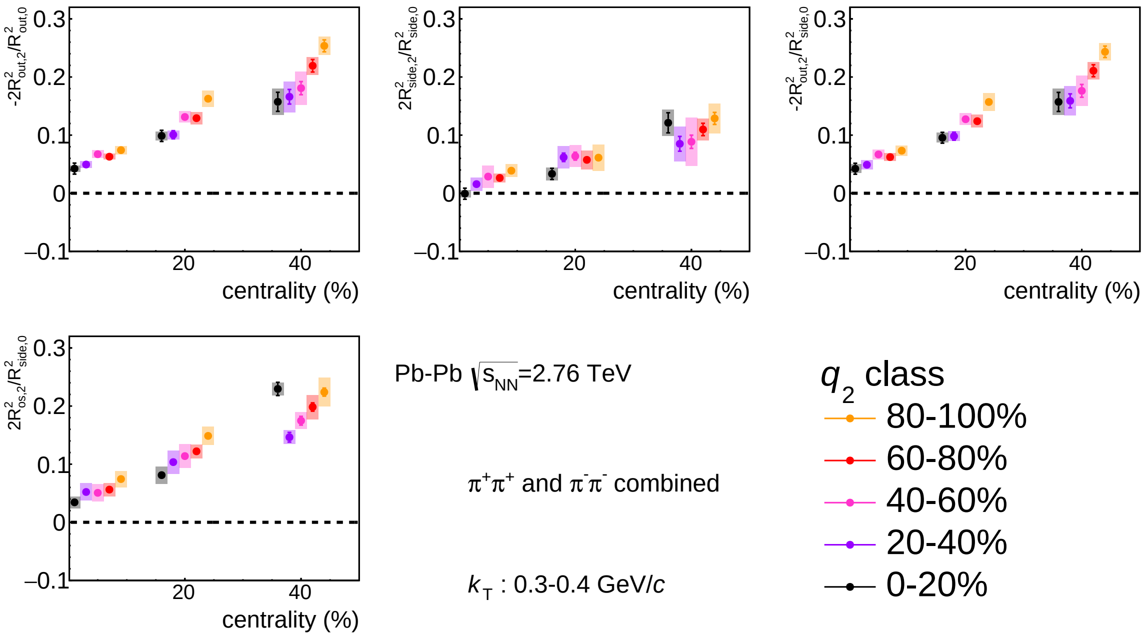

Figure 5.6: Each 20% q_2 selection is applied to relative amplitudes of squared HBT radii (R_{out}, R_{side}, and R_{os}) of charged pion pairs with respect to Ψ_2 for k_T 0.3-0.4 GeV/$c$as a function of centrality measured in Pb-Pb 2.76TeV collisions. Dashed line indicates relative amplitude of HBT radii = 0. Transparent boxes represent the systematic uncertainties. All points are shifted along the x-axis for visibility.

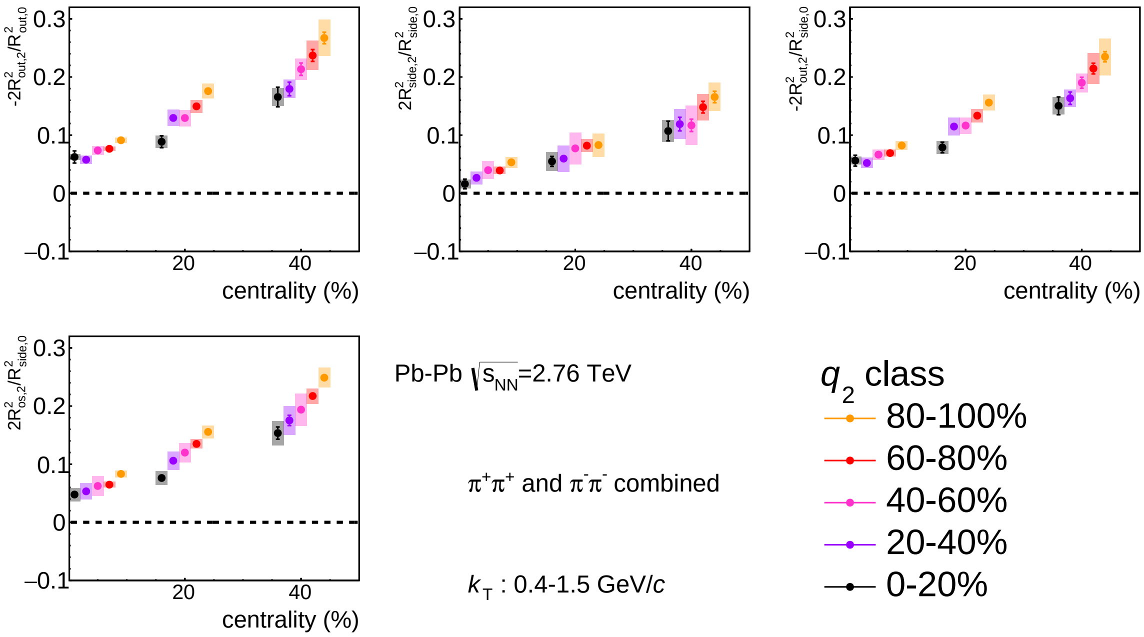

Figure 5.7: Each 20% q_2 selection is applied to relative amplitudes of squared HBT radii(R_{out}, R_{side}, and R_{os}) of charged pion pairs with respect to Ψ_2 for k_T 0.4-1.5 GeV/$c$as a function of centrality measured in Pb-Pb 2.76TeV collisions. Dashed line indicates relative amplitude of HBT radii = 0. Transparent boxes represent the systematic uncertainties. All points are shifted along the x-axis for visibility.

5.2 v_2 scaling of Final source eccentricity

Difference of the initial geometry within a certain centrality bin can not be selected by centrality. Therefore, in order to understand relation between initial eccentricity and final eccentricity, another probe for initial eccentricity is indispensable.

Figure 5.4 shows relative amplitude of charged pion HBT radii ($R_{\rm out}$, $R_{\rm side}$, $R_{\rm long}$, $R_{\rm os}$, $R_{\rm ol}$ and $R_{\rm sl}$) with respect to Ψ_2 with each 20% q_2 selection as a function of charged pion v_2. No q_2 selected results are simustaneously plotted as open markers. Azimuthal anisotropy (v_2) is sensitive probe to initial geometry and more preferable to use for x-axis than centrality.

Basically q_2 selection is event by event flow fluctuation selection and v_2 is strongly reflected by 20 % q_2 selection in Figure 4.3, thus x-axis is significantly changed even in a fixed centrality from Figure 5.4 to Figure 5.8. The relative amplitude of $R_{\rm out}$, $R_{\rm side}$ and $R_{\rm os}$ with q_2 selection has been observed to scale with v_2. Based on the Blast-wave model, relative amplitudes of $R_{\rm side}$, $R_{\rm out}$ and $R_{\rm os}$ are sensitive to the eccentricity in the final state. Therefore it indicates that azimuthal anisotropy in geometrical space ($2R^2_{side,2}/R^2_{side,2}$, -$2R^2_{out,2}/R^2_{side,2}$ and $2R^2_{os,2}/R^2_{side,2}$) and momentum space (v_2) are significantly correlated, and this correlation does not depend on event by event flow (initial geometry) fluctuation. One can find that -$2R^2_{out,2}/R^2_{side,2}$ is almost proportional to v_2, and intersept seems not to be zero. On the other hand, $2R^2_{out,2}/R^2_{side,2}$ has quadratic-like function rather than linear linear function and intersept is almost zero. $2R^2_{os,2}/R^2_{side,2}$ has similar shape to -$2R^2_{out,2}/R^2_{side,2}$.

The relation of azimuthal anisotropy v_2, eccentricity ε_2, and system size $N_{\rm part}^{\frac{1}{3}}$ (energy density $\frac{dN}{d\eta}$) are explored in various collision energy and geometry, and empirically elliptic flow can be defined by

$$v_2 = \varepsilon_2 \times f\left(\frac{dN}{d\eta}\right). \tag{5.2}$$

The amplitude of elliptic flow can be determined with initial geometry and system size.

ESE q_2 selection is applied with in a "fixed centrality", i.e. system size does not change with q_2 selection. Second order flow vector q_2 dependence of HBT radii modulation in a fixed centrality is driven by only the initial eccentricity.

Second order flow vector q_2 dependence of -$2R^2_{out,2}/R^2_{out,2}$ and $2R^2_{out,2}/R^2_{side,2}$ (slope as well as intercept) does not depend on centrality. Therefore relation between initial eccentricity and -$2R^2_{out,2}/R^2_{out,2}$ and $2R^2_{out,2}/R^2_{side,2}$ does not depend on centrality. Also q_2 dependence of

$2R^2_{side,2}/R^2_{side,2}$ does not depend on centrality in centrality 0-20% and 40-50%. However slope of $2R^2_{side,2}/R^2_{side,2}$ seems to be vanished in centrality 20-40$. It indicates that relation between initial eccentricity and $2R^2_{side,2}/R^2_{side,2}$(final eccentricity) might change with centrality. But this effect is negligible within the systematic uncertainties, thus more precise measurements are required.

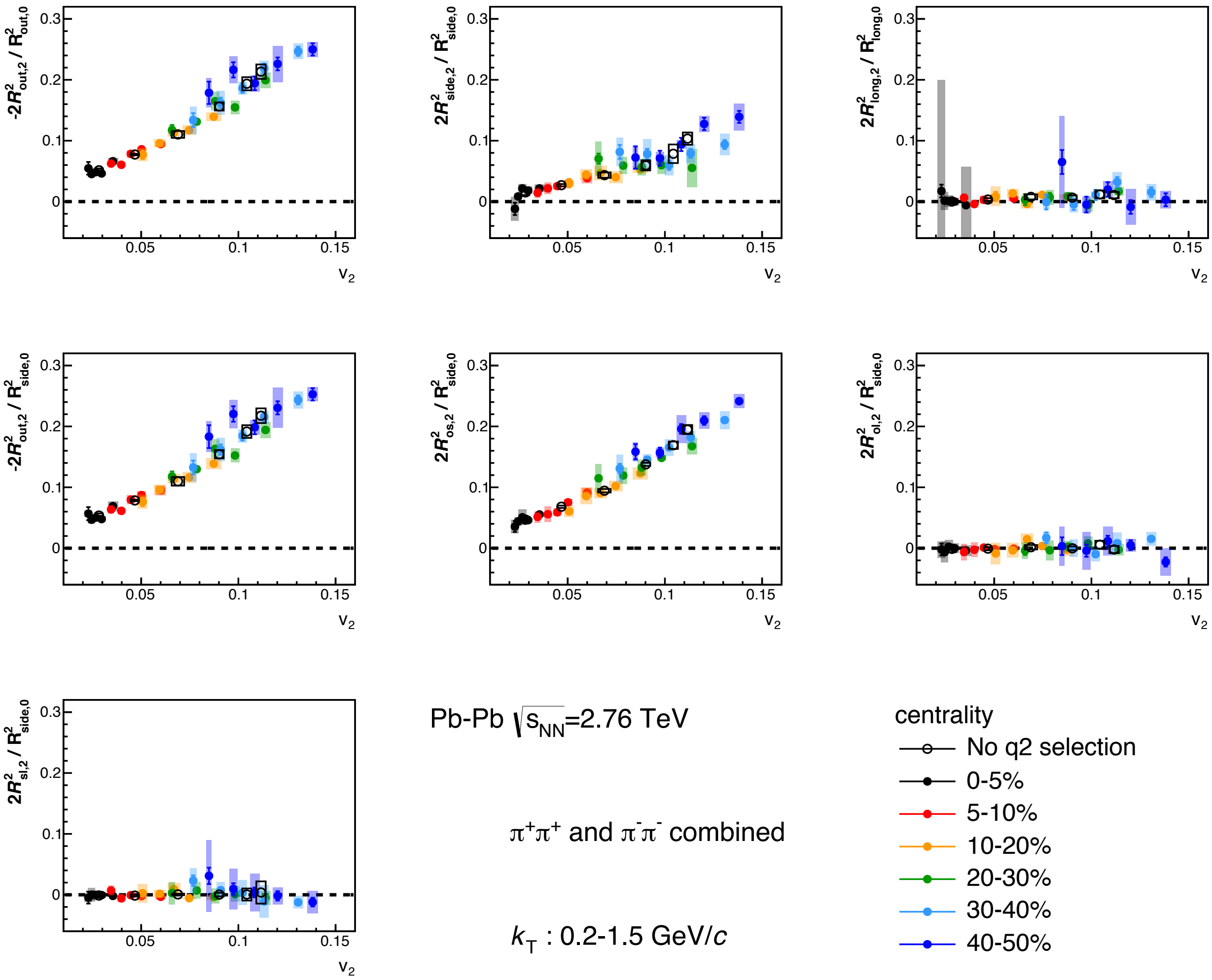

Figure 5.8: Each 20% q_2 selection, where 0-20% (80-100%) corresponds to the smallest (largest) q_2 bin, is applied to relative amplitude of squared HBT radii(R_{out}, R_{side}, R_{long}, R_{os}, R_{ol} and R_{sl}) for charged pion pairs with respect to Ψ_2 as a function of charged pion v_2 measured in Pb-Pb 2.76TeV collisions. Pair transverse momentum k_T is integrated from 0.2 to 1.5 GeV/c. Dashed line indicates relative amplitude of HBT radii = 0. Transparent boxes represent the systematic uncertainties. Relative amplitude of HBT radii without q_2 selection also dipicted as open black circle.

5.3 Interpretation of initial eccentricity difference with Blast-wave Model

In order to understand the effect of q_2 selection to relative amplitude of HBT radii with respect to Ψ_2, Blast-wave model approach which is extended to HBT correlation[63] is applied.

Blast-wave model is analytical method to extract the parameters of freeze out configuration to fit the particle spectra and azimuthal anisotropy. In this thesis, extended Blast-wave model suggested in [63] is applied. In this model, freeze out configuration is expressed with 8 parameters listed below.

- T_{f} : Freeze out temperature
- ρ_0 : Transverse flow velocity
- ρ_2 : 2^{nd}-order oscillation of transverse flow
- R_x : Source size along the event plane
- R_y : Source size perpendicular to the event plane
- α_s : Surface diffuseness of the emission source
- τ_0 : Freeze out time
- $\Delta\tau$: emission duration

Transverse source size is determined with R_x and R_y, and weighting function of source shape is given by

$$\Omega\left(r,\phi_s\right) = \frac{1}{1+e^{(\tilde{r}-1)/\alpha_s}}, \tag{5.3}$$

where α_s is surface diffuseness of the emission source and ϕ_s indicates the spatial azimuthal angle of emission point which is given by

$$\tan\left(\phi_s\right) = \left(\frac{R_y}{R_x}\right)^2 \tan\left(\phi_b\right), \tag{5.4}$$

where ϕ_b indicates the azimuthal direction of the boost. In this model, the boost angle is perpendicular to the elliptical sub-shell on which the source element is found. $\tilde{r}$ is normalized elliptical radius expressed by

Table 5.1: Fit ranges for identified hadron spectra, v_2, and HBT radii

	Spectra		
	π^+ and π^-	K^+ and K^-	p and $\bar{p}$
p_{T} (GeV/c)	0.5 - 1.13	0.4 - 1.4	0.6 - 1.69
	v_2		
	π^+ and π^-	K^+ and K^-	p and $\bar{p}$
p_{T} (GeV/c)	0.5 - 1.13	0.4 - 1.4	0.6 - 1.69
	HBT radii		
	π^+ and π^-	K^+ and K^-	p and $\bar{p}$
$\langle k_{\mathrm{T}} \rangle$ (GeV/c)	0.415		

$$\tilde{r}(r, \phi_s) \equiv \sqrt{\frac{(r\cos(\phi_s))^2}{R_x^2} + \frac{(r\sin(\phi_s))^2}{R_y^2}}. \tag{5.5}$$

Transverse flow velocity profile is expressed as follows :

$$\rho(r, \phi_s) = \tilde{r}(\rho_0 + \rho\cos(2\phi_b)). \tag{5.6}$$

In this thesis, identified hadron(π, K, p) spectra, identified hadron(π, K, p) v_2 and azimuthal angle dependence of charged pion HBT radii relative to Ψ_2 are used to Blast-wave fit. The sensitivity of spectra, v_2 and HBT radii to determine freeze-out parameters are quit different. For example, spectra shape is determined with T_{f} and ρ_0, and v_2 is sensitive to ρ_2 and R_x/R_y in particular. HBT radii are sensitive to all parameters, but R_{side} is independent of τ_0 and $\Delta\tau$. Therefore in order to constrain the fitting, T_{f} and ρ_0 are determined with spectra fitting and the other parameters are extracted with simultaneous fitting v_2 and azimuthal angle dependence of HBT radii with respect to Ψ_2, fixing the parameters T_{f} and ρ_0 obtained with spectra fitting. The surface diffuseness parameter is set to be 0 as default. The fit ranges of spectra, v_2 and azimuthal angle dependence of HBT radii are shown in Table. 5.1.

Figure 5.9 shows the Blast-wave fitting to identified hadron spectra. Positive and negative pions, kaons, and protons are fitted simultaneously. The fitting functions reproduce the data for each particle species well.

Figure 5.10 shows the Blast-wave fitting to identified hadron (pions, kaons, and protons) v_2 with 40-60% q_2 selection applied as a function of p_{T} . In all centrality, pions and kaons v_2 are well reproduced with this model up to p_{T} 1-2GeV/$c$depending on the particle species. But protons v_2 at low p_T is underestimated with Blast-wave model.

Figure 5.11 shows the Blast-wave fitting to azimuthal angle dependence of R_{out} , R_{side} , R_{long} and R_{os} with 40-60% q_2 selection applied as a function of centrality. In all centrality, R_{out} and R_{long} are well described with Blast-wave model for both average HBT radii and oscillation amplitude, while oscillation amplitude of R_{side} and R_{os} in Blast-wave model is overestimated.

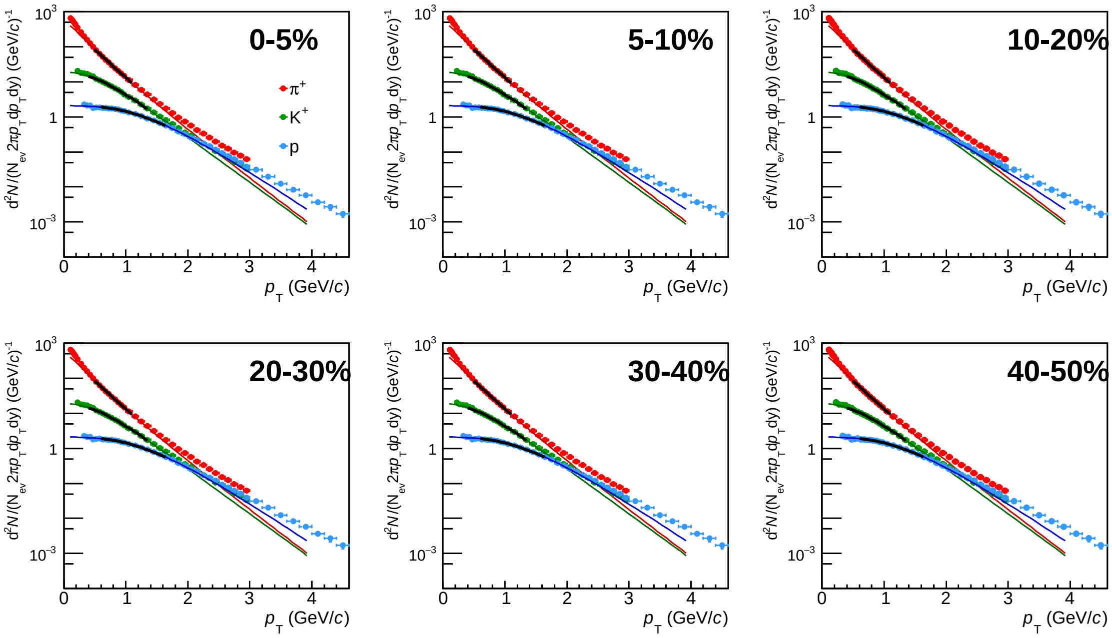

Figure 5.9: Blast-wave fitting to identified particle(π, K and p) p_T spectra as a function of centrality[9]. Difference of panels denote centrality. Error bar indicates quadratic sum of static and systematic uncertainties. Black lines shows the actual fit range and red, green and blue lines are extrapolated line of fitting functions for π, K and p, respectively.

5.3.1 Extracted parameters of freeze out configuration with Blast-wave model

Figure 5.12 shows the extracted freeze out parameters (T_f, ρ_0, rho_2, R_x^2, R_x^2/R_y^2, τ, and $\Delta\tau$) as a function of average number of participant calculated with Glauber model. No q_2 selections are applied to spectra, v_2, and HBT measurements.

The freeze-out temperature (T_f) slightly decreases with increasing $\langle N_{part} \rangle$ and flow velocity (ρ_0) becomes larger from small $\langle N_{part} \rangle$ to large $\langle N_{part} \rangle$. Source size at freeze out (R_x^2) and freeze out time (τ) becomes larger from small $\langle N_{part} \rangle$ to large $\langle N_{part} \rangle$. Also emission duration $\Delta\tau$ becomes slightly larger from small $\langle N_{part} \rangle$ to large $\langle N_{part} \rangle$. Eccentricity of final source

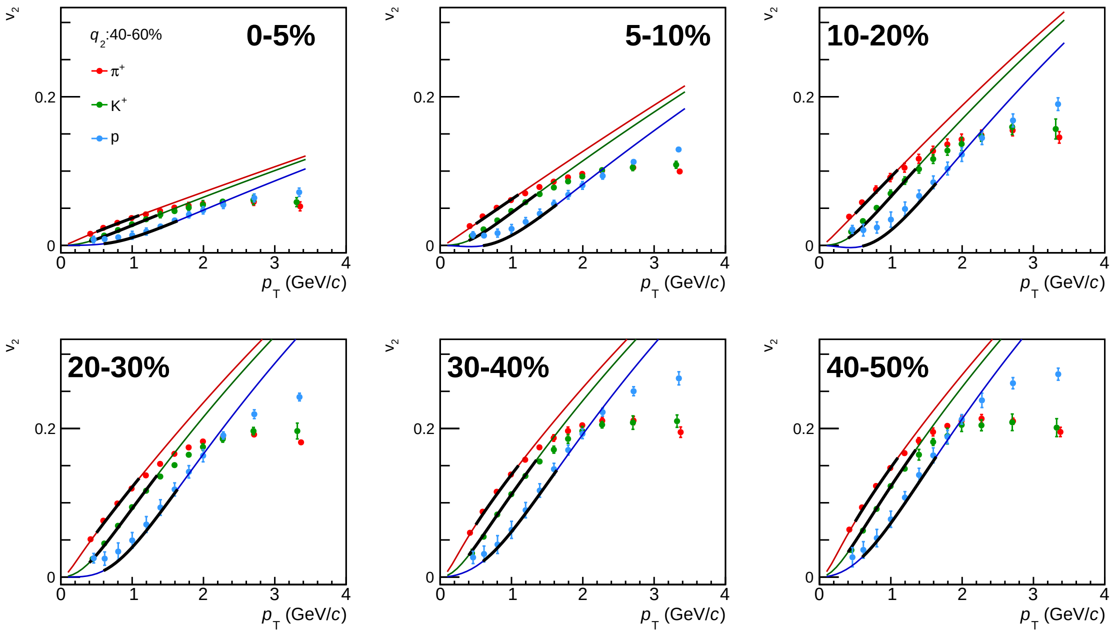

Figure 5.10: Blast-wave fitting to identified particle(π, K and p) v_2 with 40-60% q_2 selection as a function of p_{T} . Difference of panels denote centrality. Error bar indicates quadratic sum of static and systematic uncertainties. Black lines shows the actual fit range and red, green and blue lines are extrapolated line of fitting functions for π, K and p, respectively.

(R_x^2/R_y^2) increases with increasing $\langle N_{part}\rangle$.

Figure 5.13 shows the extracted freeze out parameters (T_{f}, ρ_0 , rho_2, R_x^2, R_x^2/R_y^2, τ and $\Delta\tau$) as a function of average number of participant calculated with Glauber model. For each 20% q_2 selections are applied to v_2 and HBT measurements. Spectra also changes slightly with q_2 selection, but the difference is expected to be smaller than systematic uncertainties. In this thesis, we assumes that temperature and ρ_0 do not depend on q_2 selection.

Second order modulation of flow radipidity ρ_2 becomes explicitly larger (smaller) with larger (smaller) q_2 selection. By applying Event Shape Engineering q_2 selection, v_2 is largely enhanced or suppressed, and ρ_2 is sensitive to v_2. Thus this behavior can be understood that such a correlation between v_2 and $\langle N_{part}\rangle$ dependence of ρ_2 is very similar to that of v_2. But No significant modification to R_x^2, τ and $\Delta\tau$ by q_2 selection is found. System life time (tau) and ellipticity (R_x^2/R_y^2) slightly changes with q_2 selection, i.e. tau and R_x^2/R_y^2 in large q_2 selection tends to have larger value than those in small q_2 selection. It indicates that not only velocity field but also eccentricity at freeze-out and system life time could be modified with different initial shape. But it is negligible within the systematic uncertainties.

However this Blast Wave model could not reproduce small oscillation of R_{side} , thus in order to understand geometrical information R_x^2 and R_x^2/R_y^2 , more realistic model is necessary.

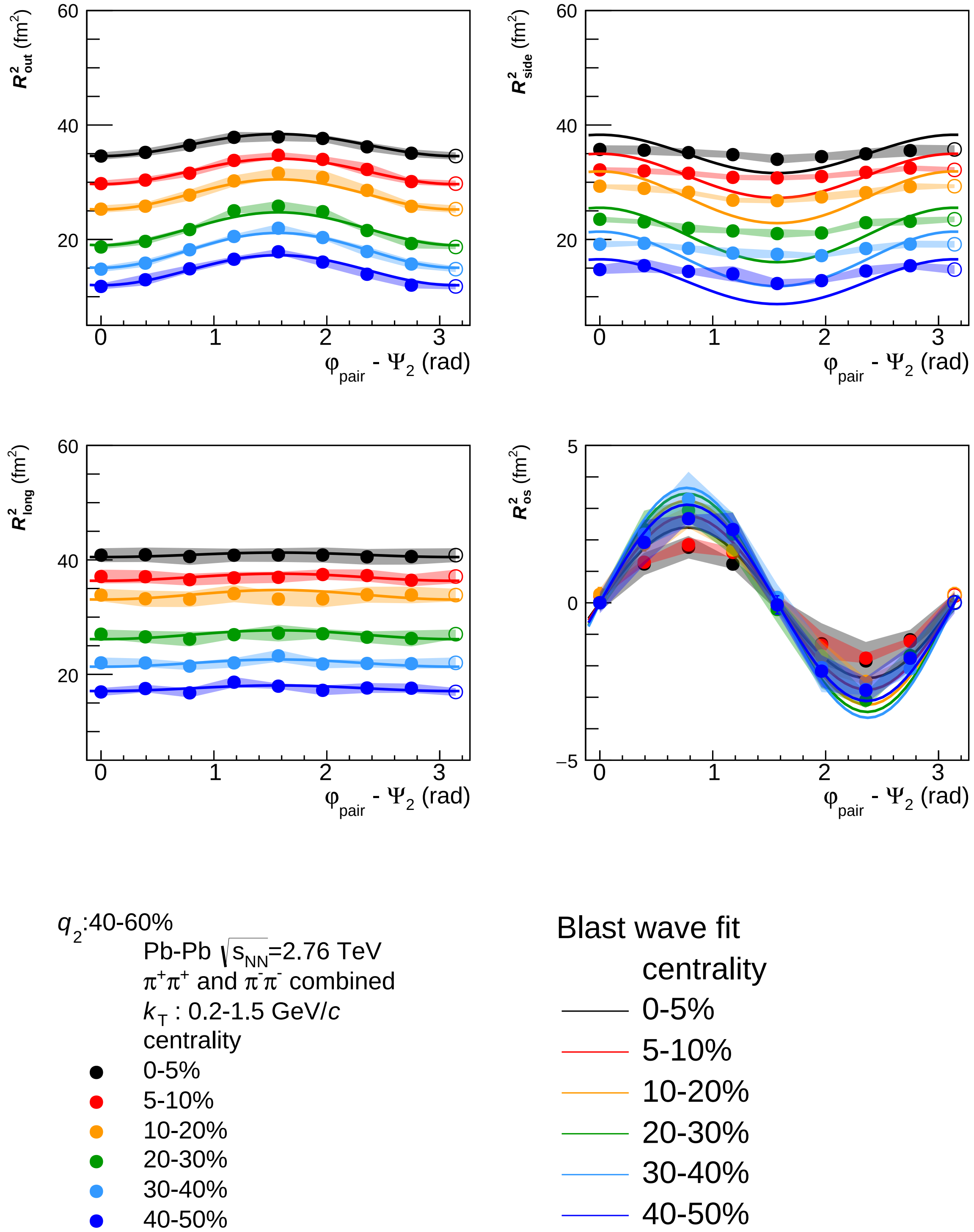

Figure 5.11: Blast-wave fitting to azimuthal angle dependence of R_{out} , R_{side} , R_{long} and R_{os} with 40-60% q_2 selection as a function of centrality. Systematic uncertainties are shown as transparent bands and statistical uncertainties are smaller than marker size.

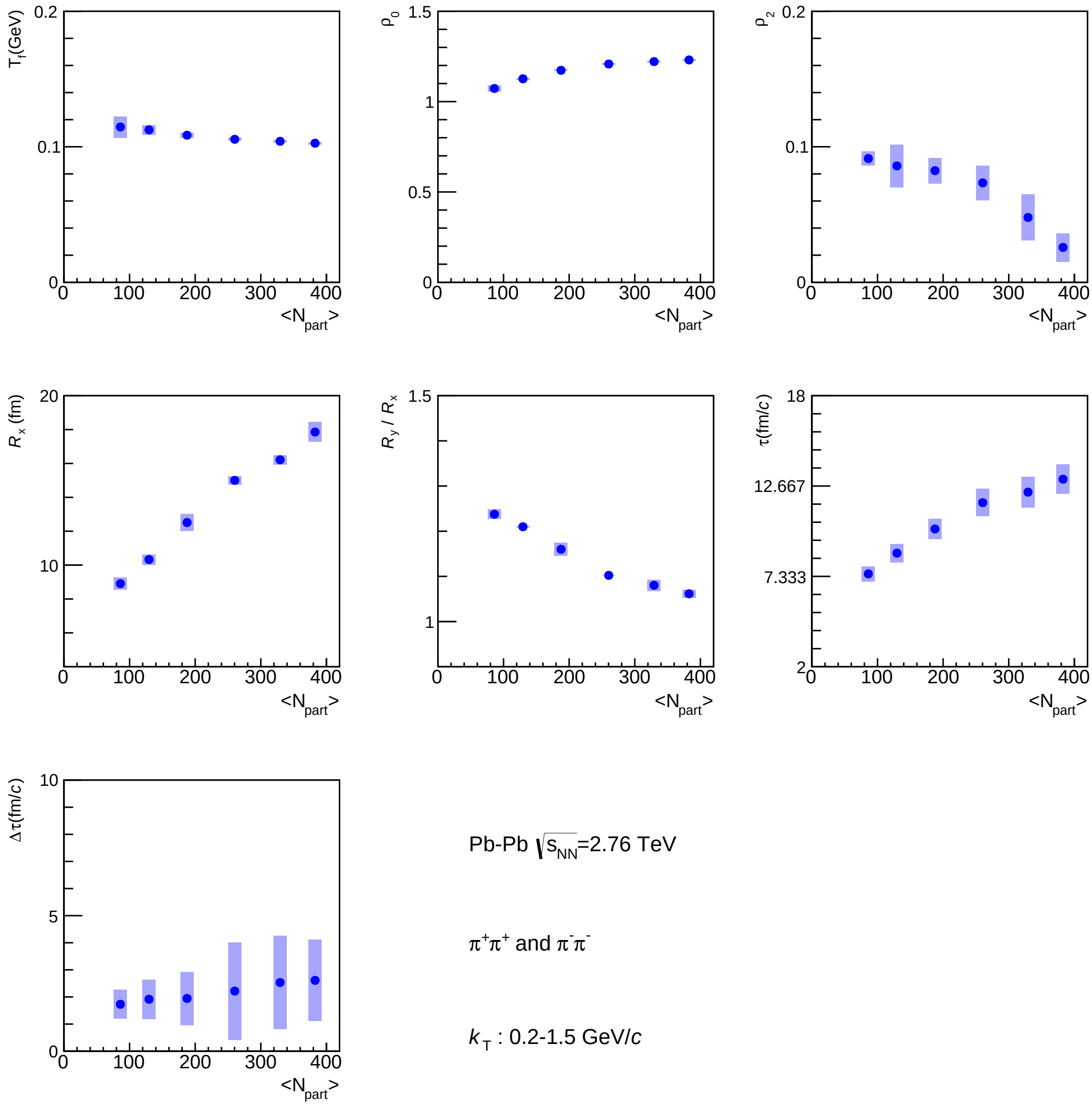

Figure 5.12: Extracted freeze out parameters with Blast Wave fitting to spectra, v_2 and HBT as a function of average number of participant calculated with Glauber model without q_2 selection. T_f and ρ_0 are extracted by fitting π, K and p spectra, and the other parameters are obtained with simultaneous fitting π, K and p v_2 and charged pion HBT radii (R_out , R_side , R_long , and R_os) with respect to Ψ_2.

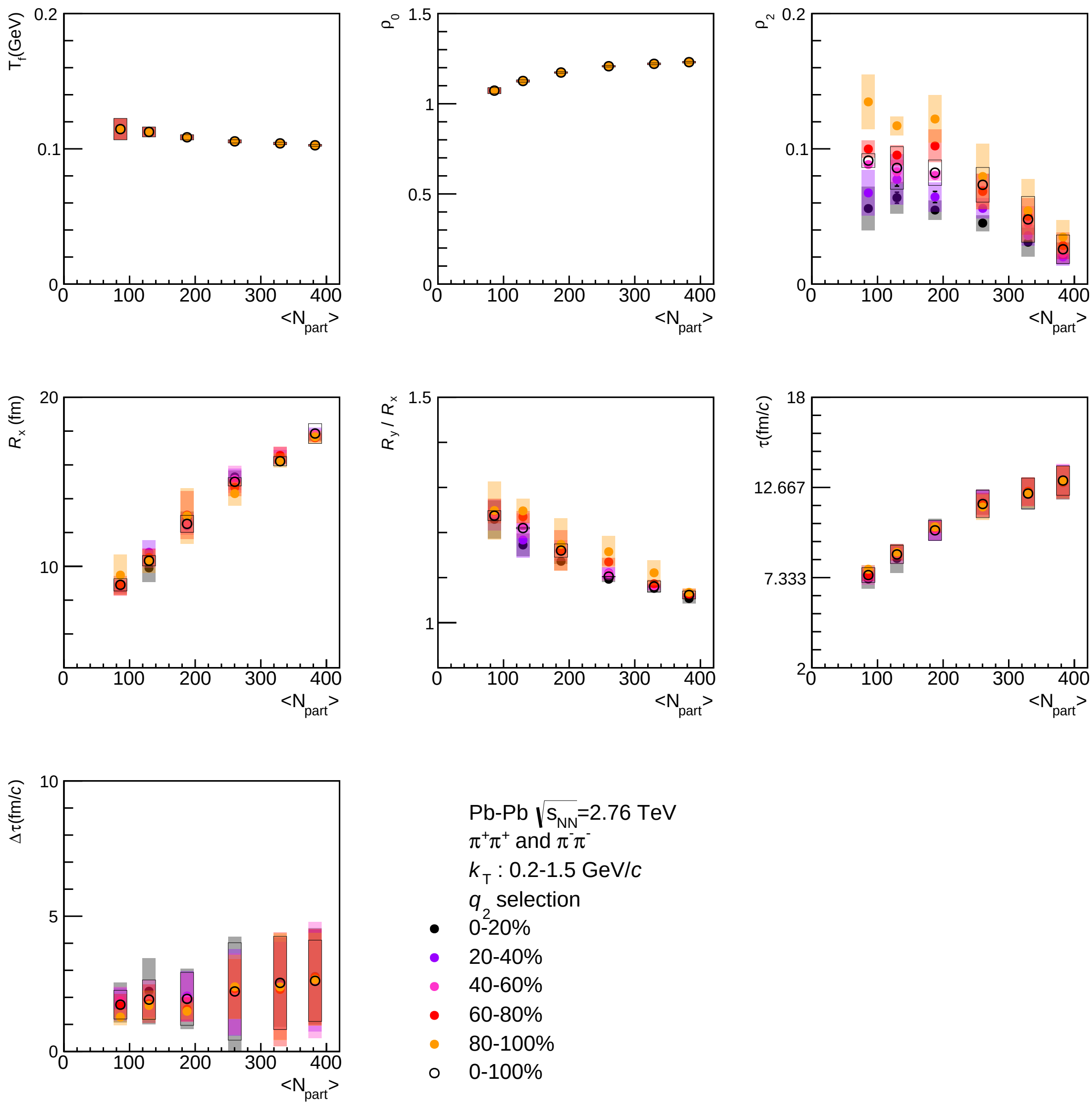

Figure 5.13: Extracted freeze out parameters with Blast Wave fitting to spectra, v_2 and HBT as a function of average number of participant calculated with Glauber model with each 20% q_2 selection. No q_2 selected results are simultaneously dipicted as open black circle. T_f and ρ_0 are extracted by fitting π, K and p spectra, and the other parameters are obtained with simultaneous fitting π, K and p v_2 and charged pion HBT radii (R_{out} , R_{side} , R_{long} , and R_{os}) with respect to Ψ_2.

5.4 Final source triangular shape

PHENIX performed the first measurement of azimuthal angle dependence of charged pion HBT radii with respect to Ψ_3 [32], and relative amplitude of R_{out} has positive or zero and relative amplitude of R_{side} has negative or zero value. In order to extract the final source triangular shape, it is important to determine whether the relative amplitude of HBT radii with respect to Ψ_3 is positive or negative (or even zero).

Compared to Ψ_2 dependence, initial source triangular shape and triangular flow signal is much smaller. Therefore extraction of final source triangular shape is much more difficult. In LHC-ALICE experiment, owing to large multiplicity and excellent event plane resolution at forward detector, more detailed study of the final source triangular shape can be performed. In this section, the first measurement of azimuthal angle dependence of charged pion HBT radii measured in Pb-Pb collisions at 2.76 TeV are presented.

5.4.1 Centrality dependence of relative amplitude of HBT radii with respect to Ψ_3

Figure 5.14 shows relative amplitude of squared HBT radii for charged pion pairs with respect to Ψ_3 as a function of centrality obtained with Figure 4.27. Pair transverse momentum k_T is integrated from 0.2 to 1.5 GeV/c, where the mean k_T is approximately 0.4 GeV/c. Relative amplitude of R_{long}, R_{ol}, and R_{sl} is almost zero for all centrality within the systematic uncertainty. Relative amplitude of R_{out} has explicitly positive value and slightly increases from central to peripheral collisions. Positive oscillation amplitude and this centrality dependence is very similar to R_{out} oscillation with respect to Ψ_2, though oscillation amplitude of Ψ_3 is much smaller than that of Ψ_3, and relative amplitude of R_{side} has negative value in all centrality and center values slightly increase from central to peripheral. Relative amplitude of R_{os} cross term has positive or zero value and no significant centrality dependence can be found. In ALICE, explicit oscillation signals with respect to Ψ_3 and small centrality dependence are obtained.

Contrary to HBT measurement with respect to Ψ_2, $-2R^2_{out,3}/R^2_{out,0}$($-2R^2_{out,3}/R^2_{side,0}$) is positive and $2R^2_{side,3}/R^2_{side,0}$ is negative. This feature can also be found in the relative amplitude of HBT radii with respect to Ψ_2 in most central 0-5% collisions and smallest q_2 class in Figure 5.8. Common point between two different measurement are "small eccentricity in the initial state".

Therefore, when the initial geometrical source shape is almost round shape, relative amplitude of R_{out} and R_{side} has same negative sign.

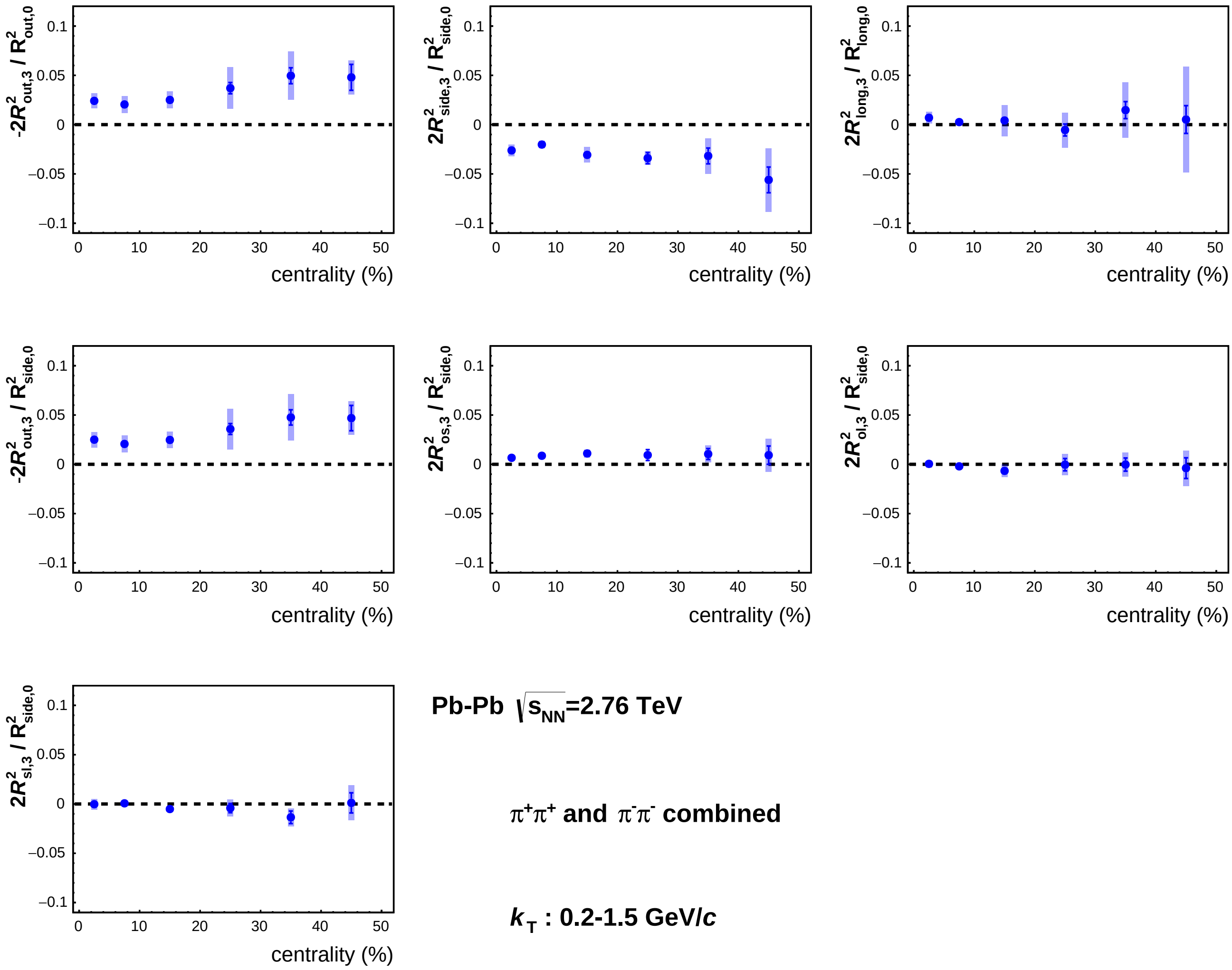

Figure 5.14: Relative amplitude of squared HBT radii(R_{out} , R_{side} , R_{long} , R_{os} , R_{ol} and R_{sl}) for charged pion pairs with respect to Ψ_3 as a function of centrality measured in Pb-Pb 2.76TeV collisions. Pair transverse momentum k_T is integrated from 0.2 to 1.5 GeV/c. Dashed line indicates relative amplitude of HBT radii = 0. Transparent blue boxes represent the systematic uncertainties.

5.4.2 k_T dependence of final source eccentricity

Figure 5.15 shows relative amplitudes of squared HBT radii for charged pions with respect to Ψ_3 as a function of pair pair transverse momentum k_{T}. Pair transverse momentum is divided for 3 bins (0.2-0.3, 0.3-0.4, 0.4-1.5GeV/c).

Relative amplitude of R_{out} ($-2R^2_{\mathrm{out},3}/R^2_{\mathrm{out},0}$ and $-2R^2_{\mathrm{out},3}/R^2_{\mathrm{side},0}$) slightly increases with increasing pair transverce momentum k_T in centrality 0-30%.

Relative amplitude of R_{side} ($-2R^2_{side,3}/R^2_{side,0}$) slightly decreases from low k_T to high k_T in centrality 0-10%, but no significant k_T dependence can be found in the other centrality bins (10-50%).

Relative amplitude of R_{os} ($-2R^2_{os,3}/R^2_{side,0}$) increases from low k_T to high k_T in all centrality bins and the slopes become larger from central to peripheral collisions.

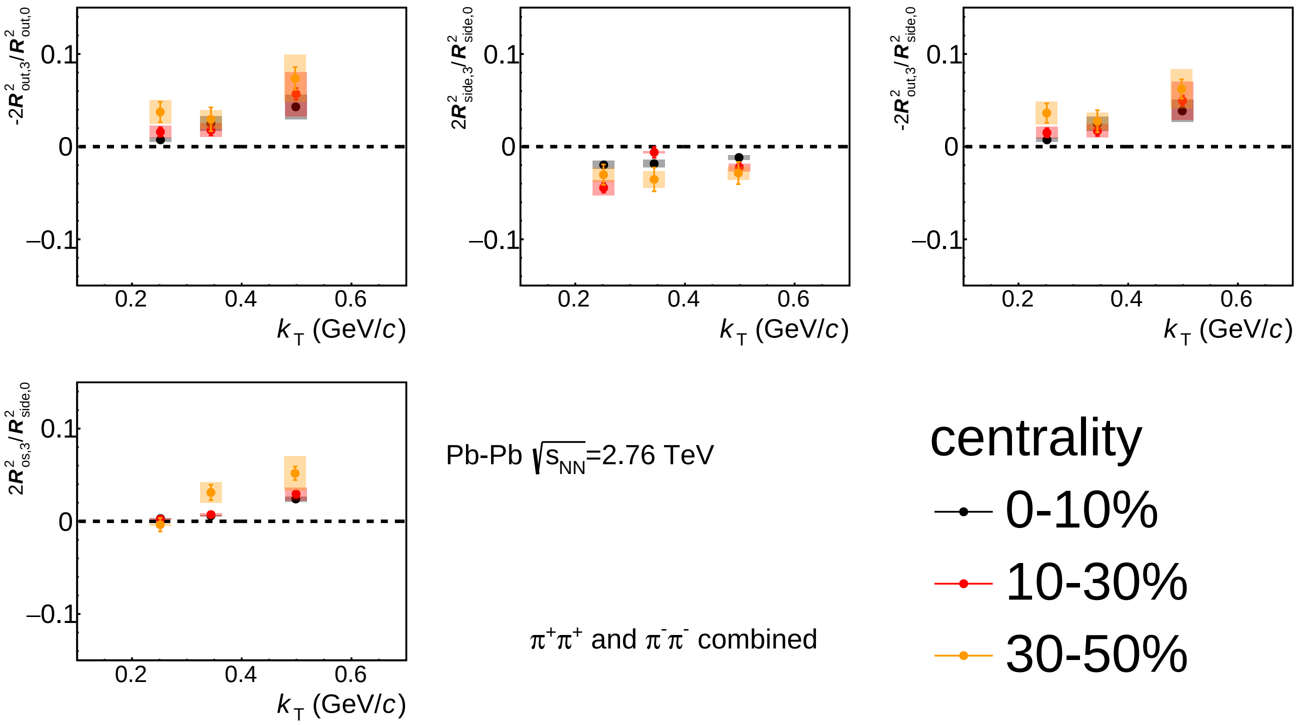

Figure 5.15: Relative amplitudes of squared HBT radii (R_{out}, R_{side}, and R_{os}) for charged pion pairs with respect to Ψ_3 as a function of pair transverse momentum k_T for 3 centrality bins measured in Pb-Pb collisions at $\sqrt{s_{NN}}$ = 2.76 TeV. Dashed line indicates relative amplitude of HBT radii = 0. Transparent boxes represent the systematic uncertainties.

5.4.3 Relative amplitudes of HBT radii relative to Ψ_3 with q_3 selection

The results of v_3 measurements with each 20% q_3 selection shows an explicit difference from v_3 without q_3 selection, which means the initial triangular shape can be selected with this q_3 selection. It indicates that event by event triangular flow fluctuation could be selected with q_3 selection. Model comparison with relative amplitude of HBT radii with respect to Ψ_3 at PHENIX suggests that oscillation of HBT radii comes mostly from triangular flow. But the relation between triangular flow and oscillation of HBT radii is still not observed experimentally. Measurements of azimuthal angle dependence of HBT radii relative to Ψ_3 with q_3 selection give us the direct approach to the relation between triangular flow and 3$^{\rm rd}$-order modulation of HBT radii.

Figure 5.16 shows relative amplitudes of charged pion HBT radii ($R_{\rm out}$, $R_{\rm side}$, $R_{\rm long}$, $R_{\rm os}$, $R_{\rm ol}$, and $R_{\rm sl}$) with respect to Ψ_3 with each 20% q_3 selection as a function of centrality. No significant modification with q_3 selection is found in relative amplitude of all HBT radii within the systematic uncertainties, though v_3 changes with q_3 selection.

Simulation result from a Gaussian toy model suggests oscillation amplitude of HBT radii with respect to Ψ_3 are dominated by triangular flow[33]. If q_3 cut can select amplitude of triangular flow, oscillation amplitude of HBT radii should change.

Three possibilities can be considered to interpret the q_3 dependence. First possibility is q_3 selectivity is not sufficient to modify the oscillation amplitude of HBT radii with respect to Ψ_3. Sensitivity of initial triangular shape can be different between HBT measurement and flow measurement. In central collisions, Ψ_3 resolution is good, but the signal of v_3 itself is smallest, whereas the signal of v_3 is relatively large and Ψ_3 resolution is not so good in peripheral. Thus our experimental precision might be insufficient to see the variation.

Second possibility is oscillation amplitude of HBT radii with respect to Ψ_3 are not dominated by triangular flow. Third possibility is triangular flow is not originated from hydrodynamical expansion.

In order to reveal relation between v_3 and relative amplitude of HBT radii with respect to Ψ_3, comparison with realistic model simulation are necessary.

5.4.4 k_T dependence of relative amplitude of HBT radii with respect to Ψ_3 with ESE q_3 selection

Figure 5.17, 5.18, and 5.18 shows relative amplitudes of squared HBT radii (R_{out}, R_{side}, and R_{os}) of charged pion pairs with respect to Ψ_3 as a function of centrality measured in Pb-Pb 2.76TeV collisions for k_T 0.2-0.3, 0.3-0.4, and 0.4-1.5 GeV/c, respectively.

For the lowest k_T bin (0.2 - 0.3 GeV/c), no significant q_3 dependence can be found in relative amplitude of R_{out} and R_{os} (-$2R^2_{out,3}/R^2_{out,0}$, and -$2R^2_{out,3}/R^2_{side,0}$, and $2R^2_{os,3}/R^2_{side,0}$). Relative amplitudes of R_{out} and R_{os} are positive or almost zero. In centrality 0-30%, relative amplitude of R_{side} decreases with increasing q_3.

In mid and high k_T bins (0.3 - 1.5 GeV/c), no significant q_3 dependence can be found for relative amplitudes of R_{out}, R_{side}, and R_{os}).

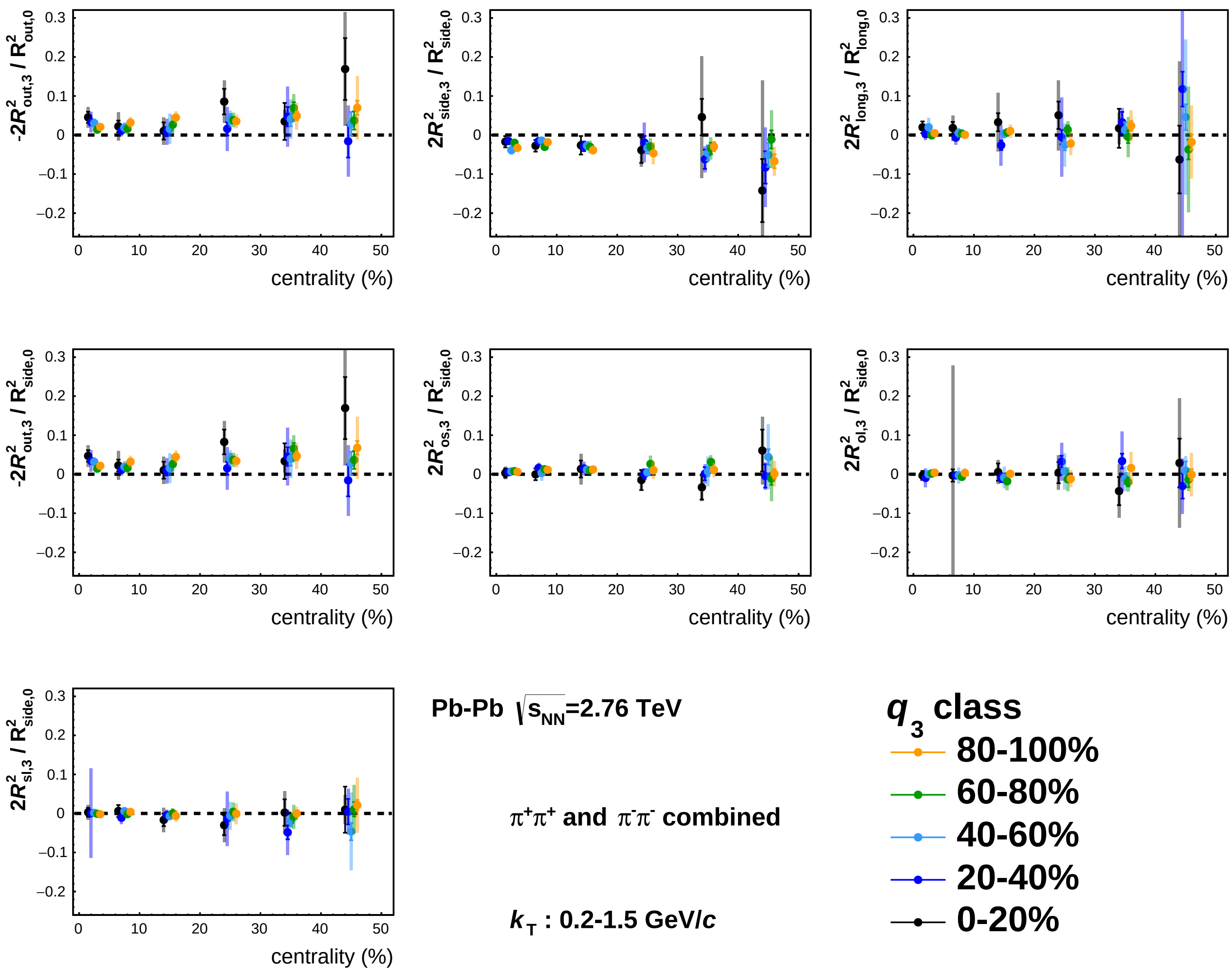

Figure 5.16: Each 20% q_3 selection is applied to relative amplitude of squared HBT radii(R_{out}, R_{side}, R_{long}, R_{os}, R_{ol}, and R_{sl}) for charged pion pairs with respect to Ψ_3 as a function of centrality measured in Pb-Pb 2.76TeV collisions. Pair transverse momentum k_T is integrated from 0.2 to 1.5 GeV/c. Dashed line indicates relative amplitude of HBT radii = 0. Transparent boxes represent the systematic uncertainties. All points are shifted along the x-axis for visibility.

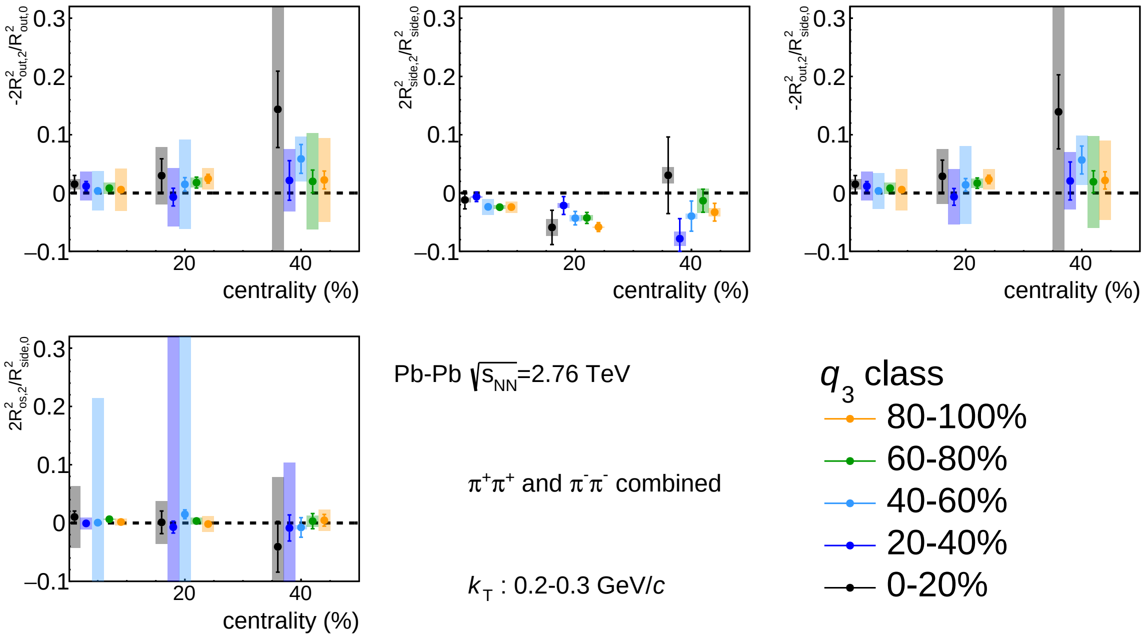

Figure 5.17: Each 20% q_2 selection is applied to relative amplitudes of squared HBT radii (R_{out}, R_{side}, and R_{os}) of charged pion pairs with respect to Ψ_3 for k_T 0.2-0.3 GeV/$c$as a function of centrality measured in Pb-Pb 2.76TeV collisions. Dashed line indicates relative amplitude of HBT radii = 0. Transparent boxes represent the systematic uncertainties. All points are shifted along the x-axis for visibility.

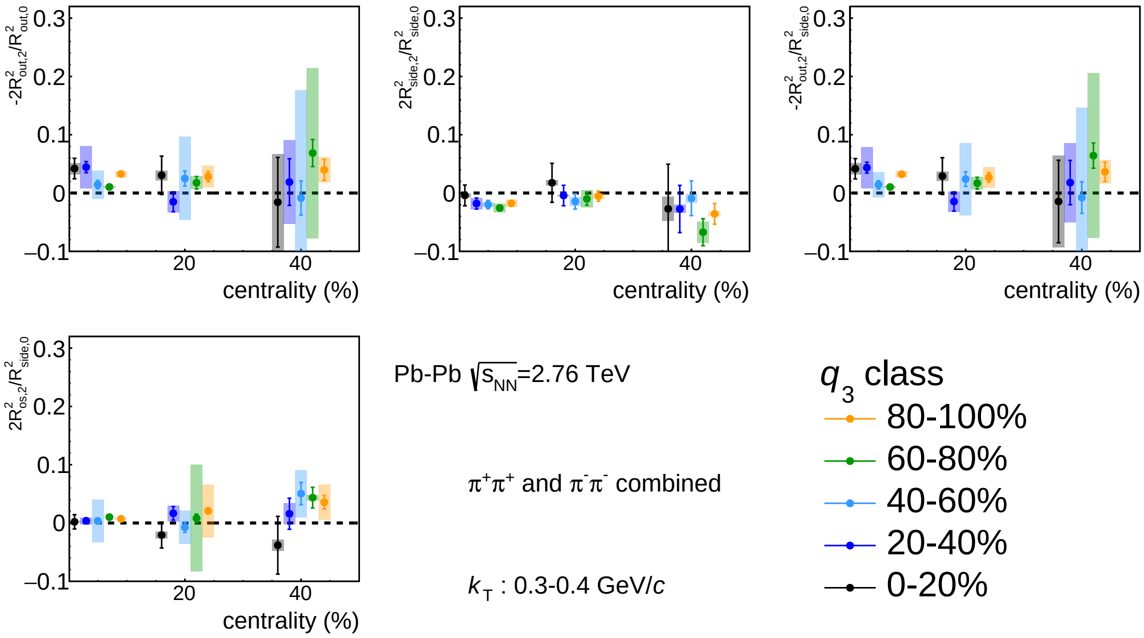

Figure 5.18: Each 20% q_3 selection is applied to relative amplitudes of squared HBT radii (R_{out}, R_{side}, and R_{os}) of charged pion pairs with respect to Ψ_3 for k_T 0.3-0.4 GeV/$c$as a function of centrality measured in Pb-Pb 2.76TeV collisions. Dashed line indicates relative amplitude of HBT radii = 0. Transparent boxes represent the systematic uncertainties. All points are shifted along the x-axis for visibility.

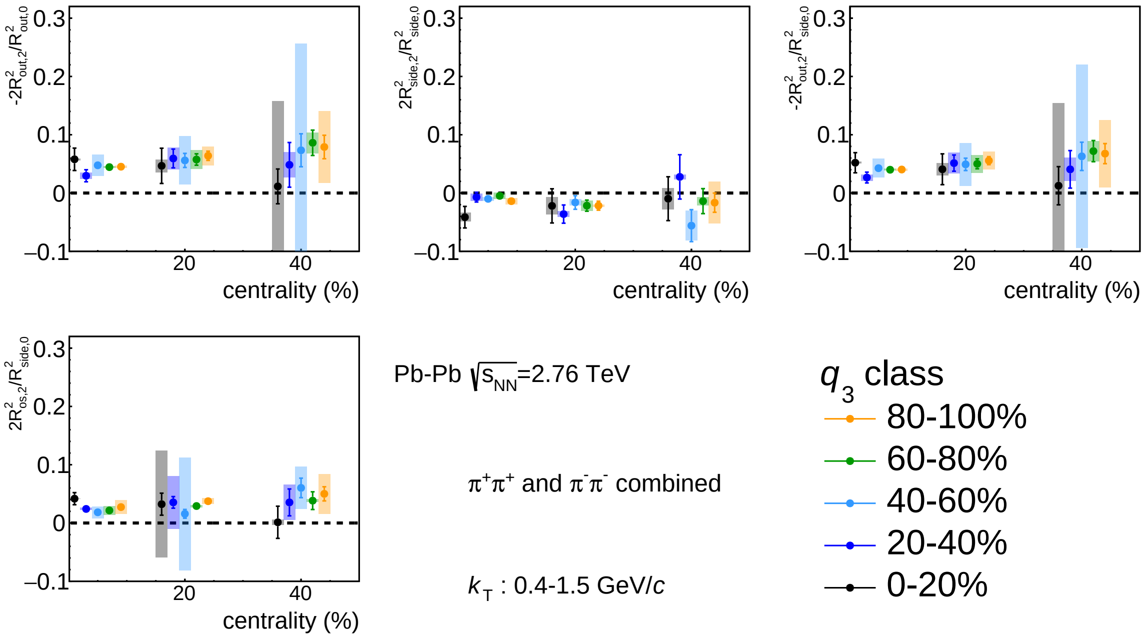

Figure 5.19: Each 20% q_3 selection is applied to relative amplitudes of squared HBT radii(R_{out}, R_{side}, and R_{os}) of charged pion pairs with respect to Ψ_3 for k_T 0.4-1.5 GeV/$c$as a function of centrality measured in Pb-Pb 2.76TeV collisions. Dashed line indicates relative amplitude of HBT radii = 0. Transparent boxes represent the systematic uncertainties. All points are shifted along the x-axis for visibility.

5.5 v_3 scaling of Final source eccentricity

As is the case for q_2 dependence of oscillation amplitude of HBT radii, it is important to investigate v_3 dependence of relative amplitudes of HBT radii relative to Ψ_3.

Figure 5.20 shows relative amplitude of charged pion HBT radii ($R_{\rm out}$, $R_{\rm side}$, $R_{\rm long}$, $R_{\rm os}$, $R_{\rm ol}$, and $R_{\rm sl}$) with respect to Ψ_3 with each 20% q_3 selection as a function of charged pion v_3. No q_3 selected results are simustaneously plotted as open markers. Azimuthal anisotropy (v_3) is sensitive probe to initial geometry and more preferable to use for x-axis than centrality.

ESE q_3 selection is applied with in a "fixed centrality", i.e. system size does not change with q_3 selection. Third order flow vector q_3 dependence of HBT radii modulation in a fixed centrality is driven by only the initial triangularity, if triangular flow is originated from initial geometrical triangularity.

Third order flow vector q_3 dependence of $-2R^2_{\rm out,3}/R^2_{\rm out,0}$ and $-2R^2_{\rm out,3}/R^2_{\rm side,0}$ do not show monotonical increasing (decreasing), more like quadratic function. $-2R^2_{\rm out,3}/R^2_{\rm out,0}$ and $-2R^2_{\rm out,3}/R^2_{\rm side,0}$ becomes small v_3 to large v_3 in small v_3 (up to 0.025) and they are increasing with increasing v_3 in large v_3 (0.025 - 0.04).

No significant q_3 dependence can be found in all the other relative amplitudes of HBT radii ($2R^2_{\rm side,3}/R^2_{\rm side,0}$, $2R^2_{\rm long,3}/R^2_{\rm long,0}$ $2R^2_{\rm os,3}/R^2_{\rm side,0}$, $2R^2_{\rm ol,3}/R^2_{\rm side,0}$, $2R^2_{\rm sl,3}/R^2_{\rm side,0}$).

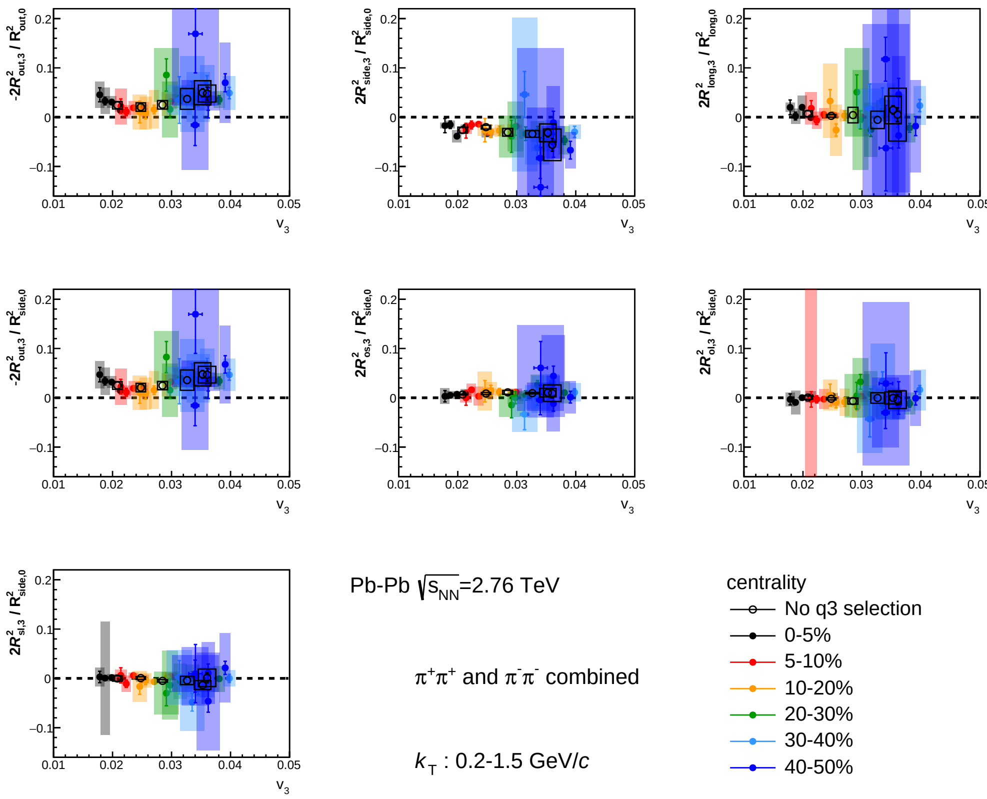

Figure 5.20: Each 20% q_3 selection, where 0-20% (80-100%) corresponds to the smallest (largest) q_3 bin, is applied to relative amplitude of squared HBT radii(R_{out}, R_{side}, R_{long}, R_{os}, R_{ol}, and R_{sl}) for charged pion pairs with respect to Ψ_3 as a function of charged pion v_3 measured in Pb-Pb 2.76TeV collisions. Pair transverse momentum k_T is integrated from 0.2 to 1.5 GeV/c. Dashed line indicates relative amplitude of HBT radii = 0. Transparent boxes represent the systematic uncertainties. Relative amplitude of HBT radii without q_3 selection also dipicted as open black circle.

Chapter 6

Conclusion

The measurements of azimuthal angle dependence of charged pion HBT radii with respect to second and third order event plane have been performed in Pb-Pb collisions at $\sqrt{s_{NN}} = 2.76$ TeV. Event Shape Engineering q_2 and q_3 selection are applied to identified hadron (π, K and p) v_2, v_3 and we has reported the new approach to relation between initial and final source shape by applying ESE technique to azimuthal angle dependence of charged pion HBT radii with respect to Ψ_2 and Ψ_3.

Explicit oscillation can be observed in azimuthal angle dependence of HBT radii($R_{\rm out}$, $R_{\rm side}$ and $R_{\rm os}$) with respect to Ψ_2. Final source eccentricity was extracted with relative amplitude of $R_{\rm side}$ and relation to initial eccentricity calculated with Glauber simulation indicates that ,in heavy ion collisions, large collective flow strongly expands the source along the short axis of elliptic shape during QGP state and final source eccentricity are significantly diluted. However initial out-plane elongated elliptic shape and centrality dependence can be observed at freeze out.

By applying Event Shape Engineering technique q_2 selection to measurement of v_2, identified hadron v_2 is significantly enhanced or suppressed for all centrality. Enhancement(suppression) of v_2 equally contributes to charged pions, kaons and protons(anti-protons), no particle species dependence can be found. Effect of q_2 on v_2 depends indeed weak on $p_{\rm T}$, however slightly larger effect can be found in lower $p_{\rm T}$. This could be interpreted anisotropic flow is driven by the low momentum particles. Also q_3 selection was applied to identified v_3 measurement. Contrary to q_2 selection to v_2, enhancement(suppression) of v_3 depends on centrality. Effect of q_3 selection is stronger in central than in peripheral. This can be considered this centrality dependence comes from insufficient Ψ_3 event plane resolution to select the initial triangular shape. As is the case in q_2 cut for v_2, the effect of q_3 selection for v_3 is independent of p_T .

Oscillation amplitude of R_{out} and R_{os} with respect to Ψ_2 significantly changes with q_2 selection and relative amplitude of R_{side} is slightly enhanced(suppressed) with q_2 selection. In most central 0-5% collisions and smallest q_2 selected events, relative amplitude of R_{side} has zero or negative value, though R_{out} oscillation has same sign to the other centrality and q_2 class. This can be interpreted initial elliptic shape might be vanished or even reversed at freeze out due to small initial eccentricity and large elliptic flow. In centrality 20-40% collisions, oscillation amplitude of R_{side} does not depends on the q_2 selection.

Blast wave approach has performed to azimuthal angle dependence of HBT radii relative to Ψ_2 with q_2 selection to interpret the difference of oscillation amplitude. second order oscillation in transverse flow explicitly enhanced(suppressed) with larger(smaller) q_2 selection, and final source eccentricity is slightly modified with q_2 selection. However freeze out time and emission duration do not show significant changes with q_2 cut.

For azimuthal angle dependence of HBT radii with respect to Ψ_3, no significant oscillation can be found in relative amplitude of R_{long} , R_{ol} and R_{sl} , but $-2R^2_{out,3}/R^2_{out,0}$ has positive value and $2R^2_{side,3}/R^2_{side,0}$ is negative value for all centrality. $-2R^2_{out,3}/R^2_{out,0}$ becomes larger from central to peripheral, while $2R^2_{side,3}/R^2_{side,0}$ slightly decrease with increasing centrality. $2R^2_{os,3}/R^2_{side,0}$ has positive or zero and no significant centrality dependence can be found.

Contrary to q_2 selection to HBT measurement relative to Ψ_2, no significant modification can be found in q_3 selection to azimuthal angle dependence of HBT radii with respect to Ψ_3, though v_3 is explicitly enhanced(suppressed) with larger(smaller) q_3 selection.

Three interpretation can be considered to this result. First one is q_3 selectivity is not sufficient to change the relative amplitude of HBT radii. Sensitivity of initial triangular shape can be different between HBT measurement and flow measurement. Second possibility is oscillation amplitude of HBT radii with respect to Ψ_3 are not dominated by triangular flow. Third possibility is triangular flow is not originated from hydrodynamical expansion.

Bibliography

[1] J. Beringer *et al.*, "Review of Particle Physics", Phys.Rev. D86 (2012) 010001

[2] S. Aoki *et al.*, "2+1 Flavor Lattice QCD toward the Physical Point", Phys.Rev. D79 (2009) 034503

[3] A. Bazavov *et al.*, "Equation of state and QCD transition at finite temperature", Phys.Rev. D80 (2009) 014504

[4] R. Snellings, "Elliptic Flow: A Brief Review", New J.Phys. 13 (2011) 055008

[5] M. L. Miller *et al.*, "Galuber Modeling in High Energy Nuclear Collisions", nucl-ex/0701025 (2007)

[6] T.Matsui, "Dynamical evolution of the Quark-Gluon Plasma and Phenomenology", Nucl.Phys. A461, 27 (1987)

[7] L. McLerran *et al.*, "Gluon distribution functions for very large nuclei at small transverse momentum", Phys.Rev.D49,3352 (1994)

[8] I. G. Bearden *et al.*, "Collective expansion in high-energy heavy ion collisions", Phys.Rev.Lett. 78 (1997) 2080-2083

[9] B. Abelev *et al.*, "Centrality dependence of π, K, and p production in Pb-Pb collisions at $\sqrt{s_{NN}}$ = 2.76 TeV", Phys.Rev. C88 (2013) 044910

[10] E. Schnedermann *et al.*, "Thermal phenomenology of hadrons from 200A GeV S+S collisions", Phys.Rev.C48 (1993) 2462-2475

[11] C. Gale *et al.*, "Event-by-Event Anisotropic Flow in Heavy-ion Collisions from Combined Yang-Mills and Viscous Fluid Dynamics", Phys.Rev.Lett. 110 (2013) no.1, 012302

[12] A. Adare *et al.*, "Measurements of Higher-Order Flow Harmonics in Au+Au Collisions at $\sqrt{s_{NN}}$ = 200 GeV", Phys.Rev.Lett. 107 (2011) 252301

[13] K. Aamodt *et al.*, "Higher Harmonic Anisotropic Flow Measurements of Charged Particles in Pb-Pb Collisions at $\sqrt{s_{NN}}$ = 2.76 TeV", Phys.Rev.Lett. **107**, 032301 (2011)

[14] S. Mohapatra *et al.*, "Measurement of the distribution of event-by-event harmonic flow in Pb-Pb collisions at $\sqrt{s_{NN}}$ = 2.76 TeV with ATLAS detector", J.Phys.Conf.Ser. 446 (2013) 012024

[15] J. Schukraft, A. Timmins and S. A.Voloshin, "Ultra Relativistic nuclear collisions: Event shape engineering", Phys.Lett.B 719 (2013) 394-398

[16] J. Jia and P. Huo, "Forward-backward eccentricity and participant-plane angle fluctuations and their influences on longitudinal dynamics of collective flow", Phys.Rev.C90 (2014) no.3, 034915

[17] G. Aad *et al.*, "Measurement of the correlation between flow harmonics of different order in lead-lead collisions at $\sqrt{s_{NN}}$ = 2.76 TeV with ATLAS detector", Phys. Rev. C92, 034903 (2015)

[18] M. Luzum and P. Romatschke, "Conformal relativistic viscous hydrodynamics: Applications to RHIC results at $\sqrt{s_{NN}}$ = 200 GeV", Phys. Rev. C 78, 034915

[19] J. Adam *et al.*, "Event shape engineering for inclusive spectra and elliptic flow in Pb-Pb collisions at $\sqrt{s_{NN}}$ = 2.76 TeV", Phys.Rev. C93 (2016) no.3, 034916

[20] R. Hanbury Brown and R. Q. Twiss, "A test of a new type of stellar interferometer on Sirius", Nature 178, 1046-104

[21] G. Goldhaber *et al.*, "Infuence of Bose-Einstein Statistics on the Antiproton-Proton Annihilation Process", Phys.Rev. 120 (1960) 300-312

[22] S. Pratt, "Coherence and Coulomb effects on pion interferometry", Phys.Rev.D 33, 72

[23] G. Bertsch *et al.*, "Pion Interferometry in Ultra Relativistic Heavy-Ion Collisions", Phys.Rev. C37 (1988) 1896-1900

[24] M. A. Lisa *et al.*, "Femtoscopy in relativistic heavy ion collisions", Ann.Rev.Nucl.Part.Sci. 55 (2005) 357-402

[25] A. Adare *et al.*, "Systematic study of charged-pion and kaon femtoscopy in Au + Au collisions at $\sqrt{s_{NN}}$ = 200 GeV", Phys. Rev. C 92, 034914

[26] S. Acharya *et al.*, "Kaon femtoscopy in Pb-Pb collisions at $\sqrt{s_{NN}}$ = 2.76 TeV", Phys.Rev. C96 (2017) no.6, 064613

[27] Y. M. Simyukov *et al.*, "On m_T dependence of femtoscopy scales for meson and baryon pairs", Nucl. Phys. A **946**, 227 (2016)

[28] J. Adams *et al.*, "Azimuthally Sensitive Hanbury Brown-Twiss Interferometry in Au+Au Collisions at $\sqrt{s_{NN}}$ = 200 GeV", Phys.Rev.Lett. 93, 012301

[29] L. Adamczyk *et al.*, "Beam-energy-dependent two-pion interferometry and the freeze-out eccentricity of pions measured in heavy ion collisions at the STAR detector", Phys.Rev. C92 (2015) no.1, 014904

[30] E. Frodermann *et al.*, "Evolution of pion HBT radii from RHIC to LHC: Predictions from ideal hydrodynamics", J.Phys. G34 (2007) 2249-2254

[31] S. A. Voloshin, "Femtoscopy of the system shape fluctuations in heavy ion collisions", J.Phys. G38 (2011) 124097

[32] A. Adare *et al.*, "Azimuthal Angle Dependence of Charged-Pion Interferometry Measured with Respect to Second- and Third-Order Event Planes in Au+Au Collisions at $\sqrt{s_{NN}}$ = 200 GeV", Phys.Rev.Lett. 112, 2223011

[33] C. J. Plumberg, C. Shen and U. Heinz, "Hanbury-Brown-Twiss interferometry relative to the triangular flow plane in heavy-ion collisions", Phys. Rev. C 88, 044914

[34] P. Bożek, "Azimuthally sensitive femtoscopy in event-by-event hydrodynamics", Phys. Rev. C 89, 044904

[35] LHC guids, https://cds.cern.ch/record/2255762/files/CERN-Brochure-2017-002-Eng.pdf

[36] The accelerator complex, http://public-archive.web.cern.ch/public-archive/en/research/AccelComplex-en.html

[37] O. S. Bruňing *et al.*, "LHC Design Report Volume I:The LHC Main Ring",CERN-2004-003-V1 (2004)

[38] N. Angert *et al.*, "CERN Heavy-Ion Facility Design Report",CERN-93-01 (1993)

[39] D. Swoboda *et al.*, "Status of the ALICE Magnet System", IEEE Transaction On Applied Superconductivity vol.12, no.1, 2002

[40] G. Dellacasa *et al.*, "Technical design report of time projection chamber", CERN-OPEN-2000-183, CERN-LHCC-2000-001

[41] G. Dellacasa *et al.*, "Technical design report of inner tracking system", CERN-LHCC-99-12 1999

[42] The most complex Silicon Detectors, http://slideplayer.com/slide/577928/

[43] Silicon Strip Detector- ALICE Collaboration -CERN, http://aliceinfo.cern.ch/SSD/

[44] V. Altini for the ALICE Collaboration, "The ALICE Inner Tracking System: performance with proton and lead beams", poster in Quark Matter2011

[45] G. Dellacasa *et al.*, "Technical design report of the Time Of Flight System", CERN-LHCC-2000-012

[46] Time of Flight for ALICE Experiment, http://www.bo.infn.it/alice/tof-over/index.html

[47] ALICE Experiment web page , http://alice.web.cern.ch/content/experiment

[48] A. Alici, "Status and performance of the ALICE MRPC-based Time-Of-Flight detector", 2012 JINST 7 P10024

[49] Cortese, P *et al.*, "Technical design report on Forward Detectors:FMD, T0 and V0", CERN-LHCC-2004-025

[50] B. Abelev *et al.*, "Centrality detemination of Pb-Pb collisions at $\sqrt{s_{NN}}$=2.76 TeV with ALICE", Phys.Rev.C **88**, 044909 (2013)

[51] P. Billoir *et al.*, "Track element merging strategy and vertex fitting in complex modular detectors", Nucl. Instr. Meth. A241 (1985) 115-131

[52] A.M.Poskanzer and S.A.Voloshin, "Methods for analyzing anisotropic flow in relativistic nuclear collisions", Phys.Rev.C 58, 1671 (1998)

[53] B. Abelev *et al.*, "Anisotropic flow of charged hadrons, pions and (anti-)protons measured at high transverse momentum in Pb-Pb collisions at $\sqrt{s_{NN}}$ = 2.76 TeV", Phys.Lett.B 719 (2013) 18-28

[54] C. Zampolli, "Particle Identification with the ALICE detector at LHC", talk in Physics at LHC 2012

[55] B. Abelev *et al.*, "Performance of the ALICE Experiment at the CERN LHC", Int.J.Mod.Phys.A 29 (2014) 1430044

[56] J. Adam *et al.*, "Particle identification in ALICE: a Bayesian approach", Eur.Phys.J.Plus 131 (2016) no.5, 168

[57] S. Pratt *et al.*, "Detailed predictions for two pion correlations in ultrarelativistic heavy ion collisions", Phys.Rev. C42 (1990) 2646-2652

[58] M. G. Bowler , "Coulomb corrections to Bose-Einstein corrections have greatly exaggerated", Phys.Lett. B270 (1991) 69-74(1991)

[59] X. N. Wang and M. Gyulassy, "HIJING: A Monte Carlo model for multiple jet production in pp, pA and AA collisions", Phys.Rev.D44 (1991) 3501-3516 LBL-31036

[60] D. Adamovà *et al.*, "Azimuthally Differential Pion Femtoscopy in Pb-Pb Collisions at $\sqrt{s_{\mathrm{NN}}}$ = 2.76 TeV", Phys.Rev.Lett. 118 (2017) no.22, 222301

[61] J. Adam *et al.*, "Centrality dependence of pion freeze-out radii in Pb-Pb collisions at $\sqrt{s_{\mathrm{NN}}}$ = 2.76 TeV", Phys.Rev. C93 (2016) no.2, 024905

[62] J. Adam *et al.*, "Higher harmonic flow coefficients of identified hadrons in Pb-Pb collisions at $\sqrt{s_{\mathrm{NN}}}$ = 2.76 TeV", JHEP 1609 (2016) 164

[63] F. Retière and M. A. Lisa, "Observable implications of geometrical and dynamical aspects of freeze out in heavy ion collisions", Phys.Rev. C70 (2004) 044907

[64] C. Adler *et al.*, "Elliptic flow from two- and four-particle correlations in Au+Au collisions at $\sqrt{s_{NN}}$ = 130 GeV", Phys. Rev. C66 (2002) 034904

[65] A. Adare *et al.*, "Systematic study of azimuthal anisotropy in Cu + Cu and Au + Au collisions at $\sqrt{s_{NN}}$ = 62.4 and 200 GeV", Phys. Rev. C92 (2015) 034913